

Mesoscale variability of the  
Northern Current in the Gulf of Lions  
and the role of bottom topography

by M<sup>a</sup> Mar Flexas



Mesoscale variability of the  
Northern Current in the Gulf of Lions  
and the role of bottom topography

MEMÒRIA

per optar al títol de Doctor en Ciències del Mar  
Programa de Doctorat en Ciències del Mar UPC - UB - CSIC  
realitzada al Laboratori d'Enginyeria Marítima LIM / UPC  
de la Universitat Politècnica de Catalunya  
i a la Technische Universiteit Eindhoven  
defensada a  
Barcelona el Juliol de 2003

per

MARIA DEL MAR FLEXAS

This dissertation has been written under the supervision of:

Dr. Marc A. Garcia

Prof. G.J.F. van Heijst

and

Prof. Agustin Sanchez-Arcilla

Granted by an FI and a BE grant from the Generalitat de Catalunya, a CLUSTER grant from the TU/e and a SOCRATES grant from the UPC.

Supported by PRECARIOS, a postgraduate's organization whose dedication and effort contribute to improve young scientists working conditions in Spain: *www.precarios.org*.

A la memòria dels nostres padrins

No todo se ha perdido;  
vienen  
a mi memoria siempre tus palabras  
—claras, firmes, sonoras—  
trayéndola, llevándola.  
ANGEL GONZALEZ

Érase una vez  
un lobito bueno  
al que maltrataban  
todos los corderos.

Y había también  
un príncipe malo  
una bruja hermosa  
y un pirata honrado.

Todas estas cosas  
había una vez  
cuando yo soñaba  
un mundo al revés.

J.A. GOYTISOLO

# Contents

<b>1</b>	<b>Introduction</b>	<b>5</b>
1.1	Motivation and objectives . . . . .	5
1.2	Strategy . . . . .	6
1.3	Overview of the thesis . . . . .	6
<b>2</b>	<b>A review on the mesoscale variability of circulation in the Gulf of Lions</b>	<b>7</b>
2.1	Introduction . . . . .	7
2.2	Overview of the Western Mediterranean Circulation . . . . .	8
2.2.1	The flow of Modified Atlantic Water . . . . .	9
2.2.2	Circulation of Levantine Intermediate Water and Tyrrhenian Dense Water . . . . .	12
2.2.3	Western Mediterranean Deep Water . . . . .	13
2.3	Mesoscale dynamics on the Gulf of Lions continental shelf . . . . .	14
2.3.1	Influence of N-NW winds . . . . .	14
2.3.2	The shelf-slope density front . . . . .	17
2.4	Mesoscale dynamics on the Gulf of Lions continental slope . . . . .	18
2.4.1	The Northern Current . . . . .	18
2.4.2	Influence of bathymetry and winds on the Northern Current . . . . .	19
2.4.3	Mesoscale variability associated to the Northern Current . . . . .	20
2.5	Open sea mesoscale dynamics . . . . .	21
2.5.1	Seaward migration of Northern Current mesoscale variability . . . . .	21
2.5.2	Deep water formation . . . . .	22
2.6	Summary and open issues . . . . .	23
<b>3</b>	<b>Flow variability in the Gulf of Lions during the MATER High Frequency Flux experiment (March–May 1997)</b>	<b>25</b>
3.1	Introduction . . . . .	26
3.2	Material and methods . . . . .	27
3.2.1	Physiography of the HFFE site . . . . .	27
3.2.2	Current meter and ancillary data . . . . .	29
3.2.3	Analytical model . . . . .	29
3.3	Results . . . . .	31
3.3.1	Statistical analysis of the currents . . . . .	31

3.3.2	Variability of the currents . . . . .	36
3.4	Discussion . . . . .	45
3.4.1	Origin of the mesoscale variability of the surface currents . . . . .	45
3.4.2	Origin of the mesoscale variability of the deep near-bottom currents . . . . .	47
3.4.3	Repercussion on the local budgets of organic carbon . . . . .	48
3.5	Summary and conclusions . . . . .	48
<b>4</b>	<b>A laboratory model of the Northern Current: jet flows over a continental slope</b>	<b>51</b>
4.1	Introduction . . . . .	51
4.2	Theoretical framework . . . . .	53
4.2.1	Governing equations . . . . .	53
4.2.2	Formulation of the problem . . . . .	56
4.2.3	Jets over a sloping bottom and jets on a beta-plane . . . . .	59
4.3	Experimental techniques . . . . .	64
4.3.1	General experimental arrangement . . . . .	64
4.3.2	Dynamic similarity . . . . .	65
4.3.3	Experimental set-up for the topographic slope . . . . .	69
4.3.4	Parabolic bottom topography experiments . . . . .	69
4.3.5	Flat bottom experiments . . . . .	70
4.3.6	Analysis of source-sink flows . . . . .	70
4.4	Flow measurements . . . . .	73
4.5	Results . . . . .	75
4.5.1	Jets over parabolic bottom ( <i>uniform</i> water depth) . . . . .	76
4.5.2	Prograde jets over sloping bottom . . . . .	79
4.5.3	Retrograde jets over sloping bottom . . . . .	87
4.5.4	Jets over flat bottom . . . . .	92
4.6	Interpretation of results and discussion . . . . .	94
4.6.1	Jets on an f-plane . . . . .	94
4.6.2	Jets over sloping bottom . . . . .	94
4.6.3	On the role of the topographic free surface . . . . .	102
4.7	Summary and conclusions . . . . .	103
<b>5</b>	<b>Numerical solution for barotropic jets over a sloping bottom: comparison to a laboratory model</b>	<b>107</b>
5.1	Introduction . . . . .	107
5.2	Numerical model . . . . .	109
5.2.1	Equations . . . . .	109
5.2.2	Configuration . . . . .	110
5.2.3	Experimental cases . . . . .	111
5.3	Simulation of the laboratory experiments . . . . .	112
5.3.1	Velocity profile . . . . .	112
5.3.2	General results using laboratory flow profiles . . . . .	113



5.3.3	Onset of jet instabilities . . . . .	118
5.4	Further investigations . . . . .	122
5.4.1	Influence of the location of the jet over the slope . . . . .	122
5.4.2	Influence of the jet width . . . . .	123
5.4.3	Influence of the velocity profile . . . . .	124
5.4.4	Synthesis . . . . .	128
5.5	Comparison with oceanic field data . . . . .	129
5.6	Summary and conclusions . . . . .	135
<b>6</b>	<b>Summary and conclusions</b>	<b>137</b>
	<b>Bibliography</b>	<b>141</b>
	<b>Castell d'iràs i no tornaràs</b>	<b>147</b>
	<b>Acknowledgements</b>	<b>151</b>
	<b>Curriculum Vitae</b>	<b>153</b>



# Chapter 1

## Introduction

Así pues, antes de leer en voz alta y  
delante de muchas criaturas unos poemas,  
lo primero que hay que hacer es pedir ayuda al duende (...)  
FEDERICO GARCIA LORCA

### 1.1 Motivation and objectives

The Northern Current flows cyclonically contouring the continental slope in the NW Mediterranean. High mesoscale variability has been reported in past studies, relating this activity to current meandering and eddy formation. Its major variability has been found in 2 – 10 days period meanders with phase speeds of 10 – 20 km/day. The study of its variability is of special interest in terms of transport of properties along and across the continental slope and continental shelf-slope interactions which lead to important biogeochemical processes.

Many authors have discussed the influence of baroclinic instability on the NC's mesoscale variability. The purpose of this thesis is to investigate the role of topography on the observed mesoscale variability patterns of the Northern Current in the vicinity of the Gult of Lions. For this purpose we will employ a field experiment, a series of laboratory experiments, and a numerical code.

At the outset we must recognize that a complete characterization of the Northern Current dynamics is not possible since a width of phenomena are at play. The observed velocity field contains contributions from the coastal trapped waves, Kelvin waves, baroclinic and barotropic instabilities, Rossby waves, the influence of river discharges, thermohaline convection, deep water formation and wind driven currents.

We will study the problem by means of laboratory and numerical experiments. Laboratory conditions enable us to simulate qualitatively some of the principal features, in an environment where most parameters can be matched. They allow an easy control of the physics: we can isolate them. But one should always be aware that laboratory simulations are not the real ocean, and that to generate a background flow like the ocean is just

impossible. A similar discourse applies to numerical simulations.

## 1.2 Strategy

We will take profit of field data from the MAST-III MATER project. The aims of the project were to study the mass transfer and exchange on the continental slope of the Gulf of Lions (off Marseille). The MATER field data will give us relevant field information (SST images and current meter data provide horizontal velocity field; hydrographic data from CTDs provides the density structure), to quantify the scales of flow variability in the Gulf of Lions. These data are useful to describe what happens in the sea. In order to go further, we investigate the barotropic dynamics in a simplified laboratory experiment, using the field data to choose appropriate laboratory conditions.

As mentioned above, our goal is to explore the effects of bottom topography in the Northern Current mesoscale variability. According to field observations the bottom topography may play a role on the observed variability. This hypothesis is tested in laboratory experiments and using some numerical tests where we can vary the topography and study the variability.

The principal aims of the laboratory experiments are to generate a slope current interacting with the topography scaled to that of the Gulf of Lions. Moreover, a current flowing in the direction opposite to that of the Northern Current will also be modelled to obtain a broader view of the problem.

Finally, we will use a robust numerical code to simulate the laboratory conditions, which will help us to verify the reliability of the laboratory observations and it will also allow us to go further in the analysis of barotropic instability.

## 1.3 Overview of the thesis

The outline of this thesis begins with a literature review of the mesoscale flow variability observed in the NW Mediterranean associated to the Northern Current in chapter 2. Chapter 3 describes the field experiments and discusses the various data obtained. Chapter 4 describes the laboratory experiments designed to provide insight into the basic physics that will attempt to explain the observations made in the field. Chapter 5 is devoted to numerical simulations used to simulate the laboratory conditions and to study the role of the initial jet profile on the stability of the current. Finally, chapter 6 delineates the principal findings of this research and summarizes the conclusions of this work.

# Chapter 2

## A review on the mesoscale variability of circulation in the Gulf of Lions

Any important civilization writes its own history,  
selectively extracts data from the past and  
sometimes presents them as inexorable laws.  
SUSANTHA GOONATILAKE

### 2.1 Introduction

The Mediterranean basin is divided into the western and eastern basins by the relatively shallow Strait of Sicily. The larger seas and basins contained in the Western Mediterranean Sea are the Alborán Sea, the Algerian basin, the Tyrrhenian Sea, the Liguro-Provençal basin and the Catalan or Balearic Sea (Fig. 2.1).

The 200 m depth isobath is commonly used in the NW Mediterranean to separate the continental shelf from the continental slope. The width of the continental shelf is quite variable in the NW Mediterranean, being sometimes specially wide, as occurs in the Gulf of Lions (Fig. 2.1). In these wide and relatively shallow regions sea breezes, strong northern winds and storms can strongly influence the flow, in contrast to waters beneath the 200 m isobath.

The continental slope separates the continental shelf from the wide open sea. Over most of the NW Mediterranean, the continental slope is a relatively narrow zone, where the bathymetry abruptly changes —the change from 200 m down to 2000 m depth occurs within a few tens of kilometers. The continental slope is often interrupted by submarine canyons. Canyons in the Gulf of Lions are irregularly distributed in contrast to those in the northern part of the Catalan coast which are regularly spaced (Fig. 2.2).

The marine circulation along the NW Mediterranean continental shelves and slopes, and in particular that in the area of the Gulf of Lions, is far from simple and well understood. During late spring and summer, the whole NW Mediterranean is strongly stratified. The seasonal thermocline is 20 – 50 m deep. In winter, the water column is rather homo-

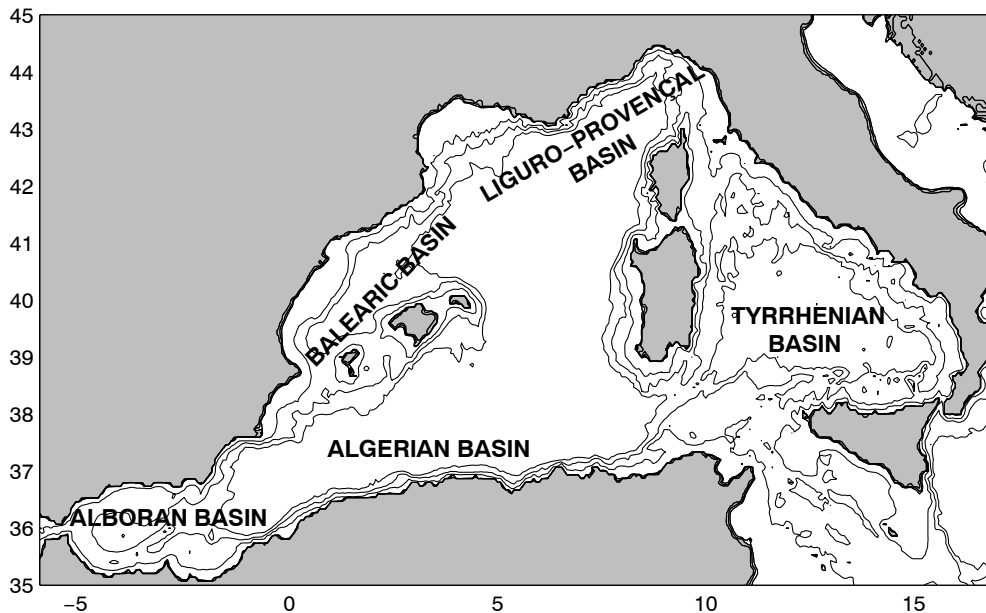


Figure 2.1: Mediterranean Sea basins (deg. North and East are positive).

geneous, specially in the open sea. The isolated and combined action of several factors like strong winds, the presence of a shelf-slope density front and a complex bottom topography due to the existence of a sloping bottom and submarine canyons commented above lead to complicated circulation patterns.

Mesoscale variability is defined as the ensemble of flow fluctuations whose periods range from the order of a few days to the order of a few tenths of days. Many events are included in this broad definition, among which we are mostly interested in mesoscale variability associated to small gyres or vortices (i.e. mesoscale eddies). These flow variability patterns are observed to modify the general circulation in the NW Mediterranean. Among other characteristics, they are able to block the general circulation, they are supposed to contribute in the exchange between the continental shelf waters and slope waters, and they are associated to vertical motions that allow the rising or sinking of water and nutrients. Therefore, they often have strong biological, geological and chemical implications.

## 2.2 Overview of the Western Mediterranean Circulation

In the Mediterranean basin, the main water masses that can be found are (i) the surface waters coming from the Atlantic Ocean, namely the Modified Atlantic Water (MAW), (ii) the Levantine Intermediate Water (LIW) and (iii) the Western Mediterranean Deep Water

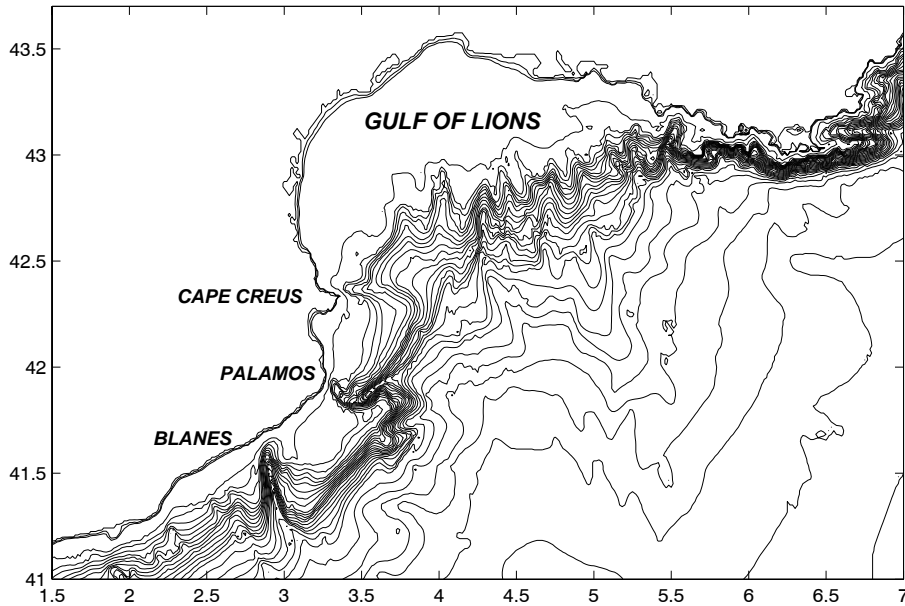


Figure 2.2: Bathymetry of the Gulf of Lions and the Catalan Sea. Isolines are separated 100 m depth (deg. North and East are positive).

(WMDW). The most recent comprehensive review written on the circulation of these water masses in the Western Mediterranean Sea is by Millot [Millot, 1999]. In this section we outline the main characteristics of the circulation of these water masses.

### 2.2.1 The flow of Modified Atlantic Water

The origin of the circulation in the Mediterranean Sea relies in its sole connection to the open ocean: the Strait of Gibraltar, a shallow and narrow aperture that connects the Mediterranean to the Atlantic Ocean. The Strait of Gibraltar allows a selective renewal of Mediterranean Sea waters. Low-density Atlantic waters intrude into the Mediterranean as surface waters, while denser Mediterranean waters (high salinity waters due to low fresh-water supplies and high evaporation) travel at mid-depths into the Atlantic Ocean.

The inflow of Atlantic waters spreads along the Algerian coast, due to the Coriolis force, resulting in a general anticlockwise flow. This surface water of Atlantic origin is modified during its travel along the Mediterranean coasts, acquiring different thermohaline characteristics—it becomes saltier and, therefore, denser. This surface water is named Modified Atlantic Water (MAW) and is confined in a layer of 100 to 200 m depth.

The general circulation of MAW is represented in Fig. 2.3. The intrusion of Atlantic water into the Alborán Sea draws two anticyclonic gyres, from which only the most westward gyre shows a permanent anticyclonic motion. The most eastward gyre is more variable, and although most of the time shows up as anticyclonic, it has also been recorded as cyclonic [Viúdez and Tintoré, 1995]. When the most eastward gyre is depicted as anticyclonic, its easternmost circulation branch that joins the Iberian peninsula to Algeria is

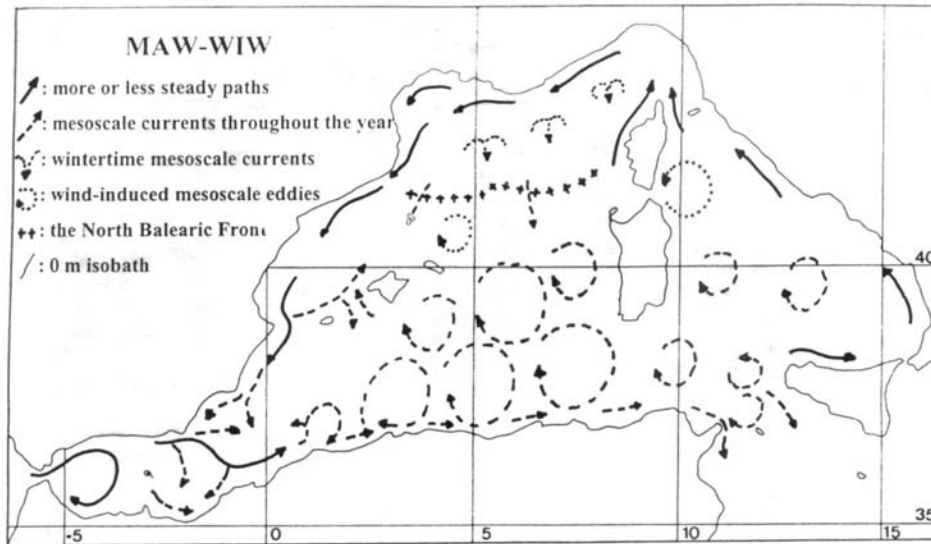


Figure 2.3: MAW path [from Millot (1999)].

named the Almería-Orán front, which has been frequently surveyed (major recent research efforts have been the EU OMEGA and MATER projects). Small cyclonic gyres have been observed to be linked to both anticyclonic gyres.

In its eastward flow, the MAW flows into the Algerian basin as the Algerian current, a relatively narrow and deep current of 30 – 50 km wide and 200 – 400 m deep at the coast, which becomes thinner (in depth) and wider (in horizontal extension) eastwards [Benzohra and Millot, 1995]. The Algerian current flows following the Algerian slope till the Channel of Sardinia. The instability of the Algerian current develops a series of coastal eddies. Although both cyclonic and anticyclonic motions have been observed, only the anticyclonic gyres last for a long time —i.e. for weeks or months. These gyres are associated with a non-wind-induced upwelling. The vertical extent of these mesoscale coastal eddies is what remains more uncertain. The Algerian current and its mesoscale phenomena have been considered as a whole, i.e. as a system where the Algerian current meanders due to its unstable character and generates a coastal mesoscale eddy and a large eddy in the deeper layer, with both axes initially not centred [Millot, 1994]. This motion has been successfully reproduced in the laboratory by Obaton [Obaton et al., 2000].

The flow of the Algerian current following the Algerian slope can be blocked by the presence of open sea eddies. The interaction of the Algerian current with an open sea eddy can deviate the Algerian current from the Algerian slope directly towards the Balearic Islands [Taupier-Letage and Millot, 1988]. These open sea eddies are considered as late stages of coastal eddies. Their eastward progression is topographically constrained by the Channel of Sardinia where such deep structures are forced to flow northwards, contributing to the unstable flow west of Corsica, to finally turn westwards to return into the Algerian basin. The extension of recent MAW from the Algerian basin into the Balearic basin is delimited by the North-Balearic front.



The MAW enters from the Algerian basin into the Tyrrhenian Sea either as a wide current or as a narrow current flowing along the Tunisian coast, to continue its cyclonic path along the Italian coasts. An occasional cyclonic eddy is placed in the northern part of the Tyrrhenian Sea, and it is associated with an upwelling induced by westerly winds. The MAW flows through the Channel of Corsica with a significant seasonal and annual variability of the flux, which is attributed to the atmospheric conditions over the Liguro-Provençal basin [Astraldi and Gasparini, 1992].

The northward currents on the east and west coasts of Corsica join to form the Northern current, which flow mainly following the continental slope in the Liguro-Provençal basin. Part of the flow is directed southwards along the coasts of Sardinia into the Algerian basin, giving to the Algerian basin a supply of MAW apart from the new MAW intruded from the Alborán sea.

The Northern Current flows following the continental slope along the French coasts and the Iberian peninsula until the Channel of Ibiza, and flows perpendicularly to a thermal front (the Pyrenees front) that separates cold waters from the Liguro-Provençal basin from warmer waters from the Balearic basin. This front shows seasonal variability and has its origin in the cold and strong northwesterlies blowing in the Liguro-Provençal basin, which are blocked by the Pyrenees and therefore damped in the Balearic basin.

The Northern Current is reinforced by the presence of a density front that separates continental waters from slope waters. This density front is observed in the Gulf of Lions and all along the eastern coasts of the Iberian peninsula (where it is named as the Catalan front), and its geostrophic adjustment enhances the surface signature of the Northern Current.

Once in the Balearic basin, at its southernmost extent, the Northern Current is divided into a flow along the northern coasts of the Balearic Islands and a southward flow intruding the Alborán Sea. The latter flow completes the entire 'cyclonic' gyre of the MAW.

### **Winter Intermediate Water**

During winter, the Northwestern Mediterranean Sea is characterized by strong cold northwesterly winds. When these winds are persistent and strong they can cool the surface MAW so it becomes denser and sinks. This newly formed water will be overlaid by MAW from the surroundings and will receive the name of Winter Intermediate Water (WIW). Therefore, this winter mechanism produces a water with the same characteristics of the MAW but with a minimum in temperature located just beneath the MAW. This mechanism of formation was proposed by Conan and Millot [Conan and Millot, 1995]. The formation of WIW is common in the whole northwestern Mediterranean sea in winter, but the coldest WIW is found in the north. The WIW follows the MAW along the continental slopes of France and the Iberian peninsula to finally intrude into the Algerian basin, although it can also be introduced directly from the Gulf of Lions if it interacts with eddies associated to the North-Balearic front.

The formation of WIW has special importance in the mixing of MAW with the under-

lying water, the Levantine Intermediate Water (LIW) —since the WIW has intermediate characteristics between MAW and LIW, the presence of WIW will facilitate their mixing.

### 2.2.2 Circulation of Levantine Intermediate Water and Tyrrhenian Dense Water

The Levantine Intermediate Water (LIW) flows underlying the MAW and the WIW. This intermediate water has its origin in the Eastern Mediterranean basin and is introduced in the Western Mediterranean basin through the Channel of Sicily. It is characterized by a maximum in temperature and salinity below 200 m depth.

Initially considered only as one single water mass, LIW nowadays is distinguished from the Tyrrhenian Dense Water (TDW), another intermediate water, cooler and denser than the LIW. The formation of TDW is due to mixing, caused by the intrusion of LIW into the Tyrrhenian Sea by cascading from 200 m to nearly 1800 m depth. Mixing is even more complex since new entered intermediate waters encounter part of intermediate waters than have been travelling along the Western Mediterranean and return from the Algerian basin into the Tyrrhenian Sea. These new and old intermediate water masses interact (the result is denser than the new-entered LIW alone) producing even more cascading, and hence, more mixing. Some studies show also that deep water (WMDW) formed in the Liguro-Provençal basin flows to the Algerian basin and finally into the Thyrrhenian Sea, where it is mixed with newly entered LIW [Rhein et al., 1999]. The result of all these mixing processes is what is known as TDW. Although TDW is denser than LIW, its path can be generalized as the same as the latter (Fig. 2.4).

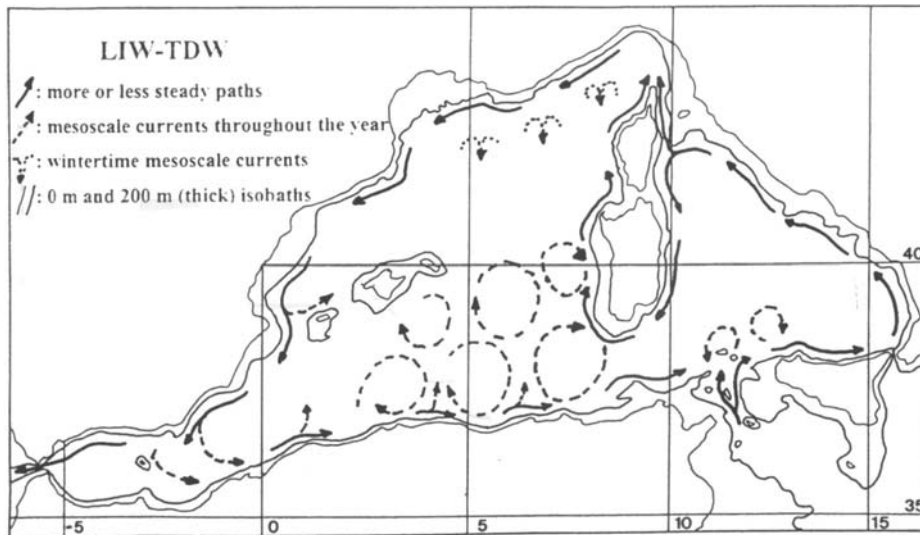


Figure 2.4: LIW+TDW path [from Millot (1999)].

In the Tyrrhenian Sea, the LIW+TDW is in geostrophic balance, flowing anticlockwisely along the continental slope, and continuing along the western coasts of Sardinia. In

the southwest coast of this island, the LIW+TDW presents its maximum variability: from being a relatively narrow vein in the south of Sardinia, it becomes wider (in horizontal direction), thinner (in depth) and cooler in the west of the island. These changes have been attributed to the interaction with open sea Algerian eddies that migrate from the Algerian slope to open waters, and also to the inherent instabilities of the intermediate water vein that is presumably able to generate anticyclonic structures. Millot [Millot, 1999] proposed to name these anticyclones as ‘Leddies’, similar to naming of the Atlantic Meddies.

The LIW+TDW continue flowing along the continental slope of Corsica in an anti-clockwise path similar to the MAW, along the slopes of the Liguro-Provençal basin (where typical  $\sigma_S$ -values, being  $\sigma$  the potential temperature, are  $13.4 - 13.5$  °C and  $38.50 - 38.55$  (salinities are normally given without units)), only disturbed by occasional winter seaward spreading. Its general path continues along the Iberian peninsula continental slopes towards the Alborán Sea and part of it towards the Algerian basin following the Almería-Orán front or the westernmost Alborán anticyclonic gyre. Once there, the LIW+TDW is no more present as a vein, but it still follows the Algerian slope, until it interacts with an Algerian eddy and it is exported northwards.

### 2.2.3 Western Mediterranean Deep Water

The deep water beneath the TDW is the Western Mediterranean Deep Water (WMDW). The WMDW is formed in the Gulf of Lions during severe winter conditions. Its origin lies in vertical mixing produced by small plumes of the order of a few hundreds of meters in diameter with vertical velocities of the order of  $10 \text{ cm s}^{-1}$  that develop into convective cells with downward vertical speeds of  $1 \text{ mm s}^{-1}$  [Gascard, 1978]. Eddies of a few km in diameter develop (maybe due to baroclinic instability) and contribute to re-stratification. The WMDW does not form every winter: during mild winters this mixing process forms intermediate waters resting above 1500 m depth.

The mean  $\sigma_S$ -characteristics of WMDW are  $12.7 - 12.80$  °C and  $38.44 - 38.46$  although they have been seen to change with a 10-year period, showing an increasing tendency in both salinity and temperature (about  $0.03$  °C/10 years and  $0.02$ /10 years) [Millot, 1999]. Waters with different characteristics have been detected close to the bottom and they have been named as Bottom Water (BW). These bottom waters can be formed during very different conditions.

The WMDW formed in the Gulf of Lions follows basically the continental slope at depths larger than 1500 m. Once it reaches the Alborán Sea, part of the flow is released up to 300 m depth by mixing processes and part is introduced into the Algerian basin, where it continues flowing along the continental slope (Fig. 2.5). In this region it acquires a general anticlockwise circulation. It is worth noting that close to the bottom, at about 2500 m depth, along-slope mean speeds are of the order of  $3 - 4 \text{ cm s}^{-1}$ , and they are larger than 1500 m above. It has been hypothesized [Millot et al., 1997] this is due to the effect of the anticyclonic eddies, which are believed to induce intense currents at the whole deep layer and at the near bottom.

The Channel of Sardinia is a key place for the WMDW circulation due to its bathymetry.

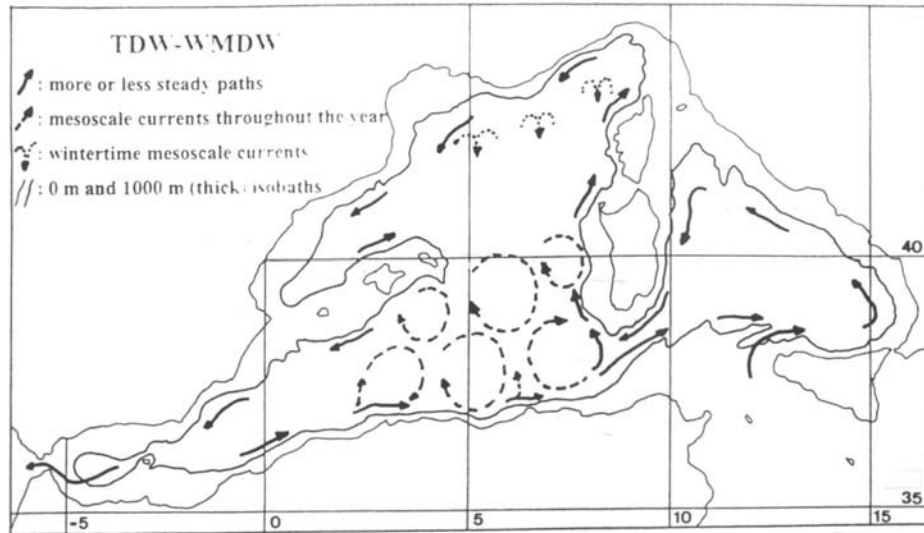


Figure 2.5: WMDW path [from Millot (1999)].

In its way off the Algerian basin, those waters flowing above 2000 m depth will be able to flow into the Tyrrhenian Sea, whereas those flowing deeper than 2000 m will be forced to flow along the western continental slope of Sardinia.

Not all the WMDW is formed in the Gulf of Lions, but the major part is introduced through the Channel of Sicily from the Eastern Mediterranean basin. This deep flow is thus trapped in the Tyrrhenian sea where it circulates anticlockwisely along the continental slope. No motion seems to be recorded in the central part of the sea. The along-slope flow continues till the Channel of Sardinia, where it joins those waters that were not able to pass the Channel of Sicily, in their flow towards the Ligurian Sea.

## 2.3 Mesoscale dynamics on the Gulf of Lions continental shelf

### 2.3.1 Influence of N-NW winds

The continental shelf waters in the Gulf of Lions show quite complex circulation patterns mostly associated to the local wind field. Stronger wind events are related to the Mistral and the Tramontane. The Mistral winds are formed between the Alps and the Massif Central and therefore blow from the N, whereas the Tramontane winds are formed between the Massif Central and the Pyrenees and blow from the NW. Both Mistral and Tramontane are redirected all along the Gulf of Lions coast showing a wide spectrum of directions, although their signature is clearly identified as intense wind events with highly constant direction which can last from days to weeks. Mistral and Tramontane join once passed the Pyrenees in a sole N-NW flow (depending on the local orography) named as Tramontane

south of Cape of Creus.

The local orography channels the N-NW winds inducing, by the action of the Coriolis force, a transport of surface water from the northeastern coast to the western coast of the Gulf which leads to upwellings in the former region and downwellings in the latter (Fig. 2.6).

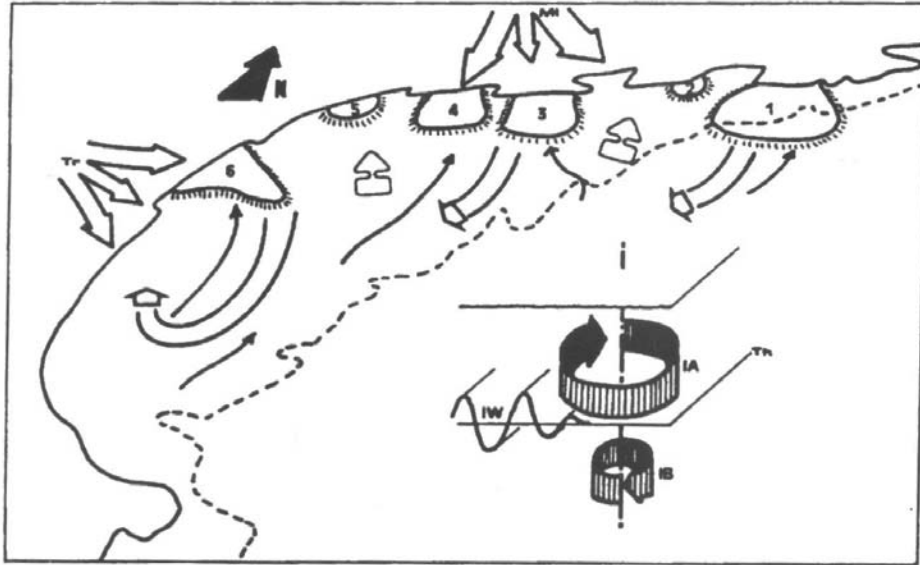


Figure 2.6: Map of upwellings: surface and bottom circulation [Fig. 2 from Millot, 1990]

The coastline of the Gulf of Lions is irregular, and presents a series of bays and capes separated by 20 – 40 km long straight zones. The upwelling zones in the Gulf of Lions are discrete, and they are located at these straight zones (Fig. 2.6). Upwellings slowly vanish within a few days after the end of the wind gust.

Anticyclonic surface circulation is observed in the southwestern part of the Gulf of Lions. Recent SST imagery analysis [Arnau, 2000] has revealed the recurrent presence of coastal eddies on the Gulf of Lions continental shelf (Fig. 2.7). Millot [Millot, 1990] suggested they are related with the location of the different wind-induced upwellings, as in his studies the surface anticyclonic motion was observed to occur in between adjacent upwelling cells. Lately, a numerical model which only considers the local (NW) wind forcing in the Gulf of Lions, could successfully reproduce these mesoscale coastal gyres [Ferré, 2001].

In the central and outer part of the continental shelf, the wind-induced bottom circulation is northwestwards, whereas in the upwelling regions bottom flows are directed towards the centre of the upwelling. If submarine canyons are close to an upwelling zone (e.g. off Toulon), the bottom circulation is observed to be upwards, towards the head of the canyon [Millot, 1990].

Another consequence of such strong and cold winds is the formation of deep water

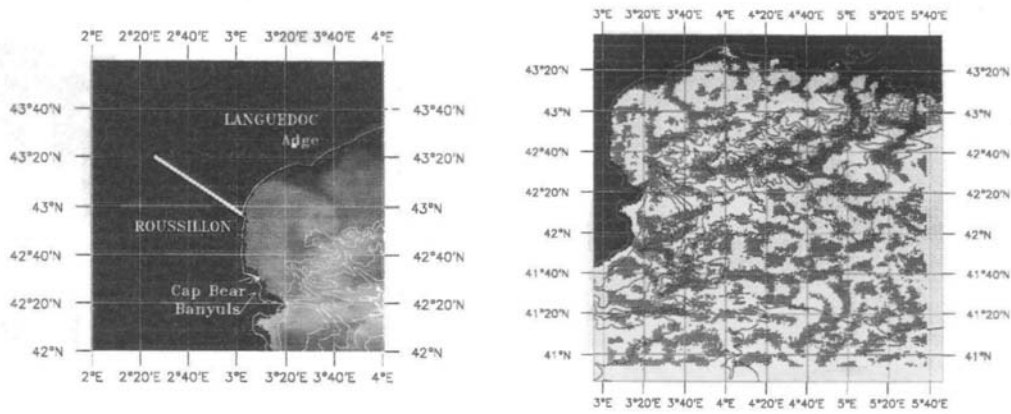


Figure 2.7: SST image Gulf of Lions continental shelf [from Arnau (2000)].

on the Gulf of Lions continental shelf. Although deep water formation is mostly found to occur in the open sea, during severe winters, the wide continental shelf existent in the Gulf of Lions also enhances deep water formation on the continental shelf. When this occurs, the newly formed deep water spreads into the open sea perpendicularly to the continental slope, as a cascade, down to 1500 m depth. This cascading is important not only from a dynamical point of view, but also in terms of biogeochemical cycles: during most of the year the Gulf of Lions continental shelf is a sink for nitrate, but during winter, dense water cascading is responsible for nitrate exportation toward the open sea [Tusseau-Vuillemin et al., 1998].

Inertial internal waves are also present on the Gulf of Lions continental shelf. They are generated from transient Mistral and Tramontane wind gusts and its direction of propagation is strongly correlated with the wind direction [Millot and Crépon, 1981] (Fig. 2.8).

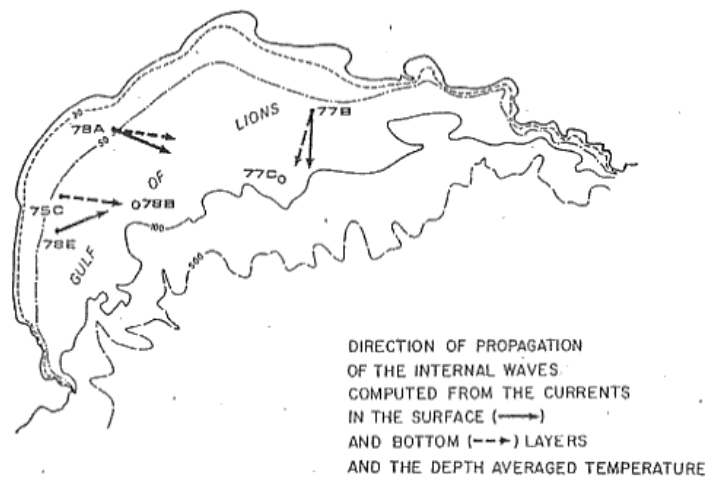


Figure 2.8: Direction of propagation of internal waves on the Gulf of Lions continental shelf [Fig. 15 from Millot and Crépon, 1981].

### 2.3.2 The shelf-slope density front

Main fresh-water discharges into the Gulf of Lions come from the Rhone river. Although the vertical extent of river discharges is not very deep, winds mix the surface on-shelf water making the river discharge impossible to separate from the shelf waters. From a dynamical point of view, the water on the continental shelf acts as a whole.

The river-influenced shelf water, which reduces its depth offshore, is separated from the open sea saltier waters by a density front, which intersects the shelf break at depth and shallows towards the open sea. The geostrophic adjustment of the density front reinforces the surface signature of the Northern Current.

In winter, the seaward extension of the density front is seen to intersect the water surface, whereas in summer is placed under the seasonal thermocline. There are important and complex biogeochemical cycles associated to this shelf-slope density front [Sournia et al., 1990] (see Fig. 2.9).

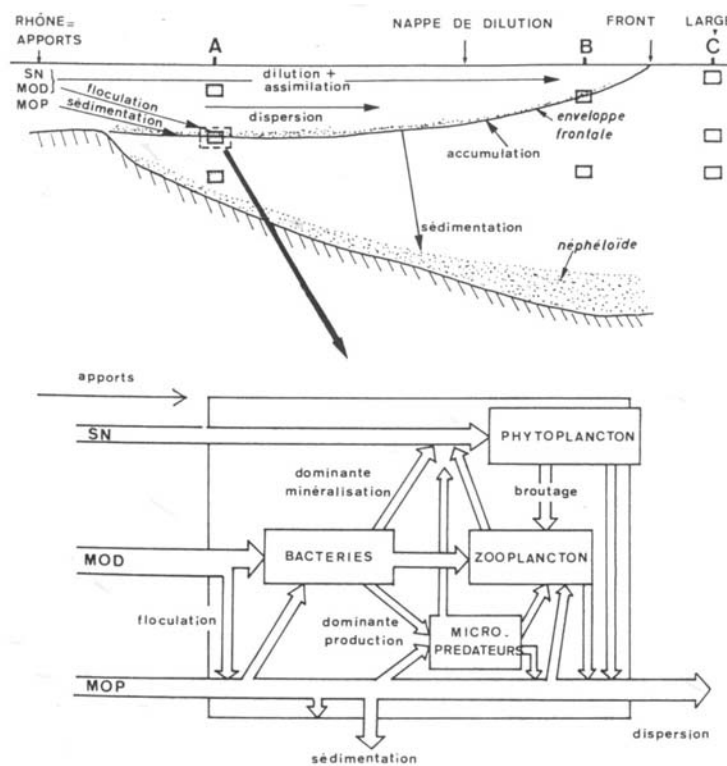


Figure 2.9: Scheme of the biogeochemical cycle [from Sournia et al., 1990].

## 2.4 Mesoscale dynamics on the Gulf of Lions continental slope

### 2.4.1 The Northern Current

The circulation on the Gulf of Lions continental slope is driven by the Northern Current. The Northern Current is the result of the general cyclonic circulation of the NW Mediterranean and therefore involves MAW, WIW when present, LIW down to 600 – 700 m depth and WMDW down to the bottom [Conan and Millot, 1995].

The Northern Current flows from the Ligurian Sea into the Gulf of Lions, where it is associated to the aforementioned shelf-slope density front. At the entrance of the Gulf of Lions the current is of about 30 – 50 km wide and flows along the lower half of the continental slope, over the 1000 to 2000 m isobaths approximately. The inner limit of the current is difficult to determine due to the complex bottom topography (submarine canyons). Surface speeds are about 30 – 50 cm s<sup>-1</sup> [Conan and Millot, 1995]. Its velocity profile is maximum at the surface, with a smooth vertical shear decreasing with depth, down to about 300 – 400 m depth. The Northern Current seems to be well represented by the combination of the barotropic (i.e. nul velocity shear with depth) and the first baroclinic modes, with predominance of the latter, especially in winter [Alb erola et al., 1995].

Compared to the Gulf of Lions, the Ligurian Sea has less wind activity, therefore its surface waters are warmer than in the former region. This allows to trace the surface flow of the Northern Current by temperature satellite imagery —it appears as a relatively warm path flowing from the Ligurian Sea into the Gulf of Lions.

### The origin of the Northern Current

The flow of the Northern Current originates in the eastern part of the Ligurian Sea, where the current flowing along the northwestern coast of Corsica joins to the current flowing along the eastern coast of the island.

The northwestern coast flow seems to be steady during all the year, apart from a recurrent intensification attributed to a seasonal migration of the density slope front [Astraldi and Gasparini, 1992].

The flow through the Corsica channel flows only in winter [Astraldi and Gasparini, 1990]. Good correlation exists between the heat lost in winter due to atmospheric processes and the heat apported by the warm water intrusion from the Corsica channel. According to Astraldi and Gasparini [Astraldi and Gasparini, 1992], the incoming flow into the Ligurian basin must restore both the heat loss due to the cold winds acting on the sea surface and the water mass loss due to the conversion of surface waters into deep waters.



## 2.4.2 Influence of bathymetry and winds on the Northern Current

### Interaction with bottom topography

The interaction of the Northern Current with the continental slope is thought to be relevant. Bottom current intensifications have been observed in several occasions, and they have been associated to bottom trapped topographic Rossby waves [Millot, 1985] [Sammari et al., 1995].

Moreover, the presence of an irregular bottom topography due to submarine canyons is also important. Whereas in other areas like the Balearic sea submarine canyons are quite regular and equidistant, in the Gulf of Lions they have different orientations and irregular interfluves with different widths (Fig. 2.2). Strong wind conditions lead to cross-canyon advection and bottom transfer along the canyon axis of suspended particulate matter [de Madron, 1994]. Observations in the Grand Rhône canyon showed that the upper-layer circulation followed the Northern Current direction (i.e. along-slope), but inside the canyon dominates a downcanyon component parallel to the canyon axis [de Madron et al., 1990]. The heads of the canyons have been seen to be pools of suspended particulate matter (SPM) moving seawards, due to the alongslope current-canyon interaction [de Madron et al., 1990]. Oppositely, when canyons are close to upwelling areas, upward (onshore) bottom flow induced by the wind is observed at the head of the canyon [Millot, 1990].

Significant inertial currents of the order of  $10 - 15 \text{ cm s}^{-1}$  are present inside canyons, at depths of about 300 m (unpublished results cited in [Millot, 1990]). Due to the interaction with the canyons, these currents show up- or down-slope direction, strongly influencing the sediment transport.

### Surface influence of NW winds

There are some evidences of the direct effect of the local wind field on the Northern Current flow. Millot and Wald [Millot and Wald, 1980] and Arnau [Arnau, 2000] reported, from satellite infrared imagery, the influence of NW winds in the propagation of the Northern Current. Millot and Wald [Millot and Wald, 1980] observed that when winds were  $\sim 10 \text{ m s}^{-1}$  the Northern Current was stopped north of Toulon, whereas when the wind decreased the Northern Current flow moved onshore, and finally accelerated along-slope when the wind stopped. Arnau [Arnau, 2000] made similar observations on the stopping and acceleration of the Northern Current by NW winds, and he also found a good correlation between the presence of wind gusts and the increase of mesoscale activity. Nevertheless, Millot [Millot, 1990] pointed out that the intrusion of the Northern Current on the Gulf of Lions continental shelf after a NW wind pulse due to the lack of NW winds is only valuable for the near surface signature of the Northern Current, whereas the Northern Current flow at depth cannot be disturbed by wind events.

### 2.4.3 Mesoscale variability associated to the Northern Current

Far from being a stable current, the Northern Current usually displays meanders with very different length scales. Its major variability has been found related to 2 – 10 days period meanders with phase speeds of 10 – 20 km day<sup>-1</sup> [Milot, 1999]. From January to mid March, the Northern Current is deeper and narrower and flows closer to the continental slope [Milot, 1999].

Mesoscale activity is observed during the whole year by satellite imagery although mesoscale measurements are more frequent (and more studied) in winter. Major mesoscale activity is recorded from late autumn to late winter, when decreases suddenly [Alb erola et al., 1995], although some authors found the mesoscale period extending from December to May [Milot, 1987] [Taupier-Letage and Milot, 1986]. Maximum flows of the Northern Current from the Ligurian Sea till the Balearic Sea are observed to occur also from December to May [Font et al., 1995] [Alb erola et al., 1995] [Conan and Milot, 1995] [Sammari et al., 1995], indicating a good correlation between maximum Northern Current fluxes and maximum mesoscale variability.

Aspects of the seasonal variability of the Northern Current and associated mesoscale phenomena were studied during the PRIMO-0, PROLIG-2 and PROS-6 experiments performed off Nice, just before the entrance into the Gulf of Lions [Alb erola et al., 1995] [Sammari et al., 1995]. From spectral analysis techniques, two ranges of frequencies seem to appear in winter: a stronger 10 – 20 days band and a weaker 3 – 6 days band [Alb erola et al., 1995] [Sammari et al., 1995].

During winter the 10 – 20 day fluctuations band presents similar amplitudes in the alongshore and transverse components, suggesting its relation to large mesoscale meanders [Alb erola et al., 1995]. From May to December, fluctuations in the 10 – 20 days band were recorded only alongslope by Sammari [Sammari et al., 1995] and were associated to current pulses of the mean flow propagating downstream at 10 km/d. This pulse-like variability is also observed in the spring observations of Alb erola [Alb erola et al., 1995], although in that occasion this frequency band was observed to reduce to shorter periods of about 10 days, maybe due to reduced instability conditions in this period.

From May to December, the 3 – 6 days period variability was associated to meanders of the Northern Current [Sammari et al., 1995]. The 3 – 6 days band mainly appeared in the flow component perpendicular to the coast, being polarized anticlockwise seawards. The variability associated to meanders was more intense in autumn than in spring-summer. In both winter and spring records by Alb erola [Alb erola et al., 1995], the 3 – 6 days band fluctuations were also associated to meandering currents and they were observed preferentially within the core of the current. The authors expect these 3 – 6 days band fluctuations to intensify in winter, being maximum in deep winter together with the longer period mesoscale activity (i.e. the 10 – 20 day fluctuation band). The meandering amplitude estimated for the 3 – 6 days band was of 30 – 60 km wavelength, propagating roughly at 10 km day<sup>-1</sup> [Sammari et al., 1995].

Downstream, measurements on the Gulf of Lions continental slope off Marseille, are in agreement with the observations off Nice. Observations from February to June 1992

done by Conan and Millot [Conan and Millot, 1995] showed very large scale meanders off Marseille reflected in the displacement of the Northern Current core of 10 – 20 km in 1-week intervals, from more than 35 km offshore to less than 20 km offshore. These horizontal extensions agree with those observed in spring 1991 by Alb erola [Alb erola et al., 1995] off Nice.

Mesoscale fluctuations off Marseille are observed in bands of slightly lower period compared to those off Nice, appearing in a 2 – 5 days band and in a 7 – 10 days band. In this region both bands are clearly associated to Northern Current mesoscale meandering, and they present similar amplitudes —therefore they are equally energetic [de Madron et al., 1999]. Moreover, a relative maximum in mesoscale activity is observed in this region in spring [Conan and Millot, 1995] [de Madron et al., 1999].

Some studies have provided evidence that the vertical variability of the Northern Current is due to a combination of the barotropic mode and the first baroclinic mode with zero-crossings at 400 – 500 m depth [Alb erola et al., 1995]. Nevertheless, the depth extension of the Northern Current mesoscale meanders remains still unclear, although it seems logical to relate it to the stratification of the water column, reaching larger depths during low stratified conditions [Taupier-Letage and Millot, 1986]. Mesoscale currents in winter are clearly barotropic and may reach  $\simeq 20 \text{ cm s}^{-1}$  at depths ranging from 100 to 1100 m depth [Taupier-Letage and Millot, 1986]. Off Marseille, deep currents are also strongly correlated with surface flows at the 2 – 5 days band [de Madron et al., 1999].

The cross-slope component of the Northern Current is seen to create cross-isobath flows near the bottom with significant vertical motions. Durrieu [de Madron et al., 1999] showed by a diffusion model how the turbulent vertical mixing of suspended particulate matter (SPM) induced by the cross-slope component yields to downward fluxes of particles comparable to the particle fluxes collected by sediment traps.

In previous studies, the origin of the mesoscale variability of the Northern Current has been related to baroclinic instability. This process was studied in the Ligurian Sea on the basis of different data sets as SST images [Cr epon et al., 1982], current meters [Sammari et al., 1995] and floats at different depths, from 600- to 1000-m depth [Gascard, 1978]). However, conclusions at this respect are not definitive and the origin of the Northern Current meandering is still unclear. Apart from baroclinic instability, other processes as barotropic instability may also play a role in the observed variability but they have not been seriously considered up to now.

## 2.5 Open sea mesoscale dynamics

### 2.5.1 Seaward migration of Northern Current mesoscale variability

The general cyclonic circulation in the NW Mediterranean creates a ‘doming’ at the open sea from the Balearic basin to the Ligurian Sea (Fig. 2.10). Off the continental slope, open sea motions are slow, although relevant mesoscale activity is observed to occur in this area

in winter [Millot, 1987] [Taupier-Letage and Millot, 1986].

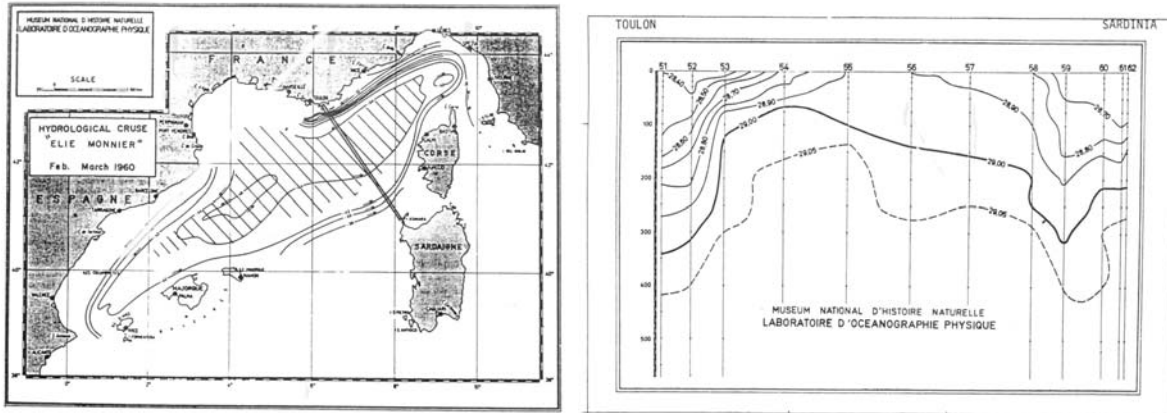


Figure 2.10: Figure 1 and 2 from Crépon and Boukthir (1987).

Migration of mesoscale structures from shelf-slope to the open sea has been reported by different authors (e.g. see [Font et al., 1995] [Millot, 1987] [Arnau, 2000]). Albérola [Albérola et al., 1995] and Taupier-Letage and Millot [Taupier-Letage and Millot, 1986] reported the seaward propagation of barotropic activity, from winter to spring, causing high variability in the open sea. Cyclonic motion was observed to increase whereas anticyclonic motion was becoming less and less noticeable. This mesoscale activity in the open sea was correlated with relatively intense mesoscale variability of the Northern Current off Nice. In this particular instance, these features occurred in December-January, two months earlier than deep water formation (February-March), which suggests the importance of the Northern Current meandering in the homogenization of the water masses before deep water formation occurs.

## 2.5.2 Deep water formation

In the central zone of the basin, stratification is weak, and winter mesoscale currents are barotropic, with large vertical extent and speeds of 20 cm/s from 100 to 1100 m depth. Deep water formation occurs during severe winters due to cold Mistral and Tramontane wind events [MEDOC-Group, 1970] by small convective cells or ‘chimneys’ with important downward vertical speeds. Winter intensification of the Northern Current has been related to deep water formation processes according to the model by Crépon and Boukthir [Crépon and Boukthir, 1987].

Deep water formation has historically been divided into three phases: preconditioning, vigorous convection and relaxation [MEDOC-Group, 1970]. All three phases are spatially highly non-uniform and they show mesoscale activity at short time scales, together with advection processes, like intrusions of LIW and surface capping [Gaillard et al., 1997]. Specifically, the preconditioning phase concerns cooling of the water surface by the effect

of the cold N-NW winds and leads to a rising and tilting of the isopycnals, affecting the horizontal and vertical density distribution of the shelf-slope front.

## 2.6 Summary and open issues

Mesoscale variability of the flow on the continental shelf of the Gulf of Lions mainly consists in up- and downwellings, surface anticyclonic motions and internal inertial currents. All these phenomena are associated to strong N and NW wind events. Mesoscale variability on the continental slope is associated to the Northern Current variability. Intensifications of the Northern Current are related to thermohaline processes, being maximum in the Ligurian Sea in winter and showing a high correlation with the intensification of mesoscale variability. Off Marseille, maximum mesoscale variability occurs also in spring.

The Northern Current flows along the 1000 to 2000 m isobaths at its entrance into the Gulf of Lions. It is a 30 – 50 km width current with surface speeds of 30 – 50 cm s<sup>-1</sup>. Formally, the NC involves MAW, WIW occasionally, LIW+TDW and WMDW, although horizontal velocities are very low below 400 – 500 m depth. During winter the Northern Current is observed to flow closer to the continental slope, presenting a narrower and deeper structure. Off Marseille, its major variability occurs in two period bands of 2 – 5 days and 7 – 10 days, respectively, whereas upstream (at the entrance of the Gulf — i.e. off Nice) it occurs at slightly higher periods (bands of 3 – 6 days and 10 – 20 days, respectively). Off Nice, the meandering amplitude of the 3 – 6 days band is of 30 – 60 km wavelength, with propagation speeds of 10 km/day. The 10 – 20 days variability band off Nice has been mostly associated to Northern Current pulses, and it reduces to a 10-days variability band in spring. There is offshore advection of mesoscale variability associated to the Northern Current towards the open sea, mainly of cyclonic sign. The origin of the mesoscale variability of the Northern Current has been normally associated to baroclinic instability, although no definitive conclusions are made up to now. Other processes as barotropic instability may also play a role in the observed variability but they have not been seriously considered up to now.

Mesoscale currents in winter are clearly barotropic and may reach  $\simeq 20$  cm s<sup>-1</sup> at depths ranging from 100 to 1100 m depth. Off Marseille, deep currents are strongly correlated with surface flows at the 2 – 5 days band. This suggests that barotropic processes may play a role, and that the interaction of the Northern Current with the bottom topography may affect the observed mesoscale variability.

Besides, the interaction between the continental shelf and slope is enhanced by the presence of submarine canyons indenting the continental shelf. Bottom intensifications of the mesoscale variability on the continental slope are associated to bottom topographic waves, but a detailed interpretation of the interaction of the Northern Current with the continental slope and more specifically its interaction with the complex canyon system still remains to be done.

In the next chapter, we will describe the results obtained from in-situ data and will test once more the hypothesis of baroclinic instability as the origin of Northern Current

meandering. Chapters 4 and 5 will be devoted to study the role of the bottom topography in the Northern Current mesoscale variability by means of a barotropic laboratory model.

## Chapter 3

# Flow variability in the Gulf of Lions during the MATER High Frequency Flux experiment (March–May 1997)

o rio que fazia uma volta atrás de nossa casa  
era a imagem de um vidro molem que fazia uma  
volta atrás de casa  
Passou um homem depois e disse: essa volta  
que o rio faz por trás de sua casa se chama  
enseada  
Nao era mais a imagem de uma cobra de vidro  
que fazia uma volta atrás de casa.  
Era uma enseada  
Acho que o nome empobreceu a imagem  
MANOEL DE BARROS

*This chapter is an adapted version of a paper published in the Journal of Marine Systems [Flexas et al., 2002].*

### ABSTRACT

Hydrological and current meter data were gathered during the High Frequency Flux Experiment that took place in the Gulf of Lions from March to May 1997, within a 20 x 40 km experimental box over the shelf edge and the continental slope offshore of Marseille. The data set has been supplemented and jointly analyzed with sea surface temperature images to characterize flow variability with a particular regard on the mesoscale effects associated to the regional circulation.

The current meter observations showed a southwestward flow characteristic of the Northern Current. It is strongest near the shelf break, constrained to flow along topography near the bottom but much less polarized over the upper and mid slope. Mesoscale

variability shows up as fluctuations around 3.5-day and 7-day periods at 250 m and 650 m depth, and around 7-day periods at 1230 m depth.

The Northern Current, as observed on satellite images, forms a 30 km wide stream with meanders displaying length scales longer than 60 km. These meanders are observed to embrace smaller structures, which are responsible for the intense mesoscale activity recorded in current meter data. Both the hydrological observations and current meter data down to 650 m depth match the superficial structures. Two major flow patterns are observed during the experiment: (i) the core of the Northern current flows south of the experimental site during March and early April, with transitory eddies moving over the experimental site; (ii) following the traverse of a westward-propagating large meander on mid-April, the Northern Current remains over the experimental site. We provide evidence that the synoptic current variability observed in the upper layer may be related to baroclinic instability. A distinct near-bottom current variability is also documented on the mid-slope. Bottom trapped topographic waves are proposed as the mechanism which produces the along-slope deep flow variability.

### 3.1 Introduction

The understanding of the dynamics of the coastal zone and its role as a preferential zone of deposition, transformation and exchanges of material, in the global cycle of biogeochemical elements has become a major research area during the last decade (e.g. see [Hall and Smith, 1996] [Liu et al., 2000]). In that context, the physical processes mediating material transport across the shelf, particularly when the shelf boundary is largely open toward the deep adjacent basin, appears to be of paramount importance. Numerous mechanisms control this transport, such as benthic boundary layer flows, coastal upwelling and downwelling, internal waves, the interaction of shelf water with boundary currents and density currents (see [Huthnance, 1995] and the references therein).

The strong dynamical processes occurring in the Gulf of Lions make this region an interesting site to study the effect of physical transport processes on the shelf-slope exchanges of material. The meteorological conditions of the Gulf of Lions in the north-western Mediterranean are characterized by an intense wind forcing, issuing primarily from the NW (Tramontane) and the North (Mistral), that causes coastal upwellings and triggers deep water formation in winter both on the shelf and offshore [Millot, 1990]. A cyclonic along-slope current, the Northern Current (NC) that forms the northern branch of the circulation in the NW Mediterranean, dominates the general circulation. The NC is associated to a permanent shelf-slope density front separating low-salinity shelf waters with continental influence from denser open-sea waters [Astraldi et al., 1994]. This current is 30 – 50 km wide; its velocity is maximum near the surface ( $\sim 50 \text{ cm s}^{-1}$ ) and decreases, nearly linearly with depth, to speeds of a few  $\text{cm s}^{-1}$  at several hundreds meters depth (see e.g. in [Lapouyade and de Madron, 2001]). The Northern Current shows a variability at seasonal scale, with a decrease of its transport in summer, and also at synoptic scale, due to the presence of meanders [Conan and Millot, 1995]. The synoptic variability of



the Northern Current is characterized by fluctuations of 2 – 6 day period and lower frequency fluctuations of 10 – 20 day period [Sammari et al., 1995] [de Madron et al., 1999]. Durrieu [de Madron et al., 1999] and Puig [Puig et al., 2000] stress the effect of these fluctuations on the cross-slope transport of particulate matter for monthly to seasonal time scales. However, the detail of the transport at short time scale induced by meanders is not well-known.

Meandering motions are commonly attributed to baroclinic instability. This process was studied on the basis of different data sets in and around the Gulf of Lions. In the Ligurian sea, upstream of the Gulf of Lions, Crépon [Crépon et al., 1982] used SST (sea-surface temperature) satellite images and Sammari [Sammari et al., 1995] used current meters moored on a cross-slope transect to infer the occurrence of baroclinic instabilities. In the Gulf of Lions, Gascard [Gascard, 1978] used floats at different depths, from 600 to 1000 m depth. Arnau [Arnau, 2000] suggested from the analysis of SST satellite images that the intense wind acting on a thermal wind (frontal) system may trigger baroclinic instabilities. However, no Eulerian observations were performed in the Gulf of Lions on the spatial and temporal scales of the hypothesized unstable baroclinic waves.

To examine these complex processes on the Gulf of Lions continental slope, a two-month intensive field study was undertaken in the framework of the "Mediterranean Targeted Project II — Mass Transfer and Ecosystem Response" (MTP II—MATER) project. The High Frequency Flux Experiment (HFFE) was a multidisciplinary experiment designed to identify the key processes controlling the particle transfer and the biological production on continental margins at the local scale (tens of kilometers). It sought in particular to determine the effect of transient hydrodynamical features (eddies, meanders) on the cross-slope transport of matter and the local budgets of biogeochemical elements. The experiment produced a set of measurements on the spatial and temporal variability of particulate fluxes, and on the hydrological, dynamical and biological conditions (e.g. [Diaz et al., 2000] [van Wambecke et al., 2001]). The objective of the present work is to examine the time-varying velocity and physical property fields and to understand the dynamics controlling the mesoscale variability of the boundary current during the experiment, and to indicate the possible repercussions on the cross-shelf exchanges of material.

## 3.2 Material and methods

### 3.2.1 Physiography of the HFFE site

The HFFE experimental site is a box of 20 km along slope x 40 km across slope offshore of Marseille over the continental slope between 260 m and 1250 m depth (Fig. 3.1). The site is localized at the place where the NC penetrates into the Gulf of Lions and presents large mesoscale motions [Conan and Millot, 1995] [de Madron et al., 1999]. The sea-floor physiography of the HFFE site bathymetry is rather complex. The continental slope is incised by numerous submarine canyons separated by narrow open slopes. East to west, the study site includes the Planier, Marseille, Grand-Rhône and Petit-Rhône canyons.

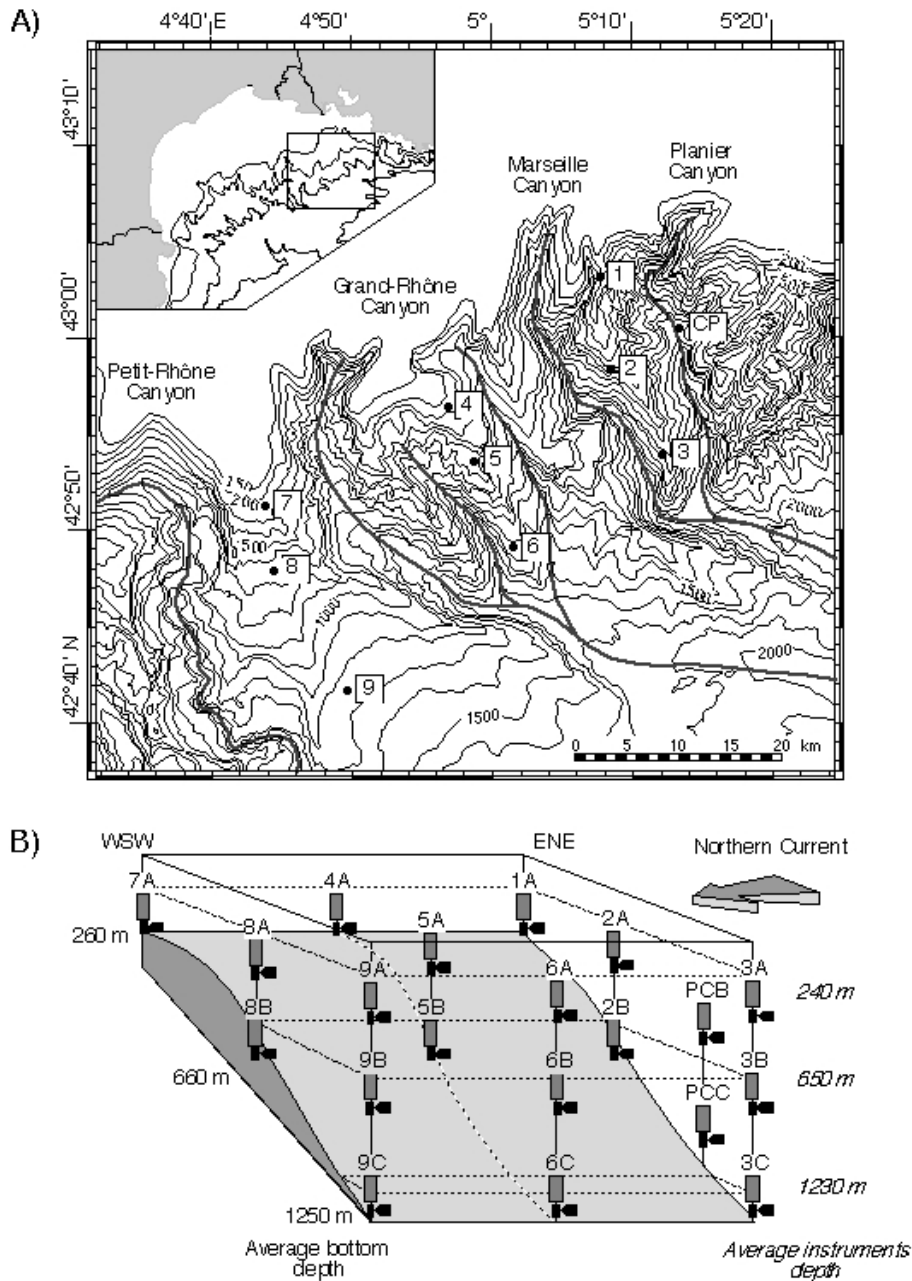


Figure 3.1: a) Bathymetric chart with mooring positions. The axes of submarine canyons in the experimental site are delineated. b) 3-D view of the mooring lines equipped with pairs of sediment trap/current meter along the three cross-slope transects. Numbers on the left side indicate mooring depths and those on the right side indicate current meter depths. Each mooring is numbered and the letter indicates the depth (A: 240 m, B : 650 m and C: 1230 m).

### 3.2.2 Current meter and ancillary data

To examine the time-varying structure of the currents, time series of velocity and temperature were made from a regular array of nine moorings distributed on three transects (Fig. 3.1). Each transect was perpendicular to the coast and located along the adjacent open slope of a canyon. Each mooring was equipped with pairs of Technicap PPS3 sediment traps and Aanderaa vector averaging rotor current meters RCM 7 and 8. The transects included a shallow mooring slightly off the shelf break with a current meter at 240 m depth, an intermediate mooring on the upper slope with current meters at about 240 m and 650 m depths, and a deep mooring on the mid slope with current meters at 240 m, 650 m and 1230 m depths.

The current meters will be noted hereafter with their respective mooring number plus a letter indicating its depth (see Fig. 3.1). The instruments were Aanderaa vector averaging rotor current meters RCM 7 and 8. The sampling rate of the current meters was set to 20 minutes. The HFFE monitoring began March 9, 1997 and ended May 14, 1997. The moorings #3, 8 and 9 were released prematurely because of an abnormal corrosion of the acoustic release ring. Two of the drifting lines (#3 and 9) were rapidly localised and recovered by fishermen offshore of the Spanish coast. The third line (#8) was recovered in August 1997 by an Italian research vessel offshore of Genoa. Factory calibrations performed prior to the experiment were used to convert the raw data. The overall quality of the data and the agreement with other temperature measurements (CTD) were good.

Five hydrological surveys were carried out throughout the monitoring period. Each cruise lasted less than 24 hours during which CTD profiles were collected with a Seabird 9/11 CTD probe on nine stations next to the moorings.

To explore the large-scale structure of the NC in the Gulf of Lions, NOAA/AVHRR satellite images were acquired during the experiment period. The processed daily mean SST fields were downloaded from DLR's GISIS web site. The data were geo-referenced and a grey table — with lighter shades indicating warmer water — was applied to produce the images. No valid SST image of the study area were available after April 30, 1997. The availability of all data gathered during the experiment is presented in Fig. 3.2.

### 3.2.3 Analytical model

A simple analytical model [Tang, 1975] is used to test if the meanders of the NC observed during the HFFE may be caused by baroclinic instabilities. The model assumes quasi-geostrophy, and a flat bottom topography. A solution may be obtained assuming a static sinusoidal solution across the mean flow and a propagating wave along the mean flow. Unstable modes appear for complex phase speed with positive imaginary part. After substitution in the linearized quasi-geostrophic potential vorticity equation, the stream function equation can be written as :

$$\frac{d^2\psi}{dz^2} - \left(\frac{N\mu}{f}\right)^2\psi = 0, \quad (3.1)$$

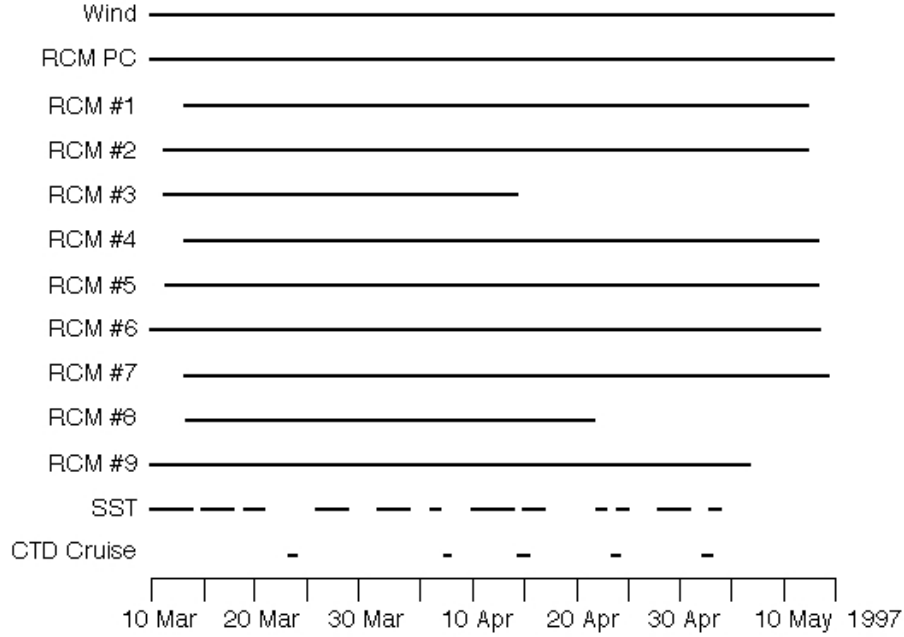


Figure 3.2: Timetable of the available data during the HFFE experiment.

where  $\psi$  is the stream function,  $N$  is the Brunt-Väisälä frequency,  $f$  is the Coriolis parameter and  $\mu^2 = k^2 + l^2$ , where  $k = 2\pi/L$  (where  $L$  is the wavelength along the mean flow) and  $l = 2\pi/D$  (where  $D$  is the distance between the nodal surfaces across the mean flow).

Consider a two-slab model with an upper layer of width  $h_1$ , surface velocity  $u_0$  and constant shear  $u_0/H$ , placed over a zero-velocity lower layer of width  $h_2$ . The general solutions from applying (3.1) to each layer can be found in [Tang, 1975]. Unstable modes appear when the phase speed  $c = c_r + ic_i$  has an imaginary part (i.e.  $c_i > 0$ ). Assuming zero vertical velocity at surface and bottom boundaries, and continuity across the interface between the two layers, it results that

$$c_r = \frac{u_0}{2} \left[ 1 - \frac{RK \tanh \kappa_1}{\kappa_1 (1 + RK)} \right], \quad (3.2)$$

$$c_i = u_0 \frac{\kappa_1 - \tanh \kappa_1}{2\kappa_1 (1 + RK)} [-(RK + a)(RK + b)]^{1/2}, \quad (3.3)$$

where  $R = \frac{N_1}{N_2}$ ,  $K = \frac{\tanh \kappa_2}{\tanh \kappa_1}$ ,  $a = 2 \frac{(\kappa_1/2) - \tanh(\kappa_1/2)}{\kappa_1 - \tanh \kappa_1}$ ,  $b = 2 \frac{(\kappa_1/2) - \coth(\kappa_1/2)}{\kappa_1 - \tanh \kappa_1}$ ,  $\kappa_1 = \mu \frac{h_1 N_1}{f}$  and  $\kappa_2 = \mu \frac{h_2 N_2}{f}$  (subscript 1 refers to the upper layer and 2 to the lower layer).

There is a cutoff wavelength which allows to separate stable from unstable waves. This can be obtained from (3.3) and takes the form:

$$R \tanh \left( \frac{h_2 \kappa_1}{R h_1} \right) = \frac{2 \coth(\kappa_1/2) - \kappa_1}{\kappa_1 \coth \kappa_1 - 1}. \quad (3.4)$$

Therefore, from  $\kappa_1$ , the model allows to obtain the characteristics of the unstable waves for a given stability condition ( $R$ ) and a given ratio of layer depths.

## 3.3 Results

### 3.3.1 Statistical analysis of the currents

#### Mean currents and fluctuations

Statistics have been computed for the HFFE current meters during the whole recording period. The moored array shows an along-slope current, strongest near the shelf break (Fig. 3.3a). Variance ellipses show that the current is constrained to flow along topography near the bottom, but is more isotropic in the upper and mid-water layers over the slope (Fig. 3.3b).

Mean currents are rather slow and towards the SW except for #3A and #8A where the mean flow is towards the NE. The mean velocity at 250 m depth is  $8.2 \text{ cm s}^{-1}$  near the shelf break (ensemble average for all current meters), decreases to  $3.5 \text{ cm s}^{-1}$  over the upper slope and increases to  $9.5 \text{ cm s}^{-1}$  over the mid slope. At 650 m depth, the mean speed is  $4.0 \text{ cm s}^{-1}$  over the upper slope and  $2.1 \text{ cm s}^{-1}$  over the mid slope. A mean speed of  $2.9 \text{ cm s}^{-1}$  is obtained at 1230 m depth.

Maximum speeds recorded at the 240 m depth current meters are  $32.3 \text{ cm s}^{-1}$  near the shelf break (at #7A),  $19.3 \text{ cm s}^{-1}$  over the upper slope (at #5A) and  $91.6 \text{ cm s}^{-1}$  over the mid slope (at #3A). The maxima at 650 m depth are  $17.7 \text{ cm s}^{-1}$  on the upper slope (at #2A) and  $8.1 \text{ cm s}^{-1}$  on the mid slope (at #3B and #6B), and the maximum speed recorded at 1230 m depth is  $12.7 \text{ cm s}^{-1}$  (at #9C).

Hereafter, the mean direction of the flow at the shelf break, which is roughly along-slope, and the direction across the mean flow are considered as the reference coordinate axes (i.e., the new reference frame is rotated 45 anticlockwisely with respect to the original frame). Positive flow directions are towards NE and inshore.

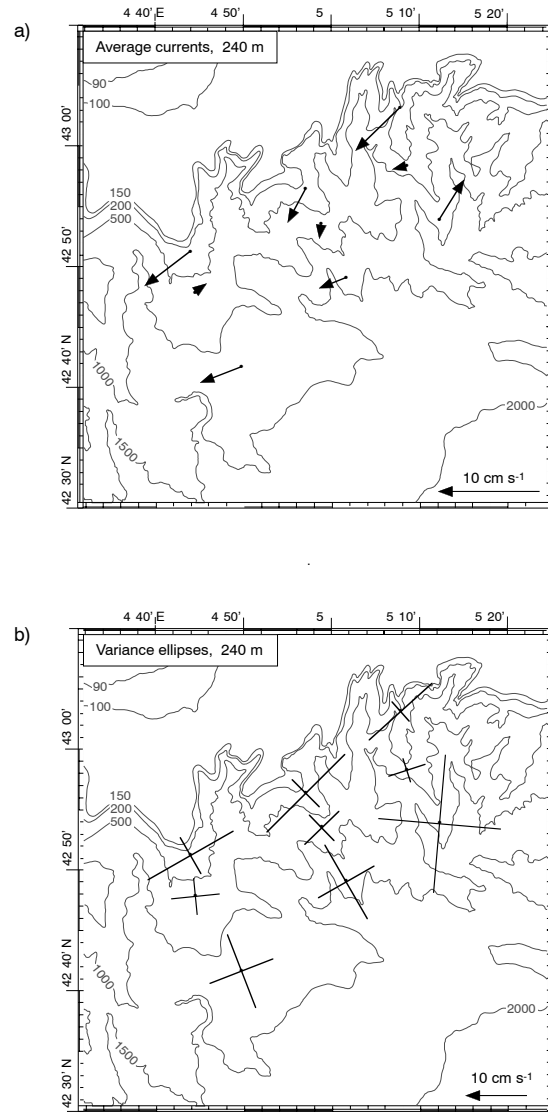


Figure 3.3: Mean currents (a) and currents ellipses (b) at 240 m. The major axis of the ellipse lies along the direction of maximum current variance and the minor axis is normal to it. The orientation of the major axis is given by  $\frac{1}{2} \tanh^{-1}(2\overline{u'v'}/\overline{u'^2} - \overline{v'^2})$ , where the primes indicate the fluctuations of the east/west (u) and north/south (v) current components around their means and the overbars the time averaging over the whole record. The length of the major and minor axes is computed to define the 95% confidence region of the fluctuations.

## Spectral analysis

Average spectral density distributions for each depth (Fig. 3.4) shows energetic oscillations around the local inertial period (17.7 h) and within the synoptic (2 – 10 days period) band. Whereas the energy of the inertial currents decreases from 250 m to 1230 m depth, the energy of the synoptic currents is minimum at 650 m depth.

Peaks around 3.5-day and 7-day periods are observed for the along-slope current component at 250 m depth. The most energetic signals are detected near the shelf-break (moorings #1, #4 and #7). At 1230 m depth, a peak around 7 days is observed for the along-slope current component and a smaller peak around 3.5 days appears for both components.

## Empirical orthogonal function

Empirical orthogonal functions (EOFs), computed from correlation between the low-pass (periods > 40h) current at 240, 650 and 1230 m depth on the mid-slope moorings, yields three modes which respectively explained 55%, 30% and 15% of the variance (Fig. 3.5). The percentage of the variance explained by each mode is similar for the different moorings. The first mode shows a significant correlation between the along-slope currents at all depth, and to a lesser extent between cross-slope currents at 240 and 650 m depth. The second mode accounts mainly for the variability of the cross-slope currents at 240 m depth together with that of the along-slope currents at 1230 m depth. The third mode shows correlated, but opposite in sign, along-slope flows at 240 and 650 m depth, and cross-slope flows at 650 and 1230 m depth.

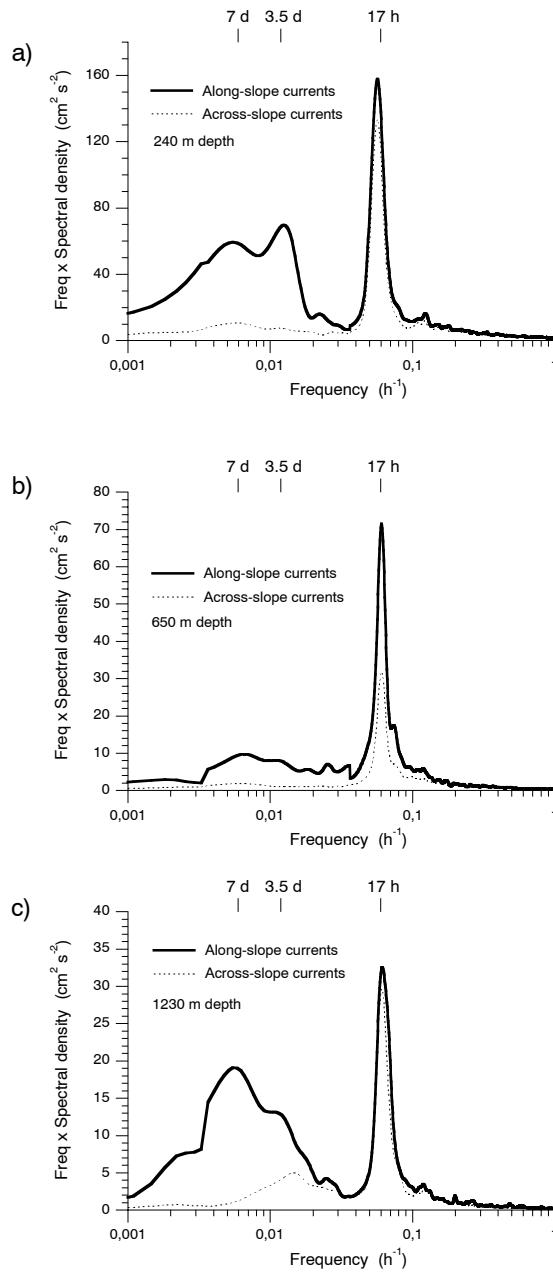


Figure 3.4: Variance-preserving spectrum of the along-slope and cross-slope current components at (a) 240 m, (b) 650 m and (c) 1230 m depth. Each spectrum is the average of all individual spectra issued from time series collected at the same depth.



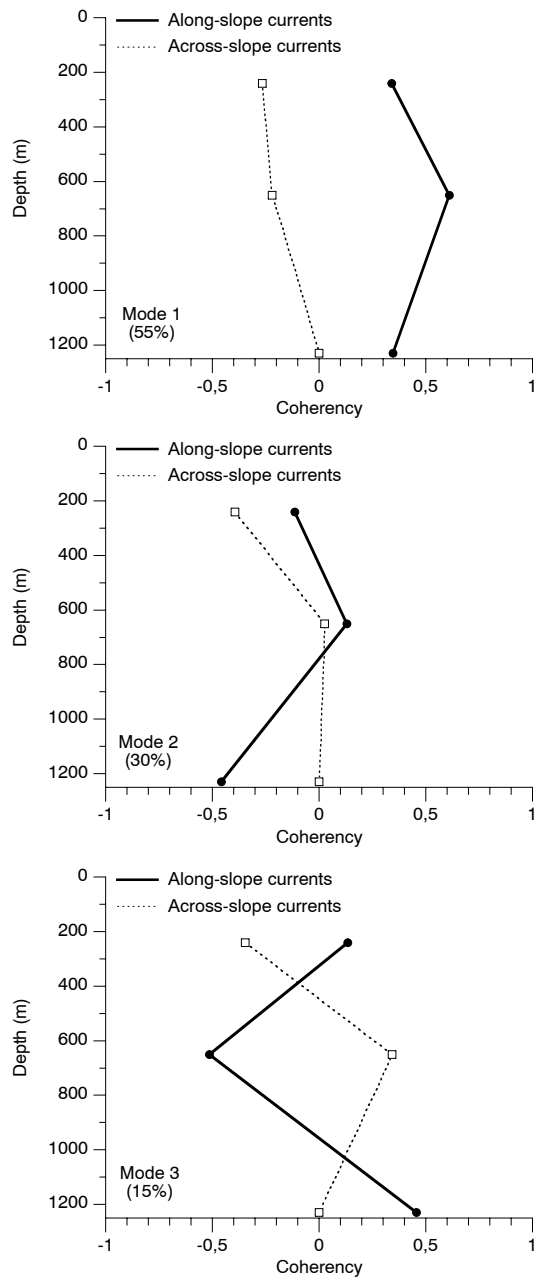


Figure 3.5: Average EOFs computed for the mid-slope moorings (#3, 6 and 9). The current time series were centred reduced before analysis. Solid and dashed lines represent along-slope and cross-slope current components, respectively.

### 3.3.2 Variability of the currents

#### Current variability in the inertial band

The near-inertial currents' time series at 240 m depth are noisier at the shelf break than on the slope. Moreover, the intensity of the near-inertial currents and the period of the most energetic oscillations increase seaward. Maximum fluctuations at the shelf break occurs for periods between 14 and 17 h. The period of maximum fluctuations ranges between 16.5 and 17.5 h for the upper slope moorings and between 17.5 and 18.3 h (around the local inertial period) for the mid-slope moorings.

Despite the large spatial and temporal variability of the near-inertial currents, major pulses of 6 – 7 days long are observed around March 22, March 29, April 8 and in a lesser extent around May 2. These events were especially visible seaward at the mid-slope moorings (Fig. 3.6). These events appear to follow bursts of strong northern wind.

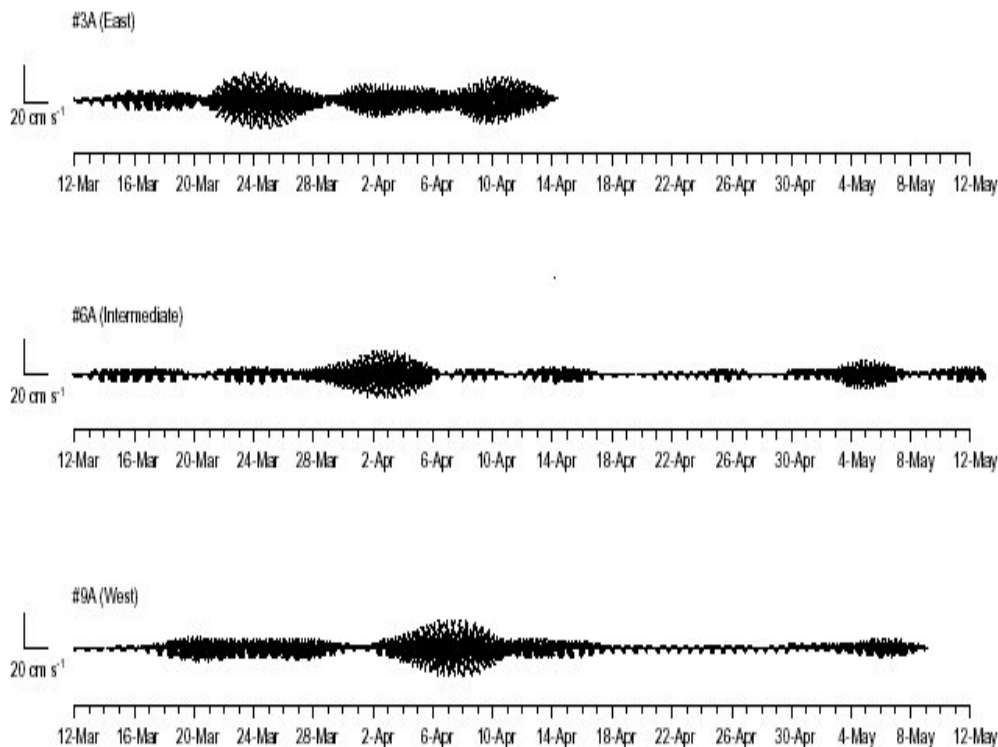


Figure 3.6: Stick plot of the near-inertial currents (16 – 21 h band pass currents) for the mid-slope moorings. Current pulses appear to follow bursts of strong northern wind that occur on March 19–20, March 29 and April 4, respectively.

## Synoptic variability of the surface currents

During the HFFE, the  $\sigma_\theta = 29.00 \text{ kg m}^{-3}$  isopycnal (chosen as representative of the structure of the shelf-slope density front) is on average located around 250 m and deepens towards the shelf-break (Fig. 3.7). The observed features basically agree with previous observations made in the Gulf of Lions during spring (e.g. see [Conan and Millot, 1995]). The depth of the isopycnal progressively decreases in depth from March to May due to seasonal effects but it also shows dramatic vertical migrations of more than 100 m between consecutive hydrographic surveys (e.g., Fig. 3.7 *b-c*).

From satellite AVHRR SST images, the surface path of the NC clearly appears as a warm stream (Figs. 3.8 and 3.9) of about 30 km width. It is observed to flow roughly in a SW direction following the general orientation of the continental slope. The sequence of SST images clearly shows the temporal evolution of the NC position, the presence of eddies detaching from the inshore edge of the current (Fig. 3.8), and the appearance and the westward propagation of a large meander (Fig. 3.9). Furthermore, filament-like structures are embedded within the NC. All these structures are responsible of much of the complex variability observed in the current meter records — even in a such small area as the HFFE site — that makes difficult to define a clear picture of the flow field solely from the current meters array. The current records at 240 m depth and SST images obtained during the HFFE are combined to describe a succession of stages (Fig. 3.10). As indicated by the EOF analysis, the main current patterns at 240 and 650 m depth are very much alike. Due to the high correlation found among SST and current meter records (see Fig 3.10), we assume that the passing of the meanders observed from satellite images is responsible of the mesoscale bands recorded by the HFFE current meters.

*From March 10th to April 7th* The SST images available during this period show that the core of the NC is located south of the HFFE site (Fig. 3.8). A large anticyclonic filament detaching from the inshore side of the NC is observed on SST images between March 9 and March 13. This large and slowly moving anticyclonic cell is also observed on progressive vector diagrams at 240 m depth on the eastern part of the HFFE site from March 14 to March 17 (Fig. 3.10*a*). From March 18 to April 7, the direction of the currents for all current-meters except for mooring #1 changes or is even inverted compared to the previous period (Fig. 3.10*b*). The SST images show several anticyclonic cells propagating westwards that momentarily cover the offshore sector of the HFFE site (Fig. 3.9 — April 2).

*From April 7th to 17th* The SST images show that a large meander forms at the eastern limit of the Gulf of Lions on March 27 and travels westward across the HFFE site (Fig. 3.9). The crest of the meander is situated on the HFFE site on April 15. The progressive vector diagrams from April 7 to April 17 indicate clearly the path of the NC traversing diagonally the HFFE site from north to south (Fig. 3.10*c*). A cyclonic motion is observed on the left side of the meander at #3A whereas anticyclonic motion occurs on its right side at #8A. A general rise of the  $\sigma_\theta = 29.0$  isopycnal is observed on April 14 (HFFE 4 cruise). The rise is most significant at #3A where it rises over a depth of 100 m (Fig. 3.7 — HFFE 4 cruise). The 29.0 isopycnal deepens near the shelf edge at #1A and

#7A. The temperature records (Fig. 3.11a) indicate that the core of the NC shifts inshore during the event, producing first a temperature increase on the mid slope (#3A) on April 8, followed by a short-lived increase on the upper slope (#2A) on April 16 and near the shelf break (#1A) on April 18.

The development and westward propagation of this large meander can be followed from its appearance at the eastern tip of the shelf on March 27 until it moves approximately halfway along the gulf's continental slope on April 18. The downstream propagation speeds estimated from successive images yields velocities between 2.3 and 8.9 cm s<sup>-1</sup> (average 5.6 cm s<sup>-1</sup>). From SST images we could infer an average wavelength of 80 km (e.g. SST image 11–12 March in Fig 3.8; 15 April in Fig 3.9). This would correspond to periods ranging between 10 – 40 days (average 16.5 days).

*From April 17th to May 12th* After April 17, the SST images show that the warm core remains over the HFFE site until the end of the experiment. Following a strong NW wind gale, the SST structures for April 22 display a disorganization of the surface flow with several cold filaments embedded within the NC core. Both SST and sub-surface currents (Fig. 3.10d) show a variable circulation on the HFFE site until May 1. The along-slope component of the current near the shelf-break also shows an intensification of the 2–4 days band pass signal from April 15 to early May (Fig. 3.11b) correlated with temperature increases of the same period (data not shown). During that period the eddy kinetic energy of the currents increases at the expense of the mean kinetic energy (data not shown). The change in the surface circulation after April 30 can not be inferred from SST images as no cloud-free image is available, but it is sketched in Fig. 3.10e from current meter recordings. These observations indicate that the NC was rather stable from May 1 to May 12.

### **Synoptic variability of the deep currents**

The deep currents (#3C, 6C, 9C) are constrained to flow along the topography and exhibit a mean southwestward flow. Synoptic fluctuations display two distinct behaviours. The most intense fluctuations have a periodicity around 7 days and are primarily directed along-slope. The fluctuations around 3.5 days period are more isotropic and rotate clockwise. Temperature fluctuations are coherent and in quadrature with the along- and across-slope current fluctuations (data not shown). The phase lag between temperature and currents indicated that local temperature variations arise from advection of a temperature gradient.

The low-pass filtered signal (>40h) of the along-slope current's component shows that the strongest fluctuations occur at mooring #9C and that the currents are somewhat coherent (Fig. 3.12a). The coherency is particularly obvious between moorings #3 and 6 with the downstream mooring having an average time lag (considering all synoptic fluctuations) of 9 hours (Fig. 3.12b).

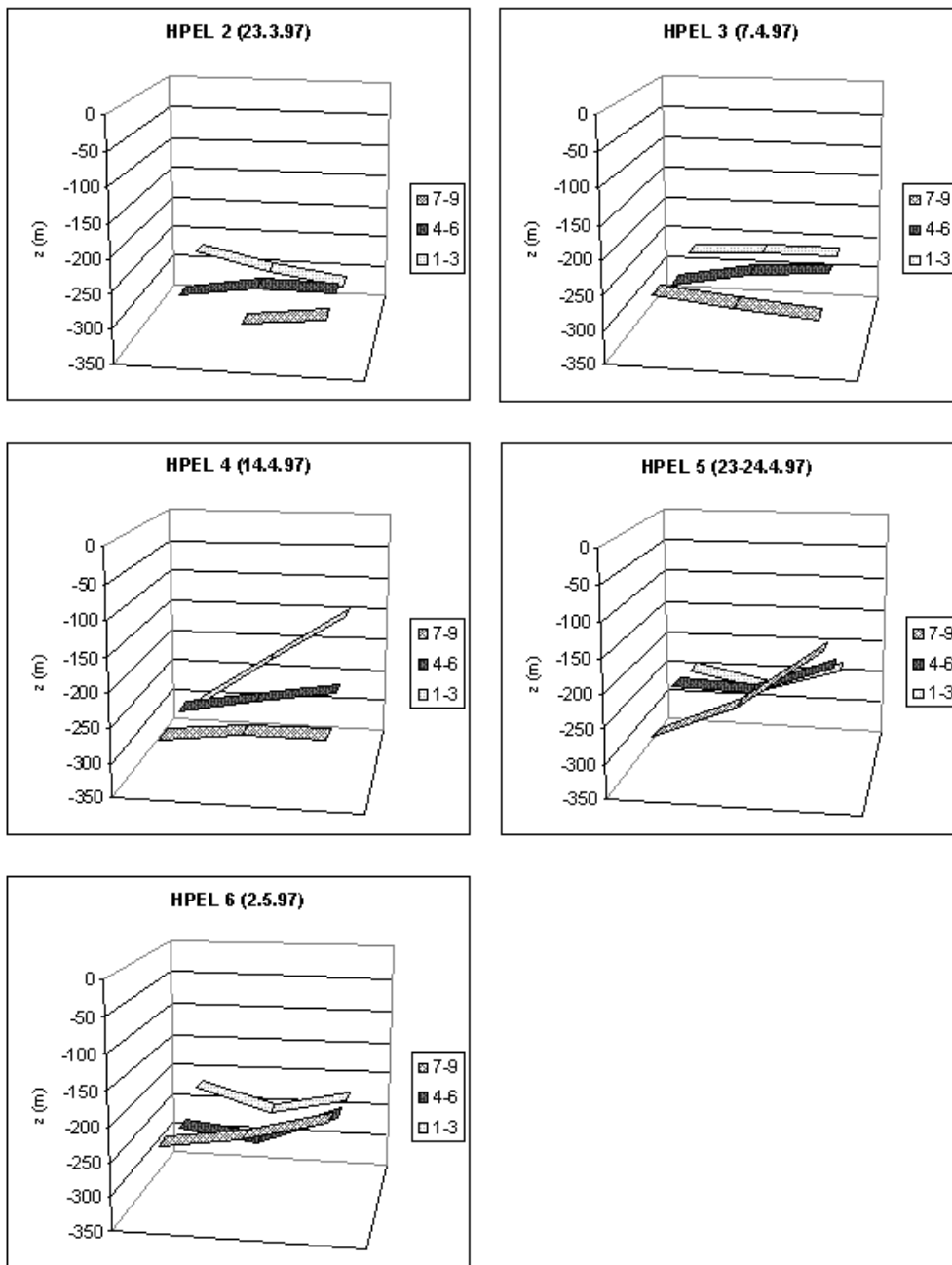


Figure 3.7: Diagrams showing the depth of the  $\sigma_\theta = 29.00 \text{ kg m}^{-3}$  isopycnal — chosen as representative of the density structure — along the three transects for the different hydrological surveys. CTD profiles were taken near every mooring.

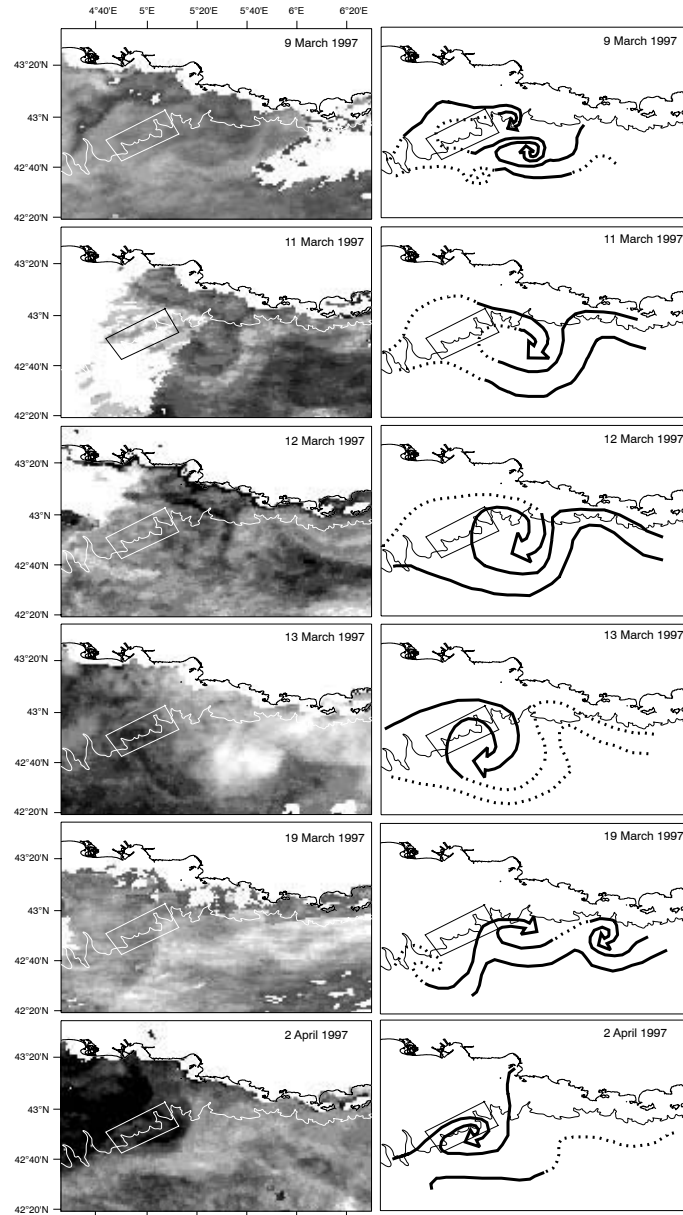


Figure 3.8: Sequence of AVHRR SST images and interpretative diagrams from March 9 to April 2, 1997 on the eastern part of the Gulf of Lions, showing the presence of the NC core south of the HFEE site and of anticyclonic structures on its inner side. The HFEE site and the 1000 m bathymetric contour are indicated. Lighter shades are warmer.

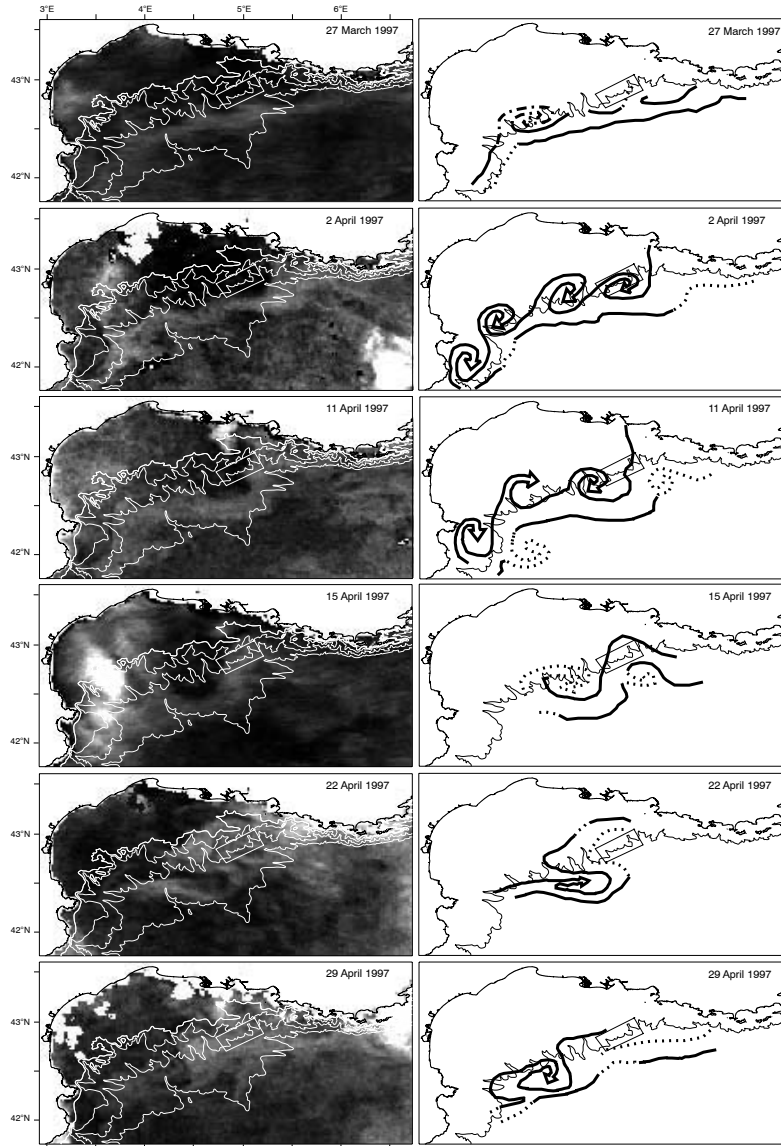


Figure 3.9: Sequence of AVHRR SST images and interpretative diagrams from March 27 to April 29 1997 on the entire Gulf of Lions, showing the westward propagation of a large meander over the eastern Gulf of Lions. The HFFE site and the 1000 m bathymetric contour are indicated. Lighter shades are warmer.

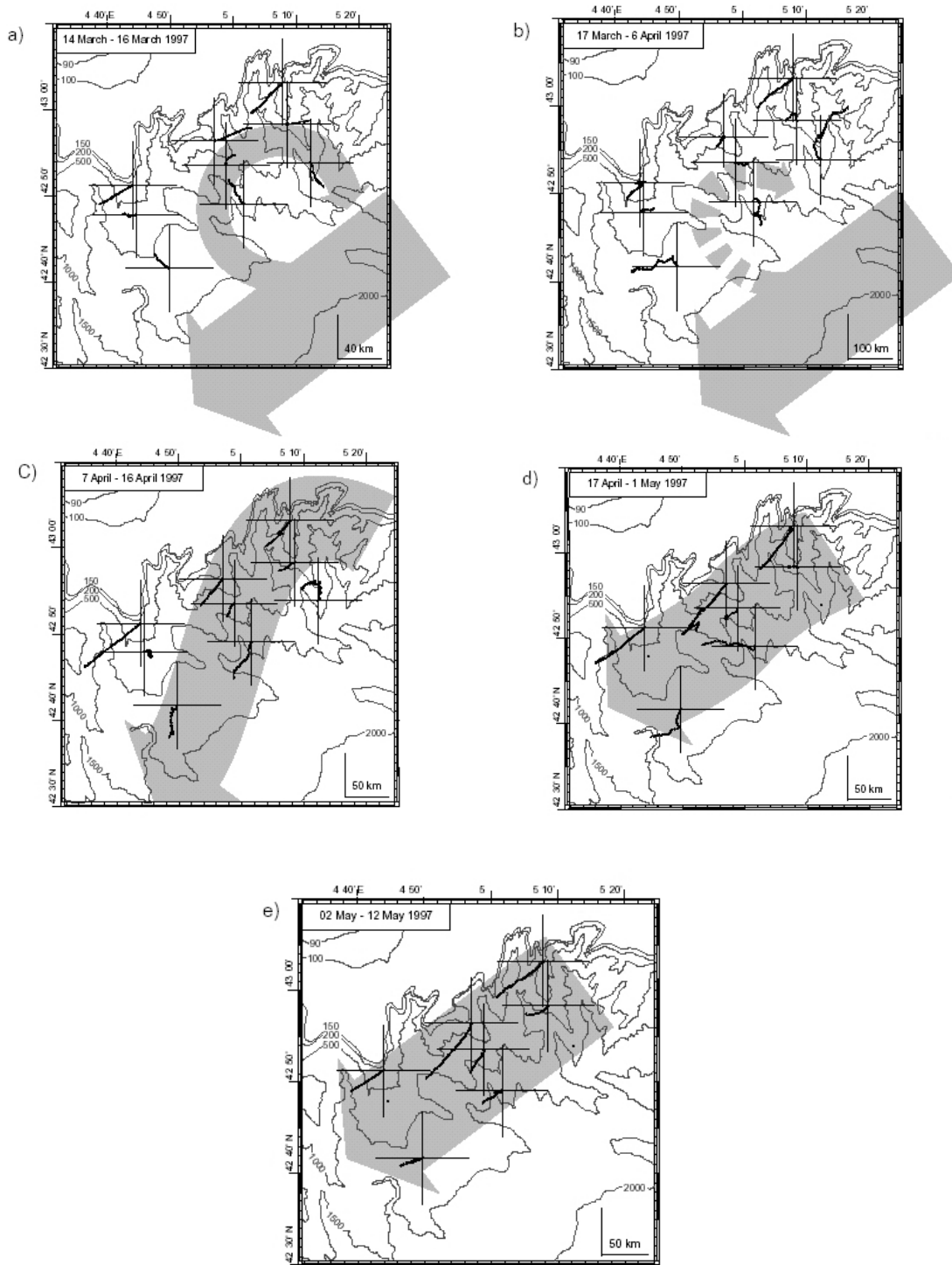


Figure 3.10: Progressive vector diagrams and schematic outline of the Northern Current core for (a) 14 – 16 March, (b) 17 March – 6 April, (c) 7 – 16 April, (d) 17 April – 1 May, and (e) 2 – 12 May, 1997. The x-y scale on the lower right corner corresponds to the axes of the progressive vector diagrams.



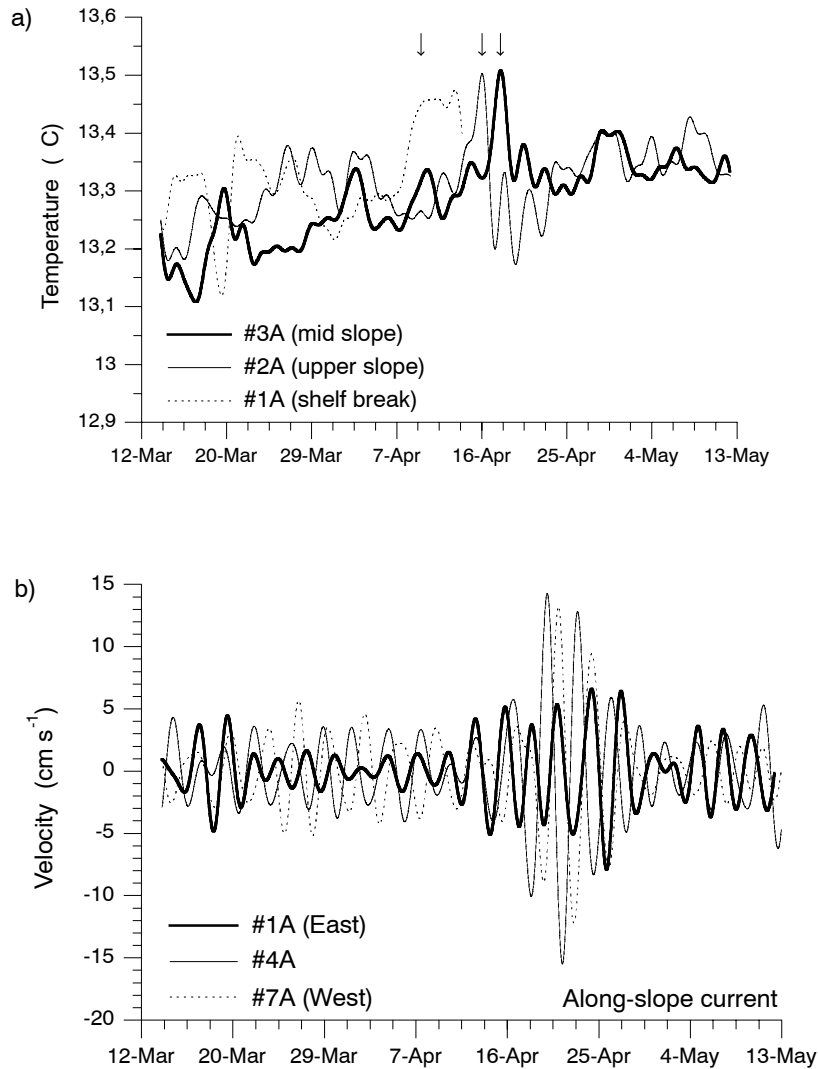


Figure 3.11: a) Low-pass filtered (> 40 h) temperature at 240 m depth for the easternmost section (moorings #1, #2 and #3). b) 2–4 days band-pass filtered along-slope currents near the shelf-break.

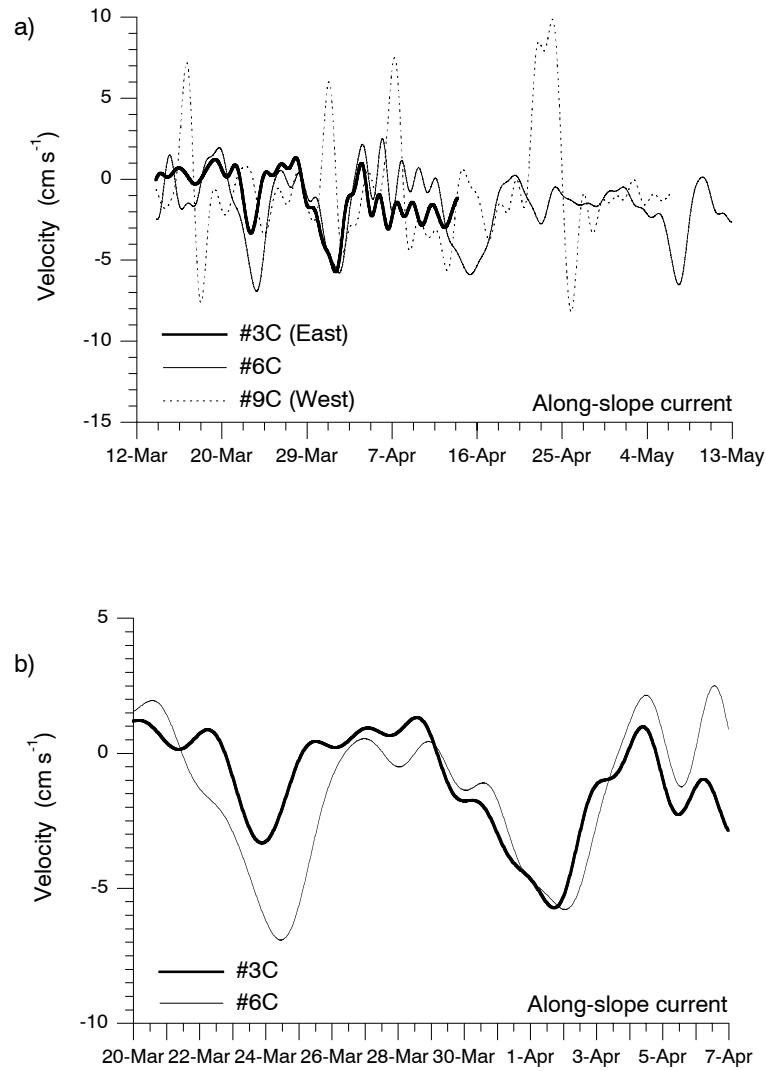


Figure 3.12: a) Low-pass filtered ( $> 40$  h) along-slope current recorded near the bottom on the mid-slope (1230 m depth). b) Detail for the easternmost (#3) and intermediate (#6) moorings.

## 3.4 Discussion

### 3.4.1 Origin of the mesoscale variability of the surface currents

The intrusion of the large meander onto the HFFE site on 7 – 17 April 1997 is well documented by SST images. The current observations at 250 m and 650 m and the hydrographic data (vertical displacements of the isopycnal) show that the meander affects a large part of the water column. The analysis of SST images collected prior to the experiment shows that this type of event is not unique, since it is observed four times during January and February 1997.

In order to discuss the origin of the NC meandering we have worked out the wavelengths and periods that might be related to baroclinic instability following the analytical model proposed by Tang [Tang, 1975], as it is stated in Section 3.2.3. The model assumes quasi-geostrophy, which is quite applicable to the NC since our estimation of the Rossby number is 0.16 (considering mean surface speed of  $50 \text{ cm s}^{-1}$ , current width of 30 km and the Coriolis parameter of about  $10^{-4} \text{ s}^{-1}$ ). This value is close to values found in earlier studies (e.g. Sammari [Sammari et al., 1995] obtained a Ro number of 0.1). There are some aspects that invalidate quasi-geostrophic theory in our case, such as the fact that the topography is particularly strong and strongly distorts the potential vorticity gradient. Moreover, the along-stream topography is very irregular. The model considered here was chosen because of its relative simplicity as a first approach to study baroclinic instability in the HFFE site.

For the case of HFFE, the input values ( $R$  and  $h_2/h_1$ ) are obtained from CTD data recorded in several occasions during the experiment. The value of  $u_0$  is linearly extrapolated from the averaged 240 m depth current meters on the mid slope (average mean speed of  $9.5 \text{ cm s}^{-1}$ ). Considering the bottom of the shear layer at 300 m depth (zero velocity) from averaged Brunt-Väisälä profiles on the mid slope, and velocity linearly increasing to the surface, we obtain a surface mean speed of  $50 \text{ cm s}^{-1}$ . Hence, the averaged values obtained from the three mid-slope sites visited five times each during the experiment are:  $h_1 = 300 \text{ m}$ ,  $h_2 = 880 \text{ m}$ ,  $N_1 = 4.4 \cdot 10^{-3} \text{ s}^{-1}$ ,  $N_2 = 8.1 \cdot 10^{-4} \text{ s}^{-1}$ ,  $u_0 = 50 \text{ cm s}^{-1}$ , leading to a stability ratio (defined in Section 3.2.3) of  $R = 5$ .

Values of  $h_2/h_1$  of 5, 3 and 2 lead to cut-off waves ranging 49 – 84 km in wavelength and  $11 - 14 \text{ cm s}^{-1}$  in phase speed with periods ranging 5 – 7 days. The maximum growth wave ranges from 70 – 125 km and  $8 - 12 \text{ cm s}^{-1}$  in wavelength and phase speed, respectively, with periods ranging 10 – 13 days. Therefore, the wavelength is a stronger function of the depth ratio than the phase speed.

In the other hand, variations in the input  $u_0$  value do not affect the wavelength, but cause strong variations in the phase speed. Values between  $20$  and  $60 \text{ cm s}^{-1}$  make the cut-off wave phase speed ranging  $5 - 15 \text{ cm s}^{-1}$  with periods ranging 5 – 16 days and the maximum growth rate wave ranging  $4 - 12 \text{ cm s}^{-1}$  with periods ranging 10 – 29 days. For the averaged values from the three mid-slope sites visited five times each during the experiment the dimensionless growth rate and phase speed are shown in Fig. 3.13. The cut-off wave has in this case a 68 km wavelength and a  $12.4 \text{ cm s}^{-1}$  phase speed which

leads to a 6.3 days period. The maximum growth wave has a 100 km wavelength, a 9.8 cm s<sup>-1</sup> phase speed and a 11.8 days period.

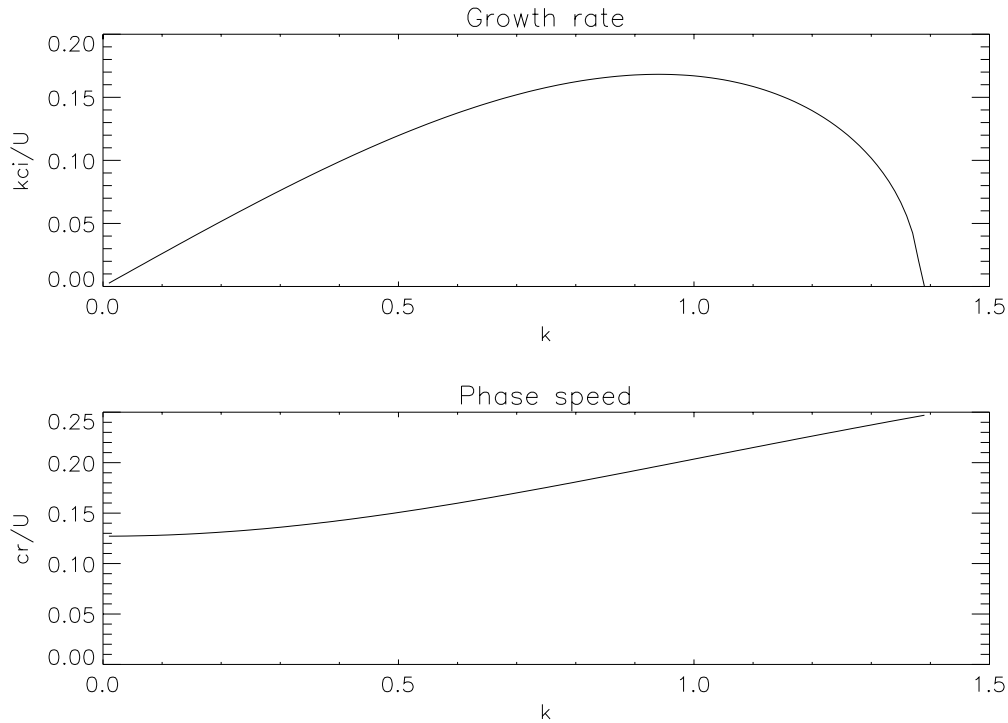


Figure 3.13: Growth rate and phase speed for the averaged values from the three mid-slope sites during HFFE.

The cut-off wavelength compares quite well with the observed NC wavelength of 60 – 80 km from SST images. The predicted cut-off period of 6.3 days indicates that large NC meanders of 10 – 40 days period inferred from SST images as well as those related to the 7-day band from current meters could be due to baroclinic instability. We have to note the high sensitivity of the model, so that the hypothesis put forward in the present study is not entirely conclusive.

Tang’s model accounts only for a unique range of unstable waves, due to the use of quasi-geostrophic theory, i.e. Eady’s classic baroclinic instability theory [Eady, 1949]. When considering primitive equations, a second mode, shorter in wavelength and faster in phase speed is solved [Barth, 1994] [Shi and Red, 1999]. Therefore a second band of shorter periods than those predicted by Tang’s model is expected to appear, such could be the 3.5 days band recorded by current meters in the HFFE.

In the analytical model used here, the effects of bathymetry have not been considered. Studies on baroclinic instability over a sloping bottom show that wavelength and growth rate are expected to decrease with respect to the values obtained with a horizontal lower boundary [Blumsack and Gierasch, 1972].

Moreover, it has been pointed out along the text that the bottom topography in the Gulf of Lions is far from smooth and simple —i.e. the continental slope has a complex bathymetry, with numerous and irregular submarine canyons. Studies of baroclinic instability over irregular along slope topography [Samelson and Pedlosky, 1990] showed how unstable waves can be trapped in the non-sloping parts. In the Gulf of Lions, canyons might play this role. However, in the HFFE we do not expect to have evidence of such waves since our mooring lines were not placed inside canyons but in their adjacent open slope.

The local mechanisms that trigger baroclinic instability are diverse since perturbations of the density field at the shelf-edge may result from the wind stress, topographic irregularities (canyons) and along-shelf variations, or changes of the shelf water characteristics due to freshwater dispersal or coastal upwelling. Further work using numerical techniques is required to gain a better understanding of baroclinic instability in the NC. Nevertheless, the repetitive appearance of large meanders at the eastern tip of the Gulf of Lions, where the shelf and the slope significantly widens, suggests that the along-shelf variation of the topography plays an important role in their formation.

The role of bottom topography on the mesoscale variability of the NC will be the focus of attention in the following chapters of this thesis. Our approach will be barotropic in order to isolate the topographic effect.

### 3.4.2 Origin of the mesoscale variability of the deep near-bottom currents

The near-bottom currents at 1230 m depth are constrained to flow along the continental slope. They show strong fluctuations within the 3–8 days band (Fig. 3.4c) and an increase of their magnitude with respect to the mid-depth currents (data not shown). The low-pass signal (Fig. 3.12) suggests, particularly for the intermediate and the easternmost moorings, a westward propagation of the along-slope current components with a short time lag.

These observations indicate that the synoptic currents could be related to a topographic wave propagating along the continental slope. Similar observations of deep near-bottom currents were firstly reported by Millot [Millot, 1985] for near-bottom current meters deployed at 1800 m depth in the Gulf of Lions, and later during the PRIMO-0 [Alb erola et al., 1995], the PROLIG-2 and the PROS-6 experiments [Sammari et al., 1995] in the Ligurian Sea. The major difference with our data is that, in our case, we observe two main peaks within the 3–8 days band with different characteristics: (i) along-slope fluctuations of 7-day period and (ii) isotropic fluctuations of 3.5-day period. The hypothesis of a propagating wave-like structure is examined here in terms of frequency. The frequency range for topographic Rossby waves is given by

$$\omega = \beta N \sin \theta \coth \left( \frac{kNH}{f} \right) \quad (3.5)$$

where  $\beta$  is the topographic slope,  $N$  is the Brunt-V ais al a frequency,  $\theta$  is the wave propagation direction with respect to the slope,  $k$  is the wavenumber,  $H$  is the mean depth

and  $f$  the Coriolis parameter ([Pedlosky, 1979], p.378). Therefore the high frequency limit corresponds to a wave propagating along-slope and is given by  $\omega = \beta N$ ; waves with lower frequency are bottom trapped.

The average slope range around the moorings #3 and #6 is  $\beta = 0.065 - 0.069$  and the buoyancy frequency range in the last 100 m of the water column (1100 – 1200 m depth) is  $N = 3.1 - 3.7 \cdot 10^{-4} \text{ s}^{-1}$ . Given these values, the threshold period in the HFFE site ranges between 2.9 – 3.6 days.

In our opinion, the 7-day period current fluctuations may correspond to a propagating topographic wave, whose period is close to the 8 days period wave reported by Millot [Millot, 1985]. The case of the 3.5-day period fluctuations is more troublesome because — according to the values of the parameters considered — they appear on either side of the high frequency limit. The fact that Sammari [Sammari et al., 1995] found in a rather similar environment a high frequency limit at 2.5 days, suggests that the 3.5 days current variability may also be due to topographic waves.

### 3.4.3 Repercussion on the local budgets of organic carbon

Van Wambecke [van Wambecke et al., 2001] studied the spatial variations of phytoplankton and bacterial production through the six hydrological surveys performed during the course of the experiment, as well as the spatial and temporal variability of the downward fluxes of particulate organic carbon measured at each station by sediment traps deployed at 240 m depth. The comparison of primary production with measured and estimated organic carbon removal terms (sinking, cycling through the microbial food web, grazing by zooplankton) shows an imbalance. During the duration of the experiment, the system shifts from an initial situation of 'missing' carbon (removal > production) to one of 'excess' carbon (removal < production). Lateral (advective) fluxes of carbon are one of the factors invoked to balance the budgets. The initial situation, which needs an import of carbon to balance the budget, sees the NC flowing south of the HFF site and eddies roaming over the site. This situation is believed to be favourable to shelf-slope exchanges of material and carbon. Later in the experiment, the NC moved on the HFF site, hence increasing the advective along-slope transport and reducing the exchanges with the shelf. The enhanced along-slope transport possibly induces an export of carbon from the HFF site.

## 3.5 Summary and conclusions

The analysis of hydrological, current meter and SST time series collected during the HFFE in the Gulf of Lions provides evidence of complex circulation patterns at the shelf-break and on the slope mainly associated to the mesoscale variability of the NC. Topographic constraints require the near-bottom currents to flow along the slope. Maximum currents are strongest near the shelf break, where the NC path intersects the sea floor.

The AVHRR SST images show that the HFFE site is embedded in a region where significant meandering of the NC occurs and where eddy-like structures develop. The large

meanders (wavelength  $> 60$  km) embrace smaller scale structures. These flow patterns affect the entire core of the NC from the surface down to at least 650 m depth. Baroclinic instability is viewed as a possible mechanism for the generation of the NC meanders. The analytical model of Tang [Tang, 1975] predicts the development of unstable waves having wavelength and period ranges compatible with the lower frequency band recorded from current meters and with those obtained from SST observations. Although the model is quite sensitive to the input parameters, it provides a first estimate concerning the origin of the meandering of the NC. However, the present data set does not allow to separate the role of the different potential controlling factors (and, in particular, the role of bottom topography, which is misrepresented in Tang's model). A higher frequency 3.5-day band observed in current meter data is out of the frequency range predicted by the classic baroclinic instability theory and is discussed in the present work as a restriction of quasi-geostrophic theory.

The variability of the deep currents, which are to some extent independent from that of the upper layer, is dominated by 7-days period fluctuations. The along-slope propagation of these oscillations could be related to topographic Rossby waves. The position of the current on the slope and, in particular, the repeated passage of meander overlapping the shelf edge may have a significant impact in the export of matter off the shelf, thus greatly influencing shelf-slope exchanges.

The influence of bottom topography on the mesoscale variability of the NC will be investigated in the next chapters.





# Chapter 4

## A laboratory model of the Northern Current: jet flows over a continental slope

C'est de la cuisine.  
RENÉ CARCEL

*Keywords: Northern Current, slope-current, barotropic jet, laboratory model.*

### 4.1 Introduction

We are interested in investigating the dynamical behaviour of a jet (the Northern Current) over a sloping bottom topography, to explore under which circumstances and to which extent this phenomenon may contribute to the flow mesoscale variability. The Northern Current is a slope current in the NW Mediterranean which flows from the Ligurian basin into the Balearic basin. It is characterized by surface maximum velocities of 30-50 cm s<sup>-1</sup>, decreasing with depth till 300-400 m. The current transports different water masses, namely, from surface to bottom, Modified Atlantic Water (MAW), Winter Intermediate Water (WIW) when present, Levantine Intermediate Water (LIW) and Western Mediterranean Deep Water (WMDW). The Northern Current flows, at its entrance into the Gulf of Lions, over the deepest half of the continental slope, with a width of 20-30 km, as can be deduced from statistical data from Lapouyade and Durrieu [Lapouyade and de Madron, 2001] giving evidence of the Current flowing over the 1000 to 2000 m isobath. Nevertheless, the onshore limit of the Current (the 1000 m isobath) is difficult to estimate due to the complex bathymetry of the mid-slope, which is intersected by numerous irregular canyons (see Fig. 3.1).

The Northern Current has large mesoscale activity. During the MATER HFF experiment in the Gulf of Lions (March-May 1997), meandering of the Northern Current could be observed by infrared satellite images and in-situ data (Chapter 3 of this thesis). Satellite

images have clearly revealed the meandering character of the Northern Current (see e.g. Fig. 3.9, April 15) and the high mesoscale activity on the upper continental slope, which is usually apparent as a string of anticyclonic vortices (see Fig. 3.9, April 2).

The major variability in the Gulf of Lions has been found associated to the 2-10 days period band. Along-slope and transversal velocity components show the same intensity in this band; therefore this signal has been currently associated to meanders. Analysis of field data collected at the entrance of the Gulf (off Nice) have yielded oscillation periods of 3-6 days associated to wavelengths of 30-60 km and phase speeds of  $10 \text{ km day}^{-1}$  [Sammari et al., 1995]. Estimations from satellite images during the MATER HFF experiment yielded 80 km average wavelength, periods of 10-40 days (16.5 days average) and surface speeds of  $2-8 \text{ km day}^{-1}$  ( $5 \text{ km day}^{-1}$  average).

The depth extension of the Northern Current mesoscale meanders seems to be related to the stratification of the water column, reaching larger depths during low stratified conditions [Taupier-Letage and Millot, 1986]. Mesoscale currents in winter are clearly barotropic and may reach  $\simeq 20 \text{ cm s}^{-1}$  at depths ranging from 100 to 1100 m depth [Taupier-Letage and Millot, 1986]. Off Marseille, deep currents are also strongly correlated with surface flows at the 2 – 5 days band [de Madron et al., 1999]. The intensification of the Northern Current flow (normally in winter, due to thermohaline processes) is well correlated with the intensification of the mesoscale activity.

The objective of the present work is to perform a simulation of a prograde westward current, as the Northern Current, in rotating tank laboratory experiments to better understand the contribution of bottom topography to the observed variability. By definition, the Northern Current is a so-called ‘prograde westward current’. ‘Prograde’ refers to a current which flows in the same direction as the direction of rotation, whereas a counter-rotating current is known as a ‘retrograde’ current [strictly speaking, these terms only have a meaning for the case of a rotating tank]. A current which leaves the shallower side on its right is known as a ‘westward’ current, whereas those currents which flow with the shallower side on their left side are known as ‘eastward’ currents. This terminology is based on the topographic simulation (e.g. in a rotating tank) of the latitudinal variation of the Coriolis parameter: shallower and deeper regions are referred to as ‘North and ‘South, respectively. Moreover, it is common in the literature to denominate currents with a narrow structure as ‘jets’. In analogy with previous studies, in this text we will refer to the Northern Current either as a ‘current’ or as a ‘jet’.

In this chapter we will study the behaviour of the along-slope current associated with the continental slope. In order to isolate the topographic effect, we will adopt homogeneous density conditions. We will also perform a set of experiments with constant fluid depth to provide a reference for the results with the sloping bottom. Finally, in order to understand the balance of vorticity generated by both the horizontal shear and the vertical squeezing/stretching due to the bottom topography, we will perform experiments of current reversal (i.e. a retrograde current) by forcing the flow in the opposite direction. There are technical difficulties that complicate the laboratory modelling of a slope current over a submarine canyon. The influence of canyons indenting the Gulf of Lions slope on the Northern Current mesoscale variability will be addressed in the next chapter, using a

numerical approach.

We start this chapter with a brief introduction of the governing equations. We derive the principle of conservation of potential vorticity to further explain the analogy between the variations in the Coriolis parameter and the variations in bottom topography, which we use in our discussion. We continue with the formulation of the problem and we discuss the conditions needed for shear instability to exist in the presence of a sloping bottom. We also present a review of past studies on this subject. Next, we explain the experimental techniques we used to produce the currents in the laboratory and we present the results obtained using different bottom topographies. We continue with the discussion of the different results obtained focussing on the differences in the balance of vorticity for the case of prograde and retrograde jets over a sloping bottom. Finally, we briefly discuss about the role of the free surface elevation in laboratory experiments.

## 4.2 Theoretical framework

### 4.2.1 Governing equations

Consider a homogeneous, incompressible fluid moving in a rotating system. The fluid motion is governed by the Navier-Stokes equation, which describes the balance of momentum, and the continuity equation, which represents mass conservation. In a reference frame co-rotating with the system, these equations are given by

$$\frac{\partial \vec{u}}{\partial t} + \vec{u} \cdot \nabla \vec{u} + 2\vec{\Omega} \times \vec{u} = -\frac{1}{\rho} \nabla p + \nabla \Phi + \nu \nabla^2 \vec{u} \quad (4.1)$$

$$\nabla \cdot \vec{u} = 0 \quad (4.2)$$

where  $\Phi = \Phi_c + \Phi_g$ . The gradient of  $\Phi_g$  represents conservative forces related to the gravitational acceleration and the gradient of  $\Phi_c$  denotes the centrifugal accelerations. In the homogeneous case, the reduced pressure can be expressed as

$$P = p - \rho \Phi. \quad (4.3)$$

Then, the momentum equation becomes

$$\frac{\partial \vec{u}}{\partial t} + \vec{u} \cdot \nabla \vec{u} + 2\vec{\Omega} \times \vec{u} = -\frac{1}{\rho} \nabla P + \nu \nabla^2 \vec{u}. \quad (4.4)$$

The vorticity of the velocity field is defined as  $\vec{\omega} = \nabla \times \vec{u}$ . By taking the *curl* of (4.4), the vorticity equation is

$$\frac{\partial \vec{\omega}}{\partial t} + \vec{u} \cdot \nabla \vec{\omega} = (2\vec{\Omega} + \vec{\omega}) \cdot \nabla \vec{u} - (2\vec{\Omega} + \vec{\omega}) \nabla \cdot \vec{u} + \frac{\nabla \rho \times \nabla P}{\rho^2} + \nu \nabla^2 \vec{\omega}. \quad (4.5)$$

The baroclinic vector  $\nabla \rho \times \nabla P$  vanishes for a constant  $\rho$ . Thus, for an incompressible barotropic fluid, the vorticity equation is

$$\frac{\partial \vec{\omega}}{\partial t} + \vec{u} \cdot \nabla \vec{\omega} = (2\vec{\Omega} + \vec{\omega}) \cdot \nabla \vec{u} + \nu \nabla^2 \vec{\omega}. \quad (4.6)$$

The sum of planetary and relative vorticity ( $2\vec{\Omega} + \vec{\omega}$ ) is known as the absolute vorticity.

## 2D motion

In a geophysical context, horizontal scales are of some orders of magnitude larger than vertical scales – i.e. basin and ocean extensions are much larger than the water depth, converting oceans into thin layers of water. Moreover, in geophysical motions the horizontal velocities are about two orders of magnitude larger than vertical velocities. Therefore, geophysical flows can be assumed to be, in a first approximation, 2D flows.

In a physical context, as in the laboratory, we acquire a 2D flow by rapidly rotating the system. When the fluid is rapidly rotating and the viscous forces are negligible, the Navier-Stokes equation reduces to the balance of the Coriolis force and the pressure gradient force, i.e. the geostrophic balance equations (in cartesian coordinates):

$$-fv = -\frac{1}{\rho} \frac{\partial P}{\partial x} \quad (4.7)$$

$$+fu = -\frac{1}{\rho} \frac{\partial P}{\partial y} \quad (4.8)$$

$$0 = -\frac{1}{\rho} \frac{\partial P}{\partial z} \quad (4.9)$$

$$\frac{\partial u}{\partial x} + \frac{\partial v}{\partial y} + \frac{\partial w}{\partial z} = 0. \quad (4.10)$$

In the horizontal momentum equations  $f = 2\Omega \sin\varphi$  is the so-called Coriolis parameter, with  $\Omega$  the Earth rotation and  $\varphi$  the geographical latitude.

The vertical derivatives of (4.7) and (4.8) for constant  $f$  and  $\rho$  lead to

$$\frac{\partial u}{\partial z} = \frac{\partial v}{\partial z} = 0, \quad (4.11)$$

which implies that the velocity field has no vertical shear and that all particles in the same vertical move in concert. This is known as the Taylor-Proudman theorem.

Taking the horizontal derivatives of (4.7) and (4.8), we obtain that for constant  $f$  and  $\rho$ , the horizontal divergence of the flow  $div(\vec{u}) = \frac{\partial u}{\partial x} + \frac{\partial v}{\partial y} = 0$ . Then, from the continuity equation we find that  $-\frac{\partial w}{\partial z} = 0$ , which means that the vertical velocity is the same at all depths. If the flow is limited by a horizontal (e.g. bottom) boundary, the vertical velocity at that boundary must be zero. Thus, the vertical velocity should be zero everywhere in the fluid, and the flow is strictly 2D.

## Generalization to non-geostrophic flows

In order to allow for topographic effects, the local and non-linear terms need to be included in the momentum equations. If the horizontal flow field is initially independent of depth,

it will remain so at all future times:  $\frac{\partial u}{\partial z} = \frac{\partial v}{\partial z} = 0$ . Thus, for a homogeneous fluid of depth  $h(x, y, t)$  over arbitrary topography  $h_b(x, y)$ , the governing equations are:

$$\frac{\partial u}{\partial t} + u \frac{\partial u}{\partial x} + v \frac{\partial u}{\partial y} - fv = -\frac{1}{\rho} \frac{\partial P}{\partial x} + \nu \nabla^2 u \quad (4.12)$$

$$\frac{\partial v}{\partial t} + u \frac{\partial v}{\partial x} + v \frac{\partial v}{\partial y} + fu = -\frac{1}{\rho} \frac{\partial P}{\partial y} + \nu \nabla^2 v \quad (4.13)$$

$$0 = -\frac{1}{\rho} \frac{\partial P}{\partial z} + \nu \nabla^2 w \quad (4.14)$$

$$\frac{\partial u}{\partial x} + \frac{\partial v}{\partial y} + \frac{\partial w}{\partial z} = 0. \quad (4.15)$$

Such a flow is known as *barotropic*.

Since the fluid is homogeneous, the dynamic pressure  $P$  is independent of  $z$ , thus  $P(x, y, t) = \rho gh(x, y, t)$ . Then, the momentum equations are:

$$\frac{\partial u}{\partial t} + u \frac{\partial u}{\partial x} + v \frac{\partial u}{\partial y} - fv = -g \frac{\partial h}{\partial x} + \nu \left( \frac{\partial^2 u}{\partial x^2} + \frac{\partial^2 u}{\partial y^2} \right) \quad (4.16)$$

$$\frac{\partial v}{\partial t} + u \frac{\partial v}{\partial x} + v \frac{\partial v}{\partial y} + fu = -g \frac{\partial h}{\partial y} + \nu \left( \frac{\partial^2 v}{\partial x^2} + \frac{\partial^2 v}{\partial y^2} \right). \quad (4.17)$$

Equation (4.15) allows horizontal divergence to be non-zero, i.e. allows flow across isobaths. Since  $u$  and  $v$  are  $z$ -independent, the continuity equation (4.15) can be integrated in the vertical. Integrating from the bottom  $z = h_b$  to the free surface  $z = h + h_b$ , the continuity equation can be expressed as:

$$\frac{\partial h}{\partial t} + \frac{\partial(hu)}{\partial x} + \frac{\partial(hv)}{\partial y} = 0. \quad (4.18)$$

The system of equations constituted by (4.16), (4.17) and (4.18) is known as the *shallow-water equations*.

In order to explore the horizontal divergence in this situation, we take the cross-derivatives of (4.12) and (4.13), and subtract the former from the latter. This leads to the vorticity equation

$$\frac{D\omega}{Dt} + \left( \frac{\partial u}{\partial x} + \frac{\partial v}{\partial y} \right) (f + \omega) = \nu \left( \frac{\partial^2 \omega}{\partial x^2} + \frac{\partial^2 \omega}{\partial y^2} \right), \quad (4.19)$$

where  $\omega = \frac{\partial v}{\partial x} - \frac{\partial u}{\partial y}$  is the relative vorticity,  $D/Dt$  is the material derivative  $\frac{D}{Dt} = \frac{\partial}{\partial t} + u \frac{\partial}{\partial x} + v \frac{\partial}{\partial y}$ ,  $\left( \frac{\partial u}{\partial x} + \frac{\partial v}{\partial y} \right)$  is the horizontal flow divergence.

For the case of an inviscid flow, (4.19) reduces to

$$\frac{D\omega}{Dt} + \left( \frac{\partial u}{\partial x} + \frac{\partial v}{\partial y} \right) (f + \omega) = 0. \quad (4.20)$$

The continuity equation (4.18) can also be written as

$$\frac{\partial u}{\partial x} + \frac{\partial v}{\partial y} = -\frac{1}{h} \frac{Dh}{Dt}. \quad (4.21)$$

Combining (4.20) with (4.21) one arrives at

$$\frac{D}{Dt} \left[ \frac{f + \omega}{h} \right] = \frac{Dq}{Dt} = 0. \quad (4.22)$$

This expression is known as the principle of conservation of potential vorticity,  $q$ , and implies that the relative vorticity of the fluid will change if it experiences depth variations. Similarly, variations in the Coriolis parameter will have the same effect.

Inviscid topographic effects on a rotating homogeneous fluid flow are described by (4.20) and (4.21), or by (4.22): changes in relative vorticity are associated to stretching/squeezing of fluid columns when the fluid experiences changes in depth.

Moreover, from (4.22) one can also deduce that for a fluid with  $\omega = 0$  (e.g. a fluid at rest), a gradient in ambient potential vorticity  $q = \frac{f}{h}$  can be acquired by a variation in the fluid depth  $h$  by suitable bottom topography, or by a variation in the Coriolis parameter  $f$ . One major application of this analogy is the possibility of simulating the beta effect (i.e. a linear variation of  $f$  with the northward coordinate  $y$ ) in the laboratory, by using a linearly sloping topography (see e.g. [van Heijst, 1994]).

## 4.2.2 Formulation of the problem

In the absence of rotation, shear layers may be unstable thus leading to the formation of vortices. When the system is rotating, the velocity gradient in the shear layer needs to exceed a critical value for instability to occur. In the absence of beta effects (i.e. for  $f$  constant), the shear layer instability has the appearance of a Kelvin-Helmholtz instability: a chain of vortices of the same sign as the ambient shear develop [Drazin and Reid, 1981] (Fig. 4.1a). An additional mechanism for instability is present if there are ambient potential vorticity gradients (caused by variations in the bottom topography or, analogously, by variations in the Coriolis force, as discussed above). In this case the resulting instability is a Rossby wave (Fig. 4.1b).

Consider the flow of a homogeneous, inviscid fluid, with the surface boundary flat and horizontal, on an  $f$ -plane. Let the bottom boundary be given by an arbitrary topography in the across-slope direction  $h(x)$ . The potential vorticity equation (4.22) can be re-written as:

$$\frac{\partial q}{\partial t} + u \frac{\partial q}{\partial x} + v \frac{\partial q}{\partial y} = 0, \quad (4.23)$$

where  $q = ((\frac{\partial v}{\partial x} - \frac{\partial u}{\partial y}) + f)/h$ .

Consider an arbitrary along-slope mean flow  $\bar{v}(x)$ , disturbed by small perturbations given by  $u'(x, y, t)$  and  $v'(x, y, t)$ . Then, the potential vorticity can be also written as the sum of a reference potential vorticity and a potential vorticity fluctuation, i.e.  $q =$

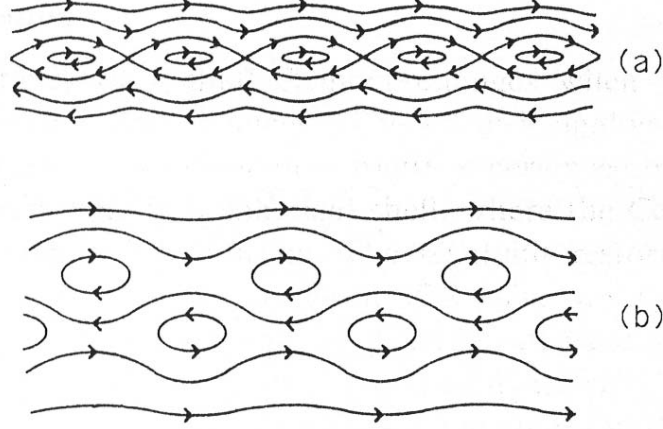


Figure 4.1: Sketch of ideal streamfunctions, viewed from a reference frame moving with the structures. (a) Shear-induced vortex chain (Kelvin-Helmoltz-like instability or ‘cat-eye’ pattern). (b) Rossby wave. From [Solomon et al., 1993].

$\bar{q}(x) + q'(x, y, t)$ . Substituting into (4.23), and after linearizing higher-order terms (i.e. considering the products of perturbations small), a linearized perturbation equation can be written as:

$$\frac{\partial q'}{\partial t} + u' \frac{d\bar{q}}{dx} + \bar{v} \frac{\partial q'}{\partial y} = 0, \quad (4.24)$$

where  $\bar{q} = (\frac{d\bar{v}}{dx} + f)/h$  and  $q' = ((\frac{\partial v'}{\partial x} - \frac{\partial u'}{\partial y}) + f)/h$ .

If the bottom boundary does not change in time, the continuity equation (4.18) can be linearized as:

$$\frac{\partial(hu')}{\partial x} + \frac{\partial(hv')}{\partial y} = 0. \quad (4.25)$$

Thus, the velocity components can be expressed in terms of a perturbation stream function  $\psi'$  as

$$u' = -\frac{1}{h} \frac{\partial \psi'}{\partial y} \quad v' = +\frac{1}{h} \frac{\partial \psi'}{\partial x} \quad (4.26)$$

(the flow is assumed to be along streamlines  $\psi = \text{constant}$ ). Substitution of (4.26) in (4.24) leads to the equation for the stream function  $\psi$

$$\left( \frac{\partial}{\partial t} + \bar{v} \frac{\partial}{\partial y} \right) \left( \nabla^2 \psi' - \lambda \frac{\partial \psi'}{\partial x} \right) + \chi \frac{\partial \psi'}{\partial y} = 0, \quad (4.27)$$

where

$$\lambda(x) = \frac{1}{h} \frac{dh}{dx} \quad (4.28)$$

and

$$\chi = \lambda f + \lambda \frac{d\bar{v}}{dx} - \frac{d^2 \bar{v}}{dx^2}. \quad (4.29)$$

Thus, admitting a wave-like solution of amplitude  $\phi$  in the along-slope direction  $y$  as

$$\psi'(x, y, t) = \phi(x)e^{ik(y-ct)}, \quad (4.30)$$

where  $k$  is the wave number in the  $y$  direction,  $c$  is the phase speed of the wave and  $A(x)$  is the amplitude of  $\psi'$ . Substituting in (4.27), we obtain the following second-order differential equation for the amplitude  $\phi(x)$ :

$$\frac{d^2\phi}{dx^2} - \lambda\frac{d\phi}{dx} - k^2\phi + \frac{1}{(\bar{v} - c)}\chi\phi = 0. \quad (4.31)$$

We need to know the velocity profile  $\bar{v}$  in order to determine the boundary conditions required to solve (4.31). This will allow us to find the homogeneous system of equations for the constants of integration, and to find the non-trivial solution (i.e. solving the determinant = 0). Then, one derives the dispersion relation for the wave speed  $c$ , as a function of the wavenumbers, and the velocity  $\bar{v}$  of the mean flow. This allows to establish the instability criterion, i.e. when  $c_i > 0$ .

Regardless of the velocity profile, one can establish a necessary (but not sufficient) condition for instability through the integral of (4.31) over the boundary conditions. Let us consider as boundary conditions rigid lateral walls (as in e.g. [Cushman-Roisin, 1994] where the normal velocity component must vanish  $u' = 0$ ):

$$\phi(x) = 0, \quad \text{at} \quad x = -b/2 \quad \text{and} \quad x = b/2. \quad (4.32)$$

For an unstable disturbance (i.e. when  $c_i > 0$ ) one can obtain that

$$\int_{-b/2}^{+b/2} \chi \frac{c_i}{(\bar{v} - c_r)^2 + c_i^2} \frac{|\phi|^2}{h} dx = 0 \quad (4.33)$$

(from [Li and McClimans, 2000]). Therefore, the necessary condition for instability to occur is that  $\chi$  must be zero somewhere in the domain, i.e.  $\chi$  must change sign within the domain  $(-b/2, b/2)$ . Since  $\chi$  can be re-written as

$$\chi = -h \frac{dq}{dx}, \quad (4.34)$$

a necessary condition for instability to occur is that the derivative of the potential vorticity profile must change sign within the domain, i.e. *the potential vorticity profile must have an extremum within the domain.*

Note that for the case when the topography is flat and beta-effects are neglected, the necessary condition for instability leads to the condition that the *absolute vorticity* profile contains a relative maximum or minimum somewhere in the domain.

In the present study, we will measure the velocity profile in the laboratory experiments and we will solve the problem numerically (in the next chapter). We will perform a set of laboratory experiments to study shear instability on an f-plane, and a second set of experiments to consider the case with a sloping bottom.



## Wave speed and wave growth rate

The wave speed and growth rate of the perturbations is bounded. For the case of an f-plane, a derivation of both quantities is given by Howard [Howard, 1961]. The bound for the phase speed is given by

$$U_{min} < c_r < U_{max} \quad (4.35)$$

where  $c_r$  is the real part of the phase speed and  $U_{min}$  and  $U_{max}$  are the minimum and maximum values of the zonal flow  $\bar{u}(y)$ , respectively. Therefore, there will be a location where the wave matches the velocity of the ambient flow. The wave-flow interaction occurring at this location will allow the wave to grow at the expense of the mean flow.

The study of the imaginary part of the phase speed allows to obtain the bound for the growth rate. According to Howard's semicircle theorem [Howard, 1961], the perturbation growth rate has an upper bound given by

$$c_i \leq \frac{U_{max} - U_{min}}{2}. \quad (4.36)$$

### 4.2.3 Jets over a sloping bottom and jets on a beta-plane

As discussed above, due to the conservation of potential vorticity (4.22) there is an analogy between the variations in the Coriolis parameter and the variations in the bottom topography. This analogy allows us to compare our results of jets over a sloping bottom with past studies of jets on a beta-plane. This need comes from the fact that few laboratory studies have been done on the instability of a slope-current; in contrast, there is an important number of previous studies on the behaviour of currents on a beta-plane.

The stability of a cosine-type slope-current has been studied analytically by Li and McClimans [Li and McClimans, 2000]. The authors discuss the stabilizing role of the slope and the destabilizing role of the Rossby number,  $Ro$  (i.e. the non-dimensional number that compares the advective term and the Coriolis force term; it will be defined later on in Section 4.3.2), in determining the instability of the current. According to their results the bottom slope in the Barents Sea is capable of stabilizing a cosine-profile jet flow with a  $Ro$  number of up to 0.2. They found that eastward jets were more stable than westward currents. More generally, they pointed out that 'there is a critical value for  $Ro$  under which a jet flow is stable for any natural jet and slope profiles'.

Eastward and westward jets on a beta-plane are known to show very different behaviours. A stability analysis performed by Sommeria [Sommeria et al., 1991], for a  $sech^2$ -type velocity profile showed that eastward jets were more easily stabilized than westward jets. More precisely, the authors point out that the beta-effect must be three times stronger to stabilize a westward jet than to stabilize an eastward jet with the same  $sech^2$  profile. This is in qualitative agreement with the above-mentioned results from Li and McClimans [Li and McClimans, 2000] for a slope current with a cosine velocity profile.

In laboratory experiments, westward jets were broad and turbulent [Sommeria et al., 1988] [Sommeria et al., 1991], and lead to robust vortices of the same sign as the ambient shear. In the experiments by Sommeria [Sommeria et al., 1988], the authors were simulating a

source-sink flow on a beta-plane. They observed that the westward jet broadened for increasing flow speeds, until for very large flow speeds it filled the tank. The experiments presented a strong asymmetry between cyclonic and anticyclonic shear, due to curvature. Since in their experiments westward flows were flowing anticyclonically, cyclonic shear was dominant, and the instability of the cyclonic shear layer developed into cyclonic vortices, varying in number from 5 to 1 as the flow speed was increasing in different experiments.

On the other hand, eastward jets were always narrow and wavy [Sommeria et al., 1989] (Fig. 4.2). The authors generated a source-sink flow on a beta-plane (with bottom depth linearly increasing in radial direction) flowing in eastward direction. The potential vorticity profile presented a steep gradient in the middle of the jet, induced by the advection of positive and negative potential vorticity generated at the sinks and at the sources, respectively, towards the centre of the jet. The step gradient in potential vorticity was observed to act as a barrier for mixing between particles inside and outside the jet. Mixing was mainly due to intermittent ejection of potential vorticity (visualized with dye, regarding the fact that potential vorticity and dye are both quasi-conserved for each fluid particle) from the jet. Linear stability analysis for a  $sech^2$  velocity profile predicted that the only unstable mode for an eastward jet was a sinuous mode, explaining the wavy shape observed. Moreover, the wavy pattern was quasi-steady, as a result of a balance of the eastward advection by the mean flow and the westward propagation of Rossby waves.

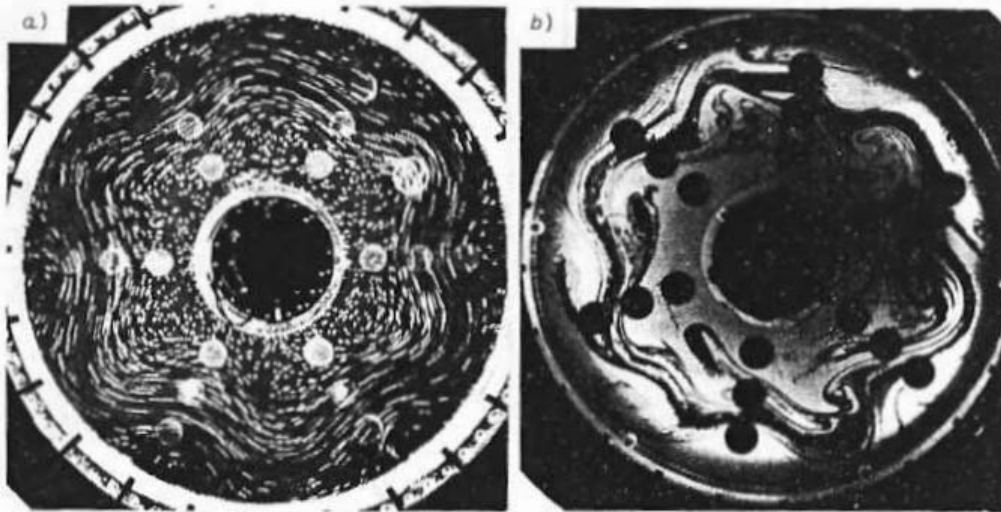


Figure 4.2: (a) An eastward jet with six waves, visualized by taking a short time exposure of particles suspended in the flow. (b) When dye is injected into the jet it follows the fluid flow and shows the wavy pattern characteristic of eastward jets, as can be seen in this state of seven waves. From [Sommeria et al., 1991].

In similar laboratory experiments performed by Solomon [Solomon et al., 1993], vortices generated at both shear layers of the jet showed different velocity propagations, due to the effect of curvature. When the flow speed increased (in different experiments) the

shift between the two vortex chains was observed to reduce, until the chains finally had the same propagation speed —the vortices locked. For locked states the propagation speed of the vortices in the eastward case was reduced to less than a third of the mean flow, in accordance to what is expected for a Rossby wave. On the contrary, locked states of westward jets did not show any variation in the propagation speed of vortices.

Marcus and Lee developed a theory [Marcus and Lee, 1998] to explain the differences observed between eastward and westward jets on a beta plane. The main highlights of their theoretical analysis are that the jet becomes unstable through the instability of both shear layers, developing Kelvin-Helmholtz-like billows at either side of the jet, each of which is coupled with a Rossby wave (Fig. 4.1). Each side of the jet shows a discontinuity in the potential vorticity profiles across the jet. In the eastward jet, the discontinuities apparent in potential vorticity sections tend to move together, the jet becomes narrower and is placed in a zone with a strong gradient of potential vorticity (Fig. 4.3). The Rossby-waves associated with the instability of each side of the jet are also moved together and they merge into one stronger wave, responsible of the jet meandering. On the other hand, in westward jets the potential vorticity discontinuities are shifted apart from each other (Fig. 4.4). The jet is broad and Rossby waves are weak, so they are almost non-perceptible. Their model shows Rossby waves are placed at the potential vorticity discontinuities, causing the discontinuities to oscillate in radial direction, whereas vortices are placed at regions of constant potential vorticity.

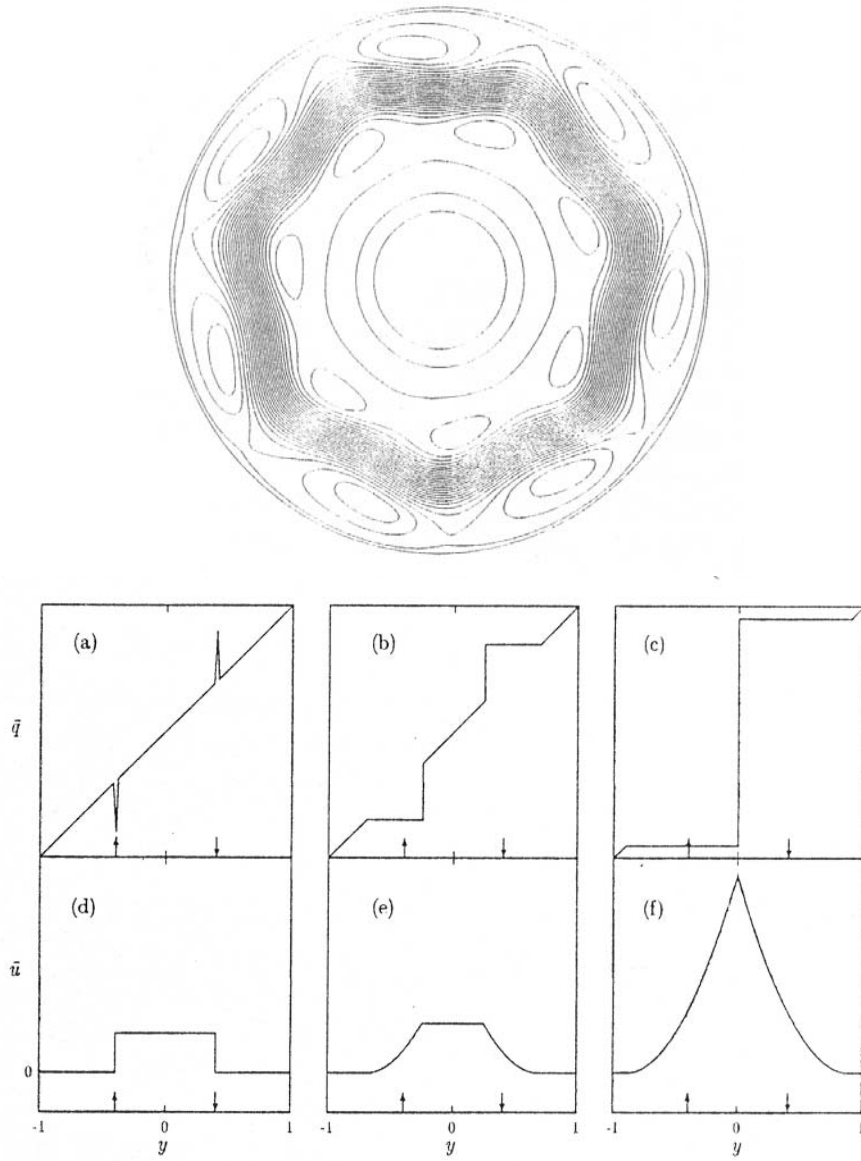


Figure 4.3: Top: Streamfunction of a numerically computed locked eastward jet viewed in the rotating frame where the flow is stable. Bottom: Eastward jet model for different flow speeds, for (a) PV profile for the primary flow; (b) PV profile at higher flow rate for the unlocked jet; (c) PV profile at still higher flow rate for the locked jet; (d), (e) and (f) are the velocity profiles corresponding to (a), (b) and (c), respectively. Vertical arrows indicate the position of the forcing rings used to generate the jet flow. From [Marcus and Lee, 1998].

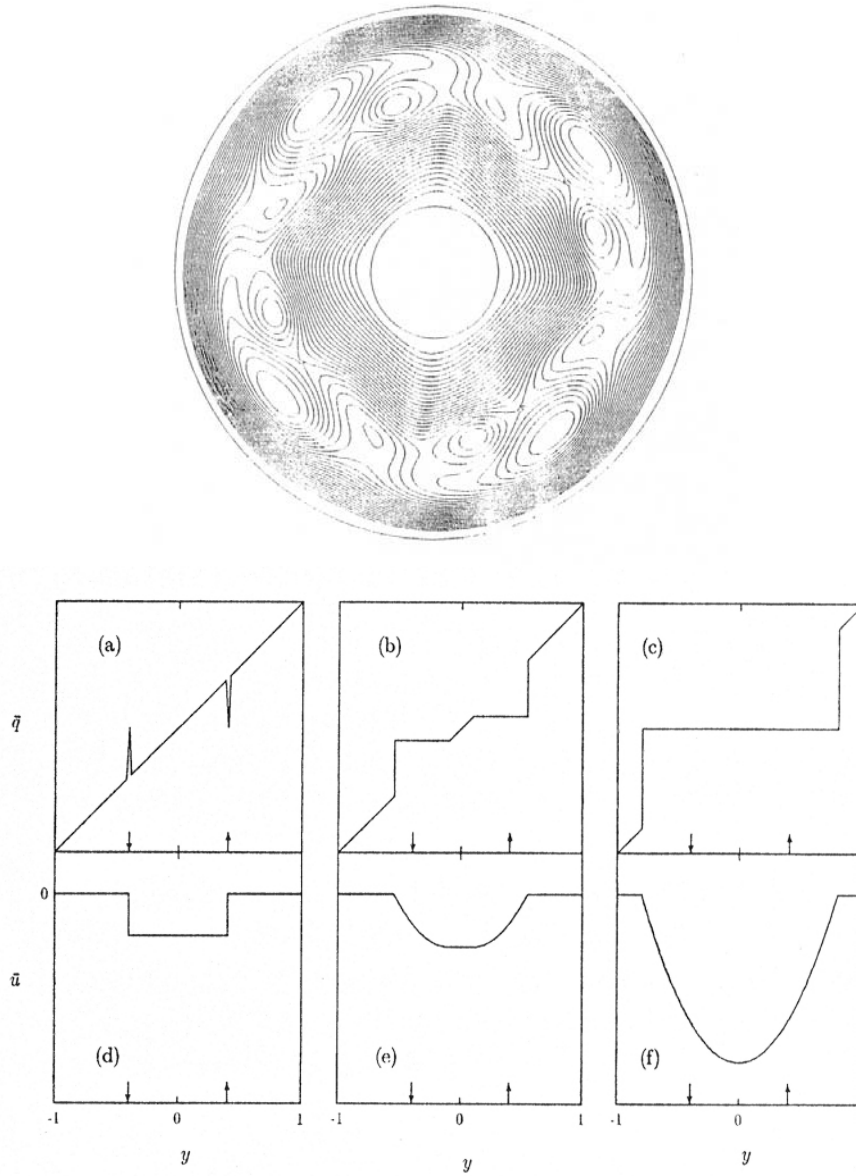


Figure 4.4: Top: Streamfunction of a numerically computed locked westward jet viewed in the rotating frame where the flow is stable. Bottom: Westward jet model for different flow speeds, for (a) PV profile for the primary flow; (b) PV profile at higher flow rate where the two regions of constant PV are not linked together; (c) PV profile at still higher flow rate where the two regions of constant PV are linked together; (d), (e) and (f) are the velocity profiles corresponding to (a), (b) and (c), respectively. Vertical arrows indicate the position of the forcing rings used to generate the jet flow. From [Marcus and Lee, 1998].

## 4.3 Experimental techniques

### 4.3.1 General experimental arrangement

In our experiments, we have generated the current in the laboratory by applying a source-sink technique. Three different topographies have been used: (i) a sloping bottom (scaled to that of the Gulf of Lions), (ii) a flat bottom, and (iii) a parabolic bottom, which mimics the free surface elevation of a fluid under a fixed rotation speed of  $0.7 \text{ s}^{-1}$ , in order to assure a uniform fluid depth.

The laboratory experiments were performed in two different containers: a circular tank of 46 cm radius (for flat and slope experiments) and a rectangular tank of 100 x 150 cm (for parabolic bottom experiments), both placed on a rotating table. The table was rotating in cyclonic direction. In order to perform experiments with a constant fluid depth and to compare them to those performed with the sloping bottom, the rotation speed used in all experiments was  $0.7 \text{ s}^{-1}$ .

The experimental jet was generated by placing two concentric ring-shaped hoses at the bottom of the tank, separated by a distance of 9.6 cm. The hoses were perforated with 1.2 mm holes spaced at 1 cm intervals. In order to avoid reflection, the hoses as well as the bottom of the tank were painted black. The two hoses were connected to a pump and to a flowmeter in order to regulate the flow rate, performing a closed circuit (Fig. 4.5). This technique is similar to that used in [Trieling et al., 1998] to create an annular shear flow. Fluid is pumped through one hose (i.e. the source ring) and extracted through the other hose (i.e. the sink ring). The fluid was fed to the source ring after being conducted through an air filter to eliminate possible air bubbles in the fluid. The fluid density was homogeneous in all experiments.

The continuous pumping of a constant amount of fluid from the ring source to the ring sink generates a radial flow at the bottom of the tank. Due to the effect of rotation this radial flow will deviate to the right, generating a cyclonic/anticyclonic jet, depending on the outer/inner position of the source ring. Momentum will be transferred from the bottom boundary layer to the whole fluid column, obtaining a barotropic axisymmetric current. The sense of rotation of the jet is inverted by exchanging the source and the sink.

The tank is left spinning up until the fluid has acquired solid-body rotation. This occurs typically after the Ekman spin-up time:

$$T_E = \frac{H}{\sqrt{\nu\Omega}}, \quad (4.37)$$

where  $\nu$  is the eddy viscosity of the fluid and  $\Omega$  is the rotation rate. For a typical fluid depth of 20 cm and a rotation rate of about  $1 \text{ s}^{-1}$  this occurs approximately after 4 minutes. Since  $T_E$  is an e-folding time, we consider the time the fluid needs to acquire solid-body rotation after spinning-up the tank is about 20 minutes. After that, the pump is switched on. We consider that the time it takes the jet to acquire its stable state is at least  $2 * T_E$ , i.e. approx. 10 minutes.

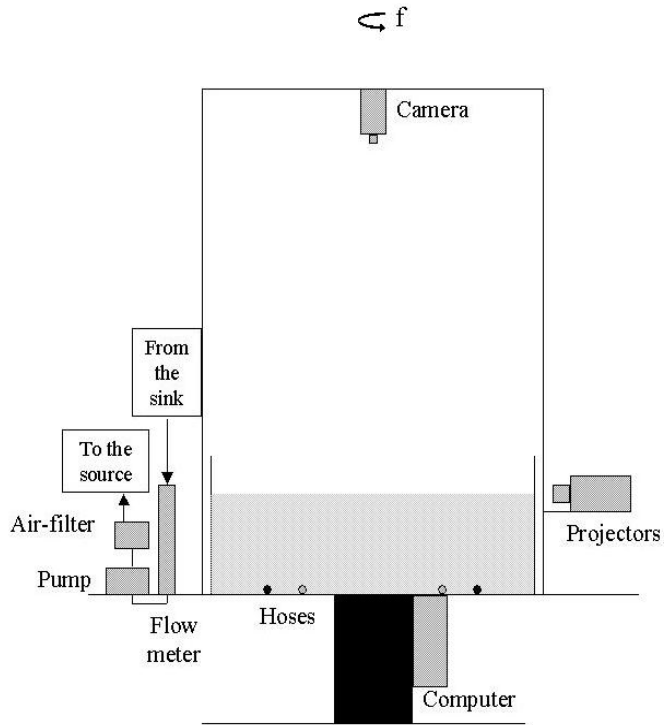


Figure 4.5: Scheme of the source/sink arrangement in the rotating tank.

The initial time ( $t = 0$ ) of each experimental run is set at the switching on of the pump. The flow meter range used in the experiments is 15 - 140  $\text{lh}^{-1}$ .

### 4.3.2 Dynamic similarity

In order to maintain dynamic similarity between the real ocean case and the laboratory set-up, we need to non-dimensionalize the equations of momentum, continuity and the boundary conditions. Consider a continental slope of width  $2L$ , and a jet flowing over the lower half of the slope with a typical speed  $U$  and a width  $L$  (Fig. 4.6). Let the water depth be  $D$  at the lowest (i.e. deepest) part of the slope and  $D - H$  over the mid-slope, for any arbitrary bottom profile  $h(x)$ , being the cartesian coordinates  $x$  and  $y$  the across- and along-slope directions, respectively. The background rotation is given by  $f = 2\Omega$ .

The horizontal velocity components  $u$ ,  $v$  are non-dimensionalized by

$$u^* = \frac{u}{U} \quad v^* = \frac{v}{U}, \quad (4.38)$$

whereas the vertical velocity component  $w$  follows from the continuity equation (4.2):

$$w^* = \frac{wL}{UD}. \quad (4.39)$$

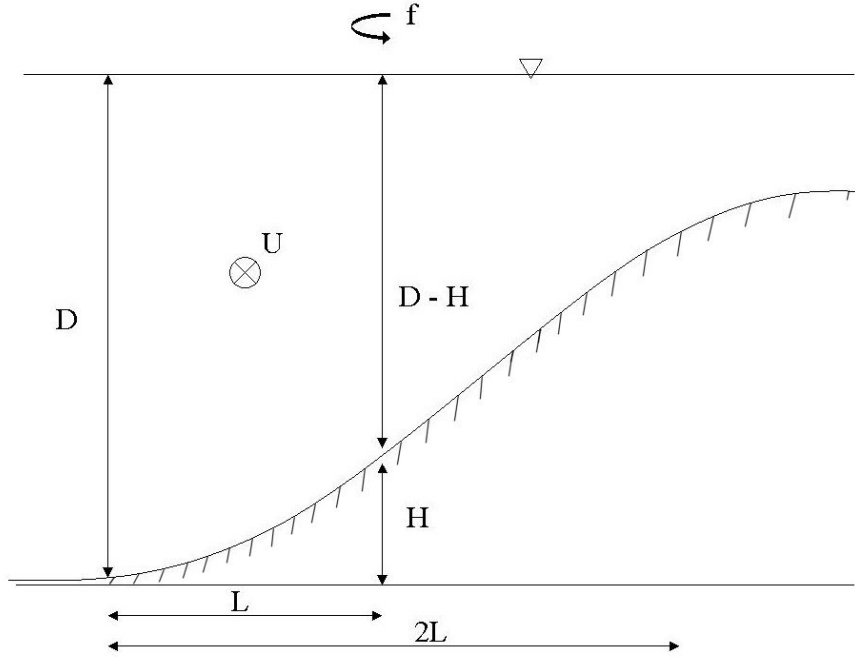


Figure 4.6: General scheme of a jet flowing over a continental slope

The non-dimensional spatial and temporal variables  $x$ ,  $y$ ,  $z$  and  $t$  are

$$t^* = t \frac{U}{L} \quad x^* = \frac{x}{L} \quad y^* = \frac{y}{L} \quad z^* = \frac{z}{D}. \quad (4.40)$$

Assuming that the pressure gradient force is balanced by the Coriolis force, the pressure can be non-dimensionalized as:

$$P^* = \frac{P}{\rho f U L} \quad (4.41)$$

Substituting (4.38) – (4.41) into the governing equation given by (4.4) we obtain the non-dimensional momentum equations:

$$Ro \left[ \frac{\partial u^*}{\partial t^*} + u^* \frac{\partial u^*}{\partial x^*} + v^* \frac{\partial u^*}{\partial y^*} + w^* \frac{\partial u^*}{\partial z^*} \right] - v^* = -\frac{\partial P^*}{\partial x^*} + E_H \left[ \frac{\partial^2 u^*}{\partial x^{*2}} + \frac{\partial^2 u^*}{\partial y^{*2}} \right] + E_V \left[ \frac{\partial^2 u^*}{\partial z^{*2}} \right] \quad (4.42)$$

$$Ro \left[ \frac{\partial v^*}{\partial t^*} + u^* \frac{\partial v^*}{\partial x^*} + v^* \frac{\partial v^*}{\partial y^*} + w^* \frac{\partial v^*}{\partial z^*} \right] + u^* = -\frac{\partial P^*}{\partial y^*} + E_H \left[ \frac{\partial^2 v^*}{\partial x^{*2}} + \frac{\partial^2 v^*}{\partial y^{*2}} \right] + E_V \left[ \frac{\partial^2 v^*}{\partial z^{*2}} \right] \quad (4.43)$$

$$Ro \delta_1^2 \left[ \frac{\partial w^*}{\partial t^*} + u^* \frac{\partial w^*}{\partial x^*} + v^* \frac{\partial w^*}{\partial y^*} + w^* \frac{\partial w^*}{\partial z^*} \right] = -\frac{\partial P^*}{\partial z^*} + E_H \delta_1^2 \left[ \frac{\partial^2 w^*}{\partial x^{*2}} + \frac{\partial^2 w^*}{\partial y^{*2}} \right] + E_V \delta_1^2 \left[ \frac{\partial^2 w^*}{\partial z^{*2}} \right] \quad (4.44)$$

where

$$Ro = \frac{U}{fL} \quad \text{is the Rossby number,} \quad (4.45)$$



$$E_H = \frac{\nu}{fL^2} \quad \text{is the horizontal Ekman number,} \quad (4.46)$$

$$E_V = \frac{\nu}{fD^2} \quad \text{is the vertical Ekman number,} \quad (4.47)$$

$$\delta_1 = \frac{D}{L} \quad \text{is a geometric factor.} \quad (4.48)$$

Moreover,  $E_H = E_V \delta_1^2$ .

The continuity equation takes the form

$$\frac{\partial u^*}{\partial x^*} + \frac{\partial v^*}{\partial y^*} + \frac{\partial w^*}{\partial z^*} = 0. \quad (4.49)$$

The boundary conditions of the flow are:

$$\vec{v}(x=0) = 0 \quad \vec{v}(x=L) = 0, \quad (4.50)$$

or, in non-dimensional form:

$$\vec{v}^*(x^*=0) = 0 \quad \vec{v}^*(x^*=1) = 0. \quad (4.51)$$

The boundary slope profile  $h(x)$  satisfies:

$$h(x=0) = 0 \quad h(x=L) = H, \quad (4.52)$$

which in non-dimensional form is:

$$h^*(x^*=0) = 0 \quad h^*(x^*=1) = \delta_2, \quad (4.53)$$

with

$$\delta_2 = \frac{H}{D} \quad (4.54)$$

being the non-dimensional depth ratio.

Considering that  $E_H = E_V \delta_1^2$ , there are four non-dimensional numbers to take into account: the *Rossby number*  $Ro$ , the *vertical Ekman number*  $E_V$ , the *geometric factor*  $\delta_1 = \frac{D}{L}$ , and the *depth ratio*  $\delta_2 = \frac{H}{D}$ .

For simplification, we consider that the Gulf of Lions consists of four distinctive regions: (i) a flat continental shelf 200 m isobath; (ii) the upper half of the continental slope with no forced flow, from 200 to 1100 m; (iii) the lower half of the continental slope over which the Northern Current flows, from 1100 to 2000 m; (iv) the flat abyssal plain at 2000 m depth. A scheme of the real-case dimensions and the model dimensions is given in Fig. 4.7.

The angle of the sloping bottom chosen for our laboratory experiments is  $33^\circ$ . This value is determined as a compromise between an appropriate horizontal length scale  $L$  and fluid depth  $D$ , and by the conservation of the depth ratio  $\delta_2 = \frac{H}{D}$ . Too small angles lead to a shallow set-up, where bottom friction effects become more important. In contrast,

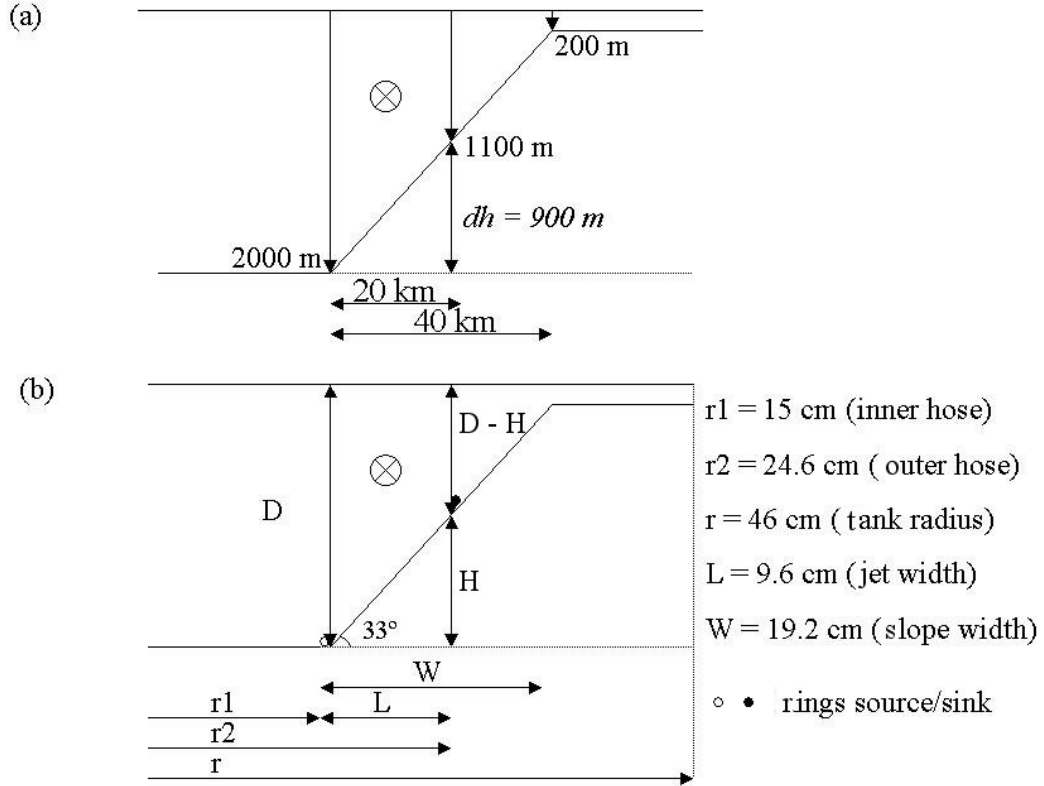


Figure 4.7: (a) Dimensions of the Gulf of Lions continental slope, and (b) dimensions of the laboratory sloping bottom

too large angles lead to very narrow jets, and because we are generating the jet with a source-sink mechanism, we need a reasonable width to generate a geostrophic flow interior (see Section 4.3.6).

Therefore the values of the non-dimensional numbers are chosen as follows:

*The depth ratio  $\delta_2 = \frac{H}{D}$ :* The value for the Gulf of Lions case is  $\delta_2 = 0.45$  (Fig. 4.7). Considering the experimental set-up in Fig. 4.7, for a jet of 9.6 cm width,  $H = 6.23 \text{ cm}$ . Therefore  $D_{lab} = \frac{H}{0.45} = 13.7 \text{ cm}$ .

*The Rossby number:* The Rossby number  $Ro$  is given by  $Ro = \frac{U}{fL}$ , with  $U$  the maximum speed of the jet,  $f$  the Coriolis parameter and  $L$  the width of the current. The Northern Current has average values of 20 – 30 km width and a surface speed of 30 – 50  $\text{cm s}^{-1}$ ; these values lead to  $Ro$  values ranging from 0.1 to 0.25. In our experiments, we varied the Rossby number between 0.04 and 0.28.

*The vertical Ekman number:* The vertical Ekman number is given by  $E_v = \frac{\nu}{fD^2}$  where  $\nu$  is the viscosity and  $D$  is the water depth at the deepest part of the jet. For the oceanic case, considering a Coriolis parameter of  $10^{-4}\text{s}^{-1}$ , a water depth of 2000 m and  $\nu = 10^{-2}$

$\text{m}^2\text{s}^{-1}$ , the vertical Ekman number is  $2.5 \cdot 10^{-5}$ . For the laboratory case, where  $f = 2\Omega$  (in our case  $\Omega = 0.7 \text{ rad s}^{-1}$ ), the fluid depth is 13.7 cm and the molecular viscosity  $\nu = 10^{-6} \text{ m}^2\text{s}^{-1}$ ,  $E_V = 3.8 \cdot 10^{-5}$ . Therefore, the vertical Ekman number in both cases is of the same order of magnitude.

*The geometric factor  $\delta_1 = \frac{D}{L}$ :* The geometric factor is restricted by the dimensions of our facility. In the ocean this ratio is of the order of 0.1 ( $D = 2000 \text{ m}$ ;  $L = 20 \text{ km}$ ), while in our laboratory cases it is of the order of 1 ( $D = 13.7 \text{ cm}$ ;  $L = 9.6 \text{ cm}$ ). The only way of approaching  $\delta_1 = 0.1$  would be by using a bigger tank.

### 4.3.3 Experimental set-up for the topographic slope

The continental slope topography is built from plaster. A wooden cone of  $33^\circ$  slope was constructed and used as a mold to obtain the plaster model. The plaster model is painted in black using water-proof paint to avoid reflections. In order to simplify the set-up, the continental shelf and the abyssal plane are simulated in the laboratory as two flat surfaces. Two concentric hoses were placed on the bottom topography at a radial distance 9.6 cm apart. The hoses were placed on top of the topography, at a radius of  $r_1 = 15 \text{ cm}$  and at  $r_{12} = 24.6 \text{ cm}$  from the centre of the tank (Fig. 4.7). The fluid depth at the deepest part of the set-up (i.e. at  $r \leq r_1$ ) was of 13.7 cm, whereas at the shallowest part of the set-up (i.e. at  $r_1 + W$  in Fig. 4.7) the fluid was 1.3 cm deep. In all experiments the rotation speed was  $0.7 \text{ s}^{-1}$ .

### 4.3.4 Parabolic bottom topography experiments

The objective of this set of experiments is to generate a current which is not affected by any topography —i.e. a current on an f-plane. To achieve this, we need to counter-balance the free surface elevation created by rotation so that the water depth is strictly uniform everywhere in the domain.

The rotation of the fluid in the laboratory will cause an elevation of the free surface,  $\eta_{exp}(r)$ , which can be obtained from the balance between the centrifugal force and the pressure gradient force, after integrating over the radius  $r$

$$\eta_{exp}(r) = \frac{\Omega^2 r^2}{2g} \quad (4.55)$$

where  $\Omega$  is the rotation rate. For a rotation rate of  $1 \text{ s}^{-1}$ , the elevation of the free surface is of just a few millimeters.

In the experiments with the topographic slope the effect of the free surface elevation is negligible because the variations in depth due to the bottom slope are larger than those due to the free surface elevation. In fact, the only region of the experimental set-up where this effect could be important is on the continental shelf, where the local depth is minimum. But since the initial flow is far from this shallow region, this effect has been neglected.

Nevertheless, in order to perform the experiments on an f-plane,  $\eta_{exp}(r)$  might be important. According to (4.22), the elevation of the free surface can create a gradient of

ambient potential vorticity similar to that caused by the variation of the bottom topography, or by the variation of the Coriolis parameter in geophysical flow situations (see e.g. [van Heijst, 1994]).

Therefore, in order to eliminate the effect of the free surface elevation we worked with a constant rotation rate  $\Omega$  and we used a parabolic bottom topography which is identical to the free surface elevation at this rotation rate. In this way the fluid domain has effectively a uniform depth. We have used the parabolic bottom experiments as a reference to compare to the slope experiments.

The parabolic bottom that we use here mimics the free surface elevation profile created with a rotation speed of  $0.7 \text{ s}^{-1}$ . The experiments were performed in the rectangular tank, for which the parabolic bottom topography was built. The inner and outer hoses were placed at  $r_1 = 15 \text{ cm}$  and at the same position as in the slope experiments (Fig. 4.7). The fluid depth was  $13.7 \text{ cm}$ .

### 4.3.5 Flat bottom experiments

As discussed in subsection 4.3.4, the elevation of the free surface will not be important in the experiments with the topographic slope because the depth variations due to the bottom topography are much larger than the surface elevation due to rotation. But this effect might be important when simulating a current over a flat topography, because the elevation of the free surface generates a gradient in ambient potential vorticity which may affect the dynamics of the flow.

In order to evaluate the effect of the free surface elevation due to the rotation of the fluid we perform a series of experiments in which no topography is used (bottom slope = 0). The experiments are performed in the same circular tank as the experiments with the topographic slope. The fluid depth was of  $14 \text{ cm}$  (before rotation starts). The rotation rate of the rotating table was fixed at  $0.7 \text{ s}^{-1}$ . In this case the two concentric rings were placed at a distance  $r_1 = 17 \text{ cm}$  and  $r_2 = 25 \text{ cm}$  from the centre of the tank —therefore the jet width is set at  $8 \text{ cm}$ .

### 4.3.6 Analysis of source-sink flows

Different types of flows can be generated by means of source-sink configurations (see e.g. [van Heijst, 1994]) and references therein). Consider two concentric rings placed on the bottom of a flat cylindrical container (Fig. 4.8). One ring will act as a source, pumping fluid into the tank, and the other ring will act as a sink, extracting fluid from the tank. The transport from the source to the sink is carried out by the bottom Ekman layer at the horizontal plane. The bottom Ekman layer have a typical thickness

$$\delta_E = LE^{1/2}, \quad (4.56)$$

where  $E$  is the horizontal Ekman number, which in the laboratory can be defined as  $E = \frac{\nu}{\Omega L^2}$ , where  $L$  is a typical horizontal lengthscale.

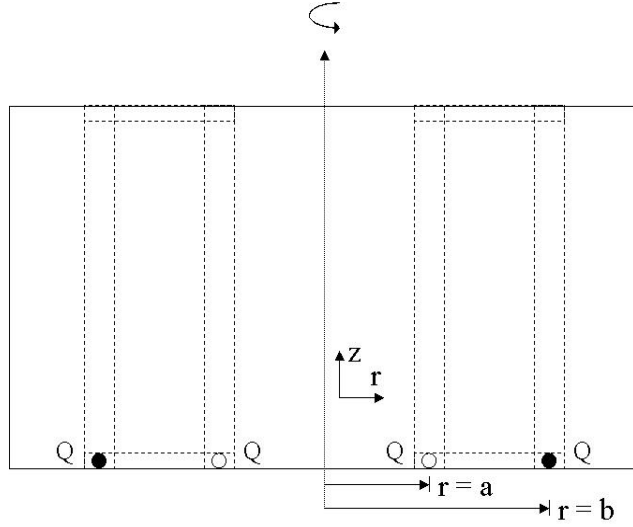


Figure 4.8: Stewartson and Ekman layers of a source-sink flow generated by two concentric rings (white: ring source; black: ring sink) placed at the bottom of a rotating tank

Momentum will be transferred from the Ekman layer to the upper layer until a geostrophic flow is acquired in between both rings. Free vertical shear layers arise on the source and sink rings, acting as a transition between the generated geostrophic flow and the zero-motion fluid in the rest of the container. These vertical shear layers are named Stewartson layers and consist of sub-layers of thickness

$$\delta_{1/3} = LE^{1/3} \quad \delta_{1/4} = LE^{1/4}. \quad (4.57)$$

Together with the Ekman layers, the Stewartson layers play an important role in the transport of fluid from the sources to the sinks.

Considering the typical distance between the forcing rings  $L \sim 0.1$  m, and for a kinematic viscosity of  $10^{-6}$  m<sup>2</sup>s<sup>-1</sup>, and rotation rate  $\Omega \sim 1$  s<sup>-1</sup>, the width of the Ekman layer (4.56) for our configuration is  $\sim 1$  mm. Similarly, the thickness  $\delta_{1/4}$  of the Stewartson layers (4.57) in our set-up is approximately  $\sim 1$  cm. Therefore, each half of this double layer has approximately 1 cm width.

The radial (local) Ekman flux over a topographic slope  $\alpha$  (Fig. 4.9) is given by:

$$Q_{Erad}(r) = \frac{1}{2}E^{1/2}(\sec \alpha)^{1/2}(v_B - v_I), \quad (4.58)$$

where  $v_B$  is the azimuthal velocity at the bottom of the topography,  $v_I$  is the azimuthal interior velocity out of the Ekman layer and  $\alpha = |\frac{dh}{dr}|$  is the radial bottom slope.

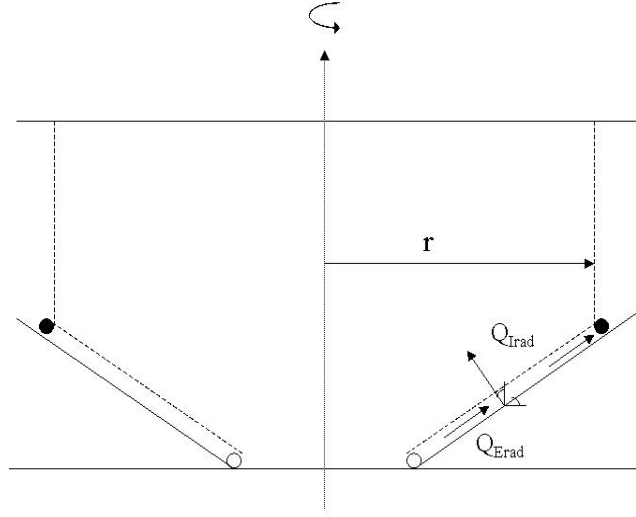


Figure 4.9: Radial Ekman flux  $Q_{Erad}(r)$  and radial flux into the interior  $Q_{Irad}(r)$  for a source-sink flow generated by two concentric rings placed over topography of slope  $= \alpha$  (white: source ring; black: sink ring).

The velocity profile in the geostrophic interior can be obtained by applying a mass/volume balance over a cylindrical control volume, with radius  $r$ . The total volume flux through this cylindrical surface from source to sink is  $Q$  (Fig. 4.9) and is given by the radial Ekman-layer flux (4.58) and a radial flux in the interior  $I$ , which in the case of non-axisymmetric geometry could be  $O(E^{1/2})$  but in our case of an axisymmetric domain this contribution is zero (i.e. there is no radial interior flow). Hence, the total flux in the whole domain is:

$$Q = Q_{Erad} \cdot 2\pi r = -\frac{1}{2} \left( \frac{E}{\cos\alpha} \right)^{1/2} \cdot v_I \cdot 2\pi r, \quad (4.59)$$

leading to the non-dimensional velocity in the geostrophic interior:

$$v_I(r) = \frac{Q}{\pi r (E/\cos\alpha)^{1/2}}. \quad (4.60)$$

In the case of a cone-shaped topography with uniform bottom slope  $\alpha$ ,  $E/\cos\alpha = E^* = \text{constant}$ , and

$$v_I(r) \sim \frac{1}{r}. \quad (4.61)$$

In the case of a flat bottom (4.60) applies with  $\alpha = 0$ , leading again to (4.61). Therefore, the velocity profile in the geostrophic interior in any case (i.e. for a flat bottom

and for a sloping bottom topography) will be proportional to  $1/r$ . In this chapter we will verify if such theoretical profiles match our laboratory results.

## 4.4 Flow measurements

Flow visualization was performed with DigImage software (see [Dalziel, 1992]). Individual particles were tracked and particle streaks were plotted, in order to observe the main flow patterns.

Flow visualization was also performed by introducing small quantities of dye. The transport of fluid from the sources to the sinks, as well as the flow direction at the Ekman layer, could be visualized by placing small dye crystals at the bottom of the tank. The two-dimensional character of the flow could be observed by injecting a thin column of dye in the vertical, from the surface to the bottom of the fluid, and observing how the dyed column was advected by the flow.

For the slope bottom and the parabolic bottom experiments, four-times higher resolution measurements of the velocity field were obtained with High Resolution Velocimetry (HPV) [van der Plas and Bastiaans, 1998], a combination of Particle Image Velocimetry (PIV) and Particle Tracking Velocimetry (PTV). Optimage powder particles were used as tracers. The surface of the fluid was illuminated by using three projectors along one side of the tank, and the flow motion was recorded with a digital camera placed in a co-rotating frame at some distance above the tank. In order to optimize the velocity image and to enhance resolution in the HPV measurements, the domain recorded was only half of the axisymmetric source-sink set-up.

The raw velocity field was interpolated onto a polar grid, of  $90 \times 60$  nodes (in azimuthal and radial direction, respectively) in a semicircular domain. The maximum internodal distance was of 1.6 cm at the maximum radius of the domain (i.e. at  $r = 46$  cm). The interpolated velocity vectors were calculated by averaging the raw velocity vectors, using a standard Gaussian weighting function, over a circle of 1.5 cm radius. To define the radius of the weighting function it was required to have at least four velocity vectors (on average) in any circular area of radius  $\sigma = 1.5$  cm. The derivatives of the horizontal velocity components (i.e. vorticity and stream function) were calculated in the post-processing by using a finite-differences technique.

The measured divergence field appears to be independent of the flow structure, indicating that the divergence field is due to experimental errors. Since we use a similar method to calculate divergence and vorticity, the typical errors on these two fields should be the same, and therefore the flow divergence would be a measure of the typical error in vorticity. According to Nguyen and Sommeria [Duc and Sommeria, 1988], the measured divergence normalized by a typical magnitude of the vorticity (defined as half the difference between the maximum vorticity values of the flow, i.e.  $\frac{1}{2}(w_{max} - w_{min})$ ) would be an indicative of the relative error in the vorticity measurements. The divergence for a typical flow of  $Q = 100 \text{ lh}^{-1}$  is less than 0.1 for 95% of the grid points (Fig. 4.10). Therefore the relative error on the measured vorticity can be estimated as less than 10%.

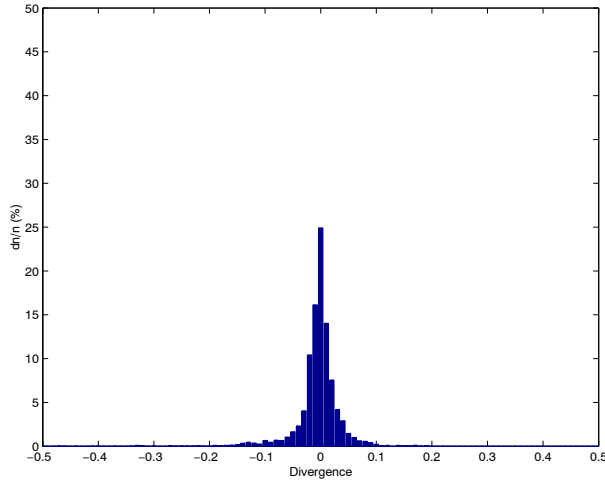


Figure 4.10: Normalized histogram of the divergence (normalized by  $\frac{1}{2}(w_{max} - w_{min})$ ) for a typical flow of  $Q = 100 \text{ lh}^{-1}$ .

One source of error in the vorticity measurements (contained in the above-mentioned vorticity error) is the background noise caused by the effect of air on the fluid surface due to rotation. In comparison, errors due to calibration and camera noise would be negligible. The measured vorticity generated by the air appears to be random and uniformly distributed across the measurement area. Maximum values are of  $-0.02 \text{ s}^{-1}$  and  $+0.02 \text{ s}^{-1}$ . Lower background noise is expected in the circular container, where the surface area of the fluid is considerably smaller.

Up to here, we have defined the Rossby number as the ratio between the advective and the Coriolis forces, using a typical velocity  $U$  and a typical jet width  $L$  (4.45). Another definition arises when we calculate the Rossby number taking into account the shear generated at each side of the jet, i.e.  $Ro_v = |\omega|/f$ , so we can calculate the Rossby number for each vorticity layer. Note that  $Ro_v^+ \simeq Ro_v^- = 2 \cdot Ro$ , since the horizontal domain where we calculate the positive and negative Rossby numbers is only half the jet width if we consider the velocity profile of the jet symmetric. We estimated both Rossby numbers (i.e. using both definitions) for the weakest flow, for which the jet was in between the forcing rings, so the estimation of the jet width was straightforward. Therefore, for the smallest flow ( $Q = 15 \text{ lh}^{-1}$ ), we obtain an averaged maximum azimuthal velocity of  $0.55 \text{ cm s}^{-1}$ , so that  $Ro = \frac{U}{fL} = 0.04$  (for a rotation rate  $\Omega = 0.7 \text{ s}^{-1}$  and a jet width of  $L = 9.6 \text{ cm}$ ). The extreme vorticity values for this averaged flow were  $+0.13 \text{ s}^{-1}$  and  $-0.15 \text{ s}^{-1}$ , obtaining that  $Ro_v^+ = 0.09$  and  $Ro_v^- = 0.11$ . The differences in positive and negative vorticity are due to the asymmetry of the velocity profile of the jet (Fig. 4.11). Therefore, it is concluded that the vorticity estimated with the interpolation  $U$  used in the present work is both a good qualitative and, to a certain extent, a good quantitative measure of the vorticity of the flow.



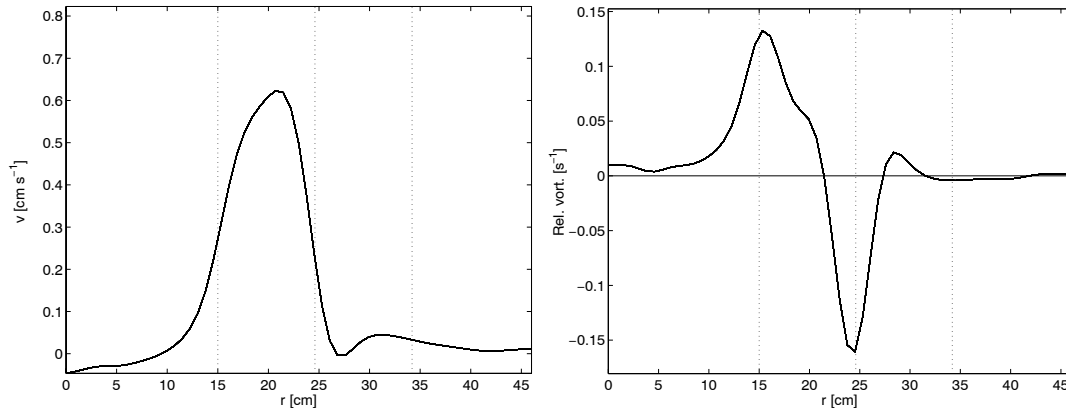


Figure 4.11: Left: Radial velocity profile of the slowest flow over sloping bottom ( $Q = 15 \text{ lh}^{-1}$ ) averaged both in time (over 20 s) and in azimuthal direction. Right: Corresponding relative vorticity. The vertical lines indicate (from left to right): (i) the sink ring, placed at the deepest edge of the sloping bottom, (ii) the source ring, placed on the mid slope, and (iii) the shallowest edge of the sloping bottom.

## 4.5 Results

Once the pump was switched on ( $t = 0$ ), small vortices appeared over the source ring (Fig. 4.12). These initial vortices will not affect the subsequent behaviour of the flow. During the first few minutes (approx. 9 minutes) of the experiment the jet develops and acquires a stable state.

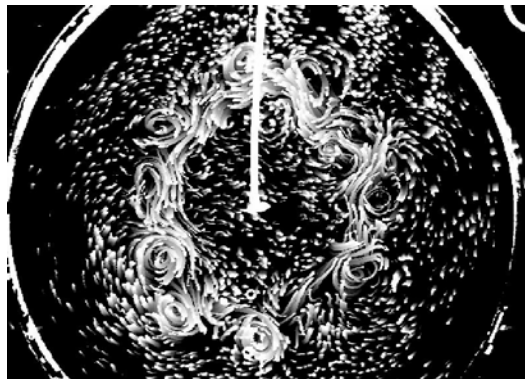


Figure 4.12: Observed flow field (for  $Q = 85 \text{ lh}^{-1}$ ) shortly after the pump was switched on ( $t = 45 \text{ s}$ ). Small vortices appear over the source ring. Their presence and number appear not to be relevant for the later (stable) state of the jet.

### 4.5.1 Jets over parabolic bottom (*uniform* water depth)

All experiments with different flow rates show approximately the same behaviour. The jet is non-axisymmetric, with non-coherent anticyclonic vortices of different size at its outer side (i.e. over the source ring) (Fig. 4.13). Cyclones are observed at the inner part of the jet, generally with smaller size than the outer anticyclones. The ‘turbulent’ nature of the jet is remarkable: the shape of the jet changes gradually in time but without showing any fixed pattern. Repetition of the same experiments but using higher resolution (i.e. using HPV) corroborate the results for the *prograde* jet (Fig. 4.14). Moreover, we performed experiments for the *retrograde* jet (Fig. 4.14) and the results for both jet directions were mainly similar, although the retrograde jet was observed to be less organized than the prograde jet. All experiments showed unstable flows, as is to be expected from the fact that the shear layers on either side of the jet possess an extremum in the absolute vorticity profiles (Fig. 4.15): vortices are observed to form in both shear layers (Fig. 4.14).

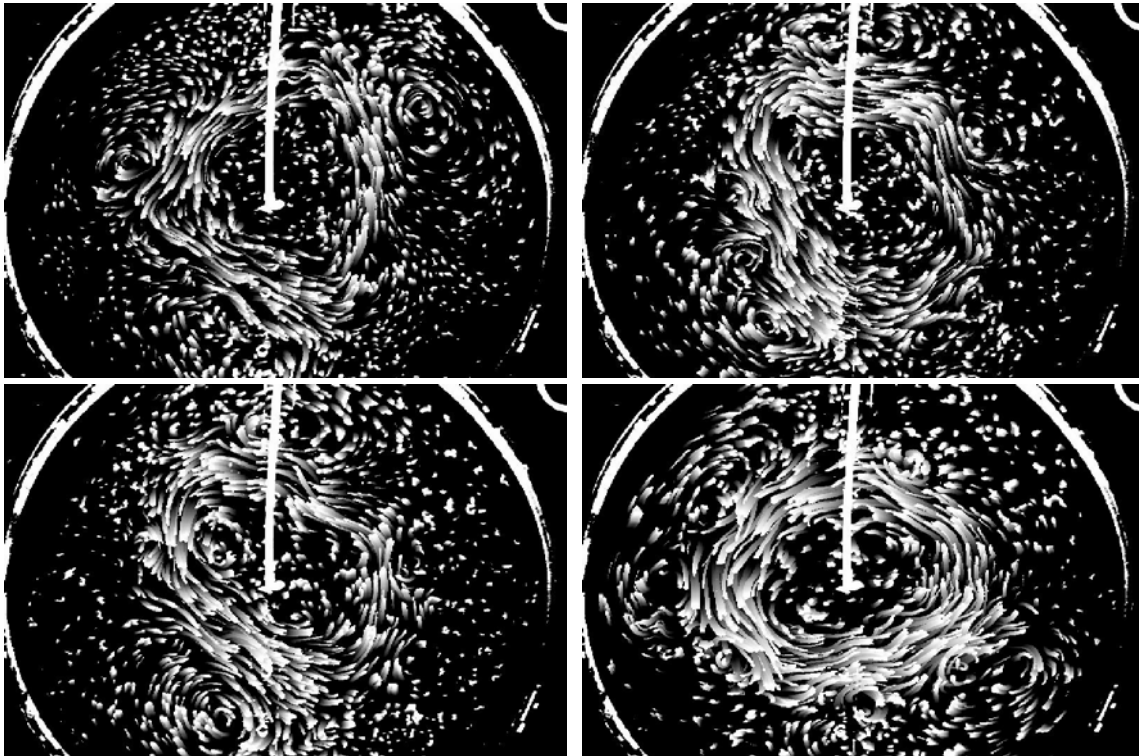


Figure 4.13: Particle streaks for a flow ( $Q = 85 \text{ lh}^{-1}$ ) over the parabolic bottom for different times (mm:ss) after switching on the pump (top left: 02:40; top right: 07:00; bottom left: 07:40; bottom right: 10:40). The flow changes in time, with no fixed pattern.

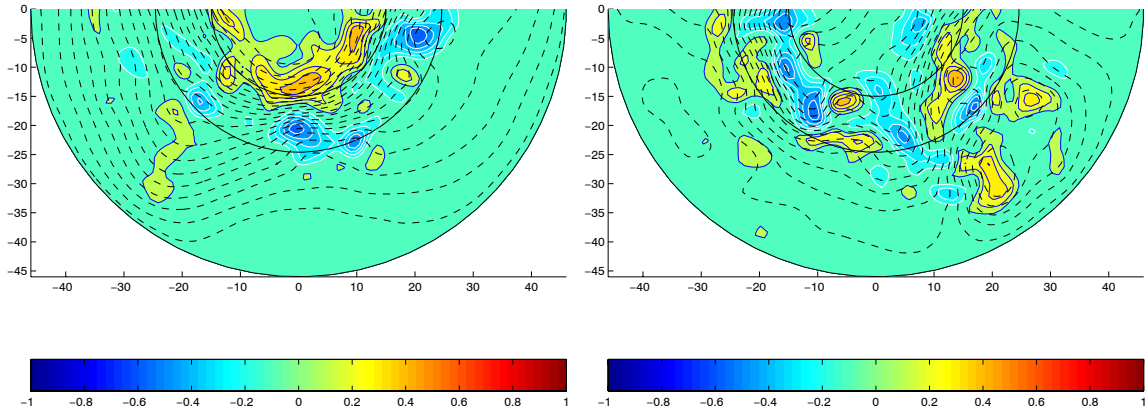


Figure 4.14: Left: Relative vorticity for a prograde jet ( $Q = 115 \text{ lh}^{-1}$ ) over a parabolic bottom. Right: Relative vorticity for a retrograde jet ( $Q = 60 \text{ lh}^{-1}$ ) over parabolic bottom.

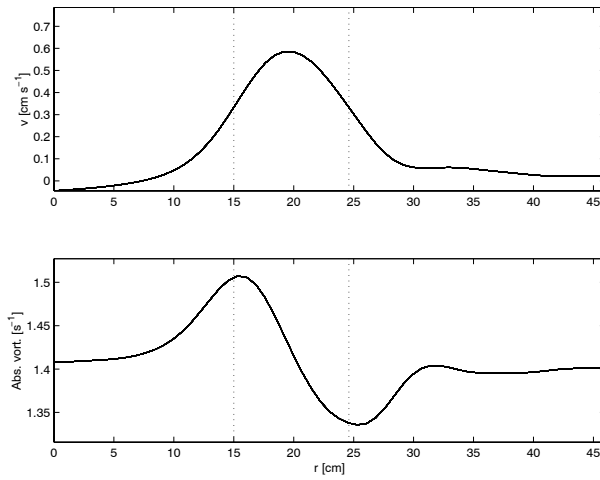


Figure 4.15: Velocity profile of the slowest prograde flow over parabolic bottom ( $Q = 15 \text{ lh}^{-1}$ ) averaged both in time (over 20 s.) and in azimuthal direction. Bottom: Corresponding absolute vorticity. The vertical lines indicate (from left to right): the sink ring, placed at  $r = 15 \text{ cm}$ , and the source ring, placed at  $r = 24.6 \text{ cm}$ .

The time-averaged jet profile for the lowest flow is shown in Fig. 4.16. The theoretical profile proportional to  $\frac{1}{r}$  discussed in Section 4.3.6 is also plotted. As it can be easily observed comparing the outer edge of both profiles (e.g.  $r = 10$  to  $15$  cm), each layer of the double-layer structure of the Stewartson layer in the laboratory jet is about 5 cm wide. This value is much larger than the 1 cm width estimated in Section 4.3.6. It should be kept in mind, however, that the Stewartson layer is a mathematical model for an ideal linear case, for a small-Ro flow. Besides, our forcing mechanism (i.e. the size of the forcing ring and the small-scale turbulence generated by the fluid passing through the small holes) contributes to this difference. The fact that each layer of the double layer structure is 5 cm wide makes the flow in the geostrophic interior (9.6 cm wide, and theoretically governed by the  $\frac{1}{r}$  profile) described instead by the overlapping of the two Stewartson layers.

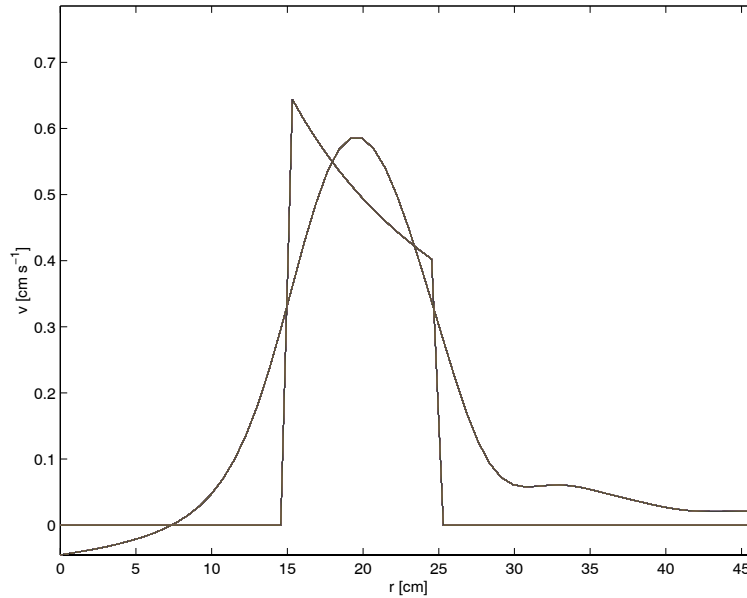


Figure 4.16: Averaged (in time, over 20 s, and in azimuthal direction) velocity profile of the slower prograde jet ( $Q = 15 \text{ lh}^{-1}$ ) over a parabolic bottom. The theoretical velocity profile is also plotted.

### 4.5.2 Prograde jets over sloping bottom

Flow visualization with DigImage using particle streaks has revealed that the current generates anticyclonic vortices at the outer side of the jet. For the weakest flow forcing (small flow rate  $Q = 15 \text{ lh}^{-1}$ ) vortices are not visible. For increasing flow rates ( $Q = 27 \text{ lh}^{-1}$  and  $Q = 33 \text{ lh}^{-1}$ ), the vortices become larger, decreasing in wavenumber (see Fig. 4.17 and Fig. 4.18). For higher flow rates ( $Q = 40 \text{ lh}^{-1}$  to  $Q = 74 \text{ lh}^{-1}$ ), a second layer of vortices

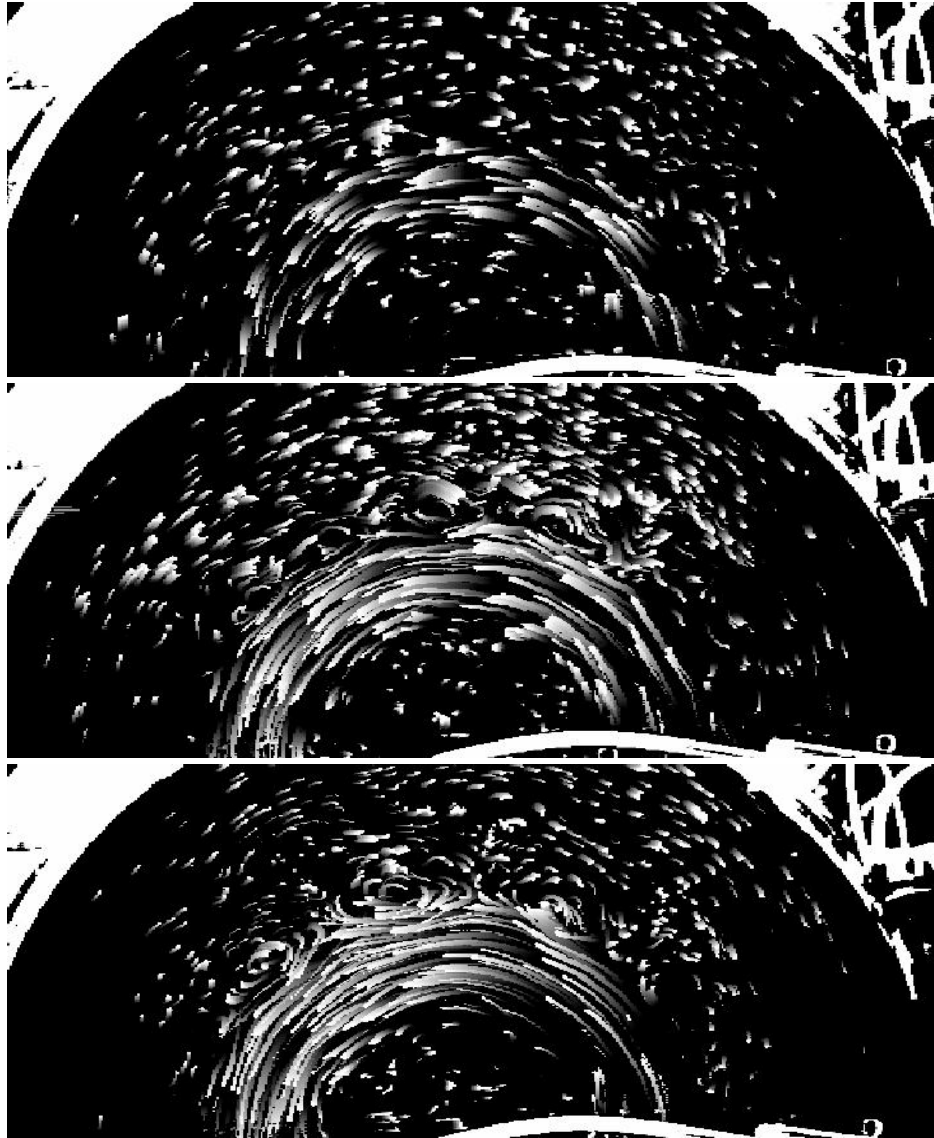


Figure 4.17: Particle streaks for three different currents of increasing intensity from top to bottom ( $Q = 15 \text{ lh}^{-1}$ ,  $27 \text{ lh}^{-1}$  and  $33 \text{ lh}^{-1}$ , respectively).

begins to appear on top of the above mentioned anticyclones (Fig. 4.18).

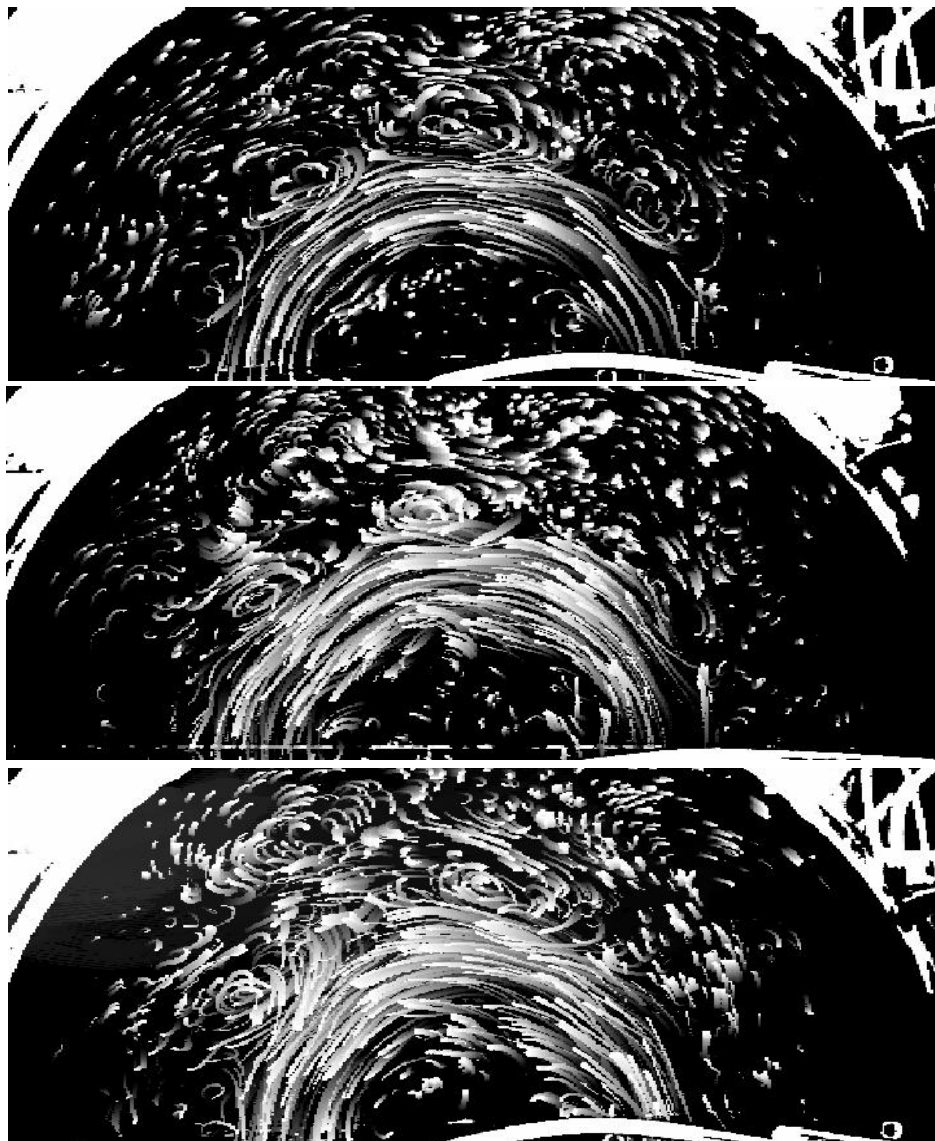


Figure 4.18: Continuation of Fig. 4.17 for three different current flows of increasing intensity from top to bottom ( $Q = 40 \text{ lh}^{-1}$ ,  $60 \text{ lh}^{-1}$  and  $74 \text{ lh}^{-1}$ , respectively).

Repetition of the experiments using higher resolution reveals interesting patterns. All experiments showed the development of unstable jets. Before or after a vortex, the potential vorticity profile presents a convex/concave shape at each shear layer. The presence of vortices modifies these curves into local extrema, fulfilling the necessary condition for instability to occur (see Section 4.2.2). For coherence with previous works [Marcus and Lee, 1998] we will refer to these points as *discontinuities*.

Therefore the velocity profile of the primary (undisturbed) flow could not be properly determined. The time-averaged velocity profile of the slowest flow is shown in Fig. 4.19, and it is compared to the theoretical profile discussed in Section 4.3.6. Similarly to what

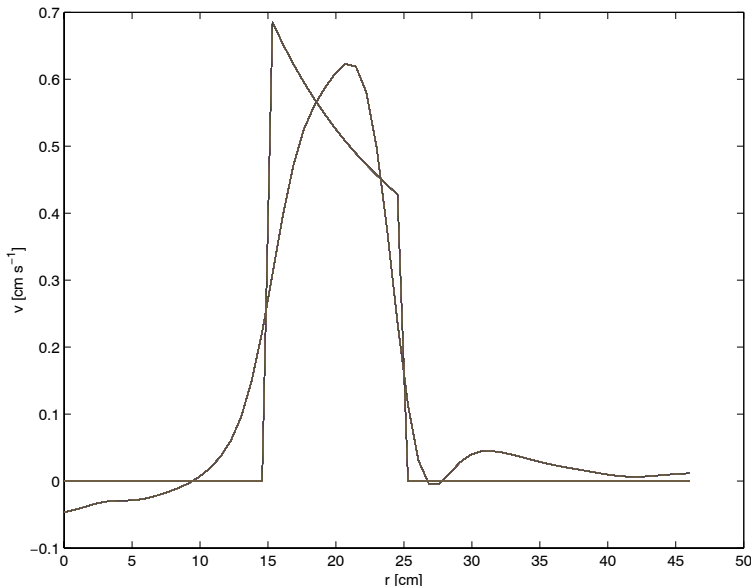


Figure 4.19: Averaged (in time, over 20 s, and in azimuthal direction) velocity profile of the slower prograde jet ( $Q = 15 \text{ lh}^{-1}$ ) over the sloping bottom. The theoretical velocity profile is also plotted.

occurred in the parabolic bottom experiments (see Section 4.5.1), each layer of the double-layer structure of the Stewartson layer in the laboratory jet is about 5 cm wide (Fig. 4.19), making the flow in the geostrophic interior (9.6 cm wide) governed by the overlapping of the two Stewartson layers. The differences between the predicted (1 cm) and obtained (5 cm) transition-layer width is, as discussed above in Section 4.5.1, due to the fact that the Stewartson layer is a mathematical model for an ideal case for a perfectly uniform, axisymmetric source/sink ring in the limit of  $Ro \rightarrow 0$ . Therefore the differences between both widths are related to our forcing mechanism. Moreover, the differences between both profiles are enhanced by the presence of the vortices, which were observed to cause the velocity peak to oscillate in the radial direction between the forcing rings.

The prograde jet shows two different types of behaviour, hereafter referred to as Regimes I and II.

Regime I occurs for jets of flowrates up to  $Q = 33 \text{ lh}^{-1}$ , which corresponds to jets

with relative vorticity less than  $0.3 \text{ s}^{-1}$ ,  $\text{Ro}_v = \frac{|\omega|}{f} \simeq 0.21$  and  $\text{Ro} = \text{Ro}_v^{+/-}/2 \simeq 0.11$ . The jet consists of two bands of vorticity, with vortices of the same sign as the horizontal shear (Fig. 4.20). Streamlines are observed to cross over the vortices, indicating they are being advected by the mean flow. The potential vorticity contour plot indicates that the jet is placed on a constant potential vorticity region. Moreover, where the anticyclones are placed, the potential vorticity displays a wave-like character. The potential vorticity profiles across the jet indicate that the vortices are placed at the potential vorticity discontinuities, i.e. on top of the source and the sink (Fig. 4.21). The jet width at  $\frac{1}{2}U_{max}$  corresponds to the distance between the forcing rings. The vortices move in the same direction as the mean flow, but with a phase speed slightly less to that of the jet speed i.e. approx. 85-90% of the maximum jet speed.

Regime II occurs for flows of flowrate  $Q \geq 40 \text{ lh}^{-1}$ , corresponding to jets with relative vorticity larger than  $0.3 \text{ s}^{-1}$  (i.e.  $\text{Ro}_v^{+/-} > 0.21$ ;  $\text{Ro} > 0.11$ ). In addition to the two bands of vortices that appear in Regime I associated to the jet shear layers, in Regime II also a layer of vortices of alternating sign is observed on the upper half of the continental slope (Fig. 4.22).

The jet width at  $\frac{1}{2}U_{max}$  is slightly larger than the distance between the forcing rings (Fig. 4.23). Streamlines cross over vortices from the jet region, indicating, as before, that these vortices are advected by the mean flow (Fig. 4.22). The potential vorticity remains homogeneous in the region where the jet is placed, apart from the outer edge of the jet, where the anticyclonic chain of vortices is located, where, as in Regime I, the potential vorticity shows a wavy-like character.

The cyclonic vortices occurring on the upper slope are coupled to the anticyclonic vortices from the anticyclonic shear layer of the jet. All the vortices are moving in the same direction as the mean flow, with a phase speed slightly less than that of the jet speed, i.e. approx. 85-90% of the maximum jet speed. Nevertheless, streamlines do not cross the upper-slope vortices, but they appear as closed isolines over the upper-slope vortex chain.

The vortices associated with the jet are separated from the vortex chain located at the shelf break by a potential vorticity gradient. The upper-slope vortex chain is able to modify this potential vorticity gradient in such a way that cyclonic vortices enhance the gradient and anticyclones smooth it. There is no tendency for the upper slope vortices to cross the shelf break. Nevertheless, for high flows of Regime II, vortices of anticyclonic sign tend to shift towards the continental shelf, whereas vortices of cyclonic sign remain on the uppermost slope, as can be observed in Fig. 4.22.



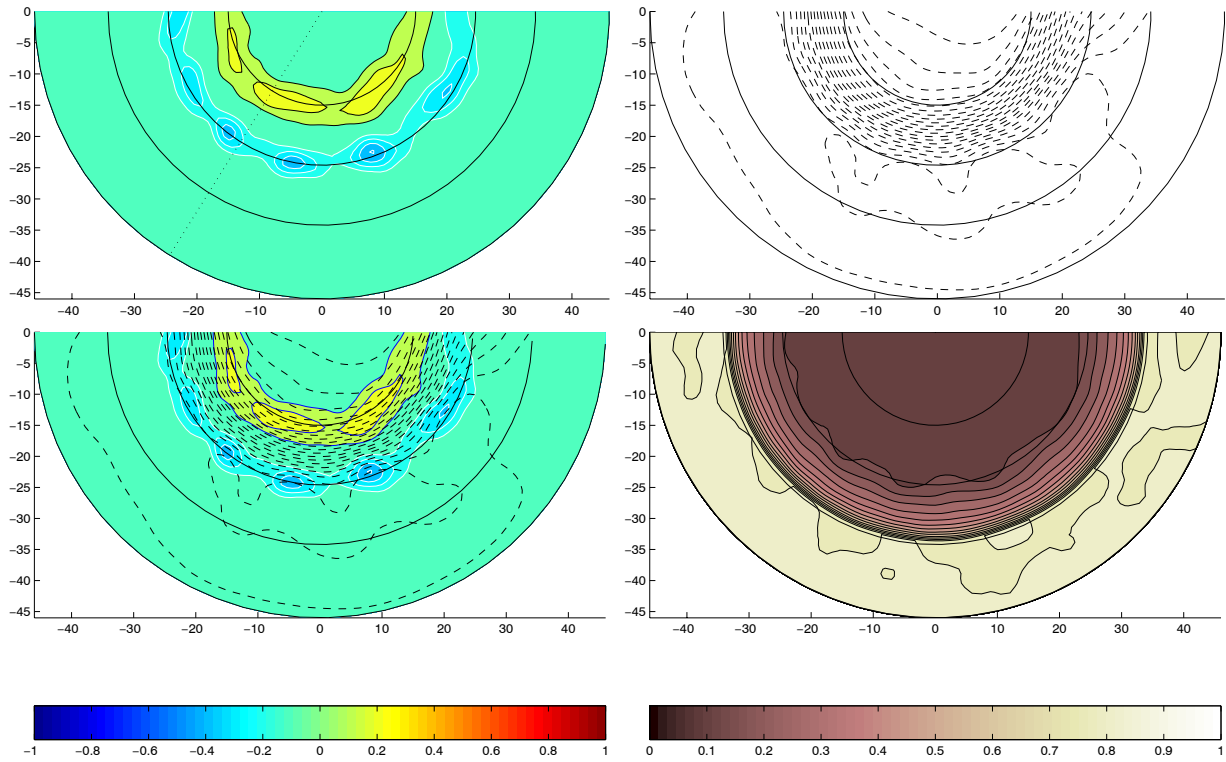


Figure 4.20: Prograde jet over the sloping bottom in Regime I for  $Q = 33 \text{ l h}^{-1}$ . Top left: Relative vorticity (separation between isolines:  $0.1 \text{ s}^{-1}$ ); Top right: Streamlines; Bottom left: Combination of both figures; Bottom right: Potential vorticity (separation between isolines:  $0.05 \text{ s}^{-1} \text{ cm}^{-1}$ ).

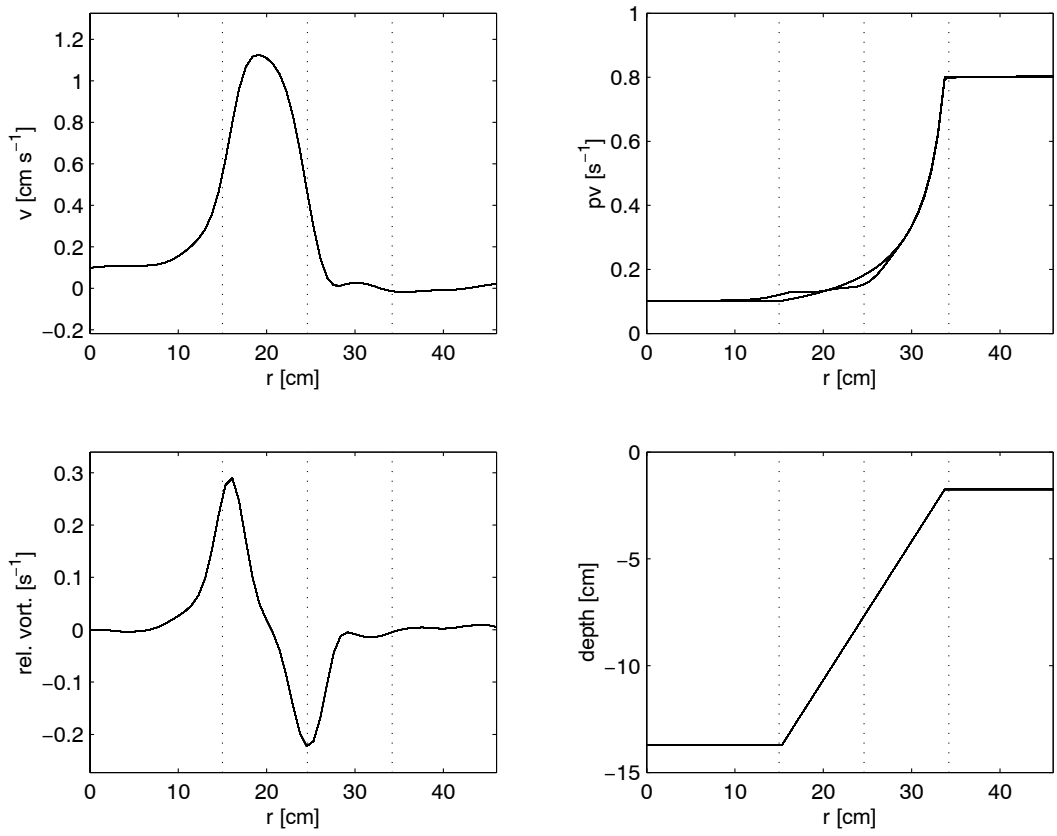


Figure 4.21: Radial profiles of velocity, relative vorticity, potential vorticity and topography for a prograde jet ( $Q = 33 \text{ lh}^{-1}$ ) over the sloping bottom in Regime I (corresponding to the section drawn in the relative vorticity plot in Fig. 4.20)

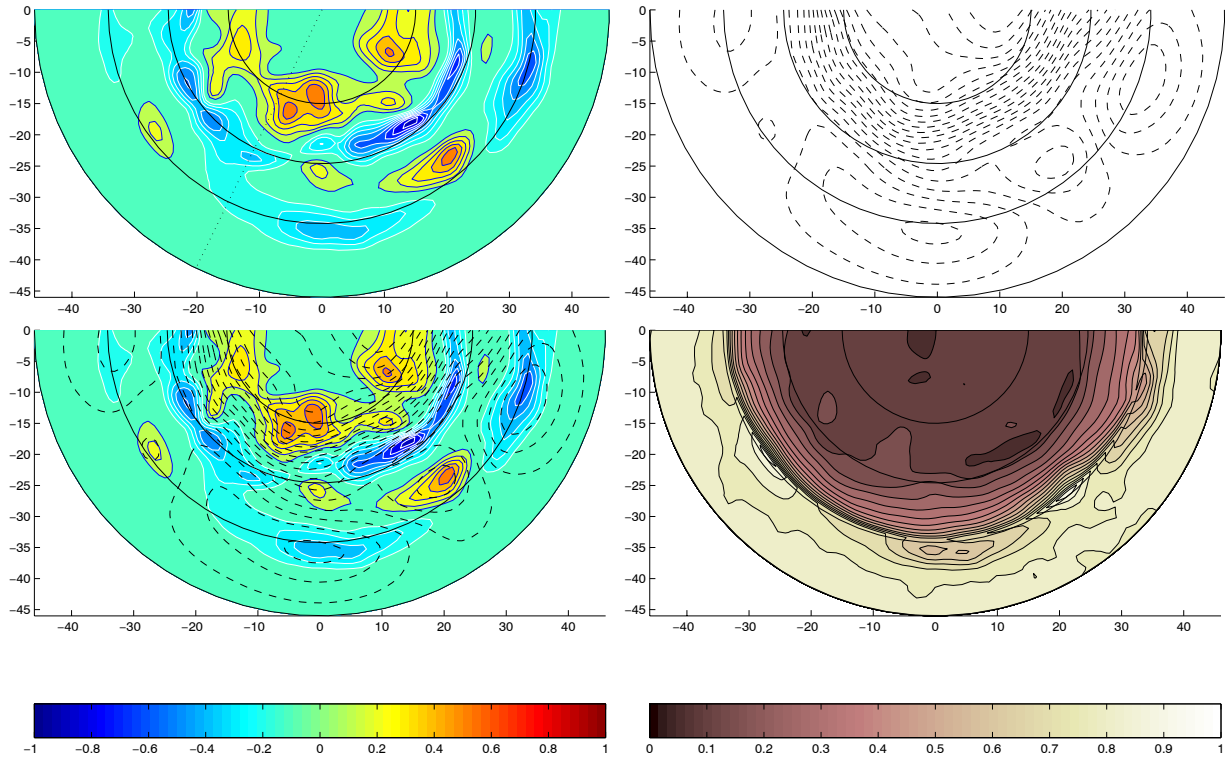


Figure 4.22: Prograde jet over the sloping bottom in Regime II for  $Q = 100 \text{ l h}^{-1}$ . Top left: Relative vorticity (separation between isolines:  $0.1 \text{ s}^{-1}$ ); Top right: Streamlines; Bottom left: Combination of both figures; Bottom right: Potential vorticity (separation between isolines:  $0.05 \text{ s}^{-1} \text{ cm}^{-1}$ ).

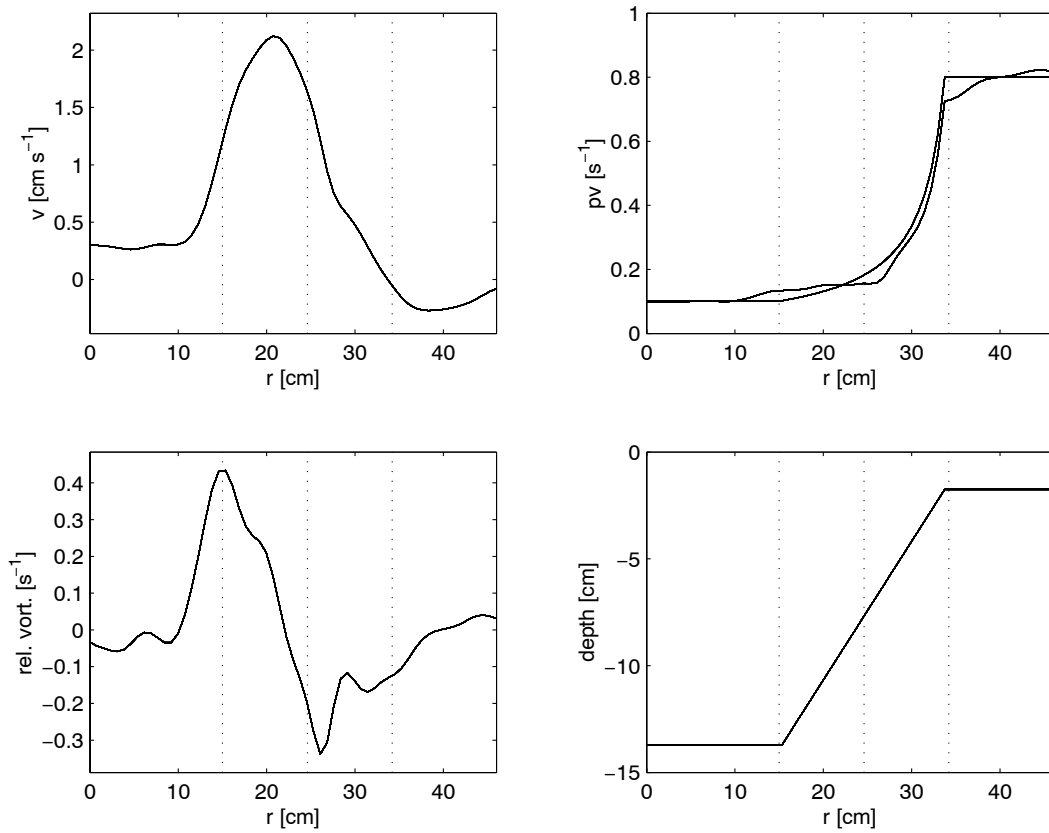


Figure 4.23: Radial profiles of velocity, relative vorticity, potential vorticity and topography for a prograde jet ( $Q = 100 \text{ lh}^{-1}$ ) over the sloping bottom in Regime II (corresponding to the section drawn in the relative vorticity plot in Fig. 4.22).

### 4.5.3 Retrograde jets over sloping bottom

In the behaviour of retrograde jets one can also distinguish two different regimes, which we shall also name Regime I and Regime II.

Regime I flows, forced with flowrates  $Q \leq 60 \text{ lh}^{-1}$ , have vorticities lower than  $0.6 \text{ s}^{-1}$  (i.e.  $\text{Ro}_v^{+/-} \simeq 0.43$ ;  $\text{Ro} \simeq 0.21$ ) and their characteristics are identical to those of Regime I for prograde jets: the jet consists of two bands of oppositely signed vorticity, with vortices of the same sign as the ambient shear (Fig. 4.24). The jet width at  $\frac{1}{2}U_{max}$  corresponds to less than the distance between the forcing rings (Fig. 4.25). The potential vorticity profiles show two discontinuities where the vortices are located (i.e. above the sink and above the source).

The potential vorticity contour shows migration of potential vorticity towards the region of the jet. Both shear layers appear separated by potential vorticity isolines, opposite of what was observed in prograde jets where the jet was flowing in a constant potential vorticity region.

Streamlines cross vortices, indicating their advection with the mean flow. The anticyclonic vortices move in the same direction as the mean flow, but with a phase speed approx. 65–75 % to that of the maximum speed of the jet. The motion of the cyclonic vortices is more difficult to follow. The cyclonic vortices appear in large areas of positive vorticity, for which the displacement speed is difficult to assess.

Regime II occurs for flow rates  $Q \geq 80 \text{ lh}^{-1}$ , for which the flows have vorticities larger than  $0.8 \text{ s}^{-1}$  (i.e.  $\text{Ro}_v^{+/-} \simeq 0.57$ ;  $\text{Ro} \simeq 0.29$ ) (Fig. 4.26). Thus, the cut-off flow rate separating Regime I and Regime II flows is somewhere between flow rates  $60 < Q < 80 \text{ lh}^{-1}$  (i.e. between  $\text{Ro} = 0.21 - 0.29$ ). A remarkable feature is the jet width at  $\frac{1}{2}U_{max}$ , which correspond to only half the distance between the forcing rings (Fig. 4.27). No motion is observed in this case on the upper slope. An intensification of the relative vorticity of the jet is observed, together with a strong meandering pattern (Fig. 4.26), similar to that observed in the flat bottom experiments (see Section 4.5.4). A remarkable feature is the coupling of vortices on either side of the current: they tend to move together, linked by the jet meandering. In fact, the vortices are observed to strongly reduce their propagation speed relative to the jet – they are rather stationary. The potential vorticity profiles are remarkably different from the rest of the experiments: the vortices are still placed at the potential vorticity discontinuities, but they are shifted closer to each other. Moreover, the potential vorticity profiles shows a strong gradient in between the two discontinuities, just where the meandering pattern is observed (Fig. 4.27).

The potential vorticity contours clearly show migration of potential vorticity towards the region of the jet. Both shear layers appear separated by potential vorticity isolines, displaying a clear meandering pattern.

The vortices are not moving, but they show a standing-wave like character, only showing slight advection in the azimuthal direction. Streamlines cross the vortices but often show closed paths over the anticyclones. The vortices are coherent, but they do not last for the whole experiment.

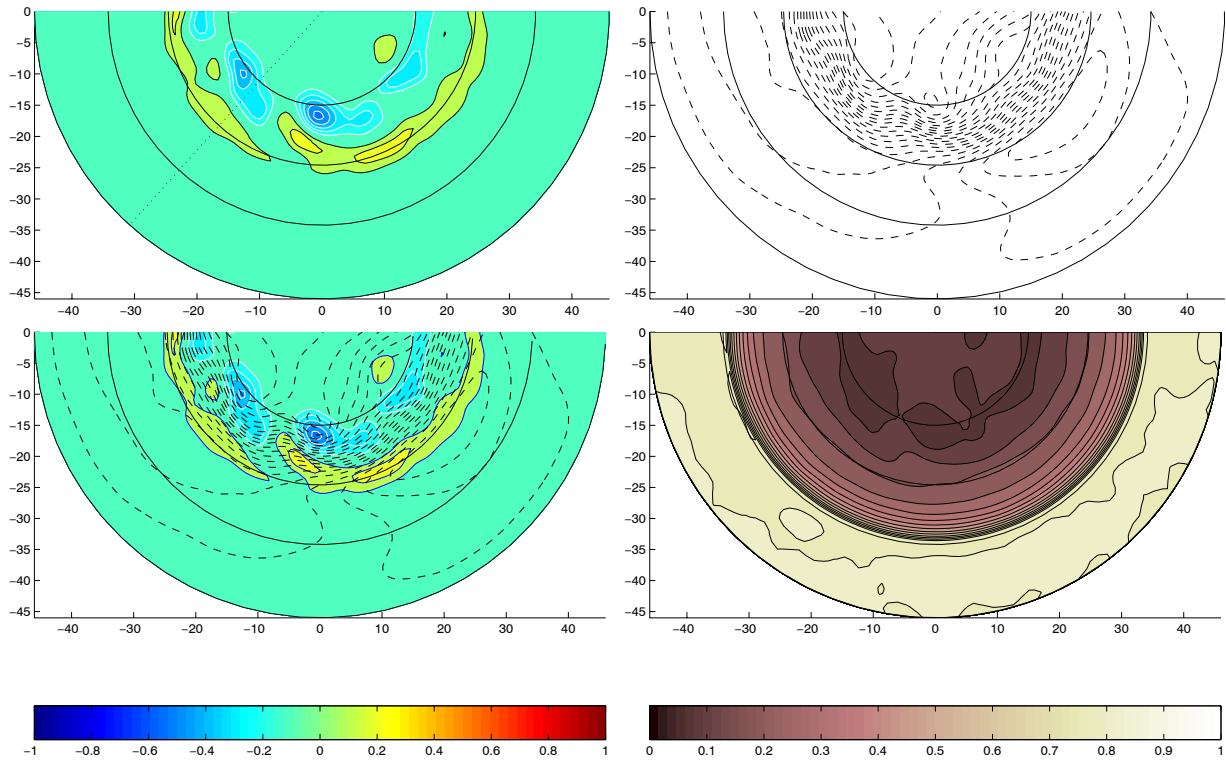


Figure 4.24: Retrograde jet over the sloping bottom in Regime I for  $Q = 33 \text{ l h}^{-1}$ . Top left: Relative vorticity (separation between isolines:  $0.1 \text{ s}^{-1}$ ); Top right: Streamlines; Bottom left: Combination of both figures; Bottom right: Potential vorticity (separation between isolines:  $0.05 \text{ s}^{-1} \text{ cm}^{-1}$ ).

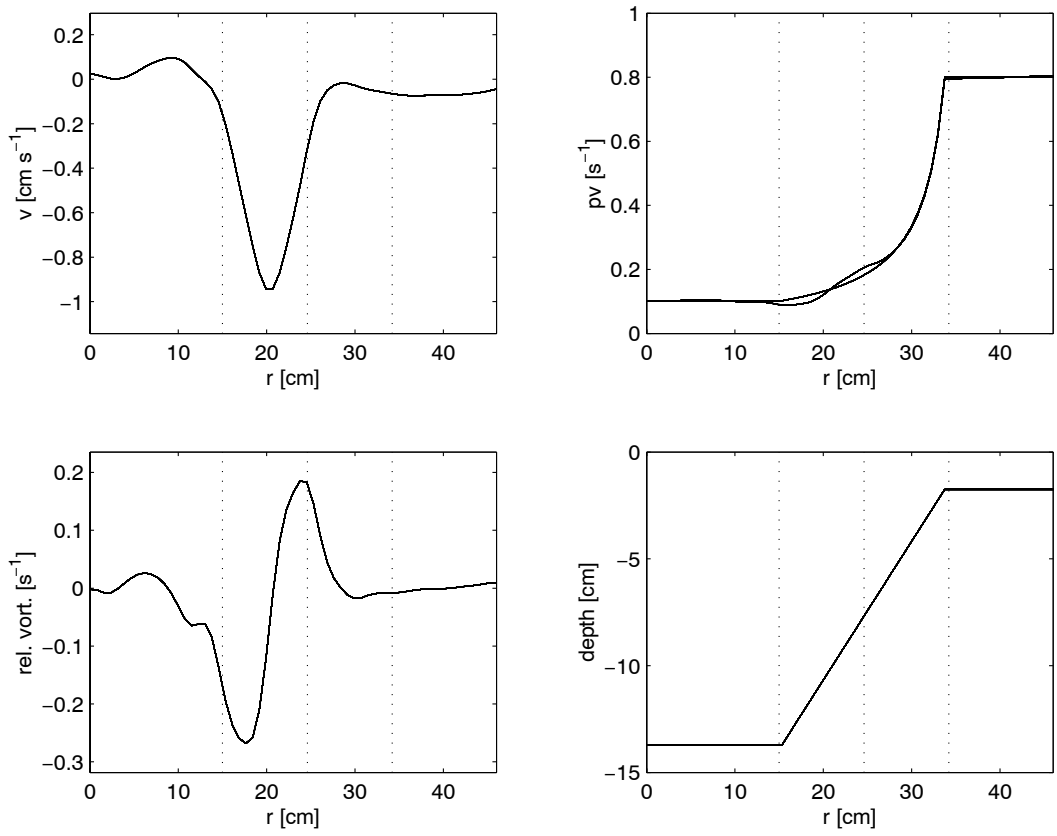


Figure 4.25: Radial profiles of velocity, relative vorticity, potential vorticity and topography for a retrograde jet of Regime I for  $Q = 33 \text{ lh}^{-1}$  (corresponding to the section drawn in the relative vorticity plot in Fig. 4.24).

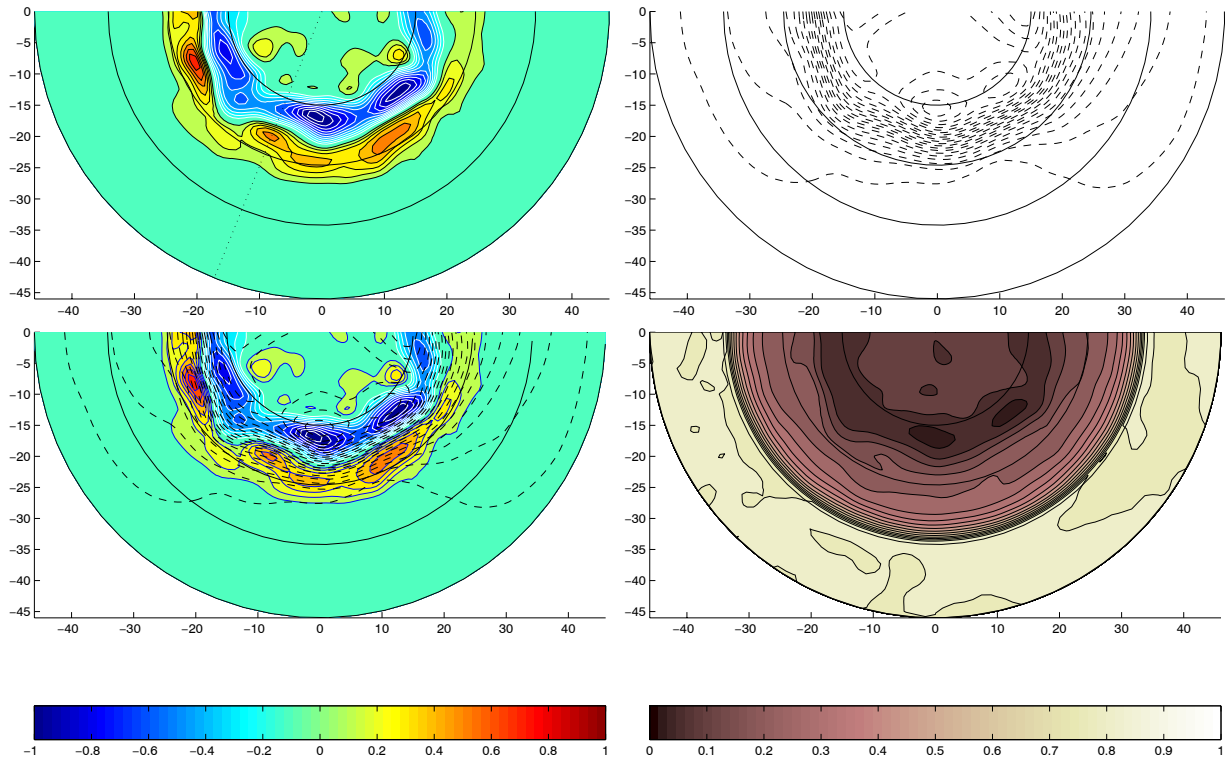


Figure 4.26: Retrograde jet over the sloping bottom in Regime II for  $Q = 80 \text{ l h}^{-1}$ . Top left: Relative vorticity (separation between isolines:  $0.1 \text{ s}^{-1}$ ); Top right: Streamlines; Bottom left: Combination of both figures; Bottom right: Potential vorticity (separation between isolines:  $0.05 \text{ s}^{-1} \text{ cm}^{-1}$ ).



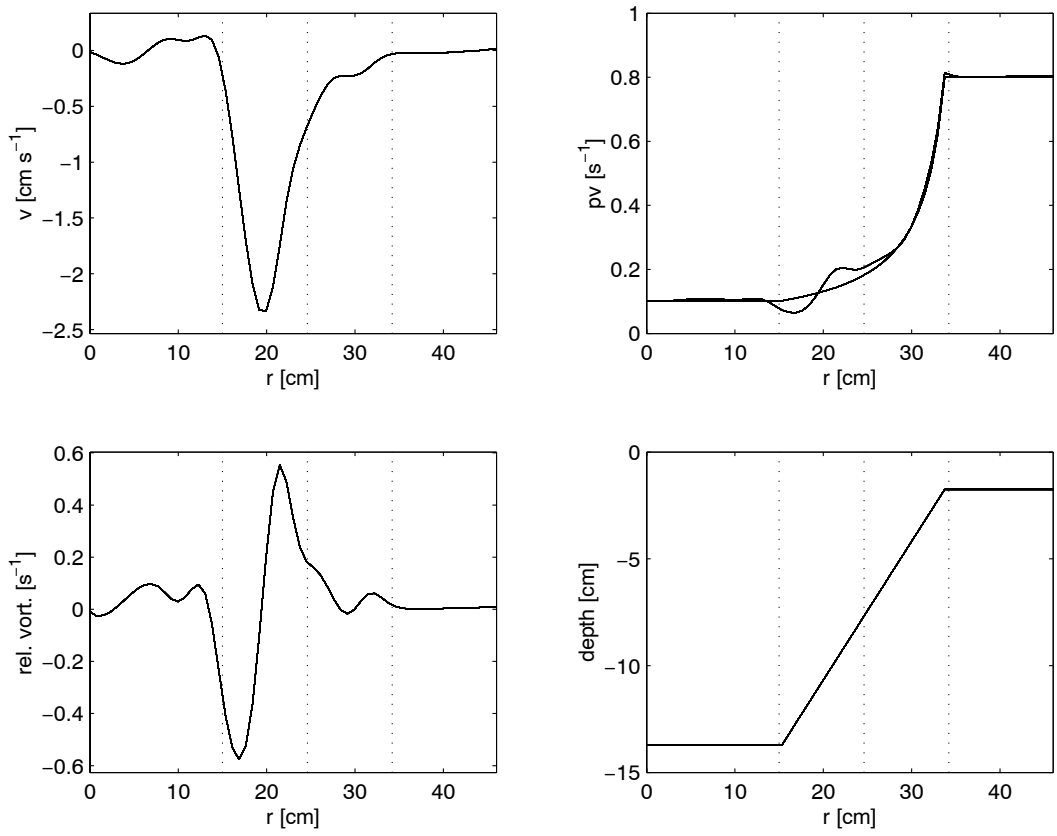


Figure 4.27: Radial profiles of velocity, relative vorticity, potential vorticity and topography for a retrograde jet of Regime II, for  $Q = 80 \text{ lh}^{-1}$  (corresponding to the section drawn in the relative vorticity plot in Fig. 4.26).

#### 4.5.4 Jets over flat bottom

Only prograde jets were simulated using the flat bottom topography. In these experiments the stable state of the jet consists of a finite number of waves, ranging from 7 to 3, as the flow rate  $Q$  increases from 15 to 80  $\text{lh}^{-1}$  (see Fig. 4.28). The wavy motion of the jet is

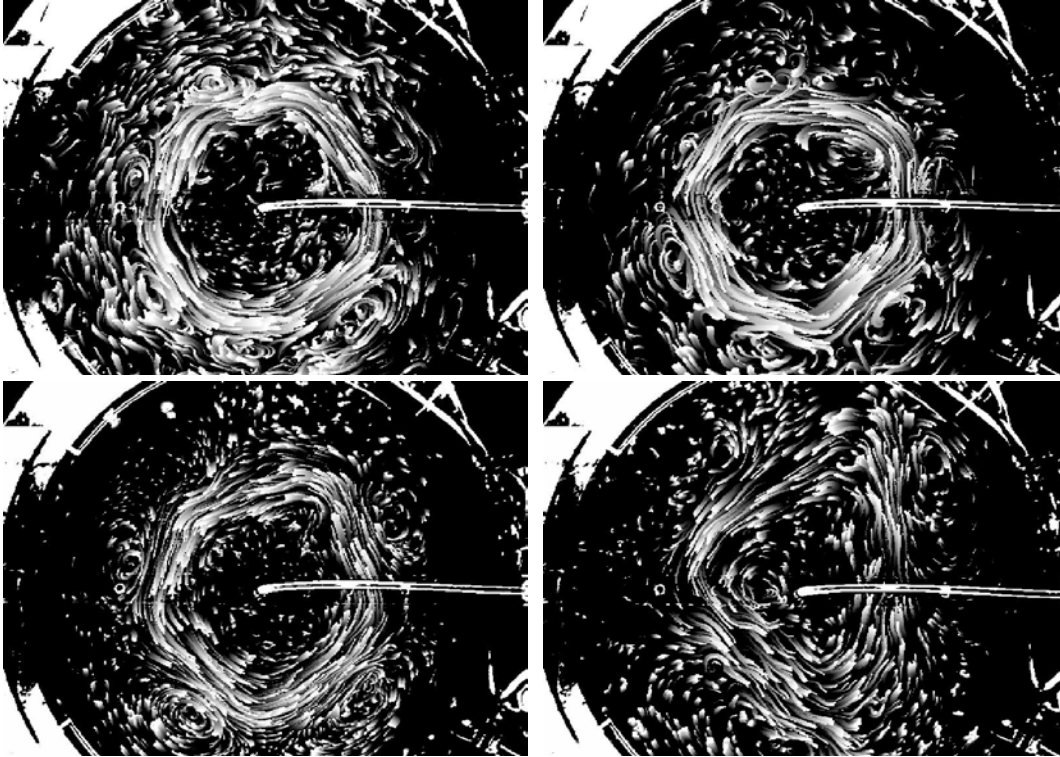


Figure 4.28: Particle streaks for a flow over the flat bottom. A wavy pattern of 7, 6, 5 and 3 waves appears for increasing flow intensities:  $Q = 15 \text{ lh}^{-1}$  (top left),  $25 \text{ lh}^{-1}$  (top right),  $53 \text{ lh}^{-1}$  (bottom left),  $80 \text{ lh}^{-1}$  (bottom right).

coupled with anticyclonic coherent vortices on its outer side and cyclonic vortices in the inner part of the current, although the latter appear with lower intensity. The waves and coupled vortices travel in co-rotation with the cyclonic jet, but with a phase speed smaller than that of the mean flow. The jet speed is proportional to the flow rate and inversely proportional to the wave number (Fig. 4.29).

The organization into a coherent wavy jet seems to originate from one single perturbation: once a wave has grown, the perturbation propagates in the same direction as the jet, and leads to the growing of other waves, finally resulting in a characteristic regular wavy pattern, see Fig. 4.28.

The undisturbed jet profile was difficult to determine due to the effect of the surrounding vortices. By using radial injections of dye in between two vortices one could observe that the jet was placed between the two forcing rings, showing maximum velocities at the inner ring and descending in intensity towards the outer ring.

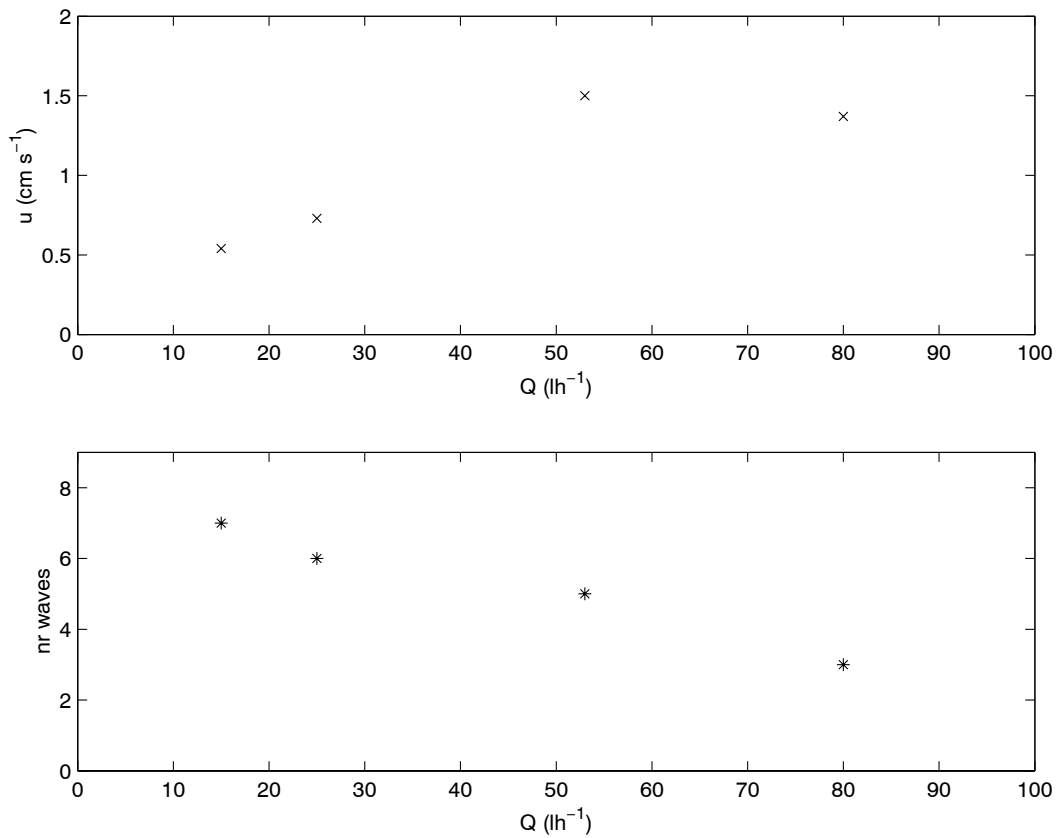


Figure 4.29: Top: Typical (maximum) velocities obtained with different flow rates. Bottom: Number of waves obtained for flows with different flow rates.

The maximum flow rate  $Q$  to be used in this set-up is about  $80 \text{ lh}^{-1}$ . Higher flow rates generate too large jets for our tank size. This can be observed in the case of the 3-wave jet, which has slower speed values than the 4-wave experiment (Fig. 4.29), probably because the 3-wave jet was constrained by the size of the container, and interfered with the walls of the tank.

## 4.6 Interpretation of results and discussion

The presence of an extremum in the potential vorticity profile of the jet is a necessary (but not sufficient) condition for shear instability. In fact, such extrema are present on either side of the current. It was observed that Kelvin-Helmholtz like instabilities developed on both sides of the jet, in all the experimental cases. This was the reason why the primary (undisturbed) flow could not be produced in the laboratory. There are noticeable differences between the time averaged profiles and the expected theoretical profiles (Fig. 4.19) mainly due to the presence of the vortices, which cause the velocity peak to oscillate in radial direction between the jet edges.

In all cases the vortices are travelling with a phase speed lower than the maximum jet speed, in agreement with the existence of a bound for the phase speed (4.35) of the instabilities .

### 4.6.1 Jets on an f-plane

Cyclonic jets (in the present parabolic bottom experiments: prograde jets) are found to be more stable than anticyclonic jets (here: retrograde jets). We have no clear answer to this different behaviour of cyclonic/anticyclonic currents; in the case of cyclonic/anticyclonic vortices, it is well known that vortices with negative spin sign are generally more unstable than positive vortices. This has been studied both in the laboratory and theoretically by Kloosterziel and van Heijst [Kloosterziel and van Heijst, 1991].

In comparison with the sloping bottom experiments, the jets on the slope were more organized than the jets on the parabolic bottom, which evidences the stabilizing role of the bottom topography.

### 4.6.2 Jets over sloping bottom

#### Slope currents at low speeds

According to the stability analysis of Li and McClimans [Li and McClimans, 2000], for any slope and jet profile there is a critical value for  $Ro$  below which a jet flow is stable. Since in the present laboratory experiments even the lowest  $Ro$  jet flow was found to be unstable, the instability threshold for our specific topography and jet profile could not be established. This would suggest that a slope current of similar characteristics to that of the Northern Current would be barotropically unstable for any flow speed.

The current's relative vorticity in both slope experiments will depend on the balance between the vorticity associated with the horizontal velocity shear and the gain/loss of vorticity due to flow in the cross-slope direction. Both components will be directly proportional to the speed of the jet.

Low speed currents will have a small component of topographically induced vorticity, and the vorticity balance will be dominated by the vorticity associated with the horizontal

shear. In case of instability, both vorticity bands of the jet will develop a shear instability with a Kelvin-Helmholtz-like pattern.

For both the prograde and the retrograde case, negative vortices will lie on the right of the jet and positive vortices on the left side of the jet. The position of the vortices relative to the jet flow direction will cause the maximum speed to concentrate in between both layers of vortices, restricting possible meandering. Thus, the jet will appear as a 'turbulent' and broad jet, formed by two layers of vortices and its width will be determined by the distance between the forcing rings, where the potential vorticity discontinuities are located.

The flow patterns observed in low speed jets are similar to those observed in parabolic bottom experiments, where only shear instability was present. This fact suggests that the effect of the sloping bottom in low speed jets in terms of topographically induced vorticity is limited. The main role of the bottom topography in low speed regimes is in the organization of the flow: the jets over the parabolic bottom were highly disorganized whereas the jet flow and the vortices are constricted by the topography.

The above-mentioned arguments are in agreement with Marcus and Lee theory [Marcus and Lee, 1998], which states that each shear layer of the jet becomes unstable and develops a Kelvin-Helmholtz-like instability and a weak Rossby-wave-like instability. The Rossby waves would be too weak to produce any meandering.

### **Prograde slope currents at high speeds**

High speed flows have a larger tendency to show other unstable patterns apart from Kelvin-Helmholtz-like instabilities (e.g. meandering-like motions) than flows with low speeds. This is reflected in a stronger tendency to present cross-slope motions, and in a larger contribution of topographically induced vorticity.

In the case of a prograde (in our case, westward) jet, the relative vorticity generated by stretching/squeezing of the water parcels moving across the slope has the same sign as the ambient shear. A water parcel from the right (negative) side of the jet moving upslope will gain negative relative vorticity, becoming more anticyclonic. If the parcel moves downslope, it will gain cyclonic vorticity, so its relative vorticity will decrease. The same occurs for a parcel from the left (positive) side of the jet: a downslope motion will enhance its cyclonic sign, whereas an upslope motion will weaken the vortex. This explains the tendency of the vortex layers to move apart, as is reflected in the potential vorticity profiles across the jet. Therefore, the prograde jet tends to be broad and 'turbulent'. Our results are in agreement with previous studies of jets on a beta-plane [Marcus and Lee, 1998] which show that in prograde jets the discontinuities in the potential vorticity profile are far apart and the associated Rossby waves are weak. This explains that prograde jets do not show a clear meandering pattern.

The main striking feature observed in the present experiments is the appearance of a chain of vortices of alternating sign on the upper slope of the prograde (westward) jet. These vortices are probably associated with a shelf-break topographic Rossby wave. The broadening tendency of prograde jets may affect the upper part of the slope, leading to the generation of a topographic Rossby wave.

The location of the Rossby waves can be more easily observed in the relative vorticity contours after subtraction of the zonally averaged vorticity due to the jet. For a Regime I prograde jet, a Rossby wave locates over the mid-slope (Fig. 4.30). For a Regime II prograde jet the Rossby wave on the upper slope also appears (Fig. 4.31 and Fig. 4.32). The mid-slope and upper-slope Rossby waves are in counter-phase.

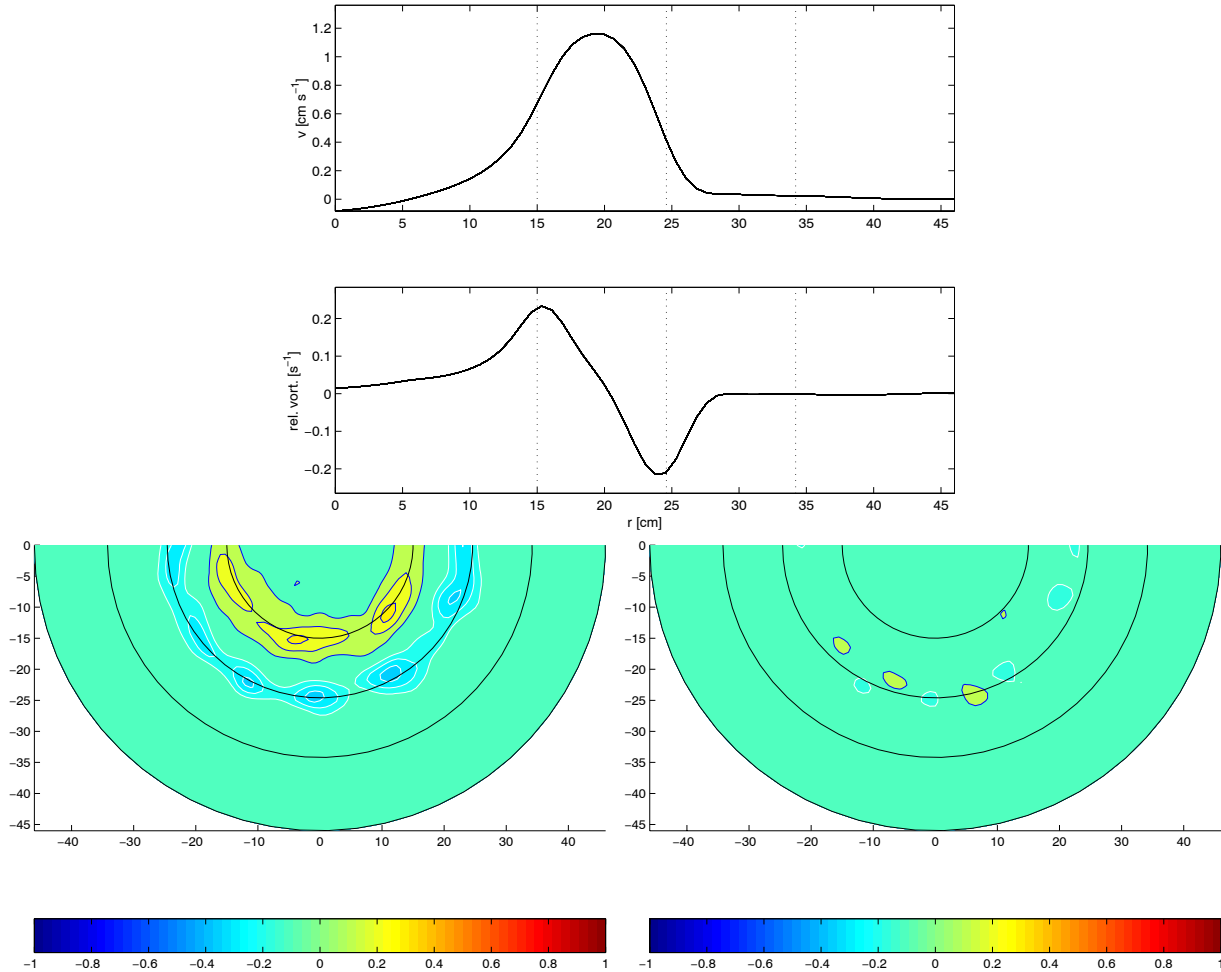


Figure 4.30: From top to bottom: (i) Velocity profile averaged in azimuthal direction; (ii) Corresponding relative vorticity profile used here. The vertical lines indicate (from left to right): the sink ring, placed at the bottom of the slope, the source ring placed on the mid-slope, and the shelf-break; (iii) Relative vorticity for a prograde jet ( $Q = 33 \text{ lh}^{-1}$ ) over sloping bottom; (iv) Corresponding relative vorticity after subtracting the mean relative vorticity due to the velocity profile.

The upper-slope Rossby wave is observed to move in concert with the instabilities of the negative shear layer of the jet. Their propagation speed is approx. 85–90% of the maximum jet speed. The fact that the upper-slope Rossby wave has the same phase speed as the Rossby wave associated with the jet’s negative shear layer, and moreover, the

fact that they are both slower than the maximum jet speed suggests that their source of energy is the mean kinetic energy of the jet —i.e. both waves extract energy from the jet. Instabilities faster than the jet’s maximum speed would not be able to gain energy and therefore, they would fade out.

The comparison of the laboratory experiments with MATER HFF experiment data is not straightforward. Firstly, because the quantities measured in the laboratory (vorticity) are not available from the field work, where we have SST images and Eulerian velocity data. Besides, because the laboratory case does not contain baroclinic effects which can be present in the oceanic case. In order to compare data from both sources, we may refer to the experiments with DigImage, in which it was observed how Lagrangian tracers were describing anticyclonic gyres. In Fig. 4.33 the particle streaks draw the envelope of two anticyclonic vortices, one from the lower-slope and one from the upper-slope, showing that after a short time the general flow picture is a chain of anticyclonic patterns located between the outer edge of the jet and the shelf break, similar to the anticyclones detected in the SST images. Only after a detailed HPV analysis, the upper-slope cyclones were evident (Fig. 4.22).

The main field evidence of the distribution of vortices comes from an indirect oceanographic tracer (surface temperature), which is therefore supposed to obey the same laws as the potential vorticity. In our Regime II prograde flows, the vortices associated with the jet are separated from the shelf-break vortex chain by a potential vorticity gradient. The upper-slope anticyclones are observed to be responsible of smoothing the potential vorticity gradient (Fig. 4.22), suggesting that a lower-slope tracer would have a major tendency to show anticyclonic patterns rather than cyclones. Therefore, SST images showing only anticyclones could be missing part of the history.

The observation of a shelf-break Rossby wave caused by a slope current flowing over the lower slope is thought to be new. This type of flow structure is neither observed in previous experiments of jets on a beta plane [Sommeria et al., 1988] [Sommeria et al., 1991] [Solomon et al., 1993] nor in previous studies on jets over a continental slope [Li and McClimans, 2000], probably due to the different configuration used here.

It is also worth noting that the cross-slope propagation of the upper-slope Rossby wave is limited by the shelf break (Fig. 4.22), a fact that evidences the role of the shelf break as a barrier for shelf-slope interactions. Exchange of matter between the shelf and the slope is therefore expected to be more related to alterations in the continental slope topography, such as submarine canyons.

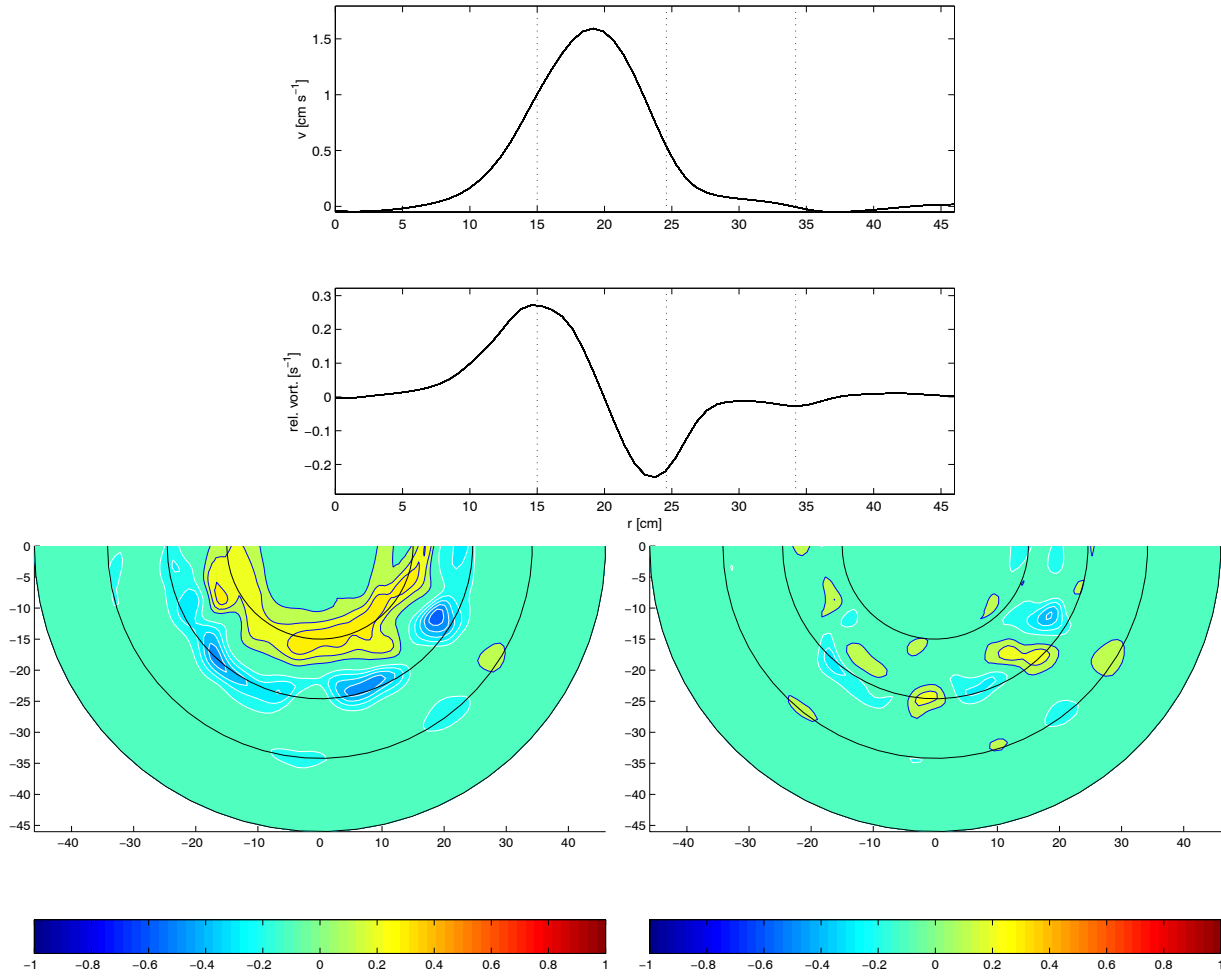


Figure 4.31: From top to bottom: (i) Velocity profile averaged in azimuthal direction; (ii) Corresponding relative vorticity profile used here. The vertical lines indicate (from left to right): the sink ring, placed at the bottom of the slope, the source ring placed on the mid-slope, and the shelf-break; (iii) Relative vorticity for a prograde jet ( $Q = 60 \text{ lh}^{-1}$ ) over sloping bottom; (iv) Corresponding relative vorticity after subtracting the mean relative vorticity due to the velocity profile.



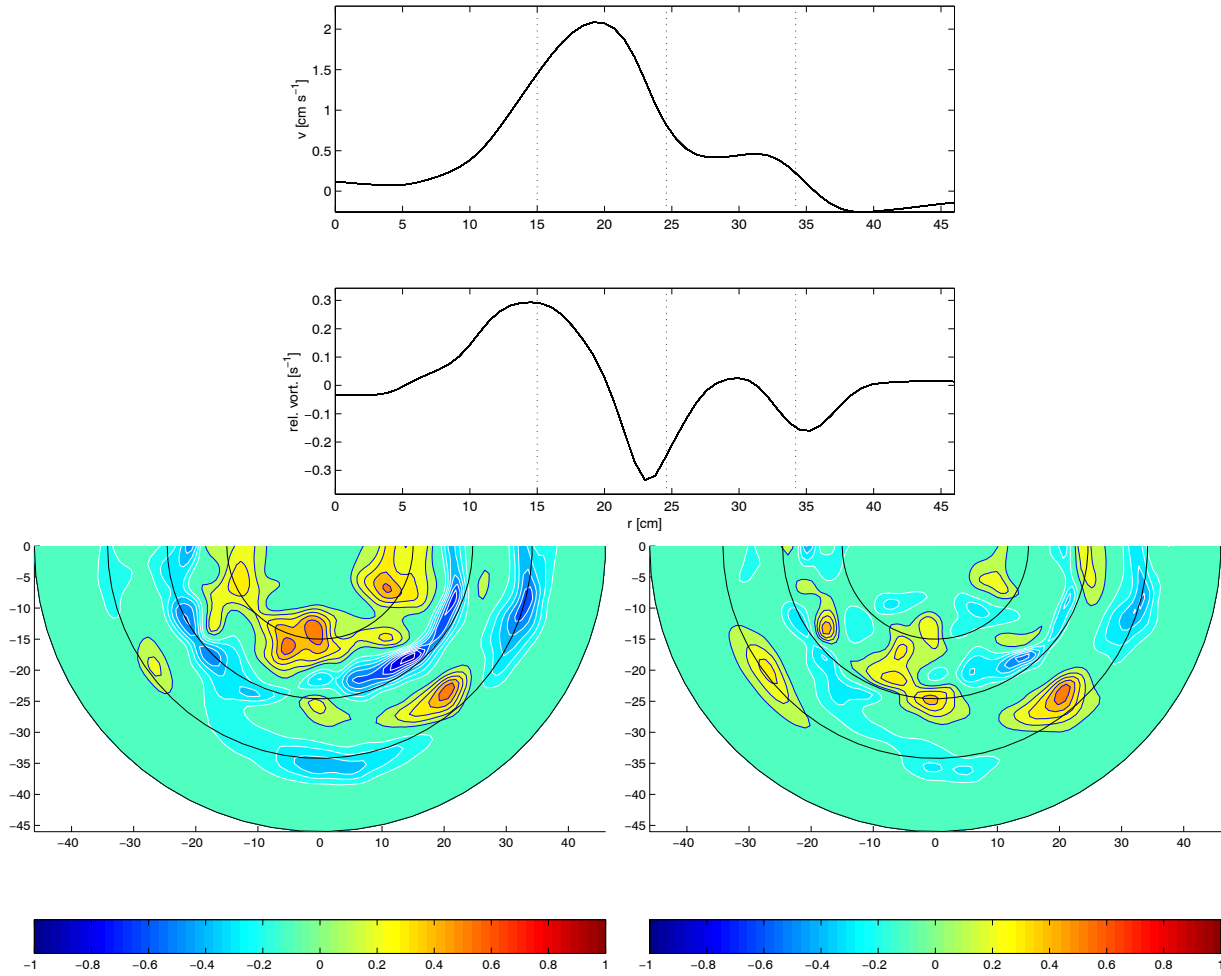


Figure 4.32: From top to bottom: (i) Velocity profile averaged in azimuthal direction; (ii) Corresponding relative vorticity profile used here. The vertical lines indicate (from left to right): the sink ring, placed at the bottom of the slope, the source ring placed on the mid-slope, and the shelf-break; (iii) Relative vorticity for a prograde jet ( $Q = 100 \text{ lh}^{-1}$ ) over sloping bottom; (iv) Corresponding relative vorticity after subtracting the mean relative vorticity due to the velocity profile.

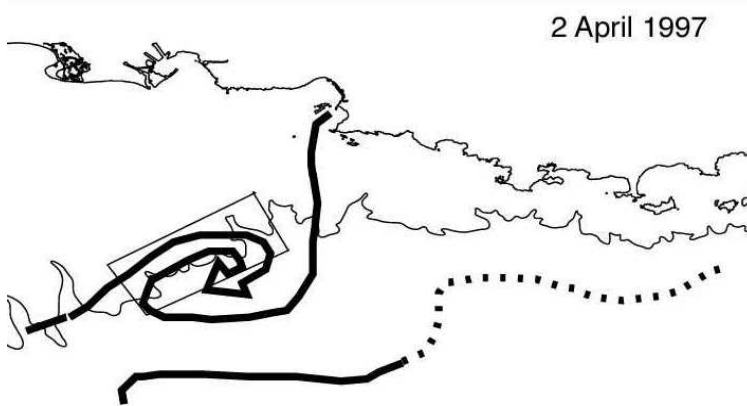
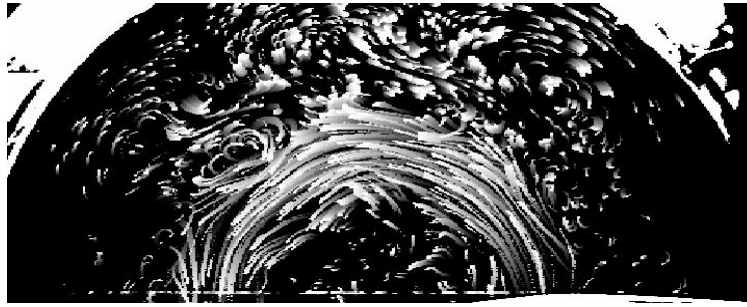


Figure 4.33: Top: Particle streaks for a jet of Regime II over the sloping topography ( $Q = 60 \text{ lh}^{-1}$ ), with a Rossby number comparable to that characterizing the Northern Current. Center: SST image showing a typical anticyclonic structure (April 2nd 1997) over the MATER experiment site (mooring sites are shown). Bottom: Corresponding scheme of the SST image; the 1000m isobath crossing the experiment site and the experimental site location are shown (from Chapter 3 in this thesis)

## Retrograde slope currents at high speeds

Opposite to what occurs in prograde jets, in the case of retrograde (eastward, in our case) jets, the vorticity generated by the horizontal shear is of opposite sign of that generated by the stretching/squeezing of the water parcels moving across the slope. According to the same reasoning as before, a parcel from the left (positive) side of the jet moving upslope will gain negative relative vorticity, so the relative vorticity of the parcel will be weakened. Instead, if the parcel moves downslope, it will gain positive vorticity so it will be reinforced. Therefore in the retrograde jet, the natural tendency for the vortices is to move together, to the centre of the jet. This will cause the jet to become narrow. The two bands of vortices can eventually overlap into one band of alternating vortices, forcing the maximum speed to concentrate in between consecutive vortices, causing the meandering of the jet.

In accordance to the theoretical model described by Marcus and Lee [Marcus and Lee, 1998], in retrograde jets the discontinuities of the potential vorticity profiles across the jet and its associated Rossby waves move together, eventually merging into a single and strong Rossby wave. Our results are in agreement with this theory: the potential vorticity discontinuities are shifted together, corresponding to a narrowing of the jet, and in the region in between the two discontinuities a large gradient of potential vorticity appears: this is where meandering occurs. Moreover, the phase speed of the vortices associated with the jet is strongly reduced when compared to those in the low speed regime — in fact, vortices are almost not moving in Regime II flows. This could be caused by the large Rossby wave, which would also give the jet a meandering appearance as observed.

The present experiments show how in eastward (retrograde) jets migration of potential vorticity occurs towards the centre of jet, whereas in the case of westward jets potential vorticity moves towards the edges of the jet. Considering that the potential vorticity gradients can act as a barrier for exchange of water properties, in eastward jets, properties from vortices of both shear layers will not mix, whereas mixing between both sides of the jet will be possible in westward currents.

The cut-off flow rate at which the slope begins to influence the vorticity balance depends on the steepness of the slope. The stronger the slope, the more difficult it is for the water parcels to be displaced in cross-slope direction. This conclusion comes from comparing the retrograde (eastward) sloping bottom experiments with the flat bottom experiments, in which the surface was acting as a mild slope, and the flow was effectively an eastward flow. In the former experiments, a flow rate was needed to be exceeded in order to observe the current meandering, whereas in the latter experiments the current showed a meandering pattern even at the lowest flow rate. This comparison shows the stabilizing role of the bottom topography and the destabilizing effect of large Rossby number (i.e. high speed flows): whereas the former factor contributes to reduce non-linearities, the latter makes them to increase, contributing to flow instability.

The characteristics of our eastward jets are in agreement with the observations of Sommeria [Sommeria et al., 1989] and Solomon [Solomon et al., 1993] in their experiments of eastward jets on a beta-plane. Their eastward jets were prograde jets, whereas ours are retrograde jets. This reveals that the bottom topography, rather than the direction of

rotation, plays a determinant role in the flow dynamics.

### 4.6.3 On the role of the topographic free surface

As discussed in Section 4.3.4, the topographic surface does not affect the flow dynamics in the slope bottom experiments, although it might play a fundamental role in the jet behaviour in the experiments with the flat bottom. This was already discussed by Carnevale [Carnevale et al., 1991].

The flat bottom experiments performed here are consistent with those performed by Sommeria [Sommeria et al., 1989] for an eastward jet on a beta-plane: the jet becomes wavy, with decreasing wave numbers for increasing flow rates. In our case, the elevation of the free surface towards the walls of the tank creates a gradient in potential vorticity converting the laboratory current in an eastward flow.

The planetary beta-effect is usually modelled in circular tanks in the laboratory by using a bottom topography (see e.g. [van Heijst, 1994]). Consider the conservation of potential vorticity (4.22) for an ocean case, where  $f = 2\Omega \sin\phi$ :

$$\frac{\omega + 2\Omega \sin\phi}{h} = \text{constant}, \quad (4.62)$$

where variations of the Coriolis parameter are considered to occur in a narrow range in latitude about a reference latitude  $\phi_0$ , such as:

$$\sin\phi = \sin\phi_0 + \frac{(\cos\phi_0)y}{R}, \quad (4.63)$$

where  $y = (\phi - \phi_0)R$  is the distance north of the reference latitude  $\phi_0$  and  $R$  is the radius of the Earth (the changes in latitude are simplified here considering small  $Ro$  number). The potential vorticity (4.62) for a fluid of constant depth is thus:

$$q_{ocean} = \omega + 2\Omega \sin\phi_0 + \beta_{ocean}y. \quad (4.64)$$

The effect of the variation of the Coriolis force with latitude is contained in the term

$$\beta_{ocean} = \frac{2\Omega \cos\phi_0}{R}, \quad (4.65)$$

named as the *beta-effect*.

In a laboratory experiment with a bottom topography  $h(r)$  given by  $h(r) = D - \alpha r$  where  $\alpha$  is the magnitude of the slope and  $D$  is some reference depth, the potential vorticity, under the restriction of a flow with small Rossby number, can be written as:

$$q_{exp} = \omega + 2\Omega \sin\phi_0 + \beta_{exp}y, \quad (4.66)$$

where  $\beta_{exp} = 2\Omega\alpha/D$  (a derivation of this result is presented by van Heijst [van Heijst, 1994]). In our case, the free surface elevation acts as a topographic slope, so we can re-write the beta-value as:

$$\beta_{exp} = \frac{2\Omega s_{exp}}{D}, \quad (4.67)$$

where  $s_{exp} = \eta_{exp}(r)/r$ ,  $\eta_{exp}(r)$  is the elevation of the free surface in our experimental set-up and  $D$  is the water depth.

From dimensional analysis, the dimensionless beta in the ocean is

$$\beta'_{ocean} = \beta_{ocean} \frac{R}{\Omega} = \cos\phi_0, \quad (4.68)$$

whereas the dimensionless beta-value in the laboratory is

$$\beta'_{exp} = \beta_{exp} \frac{L}{\Omega} = s_{exp} \frac{L}{D}. \quad (4.69)$$

Considering the experimental values of  $\Omega = 0.70 \text{ s}^{-1}$  and a tank radius of 0.46 m, according to (4.55) the elevation of the free surface at the wall of the tank is 5.1 mm. If we consider a linear approximation of the parabolic surface shape, we obtain a slope of  $s_{exp} = 0.01$ . If we would have considered the real parabolic elevation of the free surface instead of the linear approximation, the elevation which is actually relevant for the jet is smaller than 5.1 mm, also because the jet is placed at 0.25 m from the centre of the tank and not at the wall of the tank. Therefore the real topographic slope to consider is smaller than 0.01.

Considering the dimensionless beta-values for the experimental and the oceanic case must be the same, i.e.  $\beta'_{ocean} = \beta'_{exp}$ , we obtain that

$$\phi_0 = \cos^{-1} \left( s_{exp} \frac{L}{D} \right). \quad (4.70)$$

For  $s_{exp} = 0.01$ ,  $L = 9.6 \text{ cm}$  and  $D = 14 \text{ cm}$  we obtain that the conditions of our flat bottom cases correspond to a jet current flowing at 89 degrees of latitude — indeed a high latitude. The fact is that the variation of the Coriolis parameter is often neglected for the simulation of flows in high latitudes, but our results suggest that approximations to an f-plane, even at high latitudes, should be carefully considered.

In order to compare experiments with a sloping topography with experiments where topography effects are nonexistent, we must refer to parabolic bottom cases, where the parabolic bottom topography mimics the free surface elevation and assures the homogeneity of the fluid depth in the whole domain.

## 4.7 Summary and conclusions

In all our experiments the jets were observed to be unstable. This behaviour is consistent with the presence of extrema in the potential vorticity profiles of the jet for flows over a sloping topography, validating that it is a necessary condition for shear instability to occur.

Jets over a sloping bottom are observed to display two different flow regimes. For low speed flows, the jet presents similar patterns: each shear layer of the jet reveals the occurrence of Kelvin-Helmholtz-like instabilities, i.e. on either side of the jet vortices develop of the same sign as the ambient shear. For high speed flows, ‘eastward’ and

‘westward’ jets show very different patterns: eastward jets are narrow and wavy, whereas westward jets are broader and do not show any clear meandering.

These observations can be explained considering that the current’s relative vorticity in slope experiments depends on the balance between the vorticity associated with the horizontal velocity shear and the gain/loss of vorticity due to flow in the cross-slope direction. Both components (i.e. the vorticity associated to the shear and the vorticity induced topographically) are directly proportional to the speed of the jet. Low speed currents have a small component of topographically induced vorticity, and the vorticity balance is dominated by the vorticity associated with the horizontal shear. Therefore, low speed slope currents show the same patterns of instability as currents with constant depth, on either side of which only Kelvin-Helmholtz-like instabilities occur. High speed currents show different patterns because the topographically induced vorticity is different for eastward and westward flows. In the case of an eastward current, the motion of fluid columns towards the centre of the jet intensifies the horizontal shear vorticity by the induction of vorticity of the same sign, generated by the stretching/squeezing of the fluid columns. Oppositely, fluid columns moving away from the centre of the jet cause the shear-induced vorticity to be weakened by the effects of topography. Therefore the eastward jets are narrow and vorticity concentrates near the centre of the jet, as a chain of vortices of alternating sign, inducing the jet to meander. In the case of a westward flow, the vorticity generated by the horizontal flow has the same sign as the vorticity induced by the changes in the topography; therefore, across-slope displacements towards the centre of the jet weaken the vortices, whereas cross-slope displacements in the opposite direction enhance them. The jet becomes broader for higher-speed flows.

The differences between eastward and westward jets as observed in our experiments agree with the theoretical model proposed by Marcus and Lee [Marcus and Lee, 1998] for jets on a beta-plane, providing evidence that their model can be extended to any jet subjected to a gradient in ambient potential vorticity (in their case due to the beta-effect, in our case associated with the presence of the sloping bottom). Marcus and Lee’s model states that the shear layer on either side of the jet becomes unstable, showing Kelvin-Helmholtz-like instabilities coupled to a Rossby wave (in our case, topographically induced). The Rossby waves locate at the potential vorticity discontinuities. In the case of eastward jets, the potential vorticity moves towards the centre of the jet, so the two Rossby waves overlap into a larger Rossby wave that causes the jet to meander. In the case of westward jets, the potential vorticity moves out from the jet, and the associated weak Rossby waves locate at the edges of the jet.

The main striking result in our experiments is the presence of a Rossby wave on the upper slope, edging the shelf break, in the westward jet experiments. As far as we know, this observation has not been reported in any past experiment. The Rossby wave on the shelf break only appears for westward jets, whereas no motion is observed on the upper slope for eastward jets. This can be explained through the differences in the migration of potential vorticity described by Marcus and Lee [Marcus and Lee, 1998], but also through differences in the vorticity adjustment due to the balance between the vorticity induced by the horizontal shear and by the bottom topography. For westward jets, where the potential

vorticity tends to move out from the jet, and the topography induces vorticity of the same sign as the horizontal shear, widening of the jet can induce motion in the upper slope, leading to a topographic Rossby wave.

A direct comparison of the laboratory experiments with field data from the MATER HFF experiment is not straightforward. First of all, from the field data we cannot derive the vorticity distribution, and the main evidences of the distribution of vortices come from an indirect tracer (in this case, the surface temperature), which can definitely miss some flow patterns. Moreover, baroclinic effects, among others, are not considered in the laboratory model. Nevertheless, some conclusions can be made. Considering the present barotropic model, the Northern Current appears as an unstable current. The appearance of anticyclonic patterns over the upper slope of the Gulf of Lions observed in field experiments (see Chapter 3 in this thesis) could be related to barotropic instability associated to the Northern Current horizontal velocity shear. Nevertheless, baroclinic effects should be also considered.

The present laboratory model reveals also important information about the expected location of topographic Rossby waves. In the case of the Northern Current (westward current), topographic Rossby waves are expected to occur at the edges of the jet, together with a topographic Rossby wave over the shelf-break for high speed jets. The generation of the upper-slope Rossby waves deserves further interest. Their relation with the shelf break might be important on determining the exchanges between the slope and the shelf waters. When do the Rossby waves on the upper slope start to appear? What comes first, the intensification of an anticyclone from the jet's negative shear layer, which causes (for conservation of vorticity in the domain) the appearance of a positive cyclone? Or, instead, does a Rossby wave first appear on the upper slope interacting with (and also enhancing) the Rossby wave from the jet's negative shear layer? The origin of the Rossby wave on the upper slope will be analyzed in more detail in the next chapter, in which the flow is simulated numerically.

The bottom topography is effective in organizing the flow. When comparing with the flow on a sloping bottom with the flow on an  $f$ -plane, the jets over the slope are seen to be restricted to follow the isobaths and to be more organized. Moreover, the steepness of the topographic slope controls the cross-slope displacement of particles in the jet: for the same flow, we observe larger displacements for smoother slopes. This is evident when comparing the wavy pattern observed in eastward jets in our slope and flat-bottom experiments: for the same flow, with weak slopes (e.g. the experiments with a flat bottom, where the free surface elevation was acting as a mild topography), the wavy pattern was always present, whereas in the experiments using a sloping bottom a critical  $Ro$  needed to be exceeded in order to observe any meandering.

The comparison of our results to previous studies of westward and eastward flows directed opposite to the sense of rotation (in the studies of Sommeria [Sommeria et al., 1989] [Sommeria et al., 1991] and Solomon [Solomon et al., 1993] the eastward jet was a retrograde jet) allows us to conclude that the west/eastward character of the jet predominates over the prograde/retrograde character.

Finally, the analysis presented in this chapter points out the importance of the po-

tential vorticity distribution in understanding the occurrence and location of the vortices and meanders in laboratory and in oceanic currents.



# Chapter 5

## Numerical solution for barotropic jets over a sloping bottom: comparison to a laboratory model

For a painter, the model is the reality  
he has to reproduce through his art.  
For a physicist, it is the other way round.  
MARC FREIXA

### 5.1 Introduction

The Northern Current is the result of the general cyclonic circulation of the NW Mediterranean. Involves Modified Atlantic Water (MAW), Winter Intermediate Water (WIW) when present, Levantine Intermediate Water (LIW) down to 600 – 700 m depth and Western Mediterranean Deep Water (WMDW) down to the bottom [Conan and Millot, 1995]. At the entrance of the Gulf of Lions the current is of about 20 – 30 km wide and flows along the lower half of the continental slope, over the 1000 to 2000 m isobath approximately. Surface speeds are of 30 – 50 cm/s [Conan and Millot, 1995], decreasing with depth until 300 – 400 m depth. Far from being a stable current, the Northern Current usually displays meanders with very different length scales. Major mesoscale variability is recorded during the winter period [Alb erola et al., 1995] when the water column is less stratified, being well correlated to maximum Northern Current fluxes. The mesoscale period extends from December to May [Millot, 1987] [Taupier-Letage and Millot, 1986], whereas maximum flows are observed to occur also from December to May [Font et al., 1995] [Alb erola et al., 1995] [Conan and Millot, 1995] [Sammari et al., 1995]. Mesoscale currents in winter are clearly barotropic and may reach  $\simeq 20 \text{ cm s}^{-1}$  at depths ranging from 100 to 1100 m depth [Taupier-Letage and Millot, 1986]. The major mesoscale variability associated to the Northern Current has been found in 2 – 10 days period meanders with phase speeds of 10 – 20 km day<sup>-1</sup> [Millot, 1999]. From SST satellite images, the Northern

Current is observed to develop anticyclonic vortices on the upper part of the Gulf of Lions continental slope [Arnau, 2000]. Using similar images contemporary to the MATER HFF experiment, we observed the Northern Current as a 30 km wide current flowing over the lower (deepest) half of the continental slope (see Chapter 3). The upper slope anticyclonic vortices displayed average wavelengths from 40 km – 80 km, associated to phase speeds of  $2.3 - 8.9 \text{ cm}\cdot\text{s}^{-1}$  (i.e.  $2 - 8 \text{ km}\cdot\text{day}^{-1}$ ), leading to periods ranging from 5 – 40 days (see Chapter 3). Spectral analysis of current meter series at different depths showed energetic oscillations within the 2 – 10 days period band (see Chapter 3). During the MATER HFF experiment minimum mesoscale intensities take place at mid-depths, whereas bottom intensifications are currently recorded and associated to topographic Rossby waves (in agreement to Millot [Millot, 1985]). Nevertheless, in previous works off Marseille, deep currents have been found strongly correlated with surface flows at the 2 – 5 days band [de Madron et al., 1999].

Responding to our interest in the instabilities (eddies and meanders) observed from the field data, we performed a laboratory experiment in which the Northern Current was simulated using a source-sink flow arrangement in a rotating tank (see Chapter 4). The shallow part of the slope was acting as a local "north", whereas the deep part of the slope can be considered as a local "south". Under these criteria, the Northern Current is a so-called "westward" current. The typical instabilities observed in our barotropic experiments were that each shear layer of the jet developed a Kelvin-Helmholtz-like instability, associated to a weak (topographically induced) Rossby wave. In high speed westward currents ( $Ro > 0.11$ ) meandering was located at the edges of the jet. Contrarily to the observations in eastward flows, in westward jets the core of the current was not meandering.

The differences between eastward and westward jets were explained according to migration of potential vorticity (Chapter 4): in westward jets potential vorticity gradients (where topographic Rossby waves tend to locate, causing jet meandering) are observed at the outer parts of the current, whereas in eastward jets the potential vorticity gradients are placed at the centre of the jet. These differences were also discussed in terms of potential vorticity conservation, i.e. in terms of the balance existing between the gain/loss of relative vorticity due to velocity shear and the gain/loss of topographically induced vorticity due to stretching/squeezing of water parcels. The balance is different in each case, leading to the differences observed in experimental eastward/westward jets (Chapter 4).

In eastward currents, the tendency of potential vorticity discontinuities of occurring near the centre of the jet explains that no motion is observed over the upper-slope. Oppositely, the broadening tendency of westward jets allows the current to reach the upper-slope, triggering a (topographic) Rossby wave over the shelf break which is in counter-phase with the wave associated to the jet's negative shear layer (Chapter 4).

In our laboratory simulations of westward and eastward currents, low speed flows presented the typical instabilities observed to occur in shear layers, i.e. eddies were generated at each side of the jet, like Kelvin-Helmholtz billows, with the same vorticity as the shear layer sign. This similarity suggested that low speed flows were less affected by topographic gains/losses of relative vorticity. Thus, topographic Rossby waves were too weak to produce any difference in eastward/westward flows.

The laboratory simulations revealed the appearance of the upper-slope wave, which was not reported in previous works. The first objective of the numerical simulations will be to reproduce the laboratory experiments, which will allow to cross-validate both numerical and laboratory models and it will also allow to validate the above-mentioned results. Secondly, the use of a numerical model will allow to study the onset of instabilities, and to gain insight in the generation mechanisms of the upper slope Rossby wave in westward jets. Moreover, the numerical model will also allow to study the dependence of the results on the velocity jet profile, among other variables. Finally, with this numerical flow simulation we are returning to oceanic scales, obtaining magnitudes of variables (wavelength, phase speed, vorticity, etc) which can be directly compared to oceanic observations.

## 5.2 Numerical model

### 5.2.1 Equations

The model used in the present work is a two-dimensional version of the Princeton Ocean Model (POM) developed by Blumberg and Mellor [Blumberg and Mellor, 1987], which was available in our laboratory (LIM/UPC). This bottom-following sigma-coordinate model solves the primitive equations with a finite difference scheme. In our interest of reproducing our laboratory conditions, we are using a simplified version of POM to simulate a homogeneous fluid in a barotropic flow situation.

The equations solved for our case are:

$$\frac{\partial \eta}{\partial t} + \frac{\partial UD}{\partial x} + \frac{\partial VD}{\partial y} = 0 \quad (5.1)$$

$$\frac{\partial UD}{\partial t} + \frac{\partial U^2 D}{\partial x} + \frac{\partial UV D}{\partial y} - F_x - fVD + gD \frac{\partial \eta}{\partial x} = -\tau_w + \tau_b \quad (5.2)$$

$$\frac{\partial VD}{\partial t} + \frac{\partial UV D}{\partial x} + \frac{\partial V^2 D}{\partial y} - F_y + fUD + gD \frac{\partial \eta}{\partial y} = -\tau_w + \tau_b \quad (5.3)$$

where  $D \equiv H + \eta$ , being  $H(x, y)$  the bottom topography and  $\eta(x, y, t)$  the free surface elevation;  $U$  and  $V$  are the horizontal velocity components in  $x$  and  $y$  direction, respectively,  $f$  the Coriolis parameter,  $g$  the gravitational acceleration,  $\tau_w$  the wind stress,  $\tau_b$  bottom friction, and  $F_x$  and  $F_y$  the horizontal viscosity terms defined as:

$$F_x = \frac{\partial}{\partial x} \left[ H 2A_M \frac{\partial U}{\partial x} \right] + \frac{\partial}{\partial y} \left[ H A_M \left( \frac{\partial U}{\partial y} + \frac{\partial V}{\partial x} \right) \right] \quad (5.4)$$

$$F_y = \frac{\partial}{\partial y} \left[ H 2A_M \frac{\partial V}{\partial y} \right] + \frac{\partial}{\partial x} \left[ H A_M \left( \frac{\partial U}{\partial y} + \frac{\partial V}{\partial x} \right) \right] \quad (5.5)$$

where  $A_M$  is the horizontal viscosity coefficient.

These equations are solved explicitly using an ‘Arakawa C’ differencing scheme.

## 5.2.2 Configuration

The grid, the initial conditions and the boundary conditions have been chosen in order to maintain dynamic similarity between the laboratory experiments and the oceanic case.

The non-dimensional numbers which are relevant in our case (see Chapter 4 for a formal derivation of the problem) are: (i) the *Rossby number*  $Ro = \frac{U}{fL}$ , with  $U$  being the maximum speed of the jet,  $f$  the Coriolis parameter and  $L$  the width of the current; (ii) the *vertical Ekman number*  $E_v = \frac{\nu}{fD^2}$  where  $\nu$  is the viscosity and  $D$  is the water depth at the deepest part of the jet; (iii) the *geometric factor*  $\delta_1 = \frac{D}{L}$ , and (iv) the *depth ratio*  $\delta_2 = \frac{H}{D}$ , where  $H$  is the elevation of the bottom slope at the inner edge of the jet (i.e. over the mid-slope). In the laboratory experiments only three of these non-dimensional numbers were conserved (see Chapter 4):  $\delta_2 = 0.45$ ,  $Ro = 0.04 - 0.25$ , and  $E_v \sim O(10^{-5})$ . The geometric factor  $\delta_1$  could not be adjusted to oceanic conditions due to the restrictions of our laboratory facility dimensions; the difference was of one order of magnitude since  $\delta_1(lab) \simeq 1$  whereas  $\delta_1(ocean) \simeq 0.1$ . Using an oceanographic numerical model like POM we are dealing with oceanographic scales, therefore all non-dimensional numbers are considered. Furthermore, this will allow us to discuss about the importance of the geometric non-dimensional number in our laboratory experiments.

In order to obtain similarity with the rotating tank experiments we chose a rectangular domain simulating a periodic canal. Therefore, upper and lower boundaries are closed (free-slip conditions) whereas lateral boundaries are open and have periodic conditions. The horizontal grid has 60 x 90 nodes with a resolution of 1.6 km, which is convenient to solve the oceanographic structures we are interested in. Sensitivity tests show that different resolutions (different grid sizes) do not vary the resulting patterns. In terms of bathymetry, we consider a simplified topography of the Gulf of Lions consisting of four distinctive regions: (i) a flat continental shelf 200 m deep; (ii) the upper half of the continental slope (from 200 to 1100 m depth) with no forced flow; (iii) the lower (deeper) half of the continental slope (from 1100 to 2000 m depth) over which the Northern Current flows; (iv) a flat abyssal plain at 2000 m depth, again with no forced flow. In view of the fact that the laboratory flux was obtained by a continuous pumping of fluid through a source/sink mechanism placed at the bottom of the topography (see Chapter 4), bottom friction in the numerical model was chosen to be zero.

As initial conditions, an initial velocity profile is prescribed in the whole domain (Fig. 5.1). This flow pretends to simulate the laboratory conditions in which the laboratory flux was obtained, i.e. using continuous pumping of fluid through a source/sink mechanism. We shall use different initial velocity profiles for different numerical runs. A weak random (in direction) wind stress field equivalent to a  $0.7 \text{ m s}^{-1}$  wind is imposed at each time step to destabilize the system. This forcing does not generate any particular circulation pattern, neither supplies any significant amount of energy to the system. For very low forcing, the time needed for instability to generate increases proportionally, but the resulting flow patterns do not vary.

The POM is an explicit model and therefore has large numerical diffusivity, which might generate some problems when trying to define a particular horizontal viscosity value.

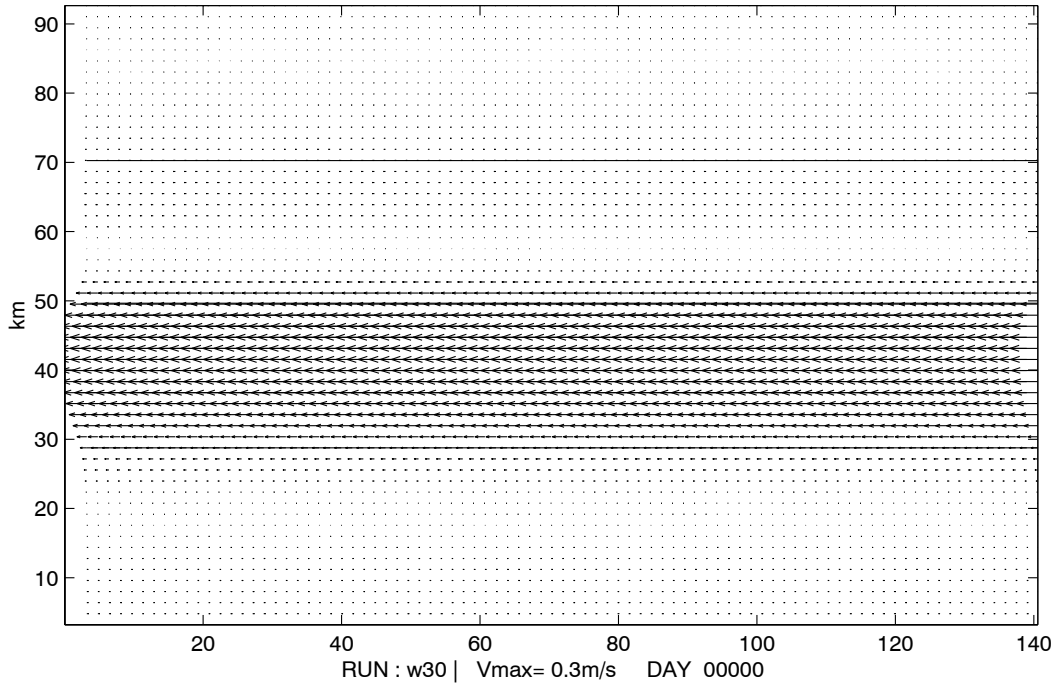


Figure 5.1: Initial velocity field imposed over the computational domain. The current is forced over the lower part of the continental slope, from 30 to 50 km in up-slope direction. In this case it represents a westward jet of maximum speed of  $30 \text{ cm s}^{-1}$ . The shelf break is indicated as a bold line.

In our case we use the turbulent eddy viscosity  $\nu = 0.01 \text{ m}^2\text{s}^{-1}$  to maintain dynamic similarity, but sensitivity tests demonstrate (data not shown) that numerical diffusivity in our configuration is of the order of  $1 \text{ m}^2\text{s}^{-1}$ . Nevertheless, the same sensitivity tests demonstrate that the model is not sensitive to the horizontal viscosity value; the only difference relies in that for large viscosities there is a delay in the instability onset.

Numerical results successfully reproduce laboratory experiments during a given period of time. Some time after the instabilities are formed (i.e. after the ‘stable’ state observed in the laboratory is successfully reproduced) the flow structures become noisy. As commented above, random atmospheric noise was imposed at each time step in order to destabilize the flow. Although it was verified that this atmospheric forcing did not cause any particular flow pattern nor did affect the typical formation of instabilities, it is pointed out here as the responsible of these observations.

### 5.2.3 Experimental cases

The first goal of this chapter is to reproduce the laboratory conditions in order to cross-validate the laboratory model and the numerical model. Thus, following the laboratory experimental cases, the variables will be the velocity speed (ranging from 20 to  $60 \text{ cm s}^{-1}$  in order to cover a convenient  $Ro$  number range) and the flow direction (see Section 5.3).

Furthermore, we shall take advantage of the numerical model to explore other flow conditions than those considered in the laboratory experiments. In order to study the role of the position of the jet over the continental slope, the current will be forced to flow over the mid-slope and over the upper-half of the slope (Section 5.4.1). Moreover, the jet width will be changed (Section 5.4.2) and the velocity profile will be modified (Section 5.4.3), in order to study how these variables might modify the resulting patterns. These experiments will produce a deeper insight and a better understanding of the dynamic processes involved.

## 5.3 Simulation of the laboratory experiments

### 5.3.1 Velocity profile

As it is well known, shear instabilities are sensitive to the velocity profile. In order to reproduce laboratory conditions we should impose the primary velocity profile, i.e. the velocity profile corresponding to the undisturbed flow. As it was discussed in Chapter 4, the primary profile cannot be obtained in the laboratory because the laboratory conditions are not ideal conditions. We consider as the best approximation to the ideal primary flow the averaged velocity profile of the slowest (less unstable) jet generated in the laboratory experiments.

For this reason, the laboratory profile used to initialize the numerical model is obtained from the weakest experimental westward flow ( $Q = 15 \text{ lh}^{-1}$ ). The velocity profile obtained in one frame has been averaged over the whole domain in the azimuthal direction (i.e. over  $\pi$  radians) and in time (over 20 s). The flow is purely azimuthal (Fig. 5.2).

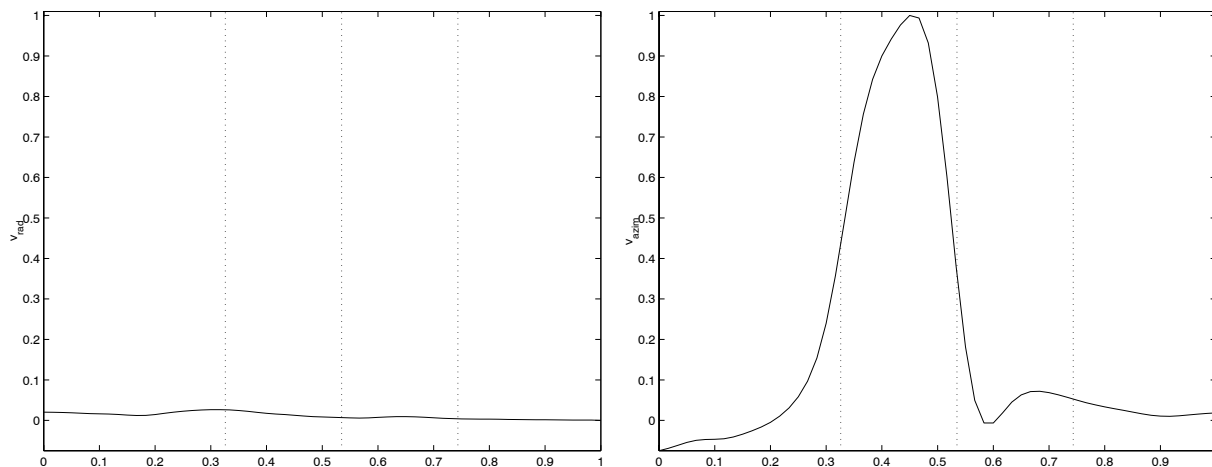


Figure 5.2: Radial (left) and azimuthal (right) velocity profiles (normalized over the maximum azimuthal velocity and plotted in arbitrary units in radial across-slope direction) of a westward jet over sloping bottom obtained from the slower experimental laboratory jet ( $Q = 15 \text{ lh}^{-1}$ ). Vertical broken lines indicate (from left to right) the deepest limit of the slope, the mid-slope, and the shelf break.

We considered this flow as the most representative of the primary (undisturbed) flow. For this reason, we have used the normalized azimuthal velocity profile to initialize all the numerical runs (for both eastward and westward flows) devoted to reproduce the laboratory experiments.

### 5.3.2 General results using laboratory flow profiles

Numerical results show good qualitative agreement with laboratory results. Similarly to the laboratory results presented in Chapter 4, numerical results also show two different flow regimes for both eastward and westward currents. The main results found in both laboratory and numerical experiments can be summarized as follows.

In all the results presented in this chapter the relative vorticity and stream function are calculated using a finite-difference scheme. In the case of the stream function the computational method considers a zero-value at one boundary of the domain and integrates in the direction normal to that boundary. For clarification of results, the relative vorticity and potential vorticity contours (except those corresponding to the relative vorticity of a westward jet of  $20 \text{ cm s}^{-1}$ ) have been smoothed using a moving-average window. The vorticity values are not affected by this smoothing.

Regime I (i.e. low speed) jets in both eastward and westward flow cases develop only Kelvin-Helmholtz-type instabilities, whereas Rossby waves remain too weak to be noticed (see Fig. 5.3 for westward currents and Fig. 5.4 for eastward currents). The main difference between laboratory and numerical results yields in the jet's positive shear layer of Regime I westward jets, which in numerical results does not develop any instability. The reason might be that the velocity gradient of the positive vorticity shear layer of the jet is underestimated; the averaged profile obtained from the laboratory experiments might be smoother than the primary (undisturbed) flow.

The limit between Regime I and Regime II westward jets is at  $Ro = 0.10$ , in agreement with laboratory results (see Chapter 4). Westward currents in Regime II (i.e. high speed;  $Ro > 0.1$ ) flows lead to a Rossby wave placed over the shelf break, in counter-phase with the Rossby wave associated to the negative shear layer of the jet (Fig. 5.5). The former wave generates a chain of vortices of alternating sign, whereas the latter causes the jet to meander over the mid-slope. Therefore, westward currents present instabilities associated to meandering over the mid slope and vortices over the upper slope, in good agreement with the laboratory results (see Chapter 4).

In Regime II eastward flows, Rossby waves concentrate near the centre of the jet, separating instabilities of both shear layers, and causing the centre of the jet to meander. No instabilities are generated over the upper slope (Fig. 5.6). The limit between Regime I and Regime II eastward jets is at  $Ro = 0.2$ , in rough agreement with laboratory results (see Chapter 4).

The differences between eastward and westward currents were explained in Chapter 4 in terms of migration of potential vorticity, in accordance to explanations given in past studies of jets on a beta-plane (e.g. [Sommeria et al., 1991] and [Marcus and Lee, 1998]). These authors observed that Rossby waves tend to occur at potential vorticity gradients,

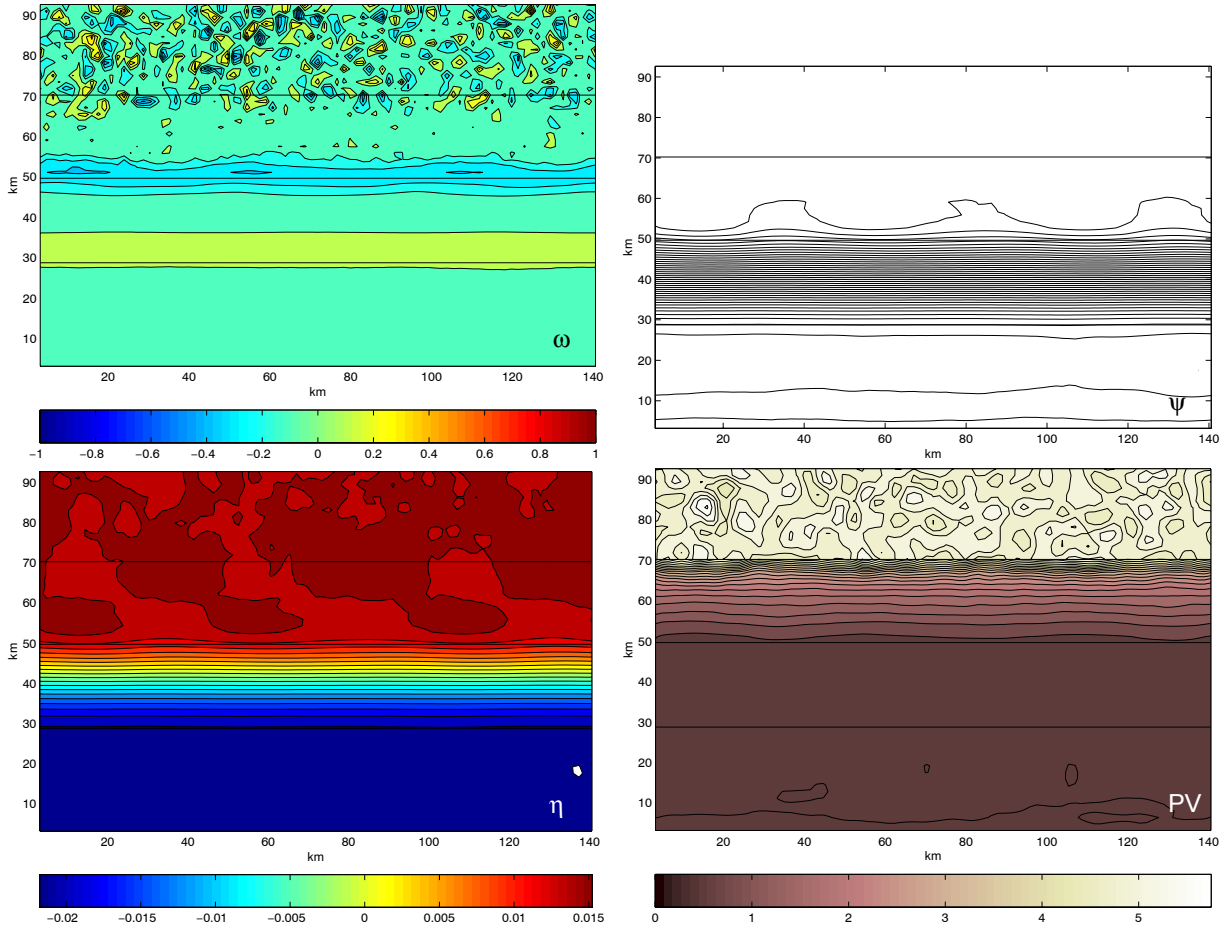


Figure 5.3: From left to right and from top to bottom: Relative vorticity (in  $s^{-1}$ ), isolines are separated by  $0.1 \cdot e^{-4} s^{-1}$ ; streamlines; free surface elevation (in m); and potential vorticity (in  $s^{-1}$ ) for a *westward* jet of initial maximum velocity of  $0.20 \text{ cm} \cdot s^{-1}$  ( $Ro = U/fL = 0.10$ ) (day 37).

which in westward currents locate at the edges of the jet, whereas the core of the current and the vortices associated remain in a region of constant potential vorticity, thus favouring mixing between positive and negative shear layers of the jet. In eastward currents, potential vorticity discontinuities tend to move towards the center of the jet, causing a strong gradient in potential vorticity in the jet core, where Rossby waves place and cause the current to meander. Moreover, the PV gradient may prevent mixing to occur between instabilities of both shear layers of the jet.

Instability wavelength, phase speed and vorticity increase for increasing  $Ro$  values, in agreement with laboratory results. Instability phase speeds are detailed in Section 5.3.3. Details of westward jets and their application to the Northern Current case are in Section 5.5.

The POM gives relevant information on the free-surface elevation field. Free-surface



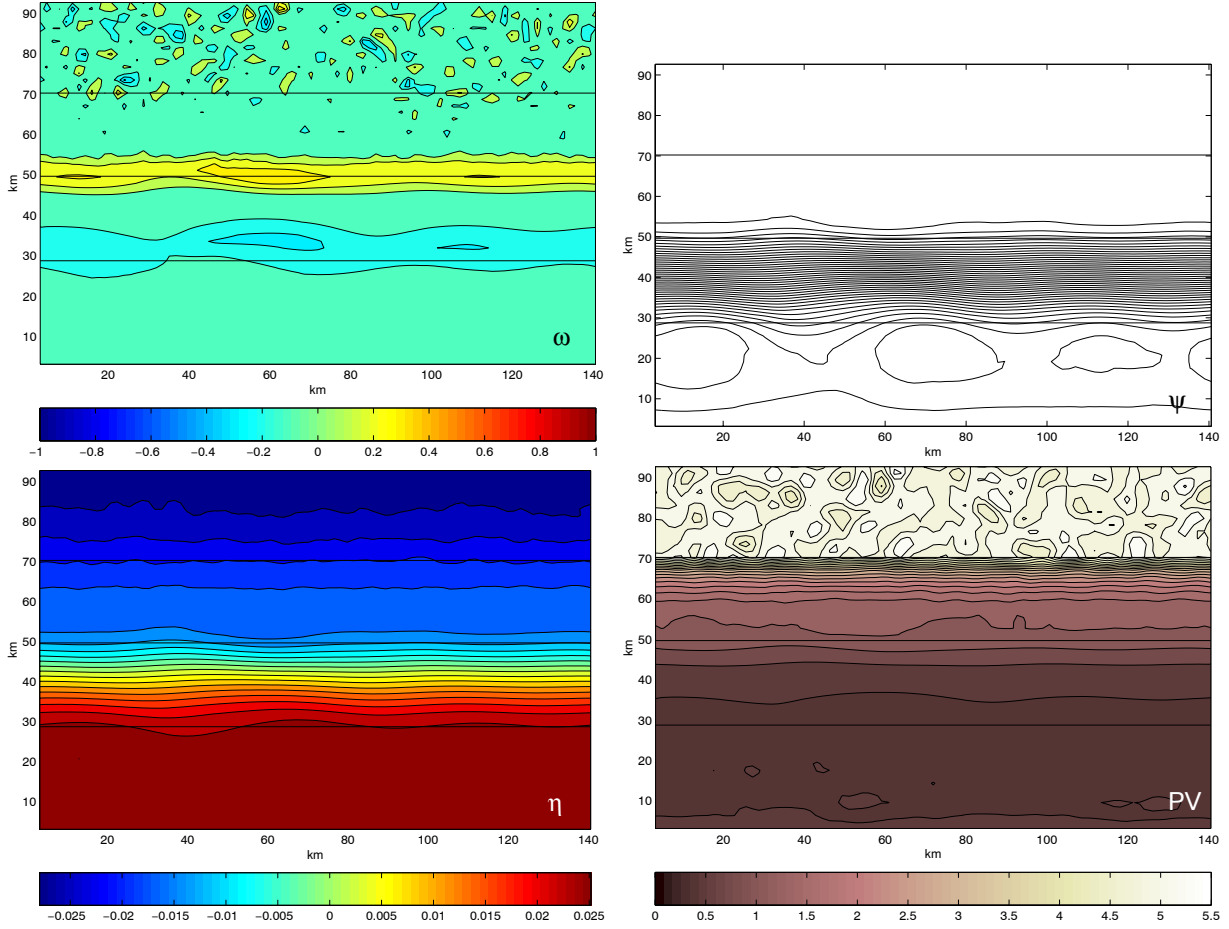


Figure 5.4: From left to right and from top to bottom: Relative vorticity (in  $s^{-1}$ ), isolines are separated by  $0.1 \cdot e^{-4} s^{-1}$ ; streamlines; free surface elevation (in m); and potential vorticity (in  $s^{-1}$ ) for an *eastward* jet of initial maximum velocity of  $0.22 \text{ cm} \cdot s^{-1}$  ( $Ro = U/fL = 0.11$ ) (day 30).

elevation reveals the meandering pattern at the core of the current in Regime II eastward jets (Fig. 5.6). In Regime II westward currents (Fig. 5.5) it reveals the meandering tendency at the edges of the current (i.e. over the mid-slope). In agreement with streamlines, they both show that cyclonic vortices over the mid-slope are associated to the crests of the jet meander whereas anticyclones over the mid-slope are associated to troughs. Moreover, the upper-slope Rossby wave vortices are associated to free-surface elevation anomalies of the order of 1 cm (from the center to the edge of each vortex). Positive anomalies are associated to cyclones and negative anomalies to anticyclones.

In summary, we may conclude that numerical simulations are in good agreement with the laboratory results. Thus, we can take advantage of this numerical configuration to continue further investigations, as we will discuss in next sections.

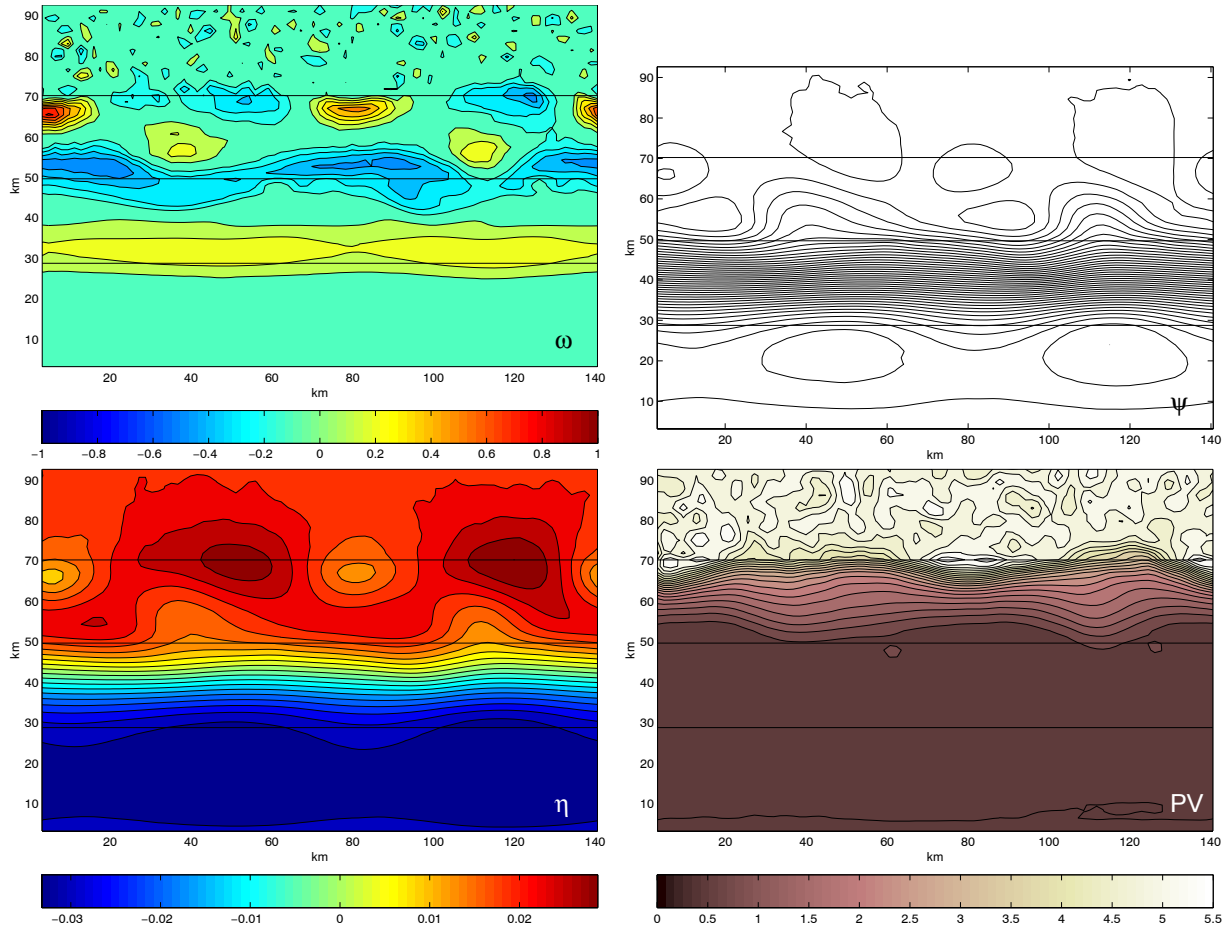


Figure 5.5: From left to right and from top to bottom: Relative vorticity (in  $s^{-1}$ ), isolines are separated by  $0.1 \cdot e^{-4} s^{-1}$ ; streamlines; free surface elevation (in m); and potential vorticity (in  $s^{-1}$ ) for a *westward* jet of initial maximum velocity of  $0.30 \text{ cm} \cdot s^{-1}$  ( $Ro = U/fL = 0.15$ ) (day 24).

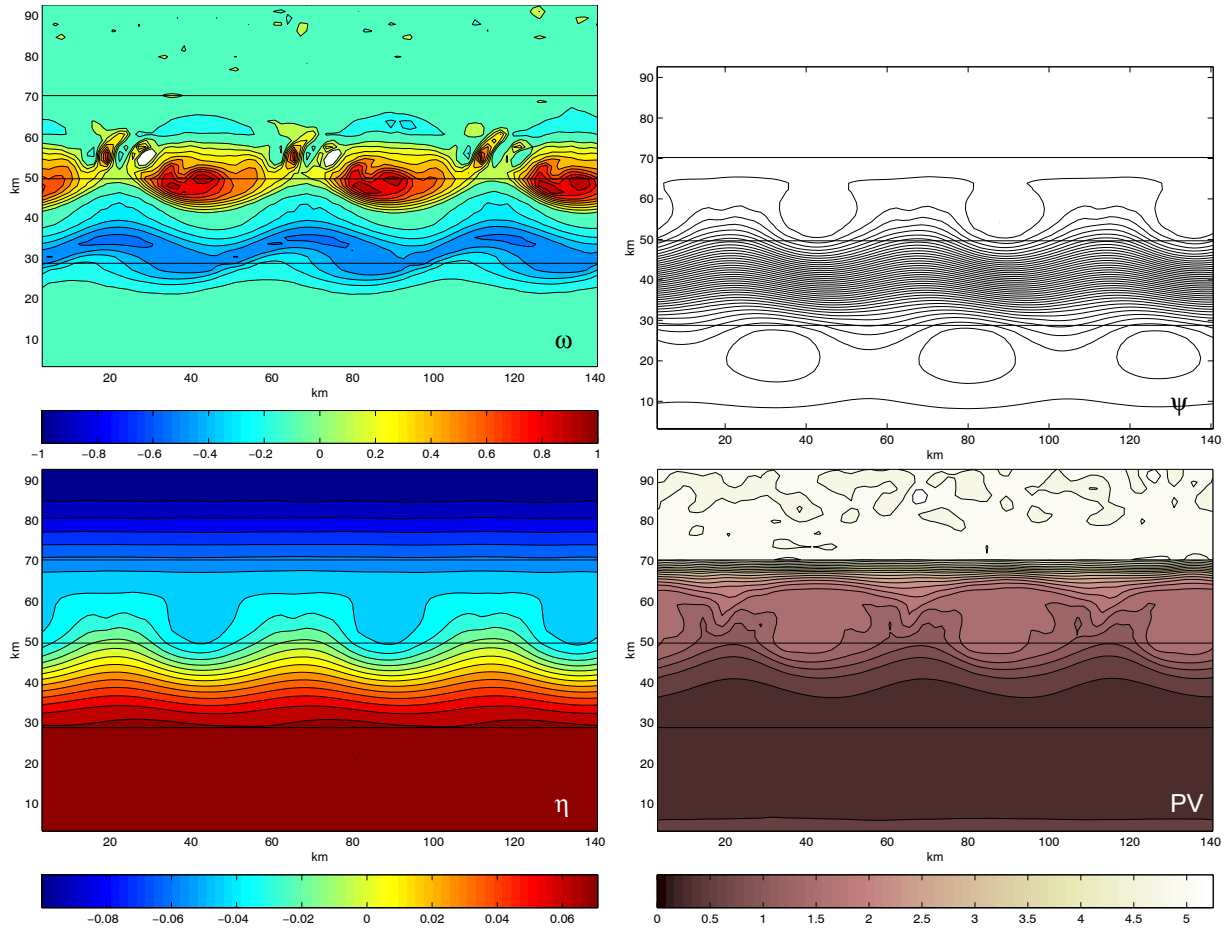


Figure 5.6: From left to right and from top to bottom: Relative vorticity (in  $\text{s}^{-1}$ ), isolines are separated by  $0.1 \times 10^{-4} \text{ s}^{-1}$ ; streamlines; free surface elevation (in m); and potential vorticity (in  $\text{s}^{-1}$ ) for an *eastward* jet of initial maximum velocity of  $0.58 \text{ cm} \cdot \text{s}^{-1}$  ( $\text{Ro} = U/\text{fL} = 0.29$ ) (day 11).

### 5.3.3 Onset of jet instabilities

In laboratory experiments we discussed the ‘stable’ state of the currents of different  $Ro$  numbers. However, we did not study the initial states, i.e. the onset of instabilities. In this section we take advantage of the numerical model to study how instabilities generate and grow. From an oceanographic point of view this subject is of main interest because it may help to understand oceanic situations in which instabilities are not fully developed. The formation of the shelf-break Rossby wave in Regime II westward currents is also discussed.

#### (a) Westward jets: Regime I

In Regime I westward jets, the negative shear layer develop negative vorticity vortices forming an eye-like pattern. While instabilities grow, they move in the same direction as the main flow, with a phase speed of 85 – 90 % of the maximum flow velocity. For example, a current flowing with a maximum speed of  $20 \text{ cm s}^{-1}$  develop shear instabilities travelling in westward direction at  $17.4 \text{ cms}^{-1}$  ( $15 \text{ km day}^{-1}$ ), i.e. a phase speed of 87 % of the maximum flow speed. These values are in agreement with laboratory observations.

Streamlines show these vortices are responsible of a slight meandering of the inner (shallower) edge of the jet (i.e. over the mid-slope) with a mean wavelength of 40 km (see Fig. 5.3). The positive shear layer is not observed to be unstable, contrarily to what was observed in the laboratory experiments for similar flow regimes, in which both shear layers where unstable. This result suggests that the relative vorticity gradient of the positive shear layer of the jet resulting from the averaged laboratory velocity profile used to initialize the model might be underestimated.

#### (b) Westward jets: Regime II

In Regime II westward jets, the negative shear layer is the first to develop instabilities, as was also observed in Regime I westward flows. Also similarly to Regime I westward jets, the negative shear layer becomes unstable while instabilities move westwards, at  $\sim 80$  % of the maximum flow speed —a westward jet flowing at maximum flow speed of  $30 \text{ cm s}^{-1}$  negative shear layer vortices move westwards at a speed of  $23.2 \text{ cms}^{-1}$  ( $20 \text{ km day}^{-1}$ ) (Fig. 5.7).

On day 18 (Fig. 5.7), a vortex pair of negative and positive vorticity sign appears close to the shelf break. This is apparently due to an increase in size of an anticyclone from the negative shear layer of the jet, which would be able to perturb the uppermost slope inducing a secondary instability. Both instabilities, i.e. those from the negative shear layer of the jet and those over the shelf break, seem to interact and grow until day 25 (Fig. 5.7) when they develop an ‘stable’ state. This ‘stable’ state is the situation reported in the laboratory observations (Chapter 4). The shelf-break wave and the mid-slope wave are in counter-phase (i.e. shifted by  $\pi$  rad), which is in agreement with the laboratory results. Both layers of instabilities (i.e. those from the negative shear layer of the jet and those over the shelf break) move westwards at about  $23.2 \text{ km day}^{-1}$  (i.e. with a phase speed of 80 % of the maximum flow velocity).

In the numerical simulations the positive shear layer of the jet becomes unstable only towards the end of the process (i.e. on day 25). When this occurs, the positive vortices from the positive shear layer are in phase with the negative vortices from the negative shear layer of the jet (see Fig. 5.7).

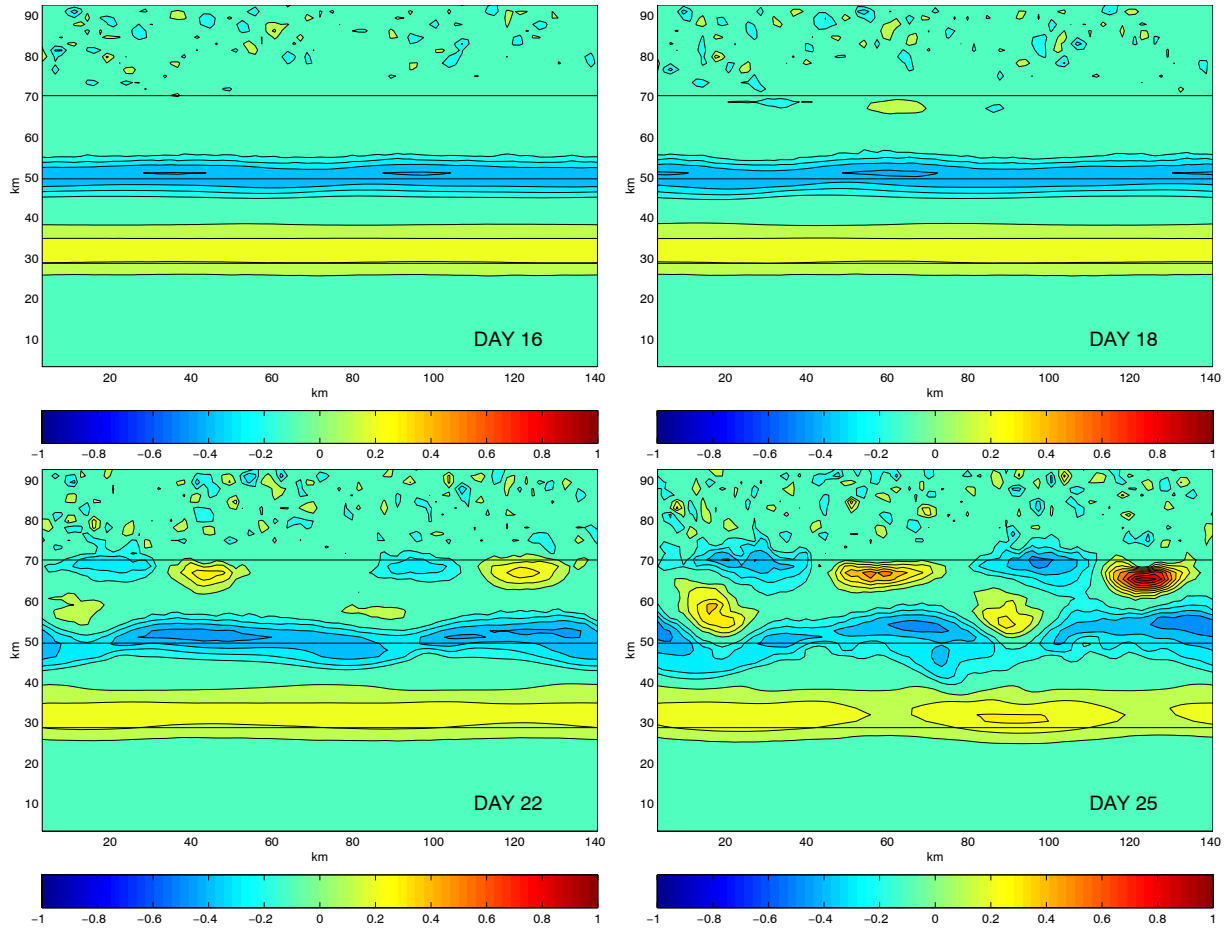


Figure 5.7: Relative vorticity of a *westward* jet of maximum flow speed of  $30 \text{ cm s}^{-1}$  from day 16 to day 25. Note that spacing between frames is irregular. Separation between isolines is  $0.1 \times 10^{-4} \text{ s}^{-1}$ .

### (c) Eastward jets: Regime I

Numerical experiments reveal that in Regime I eastward jets, instabilities from each shear layer of the jet locate in counter-phase. Numerical experiment also show that in this type of flows, instabilities can grow in two different ways.

For low speed flows (e.g. for a jet flowing at maximum speed of  $22 \text{ cm s}^{-1}$  in Fig. 5.8 the instabilities start first in the negative shear layer, developing later in the positive shear layer. Instabilities in both layers of the jet originate and grow while travelling in the same direction of the mean flow. The vortices in the negative shear layer are in counter-phase

with the vortices from the positive shear layer. They propagate in pairs at about  $8.7 \text{ cm s}^{-1}$  ( $7.5 \text{ km day}^{-1}$ ), later evolving into dipolar structures (see e.g. day 37 in Fig. 5.8). Apparently, the phase speed of the instability is not modified when it turns into a dipole, remaining at  $8.7 \text{ cm s}^{-1}$ , which represents about 40 % of the maximum speed of the jet.

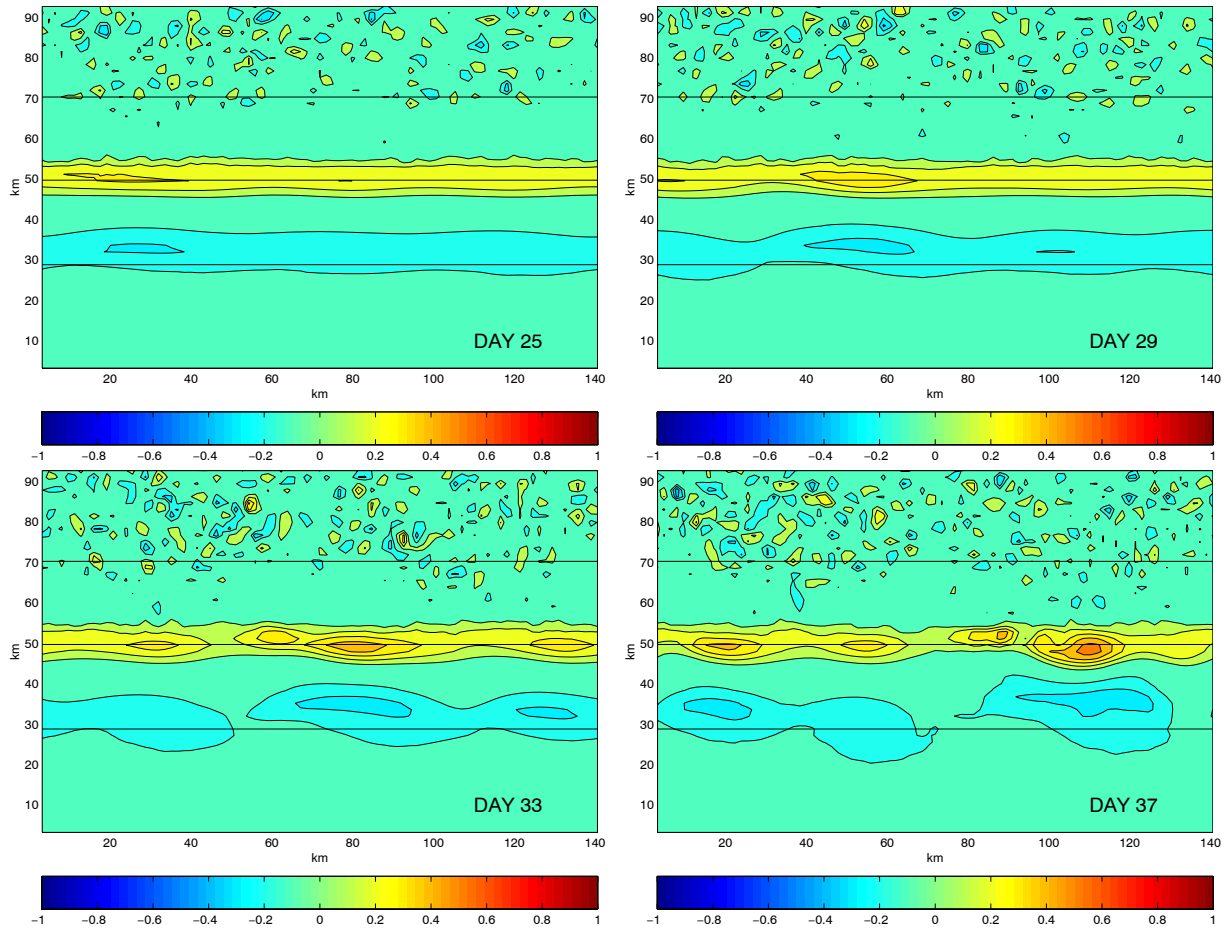


Figure 5.8: Relative vorticity of an *eastward* jet of maximum flow speed of  $22 \text{ cm s}^{-1}$ , from day 25 to day 37. Separation between isolines is  $0.1 \times 10^{-4} \text{ s}^{-1}$ .

For increasing flow rates, but still in Regime I flows (i.e. instabilities as cats-eye-like patterns, with no clear meandering at the centre of the jet), the positive shear layer of the jet becomes unstable in first place. In this case, instabilities do not propagate; instead, they grow while staying at a more or less fixed location (see Fig. 5.9). Later on, the negative shear layer of the jet gets also becomes unstable. Again, instabilities from both shear layers are in counter-phase, forming dipolar structures, which start propagating in eastward direction at a speed of  $8.7 \text{ cm s}^{-1}$  ( $7.5 \text{ km day}^{-1}$ ), i.e. with a phase speed of 40 % of the maximum flow velocity.

Vortex motions seem to occur as soon as the negative shear layer of the jet gets unstable and forms the dipole-like disposition. Thus, the dipole-like structure would be

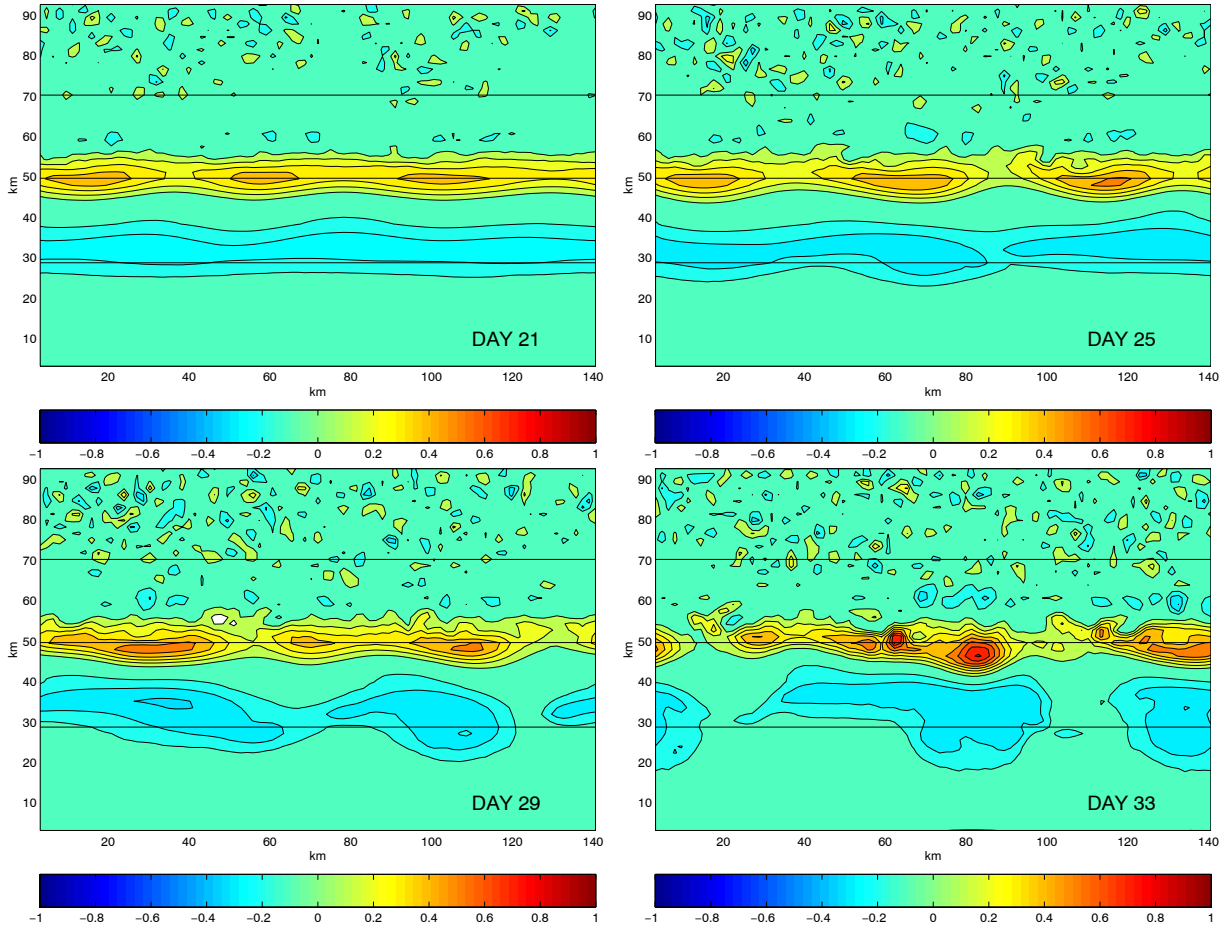


Figure 5.9: Relative vorticity of an eastward jet of maximum flow speed of  $30 \text{ cm s}^{-1}$ , from day 21 to day 33. Separation between isolines is  $0.1 \times 10^{-4} \text{ s}^{-1}$ .

responsible of the instability displacement. The phase speed of the instabilities at this point is more reduced in the numerical experiments (40 % of the maximum flow speed) than in the laboratory experiments (65 – 75 % of the maximum flow velocity). The reason for this remains still unclear to us.

In laboratory experiments we assume we could not distinguish between these two types of instability generation because we focussed on the ‘stable’ state of the jet.

#### (d) Eastward jets: Regime II

In Regime II eastward currents, shear layer instabilities locate in alternate disposition, i.e. maximum positive vorticity values from each shear layer are in phase, and the same occurs for negative vorticity maxima.

Eastward flows of Regime II develop instabilities first in the positive shear layer of the jet. Positive vortices seem to fold up, squeezing, while they grow in place. Instabilities from the negative shear layer of the jet appear later on, in phase with positive shear layer

instabilities (Fig. 5.6). This disposition enhances the meandering pattern at the centre of the jet. Instabilities do not propagate, in agreement with observations in laboratory experiments (Chapter 4).

Only in late stages of high speed flows (e.g.  $58 \text{ cm s}^{-1}$ ) instabilities can degenerate into a string of dipoles, which in this case are able to propagate eastwards at a speed of about  $23.2 \text{ cm s}^{-1}$  ( $20 \text{ km day}^{-1}$ ) (results not shown), i.e. with a phase speed 40 % to that of the maximum flow speed.

## 5.4 Further investigations

In this section we want to take advantage of our numerical set-up to further study the influence of several jet features on the development of instabilities. The questions we address in this section are hard to treat in the laboratory, mainly due to practical reasons.

### 5.4.1 Influence of the location of the jet over the slope

We are interested in studying the role of the relative location of the current over the continental slope. A reduction of the water depth over which the current flows will allow to study the influence of an increase in the non-dimensional value  $\delta_2$  on the instabilities observed. For this reason we have performed additional model runs in which the westward jet (initially flowing over the lower half of the slope) is now prescribed (i) over the mid-slope and (ii) over the upper half of the slope (Fig. 5.10).

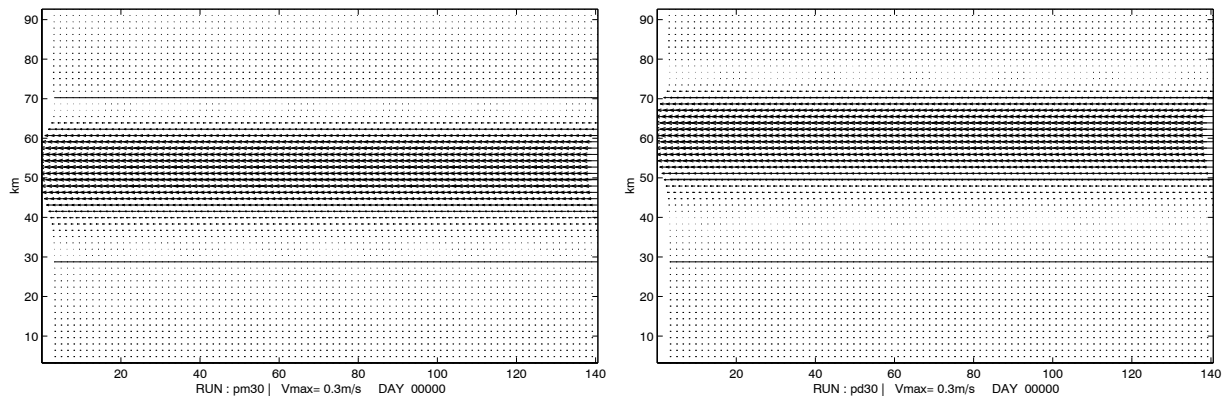


Figure 5.10: Initial flow field for a *westward* jet of maximum flow speed of  $30 \text{ cm s}^{-1}$ , flowing over the mid continental slope (left) and the upper half of the slope (right).

When the current flows over the mid slope, the onset of instabilities occurs later than when the current flows over the lower half of the slope. The shelf-break Rossby wave appears, and all mesoscale motion concentrates between the inner (shallower) edge of the current and the shelf break. Instability wavelenghts reduce in size. When the current flows over the upper half of the slope the current does not destabilize (Fig. 5.11). These results indicate an stabilizing effect of the reduction of water depth over which the current flows.



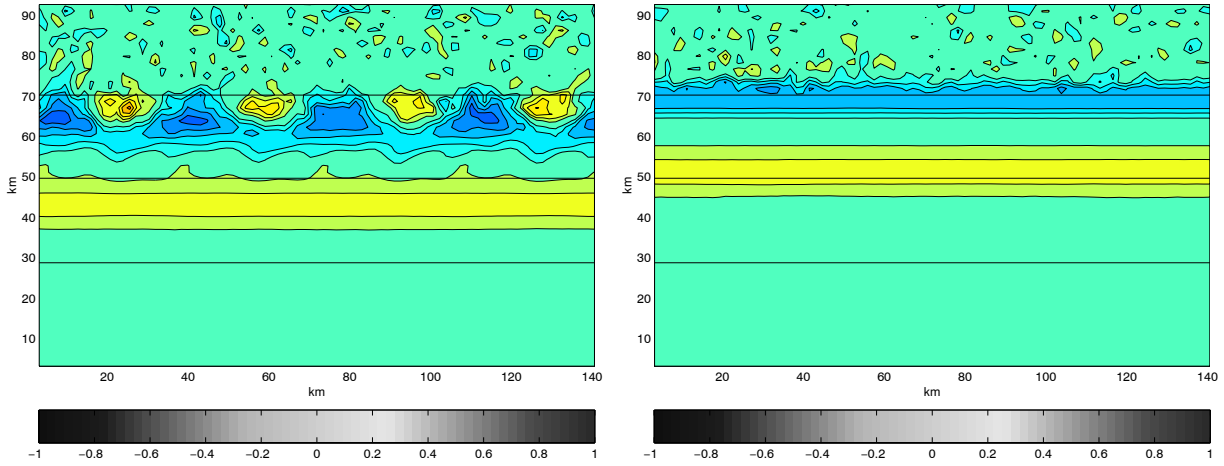


Figure 5.11: Relative vorticity (day 40) of a *westward* jet of maximum flow speed of  $30 \text{ cm s}^{-1}$ , flowing over the mid continental slope (left) and the upper half of the slope (right). Separation between isolines is  $0.1 \times 10^{-4} \text{ s}^{-1}$ .

### 5.4.2 Influence of the jet width

In order to study the role of the current width, we have carried out model runs in which this variable is reduced and increased by a factor of 2. The initial forcing in both cases is shown in Fig. 5.12. Note that in these experiments not only the Rossby number but also  $\delta_2$  varies from the laboratory cases.

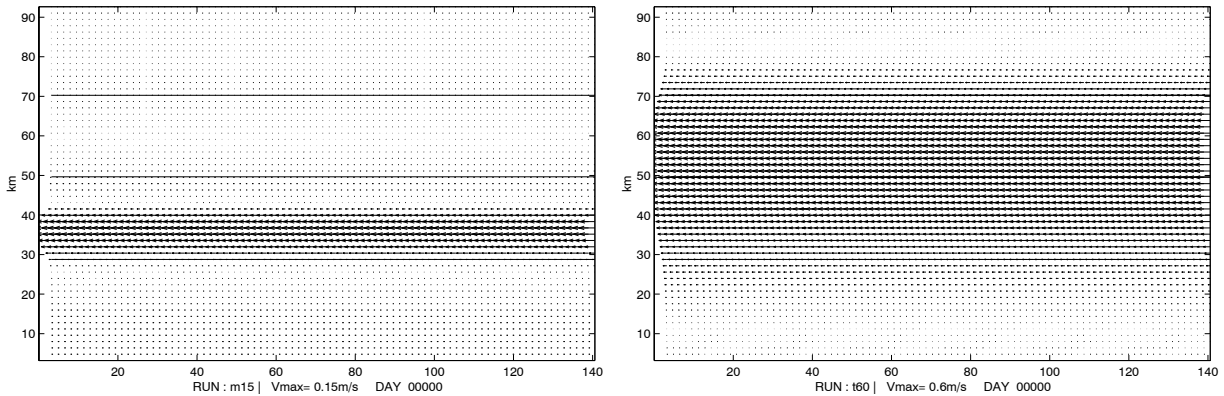


Figure 5.12: Initial flow field for a *westward* jet of maximum flow speed of  $15 \text{ cm s}^{-1}$  flowing over the deepest 1/4 of the slope (left) and for a *westward* jet of maximum flow speed of  $60 \text{ cm s}^{-1}$  flowing over the whole continental slope (right).

In the first experiment, the jet is imposed over the deepest part of the slope, from 1550 m – 2000 m depth. The shelf-break Rossby wave still appears but no other instability appears between the negative shear layer and the shelf-break (Fig. 5.13). These observations reveal the role of the shelf-break in ‘trapping’ the topographic Rossby waves. Shear

instabilities reduce in wavelength and phase speed, contrarily to what could be expected in face of results obtained for an increasing water depth (see Section 5.4.1). Results are similar for flow speeds of  $30 \text{ cm s}^{-1}$  ( $Ro = 0.3$ ) and  $15 \text{ cm s}^{-1}$  ( $Ro = 0.15$ ). We conclude that the width of the jet is responsible for the wavelength reduction and that this effect dominates over the depth increase.

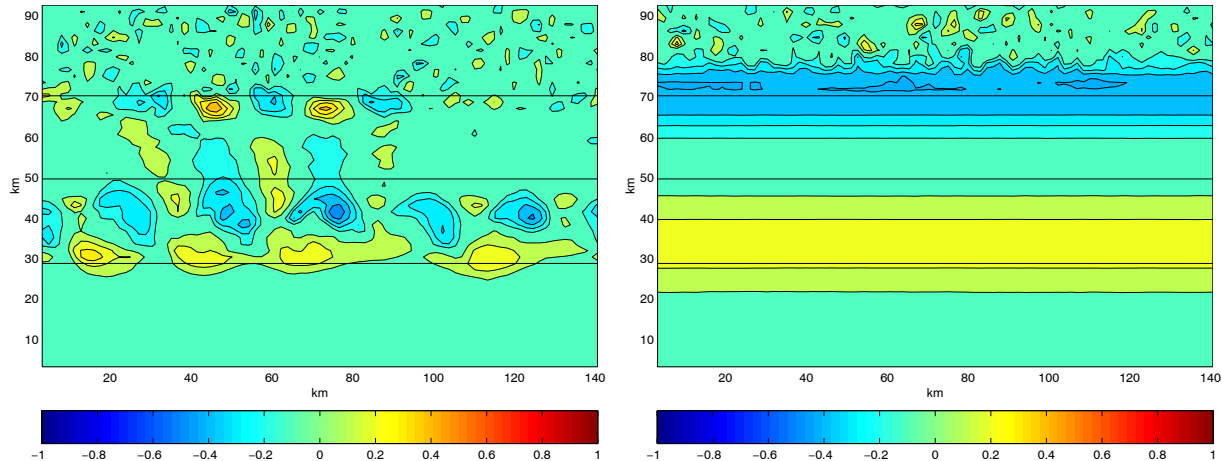


Figure 5.13: Left: Relative vorticity (day 20) of a *westward* jet of maximum flow speed of  $15 \text{ cm s}^{-1}$  flowing over the deepest 1/4 of the slope. Right: Relative vorticity (day 30) of a *westward* jet of maximum flow speed of  $60 \text{ cm s}^{-1}$  flowing over the whole continental slope (right). Separation between isolines is  $0.1 \times 10^{-4} \text{ s}^{-1}$ .

In our second experiment, the jet flows over the whole continental slope –i.e. over the 200m – 2000m deep isobaths. The current is hardly unstable (Fig. 5.13), revealing that in this case, the stabilizing effect of the reduced water depth prevails.

### 5.4.3 Influence of the velocity profile

In this section we briefly discuss the sensitivity of instabilities to the initial velocity profile introduced in the numerical model. To better assess the sensitivity of results to the velocity profile we use simplified flow distributions, like typical symmetric linear and gaussian profiles (Fig. 5.14).

Symmetric gaussian velocity profiles develop highly disorganized structures. Contrarily, symmetric linear velocity profiles develop more coherent structures, which are in good qualitative agreement with laboratory experiments as those obtained prescribing a laboratory-measured flow field as initial condition (Fig. 5.15). Thus, there is larger similarity with the laboratory results when using linear profiles rather than with gaussian profiles. In fact, there is a larger similarity of the initial relative vorticity distributions in the laboratory cases with the vorticity distributions obtained with linear profiles rather than with those obtained with gaussian profiles. This reveals that the initial vorticity distribution has a relevant role in the shape of the resulting flow instability.

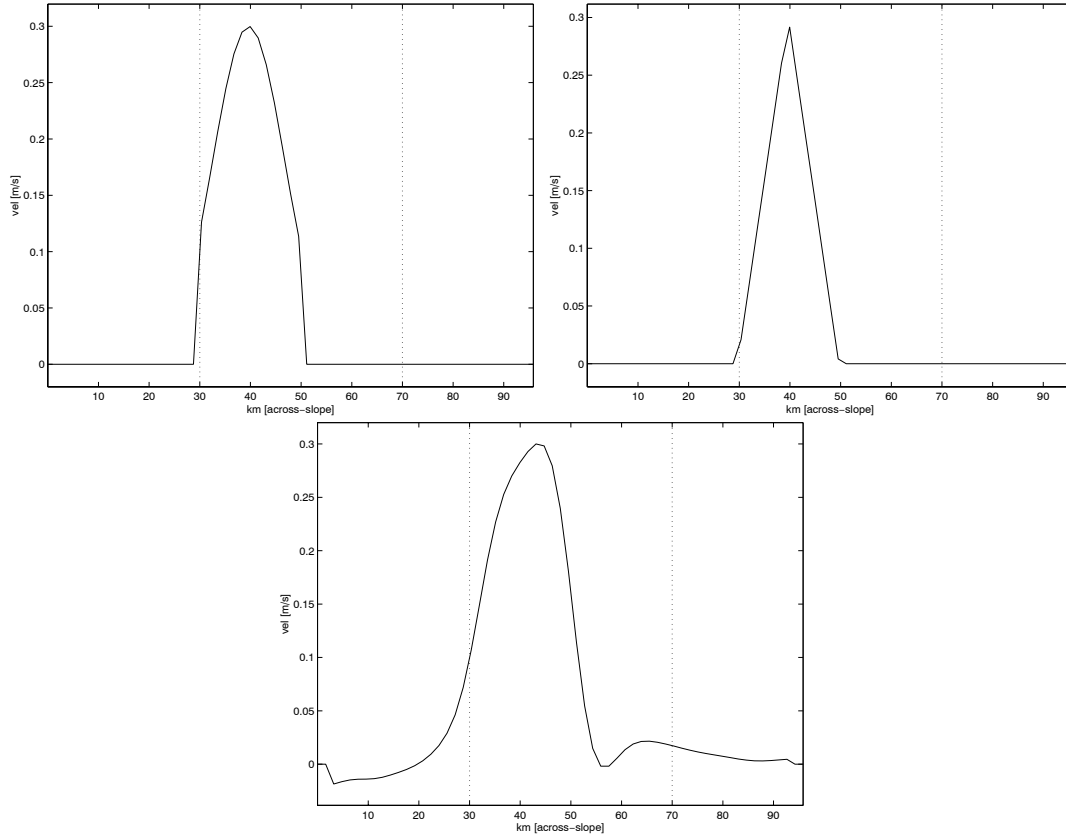


Figure 5.14: Velocity profiles of *westward* jets of maximum flow speed of  $30 \text{ cm s}^{-1}$  with a (i) symmetric gaussian profile (ii) symmetric linear profile and (iii) laboratory profile.

In order to further study the role of the interactions between both shear layers of the jet on the observed instabilities, the positive shear layer of the jet has been substituted by a constant velocity value (the maximum velocity in the linear profile) (Fig. 5.16)—in terms of vorticity, the flow now consists of a single layer of negative vorticity (Fig. 5.17). The resulting instabilities have a clear cat-eye pattern, contrasting with the squeezed vortices formed in the linear jet case. In the single vorticity layer case (Fig. 5.17), vortices are placed more down-slope than vortices obtained with the linear jet profile (Fig. 5.15), causing that in the former case meandering is limited over the mid-slope, whereas in the latter case meandering occurs over the upper half of the slope (Fig. 5.18). These differences are probably due to the interaction of vortices from each shear layer. Despite these differences, it is worth noting that wavelengths are fairly similar in both cases.

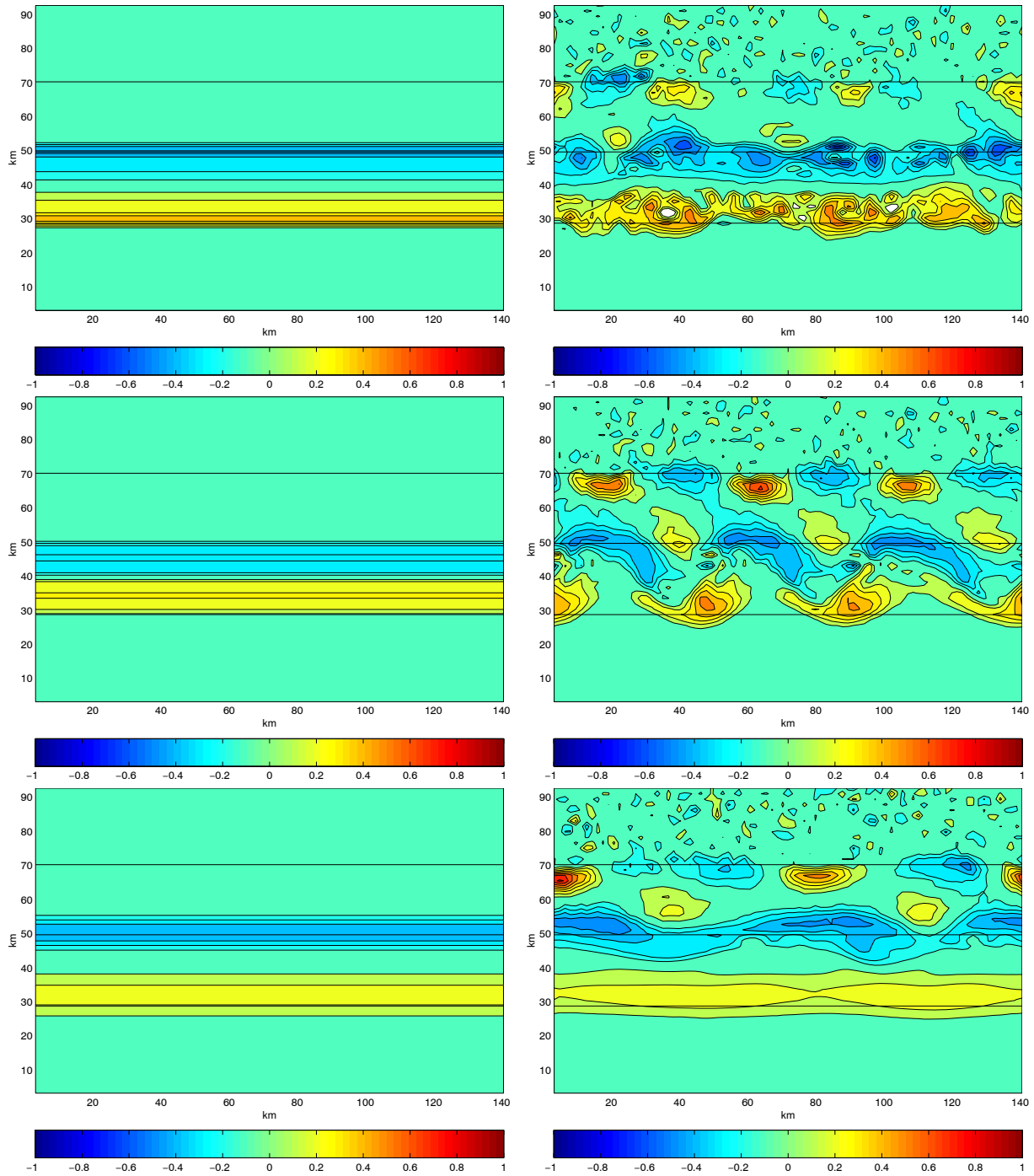


Figure 5.15: Top: Relative vorticity (day 18) of a gaussian-profile westward jet of maximum flow speed of  $30 \text{ cm s}^{-1}$ . Initial state is shown. Middle: Relative vorticity (day 15) of a linear-profile westward jet of maximum flow speed of  $30 \text{ cm s}^{-1}$ . Initial state is shown. Bottom: Relative vorticity (day 24) of a westward laboratory profile jet of maximum flow speed of  $30 \text{ cm s}^{-1}$ . Initial state is shown. Separation between isolines is  $0.1 \cdot 10^{-4} \text{ s}^{-1}$ .

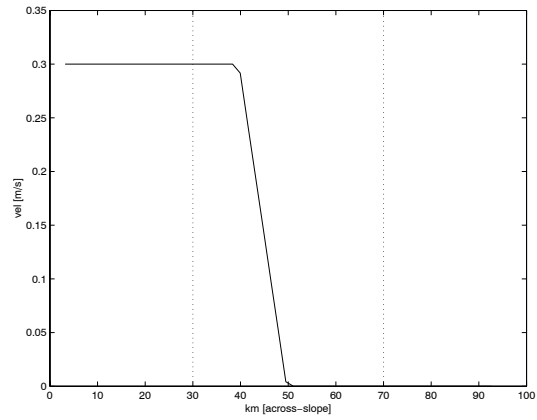


Figure 5.16: Velocity profile corresponding to a *westward* current of maximum flow speed of  $30 \text{ cm s}^{-1}$  with a single (linear) velocity shear layer.

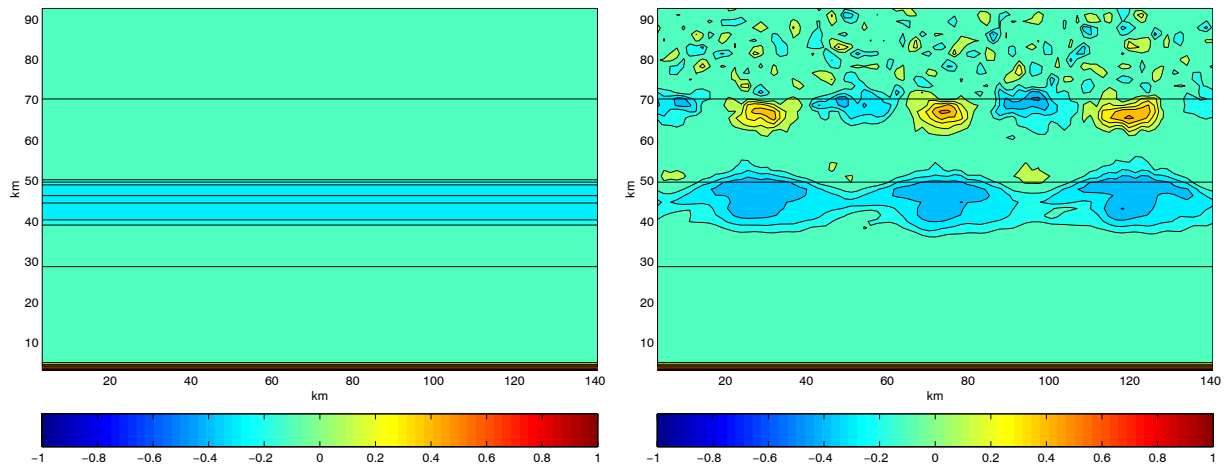


Figure 5.17: Relative vorticity of a linear negative shear layer current of maximum flow speed of  $30 \text{ cm s}^{-1}$ . Initial state is shown. Separation between isolines is  $0.1 \cdot 10^{-4} \text{ s}^{-1}$ .

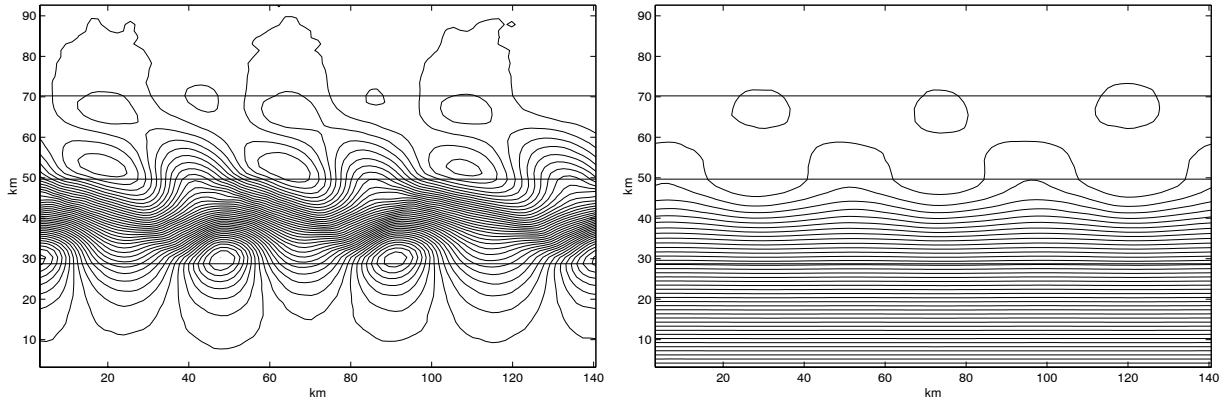


Figure 5.18: Corresponding streamlines for the symmetric linear jet from Fig. 5.15 (left) and for single shear layer current from Fig. 5.17 (right). Maximum flow speed is  $30 \text{ cm s}^{-1}$  in both cases.

The generation of the shelf-break Rossby wave for high flows is observed, independently of the velocity profile introduced. This result reveals the robustness of the shelf-break topographic wave generation.

#### 5.4.4 Synthesis

The shelf-break Rossby wave is a robust pattern. The appearance of the shelf-break Rossby wave is independent of the position of the current over the slope, the shape of the velocity shear profile of the jet, and the jet width. The only condition for its generation is to overpass a critical  $Ro$  number. When this occurs, the uppermost slope is affected by the slope current and a wave-like instability is triggered over the shelf break.

The characteristics of the generated instabilities (wavelength, phase speed, etc) depend on different factors, namely the  $Ro$  number, the water depth  $D$  over which the current flows, the width  $L$  of the current and the shape of the velocity profile. Summarizing, it is observed that:

(i) The increase in the  $Ro$  number produces an increase in wavelength and phase speed (Section 5.3).

(ii) A reduction in water depth restricts the size of instabilities (Section 5.4.1). This reduction in water depth produces an increase in the depth ratio number,  $\delta_2 = H / D$ . Therefore, there is a balance between the stabilizing role of  $\delta_2$  and the destabilizing role of  $Ro$ .

(iii) A reduction of the jet width causes a decrease of the instability wavelength (Section 5.4.2).

(iv) In the balance between the jet width and the water depth the factor that determines the instability wavelength seems to be the more restrictive one. In this way, the resulting instability will have the smaller of the two possible wavelengths (Section 5.4.2).

(v) The shape of the resulting instability seems to depend on the distribution of vorticity related to a given velocity profile. (Section 5.4.3).

(vi) The interaction between both shear layers of the jet is important. It seems to mainly influence the horizontal extension and position of the vortices in the across-slope direction.

## 5.5 Comparison with oceanic field data

In this section we emphasize the main characteristics (wavelengths, phase speed, etc) found for barotropic instabilities over a sloping bottom which may be more relevant in the context of the Northern Current.

Westward flows are observed to develop instabilities (vortices and associated meanders) at the edges of the jet. Therefore large mesoscale activity is observed, particularly over the upper half of the slope. Positive vortices over the mid-slope appear as sharp crests of the jet meanders; negative vortices are larger than positive vortices, leading to large troughs with anticyclonic tendency (Fig. 5.19 and Fig. 5.20). The picture is fairly similar to SST images, where the Northern Current appears meandering, often attached to upper-slope anticyclonic vortices (Fig. 5.21).

For increasing  $Ro$  numbers, more complicated patterns –more mesoscale activity– is observed over the upper slope. This is in agreement with oceanic data, where for larger Northern Current flows higher mesoscale activity is observed [Albérola et al., 1995].

For  $Ro = 0.1 - 0.2$  westward flows, instability wavelengths obtained both from the laboratory and the numerical experiments are of 50 – 75 km, similar to those observed in SST images. Instabilities propagate at 15 – 20 km day<sup>-1</sup>, in rough agreement with the estimated propagation speed of meanders and vortices in the Gulf of Lions of 10 – 20 km day<sup>-1</sup> [Millot, 1999]. These instabilities have associated periods of 3.3 – 3.8 days, which would be within the 2 – 10 days band (indeed in agreement with the 3.5-day band reported in Chapter 3) of mesoscale activity recorded from current meter devices.

It is also worth noting how for increasing  $Ro$  numbers the meandering of the westward current tends to place more up-slope (Fig. 5.20). This is also in agreement with oceanic observations where for increasing Northern Current flows the current was observed to flow more up-slope [Millot, 1999].

The main difference between our results and SST images is that SST images tend to show mainly anticyclonic vortices. Since a passive tracer as the surface temperature will tend to follow constant PV contours, an explanation to these observations might be given by the potential vorticity (PV) fields. It can be observed how cyclones tend to intensify PV gradients whereas anticyclones tend to smooth them –in fact, the core of the current and the upper-slope anticyclones have homogeneous PV values (Fig. 5.22). Thus, if a passive tracer as the SST is able to mark the surface path of the NC, it seems logical that it will tend to mark the anticyclones rather than the cyclones of the current instability.

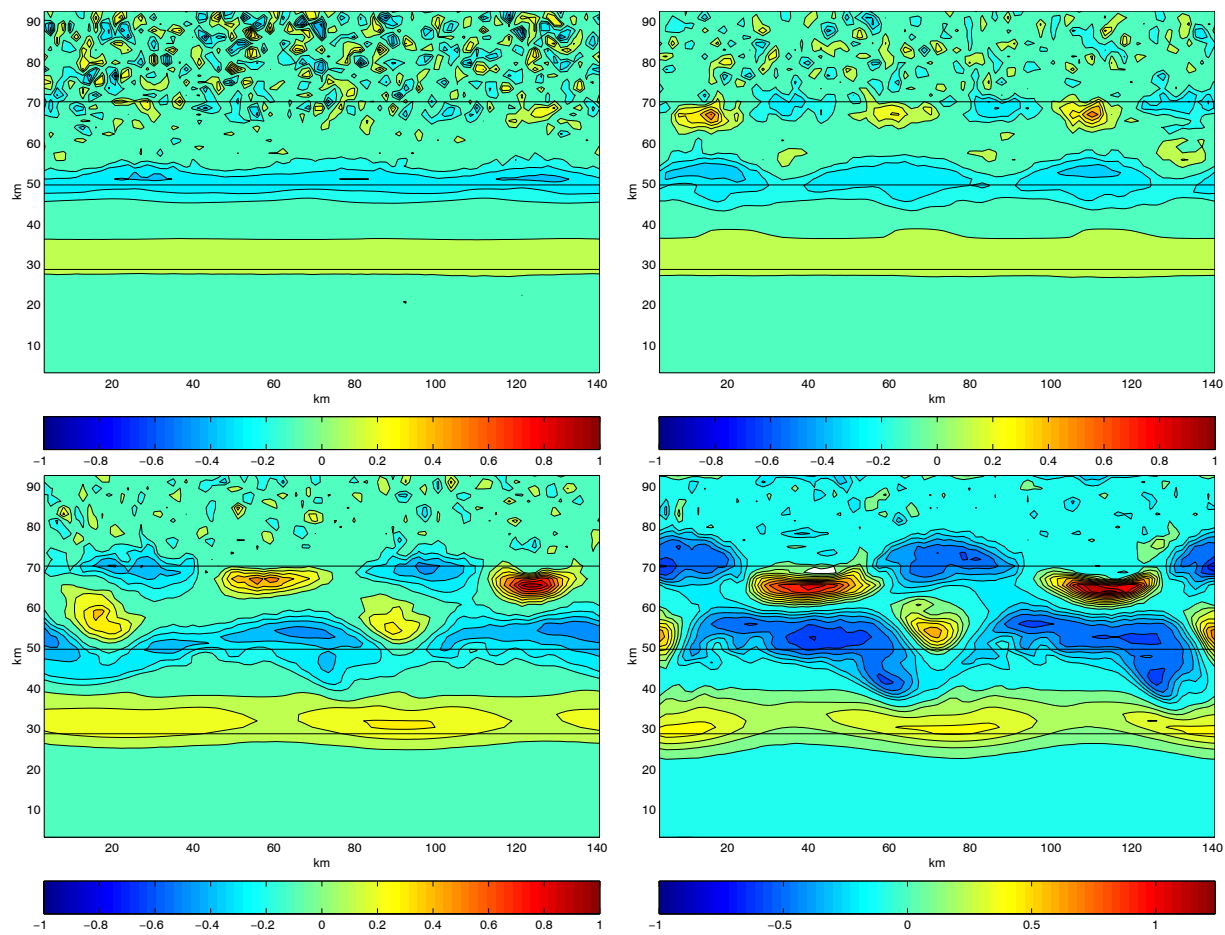


Figure 5.19: Relative vorticity for westward flows with initial maximum velocities of 0.20, 0.22, 0.30 and 0.42  $\text{cm s}^{-1}$  (from left to right and from top to bottom). Respective  $Ro = 0.10, 0.11, 0.15$  and  $0.21$ .



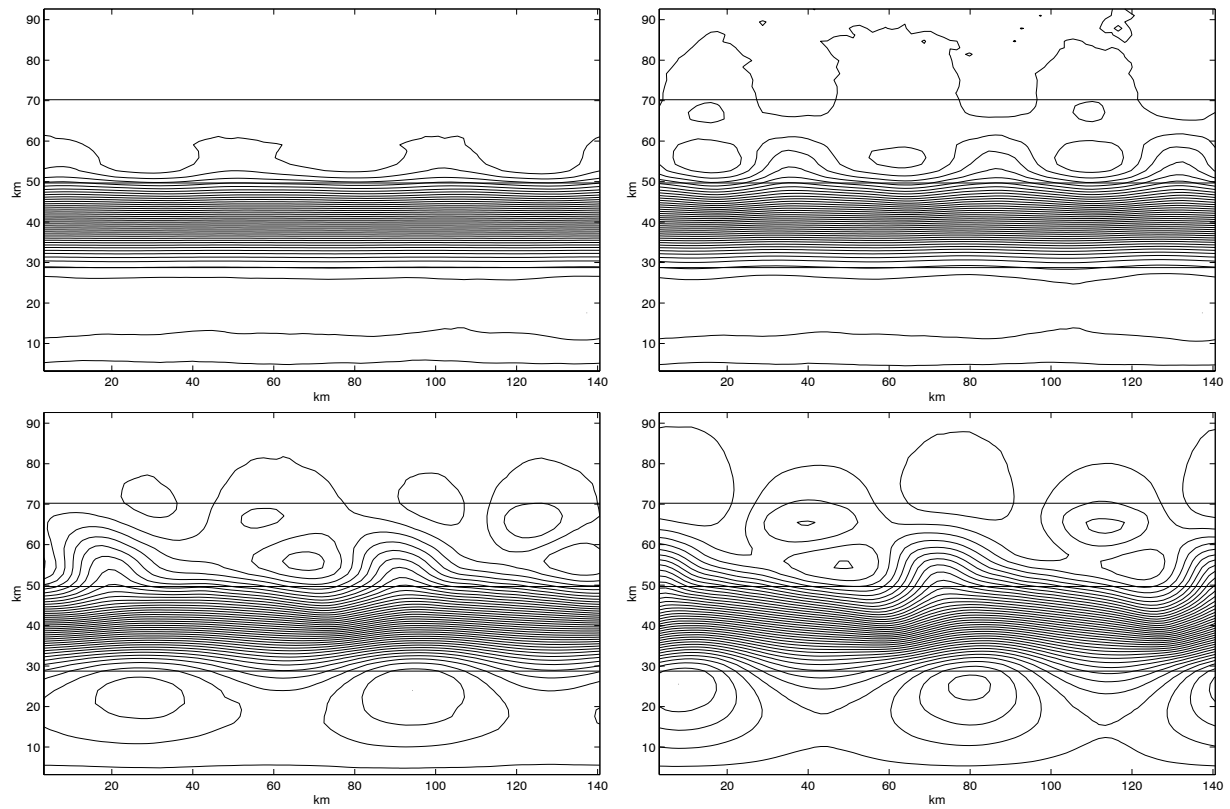


Figure 5.20: Corresponding streamlines for the westward flows in Fig. 5.19, with initial maximum velocities of 0.20, 0.22, 0.30 and 0.42  $\text{cm s}^{-1}$  (from left to right and from top to bottom). Respective  $Ro = 0.10, 0.11, 0.15$  and  $0.21$ .

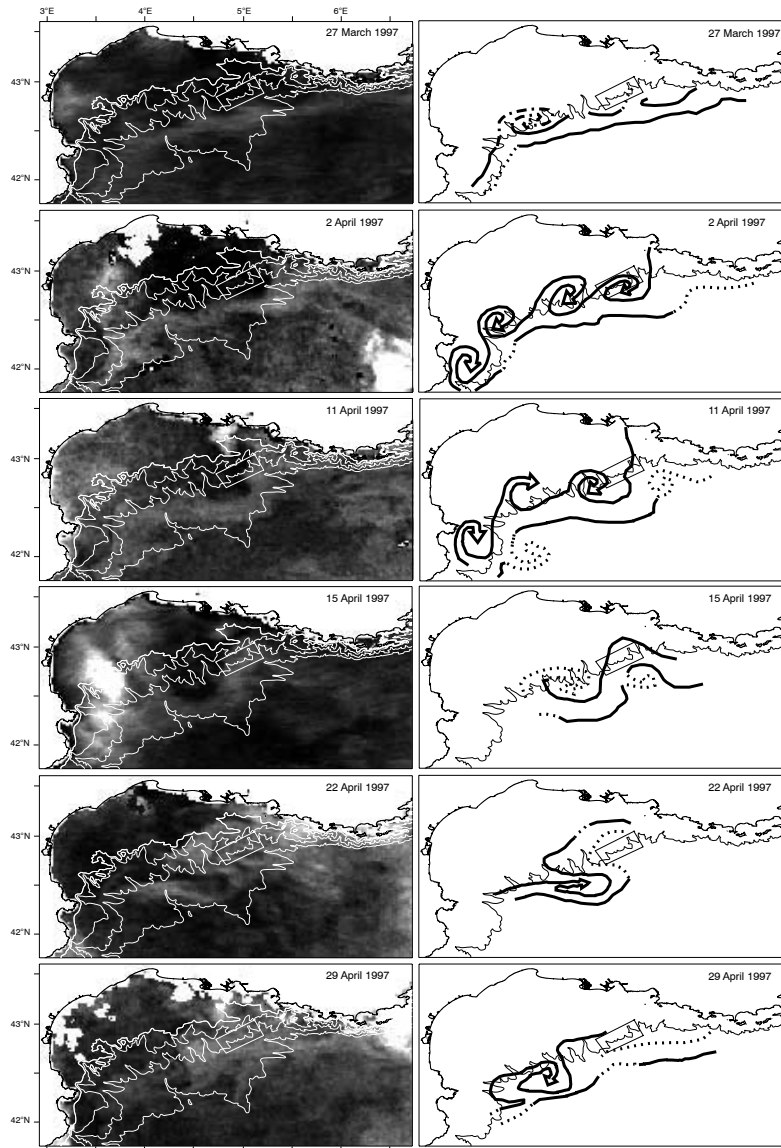


Figure 5.21: Sequence of AVHRR SST images and interpretative diagrams from March 27 to April 29 1997 on the entire Gulf of Lions, showing the westward propagation of a large meander over the eastern Gulf of Lions. The HFFE site and the 1000 m bathymetric contour are indicated. Lighter shades are warmer [Chapter 3 in this thesis].

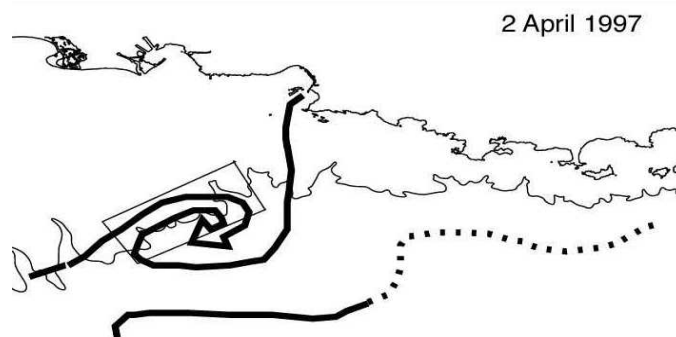
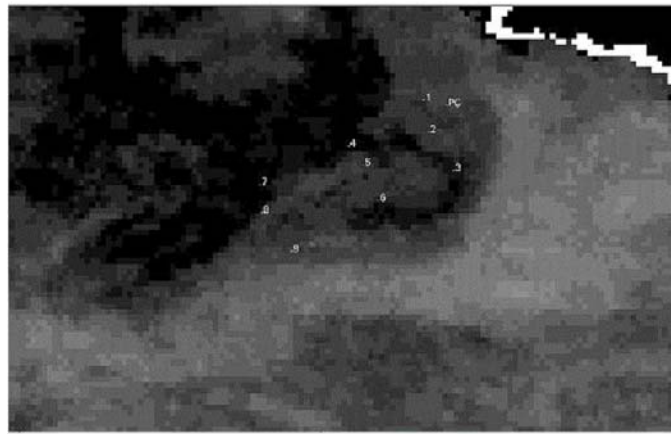
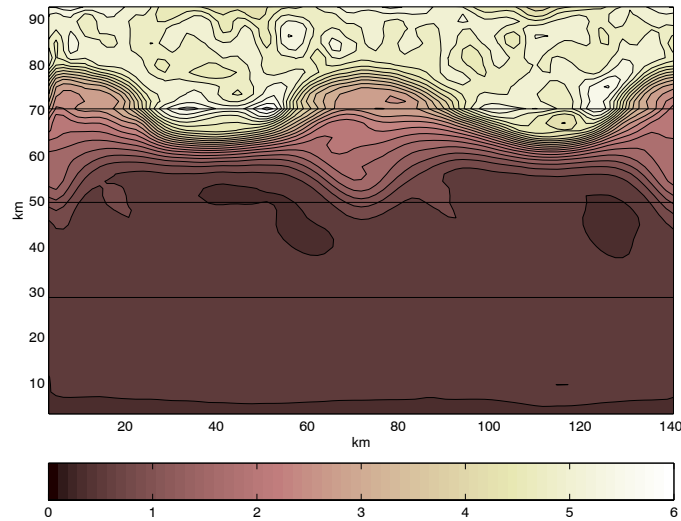


Figure 5.22: Top: Potential vorticity for a Regime II westward jet ( $Ro = 0.21$ ). Centre: SST image showing a typical anticyclonic structure (April 2nd 1997) over the MATER experiment site (mooring sites are shown). Bottom: Corresponding schematic interpretation of the SST image; the 1000m isobath crossing the experiment site and the experimental site location are shown [Chapter 3 in this thesis].

In terms of free surface elevation, the meandering of the current is distinguished, but the associated instabilities have very small free surface anomalies (Fig. 5.23). This parameter, though, looks particularly interesting for the shelf-break wave, which can present anomalies of the order of a few cm (Fig. 5.23).

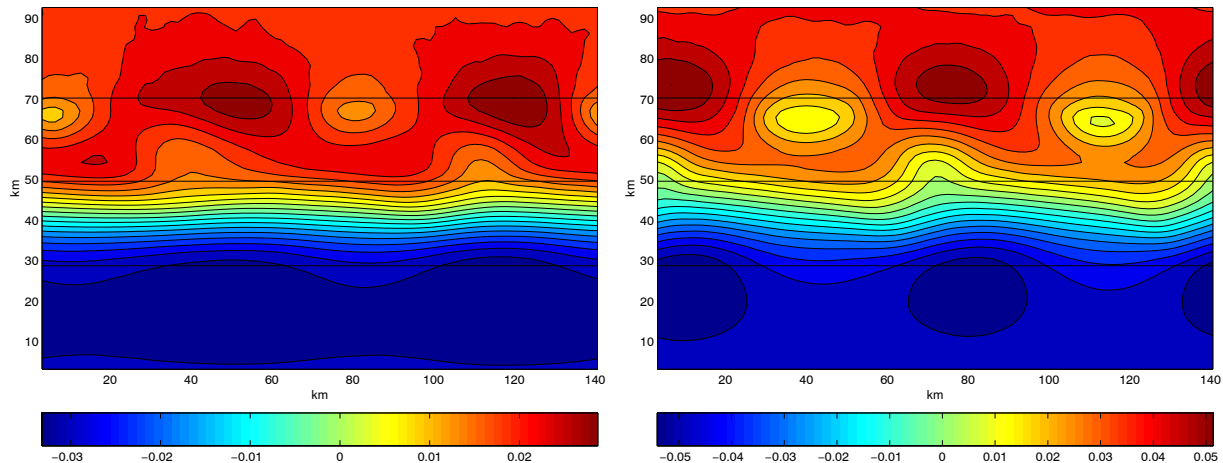


Figure 5.23: Free surface elevation (in m) of a westward current of maximum velocity of  $0.30 \text{ cm}\cdot\text{s}^{-1}$  (left) and of  $0.42 \text{ cm}\cdot\text{s}^{-1}$  (right).

The laboratory and numerical conditions studied here obviously differ from reality (i.e. oceanic conditions) due to the simplifications assumed in the experiments, which were chosen in order to reach the initial aims of this work. An important restrictive assumption is barotropicity, which was assumed in order to study the role of the barotropic instability and bottom topography on the mesoscale variability of the Northern Current. Another important difference comes from the boundary conditions, which were chosen in order to reproduce the laboratory conditions in which the jet currents were produced.

Traditionally, baroclinic instability has been thought to play a key role in the Northern Current at the Gulf of Lions. According to the work presented here, barotropic instability could also be a major factor to take into account, since the orders of magnitude of barotropic instabilities obtained for  $Ro = 0.1 - 0.2$  westward cases are similar to the mesoscale variability observed from oceanic field data. Obviously, it would be of particular interest to study the interaction between barotropic and baroclinic instability (i.e. mixed barotropic-baroclinic instability) to better understand the mechanisms which trigger and control the mesoscale variability reported at the Gulf of Lions region. The wavelength of the maximum growth rate wave resulting of mixed barotropic-baroclinic instability would lie between those for pure baroclinic instability and pure barotropic instability, and would depend on the relative strength of the two mechanisms [Tadepalli and Ferziger, 2000].

## 5.6 Summary and conclusions

In general, we have observed good qualitative and quantitative agreement between our laboratory and numerical experiments. The conclusions yielded from our numerical computations are summarized next.

Westward jets show a meandering tendency at the edges of the jet, whereas eastward jets have this meandering at the core of the current. This can be explained by PV conservation (see Chapter 4).

Westward slope currents flowing over the deeper half of the slope are able to modify the flow over the whole slope. Instabilities appear at the edges of the jet and over the shelf break. The instabilities of each side of the jet are thought to be a combination of Kelvin-Helmholtz like and Rossby-wave like structures due to the combined effect of velocity shear and topographic effects. The shelf-break Rossby wave is a robust result, which is independent of the position of the current over the slope, the shape of the velocity shear profile of the jet, and the jet width. The numerical experiments clarify that this upper-slope wave is triggered by the slope current. The only condition for its generation is to overpass a critical  $Ro$  number, which in the case of the averaged Northern Current values (i.e. those considered in Chapter 4) is  $Ro = 0.1$ .

In terms of onset of instabilities, westward jet instabilities grow while they displace in the mean flow direction with a phase speed of  $\simeq 80\%$  of the maximum flow speed. Instabilities of each shear layer are in phase, i.e. maximum positive values from each layer are aligned in across-slope direction.

For eastward jets, onset of instabilities is more variable. In Regime I eastward jets, instabilities are in counter-phase, and they move in the mean flow direction at  $\simeq 40\%$  of the maximum flow speed. The phase speed of the instabilities in Regime I eastward jets is more reduced in the numerical experiments (40 % of the maximum flow speed) than in the laboratory experiments (65 – 75 % of the maximum flow velocity). The reason for this remains still unclear to us. In Regime I flows ( $Ro < 0.2$ ), instabilities grow in two different ways: (i) for small  $Ro$  flows ( $Ro < 0.1$ ), instabilities move while they grow; (ii) for  $Ro = 0.1 - 0.2$  flows, positive instabilities grow in place (without advection) until the negative shear layer gets unstable, moment at which instabilities are in counter-phase and they start moving in the mean flow direction. We assume that this two different onset of instabilities could not be distinguished in the laboratory experiments because we were focussing on the ‘stable’ state of the jet. For Regime II eastward flows ( $Ro > 0.2$ ), instabilities grow in place without displacement. Instabilities from each shear layer are in phase, blocking any motion, and jet meandering at the core of the current is enhanced. Only for very large  $Ro$  flows ( $Ro > 0.3$ ), at late stages, negative vortices can fold up and locate in counter-phase with vortices from the positive shear layer, inducing a displacement of the instabilities of  $\simeq 40\%$  of the maximum flow speed. In summary, in eastward jets, instabilities from each shear layer appear in counter-phase when they move, and in phase when they do not displace. Therefore the relative distribution of vortices is thought to play an important role in the instability displacement.

Numerical tests varying different characteristics of the velocity profile revealed in-

interesting features. In one hand, it is observed that the  $Ro$  number has a destabilizing effect on the flow, whereas the depth ratio  $\delta_2$  has a stabilizing role. In the other hand, a reduction of the jet width  $L$  causes a decrease in the wavelength of the instabilities. Moreover, when variations in both  $L$  and  $\delta_2$  are involved, the resulting instability develops with the smallest wavelength, i.e. the instability wavelength is given by the restrictive factor. Numerical experiments using different velocity profiles revealed that the shape of the instability depends on the distribution of relative vorticity generated by the velocity profile of the jet. Besides, the interaction between both shear layers is proved to influence the horizontal extension and the position of the vortices in the across-slope direction.

As for the comparison of numerical results with oceanic data, the Northern Current often shows in SST satellite images as a meandering path over the deepest half of the continental slope, with anticyclonic vortices over the upper half of the slope. Numerical results for westward  $Ro \sim 0.1 - 0.2$  flows display meanders and vortices over the upper slope with wavelengths of 50 – 75 km and phase speeds of 15 – 20 km day<sup>-1</sup>, leading to periods ranging 3.3 – 3.8 days, in good agreement with Eulerian (current-meter) oceanic data (see Chapter 3). The correlation between the Northern Current speed and the mesoscale activity, and the up-slope migration of the Northern Current for increasing NC flow speeds, are also observed in our numerical results.

Mesoscale variability of the Northern Current is often attributed to NC meandering. Nevertheless, SST images show many anticyclonic vortices and few cyclones. A possible explanation to that is given by our results on the distribution of potential vorticity. Westward currents have homogeneous potential vorticity, the same PV than the anticyclones formed at the inner edge of the current, over the upper slope. On the contrary, cyclonic vortices separate from the mean flow by steep potential vorticity gradients. In this situation, a passive tracer (as PV and SST) that traces the NC path, would also tend to trace the anticyclonic vortices but not the cyclones. Moreover, our experiments show that anticyclones smooth PV gradients, whereas cyclones enhance them.

In conclusion, the Northern Current shows a mesoscale variability which can be largely explained in terms of barotropic instability of a westward current. Of course, baroclinic instability may also play an important role in the Northern Current variability (see Chapter 3) and it would be of the utmost interest to study the joint effect and mutual interaction of the different sources of mesoscale activity. The wavelength of the maximum growth rate wave resulting of mixed barotropic-baroclinic instability would lie between those for pure baroclinic instability and pure barotropic instability, and would depend on the relative strength of the two mechanisms [Tadepalli and Ferziger, 2000].

# Chapter 6

## Summary and conclusions

Bajo las circunstancias actuales, quiero decir que algunos problemas son más grandes que nuestros cerebros.

Eso puede ser una preocupación, pero también es una fuente de esperanza.

GEORGE STEINER

The main findings of this thesis are summarized below. Special attention is paid to highlight the new contributions of this research.

Previous studies showed that the Northern Current flows cyclonically contouring the continental slope in the NW Mediterranean. At the entrance of the Gulf of Lions this current is about 20 – 30 km wide and flows along the deepest half of the continental slope, i.e. over the 1000 to 2000 m isobaths approximately. Surface speeds are of 30 – 50 cm s<sup>-1</sup>. The velocity profile is maximum at the surface, with a smooth vertical shear decreasing with depth (due to stratification) down to about 300 – 400 m depth. Off Marseille, high mesoscale variability has been reported from Eulerian devices (current meters), relating this activity to current meandering. Mesoscale activity appears in two bands of 2 – 5 days and 7 – 10 days, respectively. Off Marseille, deep currents are strongly correlated with surface flows at the 2 – 5 days band. From SST images the path of the Northern Current appears often associated to meandering and anticyclonic activity over the upper continental slope [Chapter 2].

In the MATER HFF experiment (March – May 1997) mesoscale variability of the Northern Current is observed from current meter records, SST images and hydrographic data. The HFF experimental box is 20 x 40 km, covering the upper half of the slope (i.e. covering from 250 m to 1250 m depth isobaths). Current meter and satellite data show that the site is embedded in a region of significant Northern Current meandering and eddy activity. From SST images, meander wavelengths are estimated larger than 60 km, embracing smaller structures. These flow patterns affect upper-layer waters down to at least 650 m depth. Current meter data distinguish two narrow energetic bands centred at 3.5 days and 7.5 days, respectively, in agreement with previous studies [Chapter 3].

Baroclinic instability is viewed as a possible mechanism to explain the generation of

the Northern Current meanders. The analytical model of Tang [Tang, 1975] predicts the development of unstable waves of wavelength ( $> 60$  km) and periods compatible with the 7.5 day band recorded with current meter devices. The higher frequency band of 3.5 days is out of the frequency range predicted by the classical baroclinic instability theory and it is discussed as a restriction of quasi-geostrophic theory [Chapter 3].

Barotropic instability is studied using a laboratory model of a ‘westward’ jet flowing over the lower half of the continental slope, which considers dynamic similarity with the Northern Current [Chapter 4]. The laboratory model is cross-validated with a corresponding numerical model [Chapter 5]. Jet instabilities of currents similar to the Northern Current (i.e. westward jets) occur at the edges of the jet, showing a clear meandering tendency over the mid-slope. Westward currents of  $Ro = 0.1 - 0.2$  develop instabilities of wavelengths (50 – 75 km) similar to those observed from SST images, with periods (3.3 – 3.8 days) compatible with the 3.5 days period band recorded with HFFE current meters. The numerical experiments reveal that vortices of positive relative vorticity constitute the crests of the meander, whereas anticyclones show closed paths at the troughs of the meander. The potential vorticity has similar homogeneous values at the jet and at the anticyclonic vortices, indicating that a passive tracer able to mark the path of the current (as SST) would preferably track anticyclonic vortices (in agreement with SST image observations). Other particularities of the Northern Current are observed in the barotropic experiments: the up-slope migration of the current for increasing current velocities, and the correlation between the increase in jet speed and the intensification of mesoscale activity.

The laboratory and numerical experiments have reproduced westward jets (as the Northern Current), but also eastward jets, in order to have a full approach to better understand the role of the bottom topography on barotropic instabilities. The comparison between eastward (retrograde) and westward (prograde) jets revealed interesting aspects which are summarized below.

The currents studied in this thesis (which were in the range  $Ro = 0.04 - 0.25$ ) have all been found unstable [Chapter 4 and Chapter 5]. The bottom topography has an important role in organizing the flow and its corresponding instabilities [Chapter 4]. Increasing Rossby numbers are observed to destabilize the current, whereas larger depth ratios  $\delta_2 = H/D$  (where  $H$  is the elevation of the slope and  $D$  the water depth) have a stabilizing role on the jet instabilities [Chapter 5].

The slope current instabilities are successfully explained by the Marcus and Lee theory of jets on a beta plane [Marcus and Lee, 1998], indicating the equivalency between both types of flows [Chapter 4]. Moreover, the laboratory experiments presented here reveal the predominant role of the eastward/westward character of the jet compared to its prograde/retrograde (defined in relation with the direction of rotation of the system) character. This observation is important regarding laboratory simulations [Chapter 4]. The Marcus and Lee theory is valid for westward flows with  $Ro > 0.1$  and for eastward flows with  $Ro > 0.2$  (jets of the so-called Regime II flows in this thesis), and it states that the instabilities of each shear layer of the barotropic jet take the appearance of a Kelvin-Helmholtz-like pattern, associated with a Rossby wave (of topographic origin in our case). According to this theory, the differences between eastward and westward jets rely on the



disposition of the Rossby waves –at the centre of the current in eastward flows and at the edges of the jet in westward currents. Jets over a sloping bottom with small Rossby numbers ( $Ro < 0.1$  for westward jets;  $Ro < 0.2$  for eastward jets) show a flow pattern (the so-called Regime I in this thesis) that has common characteristics for eastward and westward flows. In these ‘small’- $Ro$  flows, Kelvin-Helmholtz-like instabilities dominate, whereas Rossby waves are too weak to produce any major difference between jets flowing in eastward or westward direction. This occurs when the topographic influence, assumed proportional to the  $Ro$  number of the jet, is small. Thus, the critical Rossby number separating Regime I and Regime II flows is proportional to the inclination degree of the topographic slope –making Regime I non-existent for very low slopes [Chapter 4].

The differences between eastward and westward slope currents observed in this work (and similar observations of jets on a beta-plane from previous works) are explained in this thesis by a simple scheme based on conservation of potential vorticity, considering there are two main components in balance: the shear-induced vorticity and the topographically induced vorticity. The signs of these two components are determined by the relative direction of the flow with respect to the inclination of the bottom topography. Once the critical Rossby number is overpassed so that the topographic effects are important ( $Ro > 0.1$  for westward jets;  $Ro > 0.2$  for eastward jets), conservation of potential vorticity tends to enhance vortices at the centre of eastward jets –eastward jets show meandering at the jet core. In westward jets, potential vorticity conservation is responsible of enhancing vortices at each edge of the jet. Thus, westward jets (as the Northern Current) are broad and meandering occurs at the jet edges [Chapter 4].

In  $Ro > 0.1$  westward flows (i.e. Regime II westward jets) a topographic Rossby wave appears over the shelf break [Chapter 4]. This result is likely observed because of the specific topography used in this work –a continental slope and a continental shelf separated by a shelf break, producing a strong change in ambient potential vorticity. Numerical simulations reveal that this Rossby wave is triggered by the slope current [Chapter 5]. The formation of the shelf-break wave is independent of the angle of the sloping bottom, since equivalent results are obtained with the laboratory model (in which the geometrical ratio is exaggerated: slope = 0.45) and the numerical model (where the slope has a realistic value: slope = 0.07). This topographic Rossby wave is a robust pattern, since it is independent of the position of the current over the slope, the shape of the velocity shear profile of the jet, and the jet width [Chapter 5]. Although this type of wave could not be inferred from the HFFE field data, it could be a focus of study in further field experiments. It also needs further analytical consideration.

Bottom intensifications over the mid-slope (at 1250 m depth) are observed in the HFF site, in principle not correlated with the upper-layer mesoscale activity [Chapter 3]. Maximum activity is observed in periods ranging 3 – 8 days, and they are traditionally associated with topographic Rossby waves [Chapter 2 and Chapter 3]. As mentioned above, in westward jets the topographic Rossby waves tend to locate at the edges of the jet [Chapter 4], which in the case of a current flowing over the lower half of the slope (as the Northern Current in the Gulf of Lions) would represent a preference for the mid-slope. This would be in principle coherent with the intensifications over the mid-slope (over the

1250 m isobath) observed in the HFF experiment [Chapter 3].

The general conclusion extracted from this thesis that tries to explain the mesoscale variability associated to the Northern Current is that both baroclinic and barotropic instability could explain part of the oceanic observations. As a consequence, mixed barotropic-baroclinic instability (which occurs at wavelengths which are between those corresponding to pure barotropic and pure baroclinic instability) is thought to play an important role on the observed mesoscale variability. The resulting wavelength would depend on the relative strength of both mechanisms.

Scientific methodologies follow organized and highly specialized schemes to produce their results. This extreme specialization, although helpful for technological purposes, may also draw science into 'blind' or narrow alleys of research, in the sense that close disciplines may mutually ignore one and other. This thesis aimed to reach some multidisciplinary by using laboratory techniques to solve an oceanographic problem. The use of parallel field and laboratory studies is not new, but allows a deeper understanding into the dynamics of field measurements by posing simpler questions.

Blindness in science not only refers to the production of narrow unipolar works. We should not despise that, as far as our scientific objectives directly depend on power schemes, our scientific knowledge is used mainly by and for 'rich' countries, deepening differences between 'North' and 'South', instead of tending to eliminate them. This elimination should be the leading aim of scientific knowledge. To overcome this paradox, Ismail Serageldin (who states that 'we are witnessing a scientific apartheid in this century' which 'will be a major problem unless science mobilization occurs' [Serageldin, 2003]) cites the example of the abolitionists. Slavery was abolished because it was an inconceivable problem of conscience, not because it were considered a technical problem nor because it were economically convenient. In fact, the presence of open civic structures has been demonstrated to press far more than economic factors.

The resulting human consequences of this aforementioned 'scientific apartheid' should urge all of us to take action. I address mine to the reader of this thesis, fully aware of a shared trust in the benefits that our work may produce. In the words of Ismail Serageldin, we cannot permit 'knowledge being taken off by those most advantaged'.

# Bibliography

- [1] C. Albérola, C. Millot, and J. Font. On the seasonal and mesoscale variabilities of the northern current during the primo-0 experiment in the western mediterranean sea. *Oceanologica Acta*, 18(2):163–192, 1995.
- [2] P.A Arnau. *Aspectos de la variabilidad de mesoescala de la circulacion marina en la plataforma continental catalana*. PhD thesis, Univ. Politècnica de Catalunya, Barcelona, 2000.
- [3] M. Astraldi and G.P. Gasparini. Influence of the climatic conditions on the winter fluxes in the corsican channel. In L.J. Pratt, editor, *The Physical Oceanography of Sea Straits*, volume C318, pages 211–224. NATO/ASI Ser., Kluwer, Boston, Massachussets, 1990.
- [4] M. Astraldi and G.P. Gasparini. The seasonal characteristics of the circulation in the north mediterranean basin and their relationship with the atmospheric-c.limatic conditions. *J. Geophysical Research*, 97:9531–9540, 1992.
- [5] M. Astraldi, G.P. Gasparini, and S. Sparnocchia. The seasonal and interannual variability in the ligurian-provençal basin. *Coastal and Estuarine Studies*, 46:93–113, 1994. In: Seasonal and Interannual variability of the Western Mediterranean Sea.
- [6] J.A. Barth. Short-wavelength instabilities on coastal jets and fronts. *J. Geophysical Research*, 99:16095–16115, 1994.
- [7] M. Benzohra and C. Millot. Characteristics and circulation of the surface and intermediate water masses off algeria. *Deep Sea Research*, 42(10):1803–1830, 1995.
- [8] A.F. Blumberg and G.L. Mellor. A description of a three-dimensional coastal ocean circulation model. In N. Heaps, editor, *Three-Dimensional Coastal ocean Models*, page 208. American Geophysical Union, 1987.
- [9] S.L. Blumsack and P.J. Gierasch. Mars: the effects of topography on baroclinic instability. *J. Atmospheric Sciences*, 29:1081–1089, 1972.
- [10] G.F. Carnevale, R.C. Kloosterziel, and G.J.F. van Heijst. Propagation of barotropic vortices over topography in a rotating tank. *J. Fluid Mechanics*, 233:119–139, 1991.

- [11] P. Conan and C. Millot. Variability of the northern current off marseilles, western mediterranean sea, from february to june 1992. *Oceanologica Acta*, 18(2):193–205, 1995.
- [12] M. Crépon and M. Boukthir. Effect of deep water formation on the circulation of the ligurian sea. *Annales Geophysicae*, 5B(1):43–48, 1987.
- [13] M. Crépon, L. Wald, and J.M. Monget. Low-frequency waves in the ligurian sea during december 1977. *J. Geophysical Research*, 87 C1:595–600, 1982.
- [14] B. Cushman-Roisin. *Introduction to geophysical fluid dynamics*. Prentice Hall, New Jersey, 1994.
- [15] S. Dalziel. *DigImage. Image Processing for Fluid Dynamics*. Cambridge Environmental Research Consultants Ltd., 1992.
- [16] X. Durrieu de Madron. Hydrographic and nepheloid structures in the grand-rhône canyon. *Continental Shelf Research*, 14(5):457–477, 1994.
- [17] X. Durrieu de Madron, F. Niffeler, and C.H. Godet. Hydrographic structure and nepheloid spatial distribution in the gulf of lions continental margin. *Continental Shelf Research*, 10:915–929, 1990.
- [18] X. Durrieu de Madron, O. Radakovitch, S. Heussner, M.D. Loye-Pilot, and A Monaco. Role of the climatological and current variability on shelf-slope exchanges of particulate matter: Evidence from the Rhône continental margin (nw mediterranean). *Deep Sea Research I*, 46:1513–1538, 1999.
- [19] F. Diaz, P. Rimbault, and P. Conan. Small-scale study of primary productivity during spring in a mediterranean coastal area (gulf of lions). *Continental Shelf Research*, 20:975–996, 2000.
- [20] P.G. Drazin and W.H. Reid. *Hydrodynamic Stability*. Cambridge University Press, Cambridge, 1981.
- [21] J.-M. Nguyen Duc and J. Sommeria. Experimental characterization of steady two-dimensional vortex couples. *J. Fluid Mechanics*, 192:175–192, 1988.
- [22] E.T. Eady. Long waves and cyclone waves. *Tellus*, 1:33–52, 1949.
- [23] B. Ferré. Influence du vent sur la circulation dans le golfe du lion et la mer catalane: Etude numerique. Master’s thesis, LIM and CNRS and CEFREM, 2001.
- [24] M.M. Flexas, X. Durrieu de Madron, M.A. Garcia, M. Canals, and P.A. Arnau. Flow variability in the gulf of lions during the mater hff experiment (march-may 1997). *J. Marine Systems*, 33-34:197–214, 2002.

- [25] J. Font, E. Garcia-Ladona, and E. Gorriz. The seasonality of mesoscale motion in the northern current of the western mediterranean: several years of evidence. *Oceanologica Acta*, 18(2):207–219, 1995.
- [26] F. Gaillard, Y. Desaubies, U. Send, and F. Schott. A four-dimensional analysis of the thermal structure in the gulf of lion. *J. Geophysical Research*, 102(C6):12515–12537, 1997.
- [27] J.C. Gascard. Mediterranean deep water formation baroclinic instability and oceanic eddies. *Oceanologica Acta*, 1(3):315–330, 1978.
- [28] J. Hall and S. Smith. First report of the jgofs/loicz continental margins task team. LOICZ reports and studies nr. 7 21, JGOFS, 1996.
- [29] L.N. Howard. Note on a paper of john w. miles. *J. Fluid Mechanics*, 13:158–160, 1961.
- [30] J.M. Huthnance. Circulation, exchange and water masses at the ocean margin: the role of physical processes and the shelf edge. *Progress in Oceanography*, 35:353–431, 1995.
- [31] R.C. Kilosterziel and G.J.F. van Heijst. An experimental study of unstable barotropic vortices in a rotating fluid. *J. Fluid Mechanics*, 223:1–24, 1991.
- [32] A. Lapouyade and X. Durrieu de Madron. Seasonal variability of the advective transport of suspended particulate matter and organic carbon in the gulf of lions (nw mediterranean). *Oceanologica Acta*, 24:295–312, 2001.
- [33] Li and McClimans. On the stability of barotropic prograde and retrograde jets along a bottom slope. *J. Geophysical Research*, 105(C4):8847–8855, 2000.
- [34] K.K. Liu, L. Atkinson, C.T.A. Chen, S. Gao, J. Hall, R.W. McDonald, L. Talaue McManus, and R. Quiones. Exploring continental margin fluxes on a global scale. *EOS, Transactions, American Geophysical Union*, 81:641–644, 2000.
- [35] P.S. Marcus and C. Lee. A model for eastward and westward jets in laboratory experiments and planetary atmospheres. *Physics of Fluids*, 10(6):1474–1489, 1998.
- [36] Méditerranée Occidentale MEDOC-Group. Observation of formation of deep water in the mediterranean. *Nature*, 227:1037–1040, 1970.
- [37] C. Millot. Evidence of a several-day propagating wave. *J. Physical Oceanography*, 15(3):258–272, 1985.
- [38] C. Millot. The structure of mesoscale phenomena in the ligurian sea inferred from the dyome experiment. *Annales Geophysicae*, 5B(1):21–30, 1987.
- [39] C. Millot. The gulf of lions’ hydrodynamics. *Continental Shelf Research*, 10(9-11):885–894, 1990.

- [40] C. Millot. Models and data: a synergetic approach in the western mediterranean sea. In P. Malanotte-Rizzoli and A.R. Robinson, editors, *Ocean Processes in Climate Dynamics: Global and Mediterranean Examples*, pages 407–425. Kluwer, 1994.
- [41] C. Millot. Circulation in the western mediterranean sea (review paper). *J. Marine Systems*, 20:423–442, 1999.
- [42] C. Millot, M. Benzhora, and I. Taupier-Letage. Circulation off algeria inferred from the mediproduct-5 current meters. *Deep-Sea Research I*, 44(9-10):1467–1495, 1997.
- [43] C. Millot and M. Crépon. Inertial oscillations on the continental shelf of the gulf of lions -observations and theory. *J. Physical Oceanography*, 11:639–657, 1981.
- [44] C. Millot and L. Wald. The effect of mistral wind on the ligurian current near provence. *Oceanologica Acta*, 3(4):399–402, 1980.
- [45] D. Obaton, C. Millot, G. Chabert d’Hières, and I. Taupier-Letage. The algerian current: comparisons between in situ and laboratory measurements. *Deep-Sea Research I*, 47:2159–2190, 2000.
- [46] J. Pedlosky. *Geophysical fluid dynamics*. Springer-Verlag, 1979.
- [47] P. Puig, A. Palanques, J. Guillén, and E. García-Ladona. Deep slope currents and suspended particle fluxes in and around the foix submarine canyon (nw mediterranean). *Deep-Sea Research I*, 47:343–366, 2000.
- [48] M. Rhein, U. Send, B. Klein, and G. Krahnemann. Interbasin deep water exchange in the western mediterranean. *J. Geophysical Research*, 104(C10):23495–23508, 1999.
- [49] R.M. Samelson and J. Pedlosky. Local baroclinic instability of flow over variable topography. *J. Fluid Mechanics*, 221:411–436, 1990.
- [50] C. Sammari, C. Millot, and L. Prieur. Aspects of the seasonal and mesoscale variabilities of the northern current in the western mediterranean sea inferred from the prolig-2 and pros-6 experiments. *Deep-Sea Research I*, 42(6):893–917, 1995.
- [51] I. Serageldin. Science, poverty and hunger: challenges for a connected world. Dir. Library of Alexandria, February 2003. Museu de La Ciència, Fundació La Caixa, Barcelona.
- [52] X.B. Shi and L.P. Red. Frontal instabilities in a two-layer, primitive equation ocean model. *J. Physical Oceanography*, 29:948–968, 1999.
- [53] T.H. Solomon, W.J. Holloway, and H.L. Swinney. Shear flow instabilities and rossby waves in barotropic flow in a rotating annulus. *Physics of Fluids A*, 5:1971–1982, 1993.
- [54] J. Sommeria, S.D. Meyers, and H.L. Swinney. Laboratory simulations of jupiter’s great red spot. *Nature*, 331:689–693, 1988.

- [55] J. Sommeria, S.D. Meyers, and H.L. Swinney. Laboratory model of a planetary eastward jet. *Nature*, 337:58–61, 1989.
- [56] J. Sommeria, S.D. Meyers, and H.L. Swinney. Experiments on vortices and rossby waves in eastward and westward jets. In A. Osborne, editor, *Non-linear Topics in Ocean Physics*, pages 227–269. North-Holland, Amsterdam, 1991.
- [57] A. Sournia, J.M. Brylinski, S. Dallot, P. Le Corre, M. Leveau, L. Prieur, and C. Froget. Fronts hydrologiques au large des côtes françaises: Les sites-ateliers du programme frontal. *Oceanologica Acta*, 13(4):413–438, 1990.
- [58] S. Tadeipalli and J.H. Ferziger. Simulation of coastal upwelling i. linear stability and the early turbulent regime. *J. Physical Oceanography*, (Submitted), 2000.
- [59] C-M. Tang. Baroclinic instability of stratified shear flows in the ocean and atmosphere. *J. Geophysical Research*, 80(9):1168–1175, 1975.
- [60] I. Taupier-Letage and C. Millot. General hydrodynamical features in the ligurian sea inferred from the dyome experiment. *Oceanologica Acta*, 9(2):119–131, 1986.
- [61] I. Taupier-Letage and C. Millot. Surface circulation in the algerian basin during 1984. *Oceanologica Acta*, 9:119–131, 1988.
- [62] R.R. Trieling, A.H. Linssen, and G.J.F. van Heijst. Monopolar vortices in an irrotational annular shear flow. *J. Fluid Mechanics*, 360:273–294, 1998.
- [63] M.H. Tusseau-Vuillemin, L. Mortier, and C. Herbaut. Modelling nitrate fluxes in an open coastal environment (gulf of lions): Transport versus biogeochemical processes. *J. Geophysical Research*, 103(C4):7693–7708, 1998.
- [64] G.A.J. van der Plas and R.J.M. Bastiaans. Accuracy and resolution of a fast ptv-algorithm suitable for hires-pv. In I. Grant and G.M. Carlomagno, editors, *Proceedings of the 8th International Symposium on Flow Visualisation*, Sorrento, Italy, 1998.
- [65] G.J.F. van Heijst. Topography effects on vortices in a rotating fluid. *Mechanica*, 29:431–451, 1994.
- [66] F. van Wambeke, S. Heussner, F. Diaz, P. Rimbault, and P. Conan. Small-scale variability in the coupling/uncoupling of bacteria, phytoplankton and organic carbon fluxes along the continental margin of the gulf of lions, north western mediterranean sea. *J. Marine Systems*, 33-34:411–429, 2001.
- [67] A. Viúdez and J. Tintoré. Time and space variability in the eastern alboran sea from march to may 1990. *J. Geophysical Research*, 100:8571–8586, 1995.





## CASTELL D'IRÀS I NO TORNARÀS

La pel·lícula *Blue Velvet*, de David Lynch, comença amb una escena torbadora: la càmera s'acosta lentament al caragol auditiu d'una orella trobada al parc, davant de casa, i es capbussa als cels pintats de la ment per mirar-hi l'arborar-se d'un malson. O pot venir-nos al cap, també, un quadre de Delacroix, igualment il·luminat amb la llum trasbalsada de l'irracional, en què una barca lluita, sola en la mar, contra el naufragi. Són mans llençades cap a una cosmogonia dantesca feta de cercles i cels i profunditats, on s'accedeix a la interpretació de la realitat deixant-se dur per un remolí. Que és ara l'orella i adés haguessin pogut ser els sols -Van Gogh-, o el Maelstrom -Verne-, o els ciclons -Conrad-, o les fugues -Bach-, o les escales de caragol -Hitchcock. A endur-se'ns les imatges que suscita en la ment un moviment circular i sostingut. I la ciència: una mirada metòdica i disciplinada, però no pas superior a les altres mirades, un camí més. Una interpretació racional del món.

Que ens posem a llegir-la sabedors que el miratge d'una explicació única del món ja s'esvaí al segle XX, que la idea d'una realitat objectiva, laplaciana i darwinista, es desféu entre els dits dels qui escrivien la física quàntica -Heisenberg, Planck- i palpaven els límits del llenguatge -Poincaré, Hoffmanstal, Wittgenstein. I ens esqueixa encara el divorci entre la veritat científica i l'autoritat, que regien plegades quan allò que la ciència postulava com a cert desembocava en una aplicació cada cop més formidable. Això avui, que obrim el diari i llegim un rebombori que n'altera els fonaments conceptuals -són immutables, encara, les lleis físiques?- mentre que el gruix de la comunitat s'aboca a les aplicacions del coneixement racional amb aquella mentalitat decimonònica. I en oceanografia, que les lleis per als corrents s'expressen en derivades parcials de segon ordre i no hi ha 'oceanografia quàntica', se segueix investigant en l' 'anàlisi objectiva' de les mesures recollides. Que som vassalls d'una dinastia periclitada quan insistim en explicacions absolutes, que cal saber-ho i mirar per les escletxes els qui mouen tramoia rere aquest decorat que ja no s'ajusta al que sabem.

Ni al que pensem, perquè en aquesta redescoberta de la subjectivitat científica llegim en els resultats, també, els valors morals que són els llibants de la carpa de la ciència, ni únics ni constants. Per exemple: la supremacia de l'home en la natura està cosida a la visió mecanicista -encara majoritària en la tecnocràcia-, i la consciència de formar part d'un sol ésser de gran complexitat -que limita l'autoritat de l'home sobre la natura-, ho és a la visió fractal nascuda a finals del segle XX. O les consideracions sobre l'atzar en la generació de les formes -també els corrents marins, meandres i remolins-, com allunyen la idea que tot és predictable; i és com si fos ahir que el tercer moviment 'espontani' en els àtoms -Epicur- es convertia en

argument per defensar la llibertat. I fins i tot, qui sap, si la consideració central d'aquesta tesi sobre la validesa dels models barotròpics -més ordenats- i baroclínics -més desgavellats i proclius a la generació d'inestabilitats- respecte d'aquestes mateixes idees morals no ens sorprendria amb implicacions inesperades. La ciència fent-se a imatge de la moral de cada temps, i forjant ètiques, i el científic rondant la cadira del savi, buida com en els contes de la Xina antiga, i una tesi doctoral que no és un mer tràmit sinó que és un treball de profunda implicació personal.

Que avui ja no és només l'actitud del qui pren la realitat que observa com a mirall -l'oceanògraf que veu en la turbulència dels corrents un reflex de les seves emocions- o com a signe que cal interpretar. Ni tampoc l'actitud de qui, convençut dels beneficis que es poden derivar del coneixement científic, s'hi posa en cos i ànima en un gest necessari. El que fou abans que això: una 'existència nòmada' -Las Palmas, Bangor, Barcelona, Grenoble, Eindhoven, Mallorca, Perpinyà- i deu anys de viatge -la meitat dels que Ulisses estigué per la Mediterrània. I a cada lloc, equips de treball -el treball de base de la ciència, avui, és col·lectiu, i fins la interpretació ho sol ser- col·laborant en aproximacions diferents a l'estudi de les inestabilitats del corrent que corre al golf de Lleó. Estudis experimentals, models analítics, models numèrics i models físics: tota una gamma de metodologies proposant resultats parcials per confegir una interpretació dels corrents marins. I la ment, voluptuosa, en el plaer de dir les coses. Però també, cru de realitat, sense drama ni llegenda, l'enginy de què s'ha de valdre una doctoranda, aquí, per aconseguir no només un finançament digne, sinó fins i tot una dedicació suficient per part del professorat. Càlculs i habilitats per no fer atots als passadissos universitaris. El perill del naufragi, tan real als viatges que s'ho valen. I Circe, que entretindria la navegant a cada un dels laboratoris amb recerques sense fi. I qui sap si cap Polifem no es miraria els argonautes-becaris com a garrins, per consumir-los -aprofitar-se'n- després... Goigs i perills del viatge.

Això és -el viatge- trenar-se al coneixement que es va fent i desfent a cada pas, al camí sense tornada que és l'elaboració de la mirada racional, a les complexitats conceptuals del llenguatge científic que han estat vistes, tantes vegades en la història, com un pas necessari en el guany de la llibertat. Vorejant, cada cop de més amunt, el risc del coneixement. Des de la tristesa de ser conscient de què ens parla Alberto Caeiro -Pessoa- fins la tragèdia de Sòfocles en què Èdip, el rei il·lustrat que respongué a l'esfinx amb lògica, s'hagué d'arrençar els ulls quan conegué la seva pròpia història. Per dir-ho avui: quin afany de saber justifica que sigui l'estament militar el recolzament principal de mètodes i infraestructures, també en oceanografia? Quines condicions imposa aquesta dependència? I, encara, el terra incert on reposen les certeses. La veritat, deia Nietzsche, és una convenció social per a la pervivència de la comunitat, i la ciència una depuració de les metàfores amb

què el llenguatge es vol fer al món. I, seguim ara, l'assaig de trobar lleis, no és una forma dissimulada d'intencions i voluntat d'aplicar-les? Com es conforma això a la descoberta, en la vastitud d'una mirada sobre la mar, d'un paisatge sense intencions, esdevingut i irrepètible?

Amb tot, però, deixar escrites en aquest llenguatge les turbulències de la mar perquè, diríem, el voler deixar dita la mirada mou la roda de la ciència. La mirada, ara que ja no pot ser el retrat passiu d'un objecte i és participar en la realitat. Deixar testimoni que hem vist les coses, que hem intentat veure'ns enmig de les coses, el remolí del coneixement adreçat a la utopia de viure entre les coses. Si fos per això l'oceanografia i l'afigurar-se dels corrents, fluències i dissipacions, si fos per això un aire de llegenda als relats dels oceanògafs... Conten que un dels llocs on més sovint s'han observat remolins dels que estudia na Mar és allà que en diuen La Malica, entre les foneres de Blanes i Palamós. I com són les coses que una rondalla per l'estil del castell-d'iràs-i-no-tornaràs hi situa una ciutat submarina on els homes poden anar per viure-hi feliços i en bona harmonia amb els peixos, però no en poden tornar. És a la rondalla que hi ha una utopia a l'altra banda de l'aigua, feta com per acostar-s'hi assumint el risc de perdre el control. I què hi ha en aquesta tesi, en el revolt per poder mirar, encara i alhora com si mai no ho haguéssim fet, una Malica a l'altra banda dels remolins? Quin castell s'hi alça d'iràs i no tornaràs?

JOAN PUIGDEFÀBREGA



## Acknowledgements

Sembla que després de tot ha arribat el moment d'acabar aquesta tesi. M'ho he passat realment bé durant aquests anys i per això tenc molt a agrair a tots els que d'una manera o altra n'heu format part.

Amb qui vull començar és amb la família. Tenc tot a agrair-vos, ja ho sabeu, i aquí ho faré potser de manera un poc telegràfica però així i tot... A mon pare en Maties i als meus padrins Catalina i Francisco, pels faros i per la mar. A n'es conco Gaspar i la tia Bel, pels estius a Can Rodella i per fer tant bé de padrins joves. A n'es conco Guillem i la tia Francisca, per fer-ho tant bé com saberen. Al meu germà, en Francesc, per haver nascut, gràcies, per ser la alegríia de la huerta. A mumare na Maite per tot el que és, tot el que m'ha ensenyat, per ensenyar-me a mirar. A en Toni per en Tristán i per donar-me la il.lusió per la ciència. A na Cati per ajudar-me a posar paraules a les coses i a en Tomeu pel seu exemple. A en Pere per ser el millor cosí del món! Als meus padrins na Catalina i en Tomeu, per les flors, pels rissos, per les ganes de viure. A tots, gràcies per recolzar-me i per no anar-vos-en.

Vull agrair als meus supervisors Marc Garcia i Agustín Sánchez-Arcilla per obrir-me les portes al món de l'oceanografia i per corregir-me aquesta tesi, per dur-me a l'Antàrtida i per enviar-me a Grenoble. I am very grateful to GertJan van Heijst for giving me the opportunity to develop part of my thesis in Eindhoven, because without his help this thesis would only be a half of what it is now. But most of all I want to thank you for the kindness you always had towards me.

I want to thank Joan Puigdefàbrega who kindly accepted to write 'El Castell d'iràs i no tornaràs' for this thesis. With his contribution I aim to point out the fact that this thesis was not made only by me, but it is the result of multiple collaborations.

Voldria seguir agraint-li a en Joan, de qui he après més que de molts de llibres, haver-me passejat per programes, equacions, ports, barques, platges i museus; es un plaer fer feina amb tu. I per descomptat a en Biel, per totes les que hem passat, per l'ajut que comporta tenir-te cada dia a la feina. A en Manolo, qui m'ha recolzat en tot moment, sobretot en els darrers anys, vull agrair-li especialment la seva confiança en mi. Vull agrair també tot aquest temps a tota la gent del LIM, y en particular a Josito por la alegríia que lleva (y por las sevillanas). Tambe vull agrair a la gent dels barcos pesquers de la Madre Guapa de Sant Carles de la Ràpita (Julians) i la Núria de Blanes (Ramon i Miquel) els passejos i les converses durant aquests anys.

I want to thank Xavier Durrieu de Madron for his interest in this work and his professionalism. It was a real pleasure to work with Ruben Trieling and all the people at TU/e –in particular I want to thank the technicians and also Wouter van Elmpt for his help processing HPV data. I am very grateful to Dr. Mathew Wells for reading and correcting this thesis. Quiero agradecer a Jose Manuel Redondo su ayuda con una beca SOCRATES para irme a Eindhoven. Ha estat també un plaer fer feina amb en Jordi Salat. A en Damià

li agrairia les nostres xerrades esporàdiques (oficials i oficioses).

Mr. Eddy DeCay, thanks a lot for inviting me to collaborate in your experiments in Grenoble in October 2000 –it was a pleasure. I am very grateful to Prof. Don Boyer and Andjelka Sridic who showed me the insides of a submarine canyon; I am grateful for your kindness and the naturalness you always had towards me. My work at CORIOLIS was a real experience thanks to all the people there. I can say it was a real privilege to see Carcel-Didelle in action. I am very grateful to Joel Sommeria for making possible my two stages there, as well as for his help with a grant to assist to the Grand Combin Summer School in Aosta on July 2002.

I want to thank the people in The Netherlands, my flatmates Ana, Alex and Athon for all the birthdays and laughs in Eindhoven and Helmond. I want to thank Michel for my first months at TU/e. A ti Gabriel, nunca podré agradecerle lo suficiente las risas en el despacho, vos lo sabés bien. Ni a Sergio el fojón y la capoeira. Thanks Mathew for your company during all this time.

A en Joanic li vull agrair tot el que hem passat junts al pis de Gràcia, perquè viure amb tu ha estat un vertader plaer. Com també ho han estat les nombroses nits al Cafè amb el Xavi i la gent del dos cantons de Torrijos amb Perla. A en Ramon, per tot el que hem fet junts. A na Sol per les classes de francès i pels sopars amb cava. A na Maite Masses, per ser la millor companya de pis que es pot tenir. A la Marta li vull agrair aquest temps que hem passat juntes a casa, per ser tant fàcil viure amb tu. Estos últimos meses se los quiero agradecer a Ma y a Inma, que llegó como llovida del cielo.

A los ya eternos, a n'Ignasi -el Jefe- y a Israel por las llamadas y las visitas cuando se puede y por el verano pasado en Banyalbufar, a en Marc per arribar quan tanta falta em feies, i per dur amb tu a n'Alfredo. A ti Alfredo, gracias por aparecer, porque estar contigo hace que quiera ser mejor persona. Porque no hi ha res com la gent que me té en compte encara que no hi sigui, gràcies Marieta i Marcos, per estar sempre pendents.

Y ya para terminar, quiero recordar desde aquí con todo el cariño del mundo a José Curbelo y a Javi Arias. Ojalá estuviérais aquí.

Como solía brindar mi abuelo en ocasiones especiales:

*Nunca menos, siempre más*

Besos grandes a todos  
M<sup>a</sup> del Mar

## Curriculum Vitae

Maria del Mar Flexas was born in Mallorca (Spain) on February 6, 1975. From 1988 to 1992 she followed pre-university education at the Institut Ramon Llull in Palma de Mallorca. In September 1992 she went to Las Palmas de Gran Canaria (Canary Islands, Spain) to study Marine Sciences at the Universidad de Las Palmas de Gran Canaria (ULPGC) and graduated in July 1997. From September 1997 to November 1998 she lived in Bangor (North Wales, UK) where she carried out an MSc program in Applied Oceanography at the School of Ocean Sciences (SOS, Univ. of Wales). She graduated with a MSc thesis on inertial oscillations over the Catalan continental shelf, under the supervision of J.H. Simpson. From November 1998 to January 1999 she was involved in an oceanographic cruise in Antarctica with the Laboratori d'Enginyeria Maritima from the Universitat Politècnica de Catalunya (LIM/UPC). After that, she moved to Barcelona where she started her PhD research at the LIM/UPC. Parallel to her PhD research, she has collaborated at the CORIOLIS facility in Grenoble (France) in a gravity currents project with Dr. Peter Thomas (Univ. Warwick, UK) in November 2000, and in a project concerning the flow over a submarine canyon with Prof. Don Boyer (Univ. Arizona, USA) in January 2001. From September 2001 to November 2002 she did part of her PhD research at the Technische Universiteit of Eindhoven (TU/e, Nederland) with Prof. GertJan van Heijst. This doctoral thesis is the result of the four-year period between Barcelona and Eindhoven.